



**HAL**  
open science

# A comprehensive study of the erosion mechanism of porous hybrid particles for biomedical applications

Ioanna Christodoulou

► **To cite this version:**

Ioanna Christodoulou. A comprehensive study of the erosion mechanism of porous hybrid particles for biomedical applications. Material chemistry. Université Paris-Saclay, 2021. English. NNT : 2021UPASF020 . tel-03626956

**HAL Id: tel-03626956**

**<https://theses.hal.science/tel-03626956v1>**

Submitted on 1 Apr 2022

**HAL** is a multi-disciplinary open access archive for the deposit and dissemination of scientific research documents, whether they are published or not. The documents may come from teaching and research institutions in France or abroad, or from public or private research centers.

L'archive ouverte pluridisciplinaire **HAL**, est destinée au dépôt et à la diffusion de documents scientifiques de niveau recherche, publiés ou non, émanant des établissements d'enseignement et de recherche français ou étrangers, des laboratoires publics ou privés.

# A comprehensive study of the erosion mechanism of porous hybrid particles for biomedical applications

**Mécanisme de dégradation de particules poreuses hybrides organiques-inorganiques pour des applications biomédicales**

**Thèse de doctorat de l'université Paris-Saclay**

École doctorale n° 571 sciences chimiques :

Molécules, Matériaux, Instrumentation et Biosystèmes (2MIB)

Spécialité de doctorat: Chimie

Unité de recherche : Université Paris-Saclay, CNRS, Institut des Sciences Moléculaires d'Orsay, 91405, Orsay, France

**Thèse présentée et soutenue à Paris Saclay, le 31 mars 2021, par**

**Ioanna CHRISTODOULOU**

## Composition du Jury

**Laure CATALA**

Professeur, Université Paris Saclay

Présidente

**Florence GAZEAU**

Directeur de Recherche CNRS, Université Paris Diderot

Rapporteur & Examineur

**Stefan WUTTKE**

Professeur, University of Basque Country

Rapporteur & Examineur

**Jean-Marc GRENECHE**

Directeur de Recherche CNRS, Université Le Mans

Examineur

## Direction de thèse

**Ruxandra GREF**

Directeur de Recherche CNRS, Université Paris Saclay

Directeur de thèse

**Christian SERRE**

Directeur de Recherche CNRS, Ecole Normale Supérieure, Ecole Normale Supérieure de Physique et de Chimie Industrielles de Paris, PSL University

Co-Directeur de thèse

**Cédric BOISSIERE**

Directeur de Recherche CNRS, Sorbonne Université

Invité



# **Acknowledgements**

## Acknowledgements

First and foremost, I would like to express my appreciation to all the members of the thesis committee, Dr. Florence Gazeau of the Université de Paris and Dr. Stefan Wuttke of BC Materials in Bilbao, Prof. Laure Catala of the Université Paris Saclay and Dr. Jean-Marc Greneche of the Université Le Mans for accepting to evaluate and discuss my work and for their insightful comments.

Bernard Bourguignon et Thomas Pino, les directeurs de l'Institut des Sciences Moléculaires d'Orsay (ISMO) pour m'avoir accueilli dans leur famille et avoir été toujours gentils avec moi.

Je voudrais exprimer ma sincère gratitude à mon superviseur, Dr Ruxandra Gref, pour m'avoir donné l'opportunité de rejoindre son équipe dans le laboratoire récemment créé à l'ISMO d'Orsay et m'avoir ouvert la porte du monde magique du "drug delivery". Ce fut un honneur pour moi de collaborer avec une personne ayant un tel enthousiasme pour la recherche. Ses idées innovantes et les discussions fructueuses que nous avons partagées ces dernières années m'ont permis d'obtenir une vision plus large de la science. Sa personnalité aimable et discrète s'est imposée dès notre première rencontre. Je lui suis très reconnaissante pour son aide et ses suggestions tout au long de mes recherches et surtout durant cette dernière année de pandémie. Malgré toutes les difficultés, elle n'a jamais perdu patience, créant toujours un environnement amical et trouvant des solutions à chaque problème.

Christian Serre, mon co-encadrant, qui a été le premier à me donner la chance de rejoindre un laboratoire français pendant mon stage de Master et m'a permis de rester à l'IMAP à Paris. Son expertise et sa connaissance approfondie des MOFs font autorité et ont été très importantes pour mes recherches théoriques et expérimentales. Je vous remercie pour toutes les discussions et votre temps précieux. Vous êtes le "ligand" essentiel qui relie tous les membres de la famille IMAP.

Dr. Cédric Boissière, mon mentor et collaborateur, merci pour l'opportunité de travailler au LCMCP, Sorbonne Université et de rejoindre votre équipe. Merci pour tous les dimanches que vous avez passés avec moi via Skype pour m'expliquer ce que signifie un coefficient d'extinction !

Tous les collaborateurs qui ont apporté énormément à ce travail.

Je souhaite remercier Dr. Christian Marlière d'avoir accepté de combiner la physique et la biochimie et pour toute son aide lors des expériences AFM et de la rédaction de notre article.

Dr. Gilles Patriarche pour avoir réalisé les études STEM-HAADF. Il était toujours disponible pour observer les échantillons.

Dr. Guillaume Maurin et Dr Pengbo Lyu de l'Université de Montpellier pour avoir fourni des simulations théoriques, qui ont été plus qu'essentielles pour mes études expérimentales.

Dr. Charlotte Martineau-Corcoc et Dr. Marianna Porcino de l'Université d'Orléans pour notre collaboration très efficace en RMN du solide, avec lesquelles je partage mon premier article.

Remerciements particuliers à Dr. Antoine Tissot et à Dr. Farid Nouar qui ont été plus que des collègues pour moi.

Dr. Antoine Tissot, mon premier superviseur pendant le Master 2, qui m'a fait aimer les MOFs, et qui a toujours été disponible pour moi plus tard, pendant mon doctorat.

## Acknowledgements

Dr. Farid Nouar, qui a consacré une grande partie de son temps précieux à m'apprendre à montrer la beauté des cristaux. Il a été d'une générosité et d'un soutien sans faille.

My team in Orsay (Lisa, Jingwen, Seray, Mai, Tom, Killian and Farah) with a special thought for Tom and Mai for helping me throughout my studies. I wish you the best for the future!! I will always be available for you!

My team in Paris (Heng, Amy, My-An, Shan, Raquel, Bingbing, Chenchen, Yuwei, Esma) and all the permanent staff (Antoine, Mathilde, Georges, Iurii, Bernard).  
Every person of ESPCI; Farid, Vanessa, Inès, Shyama, Audrey, Mathilde, Mégane, Nicolas, Pierre.

All the people that left but will always be in my heart: Andrea, Oleksy, Angelika, Kevin, Saad, Fay, Sujing, Alex, Nello, Lin, Tanmoy, Luke, John.

Seray (soon Dr.!!) the first person I met at ISMO, my office mate and my best friend. You made my life happier! Thank you for the coffee, the drinks, the trips, all the support and for letting me use your computer when I wanted to throw away mine. We will always have Paris! Thank you for everything!

My great family in Paris: Adrien, Antonis, Cleo, Eirini, Foivi, Giannis, Korina, Valadis and my best friends all around Europe: Anna Maria, Christina, Eleutheria, Eleni, Marianina, Zoe, Marianna, Stefania, Anna, Vivian and Yannis.

Ma famille en Grèce pour tout leur amour et leur soutien et mon frère Michael avec qui j'ai vécu à Paris toutes ces années. Tout ne serait pas pareil sans toi ! Merci pour ta patience.

Enfin, un grand merci à Maria, Christina et Antonis. Même si vous êtes loin, vous êtes toujours avec moi.

MERCI À TOUS!





## Abbreviations

AI	Active Ingredient
ADME	Administration, Distribution, Metabolism, Excretion
AFM	Atomic Force Microscopy
ALF	Artificial Lysosomal Fluid
AML	Acute Myeloid Leukaemia
AMP	Adenosine Monophosphate
ATP	Adenosine Triphosphate
AZT-MP	Azidothymidine 5'-Monophosphate
AZT-TP	Azidothymidine 5'-Triphosphate
BET	Brunauer Emmet Teller
BSA	Bovine Serum Albumin
CBS	Carbosilane dendrimers
CD	Cyclodextrin
CD-MOFs	Cyclodextrin Metal Organic Frameworks
CMC	Critical Micellar Concentration
CPD	Phosphorus dendrimers
CSD	Chemical Solution Deposition
DFT	Density functional theory
DLS	Dynamic Light Scattering
DDS	Drug delivery systems
DPBS	Dulbecco's Phosphate Buffer Saline
FDA	Food and Drug Administration
FFT	Fast Fourier Transform
FT-IR	Fourier-transformed infrared spectroscopy
CSD	Cambridge Structural Database
	Chemical Solution Deposition
DLS	Dynamic Light Scattering
DDS	Drug delivery systems
DPI	Dry Powder Inhaler
EDX	Energy Dispersive X-Ray
EE	Encapsulation Efficiency
FDA	Food and Drug Administration
FT-IR	Fourier-transformed infrared spectroscopy
GCs	Glucocorticoids
Gem-MP	Gemcitabine Monophosphate
GOx	Glucose Oxidase
ISO	International Organization of Standardization

HA	Hyaluronic acid
HPLC	High Liquid Performance Chromatography
MDI	Metered-dose inhaler
MIL	Materials of Institut Lavoisier
MIP	Materials of the Institut of Porous Materials of Paris
MSNs	Mesoporous Silica Nanoparticles
MTN	Mobil Thirty Nine
MTX	Methotrexate
MOF	Metal Organic Framework
MW	Microwave synthesis
LD <sub>50</sub>	Lethal Dose
NPs	Nanoparticles
NU	Northwestern University
NMR	Nuclear Magnetic Resonance
PAMAM	Poly(amido)amine dendrimers
PBS	Phosphate Buffer Saline
PCN	Porous Coordination Network
PCP	Porous Coordination Polymer
PEG	Polyethylene glycol
PLA	Poly lactic acid
PLGA	Poly lactic-co-glycolic acid
PP	Prednisolone sodium phosphate
PPI	Polypropyleneimine dendrimers
PS	Methyl prednisolone sulfate
PSPD	Position-sensitive photodiode
PXRD	Powder X-Ray Diffraction
RT	Room Temperature
SAMs	Self-assembled monolayers
SBU	Secondary Building Unit
SEM	Scanning Electronic Microscopy
STEM	Scanning Transmission Electron Microscopy
STEM-HAADF	Scanning TEM with High Annular Dark Field
SE	Spectroscopic Ellipsometry
TGA	Thermal Gravimetric Analysis
TPT	Topotecan
TEM	Transmission Electronic Microscopy
UiO	University of Oslo
UV-Vis	Ultraviolet Visible
5-Fu	5-Fluorouracil
ZIF	Zeolitic Imidazolate Framework
WAXS	Wide-angle X-ray Scattering
XPS	X-Ray Photoelectron Spectroscopy

# Table of Contents

<b>General Introduction</b>	<b>1</b>
<b>Synthèse en français</b>	<b>7</b>
<b>Chapter I</b>	
Introduction	<b>11</b>
A. Nanomedicines	13
B. Types of drug carriers	17
C. Metal Organic Frameworks (MOFs)	24
D. Characterization techniques	39
E. MOFs for drug delivery: Degradation mechanism and <i>in vivo</i> fate	49
F. Conclusions	73
G. References	74
<b>Chapter II</b>	
Degradation mechanism of porous metal-organic frameworks by in situ Atomic Force Microscopy	<b>83</b>
<b>Chapter III</b>	
Advanced characterization methodology to unravel MOF stability in extremely dilute conditions	<b>113</b>
<b>Chapter IV</b>	
Drug loading in nanoscale MOFs and release kinetics: new insights from STEM-HAADF microscopy	<b>151</b>
<b>General Discussion &amp; Perspectives</b>	<b>193</b>
<b>General Conclusion</b>	<b>207</b>
Annex	209



# **General Introduction**



## General Introduction

Nanotechnology has received enormous attention some years ago and nowadays we can clearly claim that it has been established to almost every domain of novel research.<sup>1</sup> In biochemistry, nanoparticles (NPs) can function as carriers of active ingredients (AIs) for the treatment of various diseases.<sup>2-4</sup> The choice of nanotechnology compared to conventional therapies presents some important advantages:

1. protection of unstable/poor soluble active molecules and prevention of "burst" release
2. targeted delivery of active molecules by a controlled manner, avoiding undesired side effects
3. efficient crossing of epithelial and endothelial barriers and successful intracellular diffusion
4. co-encapsulation and delivery of multiple drugs for combination therapy
5. combination of imaging and therapy by multifunctional nanovectors for several diseases (theragnostics).

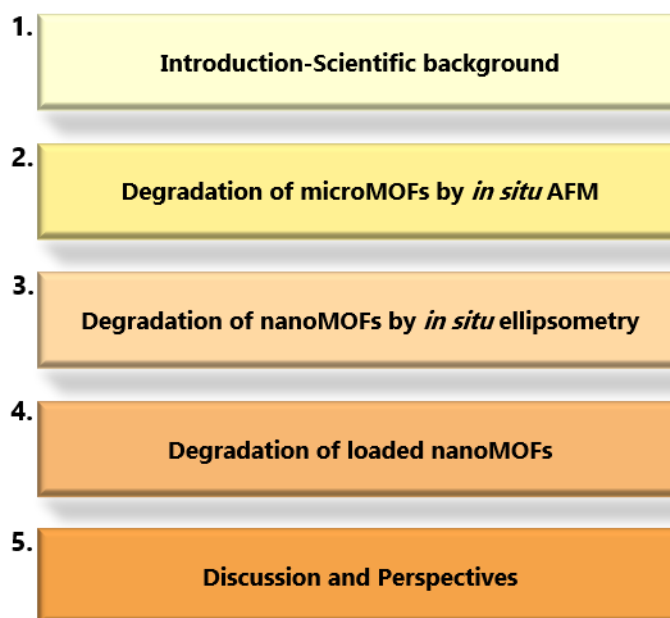
A plethora of particles have been studied as drug nanovectors since 1970s.<sup>5-7</sup> The last decade, hybrid porous particles named Metal Organic Frameworks (MOFs) have gained more and more ground as pharmaceutical carriers, thanks to their high internal surface areas, chemical and structural diversity, surface engineering and their controllable (green) synthesis down to the nanoscale.<sup>8,9</sup> Among a large variety of MOFs the iron (III) trimesate MIL-100(Fe) (MIL stands for Materials of Lavoisier Institute) is a benchmark MOF candidate for biomedical applications.<sup>10</sup> MIL-100(Fe) exhibits a mesoporous architecture built of iron trimers of metal octahedra connected by trimesate ligands delimiting mesoporous cages accessible through microporous windows. One of its main features is the presence of open metal sites able to bind directly a large variety of guest molecules (gases, vapors, drugs, enzymes, etc.). As a result of these unique features, MIL-100(Fe) can host several drugs (both hydrophobic and hydrophilic).<sup>11-15</sup> Noteworthy, it can be synthesized via "green" methods leading to particles ranging from less than 100 nm up to a few microns.<sup>16-18</sup> MIL-100(Fe) is biodegradable in body fluids and is biocompatible, as deduced from previous *in vitro/vivo* studies.<sup>19,20</sup> The term biocompatible signifies a material, which, *grosso modo*, is non toxic for the organism neither throughout its circulation inside the body nor its degradation byproducts. Kohane and Langer have aptly commented on a review paper, that

biocompatibility is a relative matter and whether a material is considered biocompatible or not, depends on the application and numerous other factors such as time and context.<sup>21</sup>

Previous studies have shown that MIL-100(Fe) is a water stable MOF under ambient conditions, but rapidly degrades upon incubation with physiological simulated conditions (phosphate buffer saline, PBS) at pH=7.4.<sup>22,23</sup> Specifically, phosphate ions attack the framework, coordinate with the iron metal sites and replace the trimesate ligand, which is finally released leading either to partial or total degradation of the particles. It is noteworthy to mention, that the stability of the framework depends on several parameters both intrinsic (nature, size, crystallinity rate of the particles) and extrinsic (pH and composition of the medium, loading and coating procedures) and the interactions with the living organism.

In the context of this thesis, we will explore some of the above parameters to better understand the degradation mechanism of MIL-100(Fe) particles.

The present manuscript is divided into five chapters, as summarized in the figure below:



1. The first chapter is a bibliographic synopsis discussing some of the materials acting as nanovectors in biomedical field, giving special attention to hybrid porous Metal



Organic Frameworks (MOFs) and especially to the iron(III) trimesate MIL-100(Fe) framework, which is the material of interest for this study. Moreover, it presents the principles of the characterization techniques used to determine the stability of the particles and finally the degradation mechanism of MOFs and their *in vivo* fate is summarized as a book chapter published in 2020.

2. In the second chapter, *in situ* Atomic Force Microscopy (AFM) was chosen to follow the degradation of micron-sized particles (microMOFs) in water and in PBS media. Two different synthetic routes were used for the formation of microMOFs presenting different crystallinities. The as-synthesized particles are stable in water, but they degrade upon incubation in the presence of phosphates ions, as already mentioned before. We also wanted to investigate the effect of the pH on the stability of the particles and we, therefore tuned the acidity of the media. This study revealed that the particles are more stable in acidic environment (pH=5.4) compared to a neutral one (pH=7.4). This was a valuable tool for the investigation of the behavior of smaller particles (nanoMOFs), which was further studied in the following chapter (chapter 3).

3. The third chapter focuses on the exploration of the same mechanism but considering smaller particles (<100 nm) in extreme diluted conditions. To achieve that, an optical based technique, named *in situ* ellipsometry was selected. Its principle is based on the measurement of optical films' thickness and for this reason thin films of MIL-100(Fe) were fabricated by dip coating. To our knowledge, this is the first time that optical thin films of MIL-100(Fe) have been studied by *in situ* ellipsometry. At a first step, the thickness of the films was precisely measured and then, films were introduced inside a liquid cell where either water or PBS was passing at a constant flow. The thickness and the composition of the films were assessed. Moreover, we followed the behavior of the same films in the presence of bovine serum albumin (BSA), the most abundant protein in the bloodstream, to study its role to the degradation mechanism of nanoMOFs.

4. The fourth chapter of the manuscript (chapter 4) is dedicated to the loading of three active molecules with or without functional groups (pristine drug, phosphorylated and sulfated form) into the internal porosity of nanoMOFs. The main goal was here to evaluate the impact of the host-guest interactions over the degradation's kinetics. Additionally, drug and ligand releases were followed upon incubation in media either rich in phosphates or in sulfates to show the influence of the complexing ions over the degradation of the MOF. Density Functional Theory (DFT) modeling was finally considered as a computational quantum mechanical technique, which helped to gain

## General Introduction

a better understanding over the intermolecular interactions, crucial parameters for the stability of the particles.

5. In last chapter a general conclusion is proposed as well as perspectives along with the annexes for supplementary information of this work.

## Synthèse en français

La nanotechnologie a fait l'objet d'une attention considérable il y a quelques années et, aujourd'hui, nous pouvons clairement affirmer qu'elle s'est implantée dans presque tous les domaines de la recherche novatrice.<sup>1</sup> En biochimie, les nanoparticules (NPs) peuvent servir de vecteurs de principes actifs (AI) pour le traitement de diverses maladies.<sup>2-4</sup> Le choix de la nanotechnologie par rapport aux thérapies conventionnelles présente certains avantages importants :

1. protection des molécules actives instables ou peu solubles et prévention de la libération prématurée.
2. l'administration ciblée de molécules actives de manière contrôlée, évitant les effets secondaires indésirables.
3. Traversée efficace des barrières épithéliales et endothéliales et diffusion intracellulaire réussie.
4. la co-encapsulation et la délivrance de plusieurs médicaments pour une thérapie combinée
5. combinaison de l'imagerie et de la thérapie par des nanovecteurs multifonctionnels pour plusieurs maladies (theragnostic).

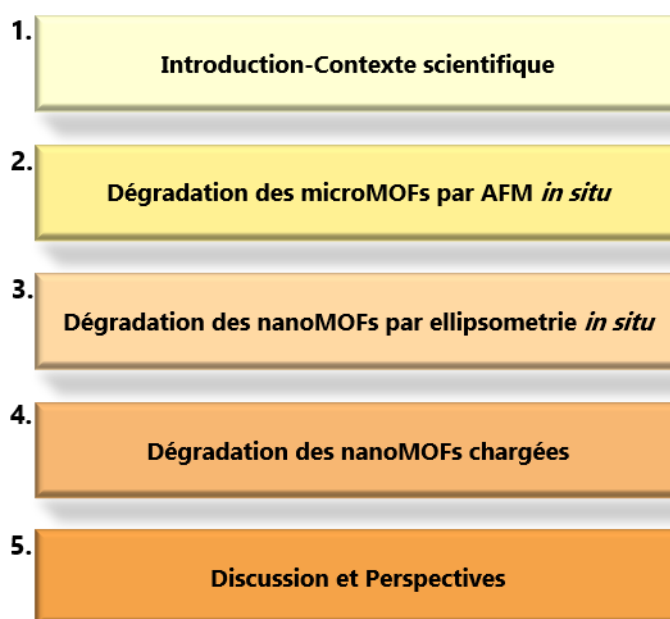
Depuis les années 1970, une multitude de particules ont été étudiées en tant que nanovecteurs de médicaments.<sup>5-7</sup> Au cours de la dernière décennie, les particules poreuses hybrides appelées "Metal Organic Frameworks" (MOFs) ont gagné de plus en plus de terrain en tant que vecteurs pharmaceutiques, grâce à leurs surfaces internes élevées, à leur diversité chimique et structurale, à l'ingénierie de surface et à leur synthèse (verte) contrôlable à l'échelle nanométrique.<sup>8,9</sup> Parmi une grande variété de MOFs, le trimesate de fer (III) MIL-100(Fe) (MIL signifie Matériaux de l'Institut Lavoisier) est un candidat MOF de référence pour les applications biomédicales.<sup>10</sup> MIL-100(Fe) présente une architecture mésoporeuse construite de trimères de fer d'octaèdres métalliques connectés par des ligands trimesates délimitant des cages mésoporeuses accessibles par des fenêtres microporeuses. L'une de ses principales caractéristiques est la présence de sites métalliques ouverts capables de lier directement une grande variété de molécules invitées (gaz, vapeurs, médicaments, enzymes, etc.). Grâce à ces caractéristiques uniques, le MIL-100(Fe) peut accueillir plusieurs médicaments (hydrophobes et hydrophiles).<sup>11-15</sup> Il est à noter qu'il peut être synthétisé par des méthodes "vertes" permettant d'obtenir des particules allant de moins de 100 nm à quelques microns.<sup>16-18</sup> Le MIL-100(Fe) est biodégradable dans les fluides corporels et est biocompatible, comme l'ont déduit de précédentes études in vitro/vivo.<sup>19,20</sup> Le terme biocompatible signifie un matériau qui, grosso modo, n'est pas toxique pour l'organisme, ni tout au long de sa circulation dans le corps, ni dans ses sous-produits de dégradation. Kohane et Langer ont judicieusement commenté dans un article de

synthèse que la biocompatibilité est une question relative et que le fait qu'un matériau soit considéré comme biocompatible ou non dépend de l'application et de nombreux autres facteurs tels que le temps et le contexte.<sup>21</sup>

Des études antérieures ont montré que le MIL-100(Fe) est un MOF stable dans l'eau dans des conditions ambiantes, mais qu'il se dégrade rapidement lors d'une incubation dans des conditions physiologiques simulées (solution saline tampon phosphate, PBS) à pH=7.4.<sup>22,23</sup> Plus précisément, les ions phosphate attaquent la structure, se coordonnent avec les sites métalliques du fer et remplacent le ligand trimésate, qui est finalement libéré, entraînant une dégradation partielle ou totale des particules. Il est important de mentionner que la stabilité de la structure dépend de plusieurs paramètres intrinsèques (nature, taille, taux de cristallinité des particules) et extrinsèques (pH et composition du milieu, procédures de chargement et de recouvrement) et des interactions avec l'organisme vivant.

Dans le cadre de cette thèse, nous allons explorer certains de ces paramètres afin de mieux comprendre le mécanisme de dégradation des particules MIL-100(Fe).

Le présent manuscrit est divisé en cinq chapitres, comme le résume la figure ci-dessous:



1. Le premier chapitre est un synopsis bibliographique discutant de certains des matériaux agissant comme nanovecteurs dans le domaine biomédical, en accordant une attention particulière aux cadres métallo-organiques (MOF) poreux hybrides et notamment au cadre MIL-100(Fe) trimésate de fer(III), qui est le matériau d'intérêt pour cette étude. En outre, il présente les principes des techniques de caractérisation

utilisées pour déterminer la stabilité des particules et enfin le mécanisme de dégradation des MOFs et leur *destin in vivo* est résumé sous la forme d'un chapitre de livre publié en 2020.

2. Dans le deuxième chapitre, la microscopie à force atomique (AFM) *in situ* a été choisie pour suivre la dégradation de particules de taille micrométrique (microMOFs) dans l'eau et dans un milieu PBS. Deux voies de synthèse différentes ont été utilisées pour la formation de microMOFs présentant des cristallinités différentes. Les particules telles que synthétisées sont stables dans l'eau, mais elles se dégradent lors de l'incubation en présence d'ions phosphates, comme déjà mentionné précédemment. Nous avons également voulu étudier l'effet du pH sur la stabilité des particules et nous avons donc ajusté l'acidité du milieu. Cette étude a révélé que les particules sont plus stables dans un environnement acide (pH=5.4) comparé à un environnement neutre (pH=7.4). Cela a été un outil précieux pour l'étude du comportement de plus petites particules (nanoMOFs), qui a été étudié plus en détail dans le chapitre suivant (chapitre 3).

3. Le troisième chapitre se concentre sur l'exploration du même mécanisme mais en considérant des particules plus petites (<100 nm) dans des conditions de dilution extrême. Pour ce faire, une technique optique, appelée ellipsométrie *in situ*, a été choisie. Son principe est basé sur la mesure de l'épaisseur des films optiques et pour cette raison, des films minces de MIL-100(Fe) ont été fabriqués par trempage. A notre connaissance, c'est la première fois que des films minces optiques de MIL-100(Fe) ont été étudiés par ellipsométrie *in situ*. Dans un premier temps, l'épaisseur des films a été mesurée avec précision, puis les films ont été introduits dans une cellule liquide où de l'eau ou du PBS passait à un débit constant. L'épaisseur et la composition des films ont été évaluées. De plus, nous avons suivi le comportement des mêmes films en présence de sérum albumine bovine (BSA), la protéine la plus abondante dans le sang, afin d'étudier son rôle dans le mécanisme de dégradation des nanoMOFs.

4. Le quatrième chapitre du manuscrit (chapitre 4) est consacré au chargement de trois molécules actives avec ou sans groupes fonctionnels (médicament pristine, forme phosphorylée et sulfatée) dans la porosité interne des nanoMOFs. L'objectif principal était ici d'évaluer l'impact des interactions hôte-guide sur la cinétique de dégradation. De plus, la libération de médicaments et de ligands a été suivie lors de l'incubation dans des milieux riches en phosphates ou en sulfates afin de montrer l'influence des ions complexants sur la dégradation du MOF. La modélisation de la théorie de la fonction de la densité (DFT) a finalement été considérée comme une technique de mécanique quantique computationnelle, qui a permis de mieux comprendre les interactions intermoléculaires, paramètres cruciaux pour la stabilité des particules.

5. Dans le dernier chapitre, une conclusion générale est proposée ainsi que des perspectives et des annexes pour des informations supplémentaires sur ce travail.

## References

1. Daemen, T. *et al.* Liposomal doxorubicin induced toxicity: Depletion and impairment of phagocytic activity of liver macrophages. *Int. J. Cancer*. **61**, 716–721 (1995).
2. Kargozar, S. *et al.* Nanotechnology and Nanomedicine: Start small, think big. *Mater. Today Proc.* **5**, 15492–15500 (2018).
3. Fan, W. *et al.* Nanotechnology for Multimodal Synergistic Cancer Therapy. *Chem. Rev.* **117**, 13566–13638 (2017).
4. Weiss, C. *et al.* Toward Nanotechnology-Enabled Approaches against the COVID-19 Pandemic. *ACS Nano* **14**, 6383–6406 (2020).
5. Gregoriadis, G. *et al.* Drug-Carrier Potential of Liposomes in Cancer Chemotherapy. *Lancet* **303**, 1313–1316 (1974).
6. Couvreur, P. *et al.* Adsorption of antineoplastic drugs to polyalkylcyanoacrylate nanoparticles and their release in calf serum. *J. Pharm. Sci.* **68**, 1521–1524 (1979).
7. Langer, R. *et al.* Polymers for the sustained release of proteins and other macromolecules. *Nature* **263**, 797–800 (1976).
8. Yang, J. *et al.* Metal–Organic Frameworks for Biomedical Applications. *Small* **16**, 1–24 (2020).
9. Wang, L. *et al.* Nanoscale metal-organic frameworks for drug delivery: A conventional platform with new promise. *J. Mater. Chem. B* **6**, 707–717 (2018).
10. Quijia, C. R. *et al.* Application of MIL-100(Fe) in drug delivery and biomedicine. *J. Drug Deliv. Sci. Technol.* **100**, (2020).
11. Anand, R. *et al.* Host-guest interactions in Fe(III)-trimesate MOF nanoparticles loaded with doxorubicin. *J. Phys. Chem. B* **118**, 8532–8539 (2014).
12. Horcajada, P. *et al.* Porous metal-organic-framework nanoscale carriers as a potential platform for drug delivery and imaging. *Nat. Mater.* **9**, 172–178 (2010).
13. Rodriguez-Ruiz, V. *et al.* Efficient ‘green’ encapsulation of a highly hydrophilic anticancer drug in metal-organic framework nanoparticles. *J. Drug Target.* **23**, 759–767 (2015).
14. Agostoni, V. *et al.* Towards an Improved anti-HIV Activity of NRTI via Metal–Organic Frameworks

# **Chapter I**

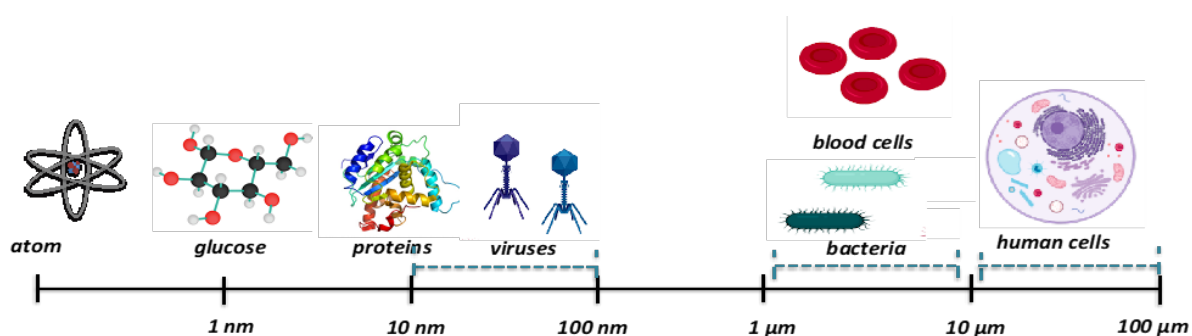
## Introduction





## A. Nanomedicines

The historical talk with the title ‘‘There’s plenty of room at the bottom’’, given by Richard Feynman in 1959 at Caltech, laid the foundations of nanotechnology and paved the way for its use at almost every aspect of modern life.<sup>1-6</sup> To better understand the ideas of the manuscript that follows, some terms should be defined. According to the International Organization of Standardization (ISO), a nano-object is a discrete piece of material with one, two or three external dimensions in the nanoscale (length ranges approximately from 1 nm to 100 nm). Nanoparticle (NP) is a nano-object with all external dimensions in the nanoscale, where the lengths of the longest and the shortest axes of the nano-object do not differ significantly. Nanotechnology is the science that deals with the design, the fabrication and the application in the nanoscale.<sup>7</sup> In the context of this thesis, NPs will be studied as therapeutic agents towards the diagnosis, treatment and prevention of diseases. More specifically, NPs act as transport agents of active ingredients (AIs) for drug delivery applications. For the rest of the manuscript, terms such as nanovectors or nanocarriers or drug delivery systems (DDS) will be used, according to the proposed terminology. A nanocarrier is small enough to enter cells, interact with them and control a biological process. **Figure 1-1** shows their size in comparison with other well-known entities such as atoms, molecules, viruses or cells.



**Figure 1-1.** Nanoscale comparison. Figures created by Biorender.

In addition to their intracellular penetration, thanks to their submicroscopic size, nanocarriers present some great advantages compared to conventional treatment. In the next part, the importance of nanomedicines will be given.

## **Nanomedicines versus conventional therapies**

The intrinsic physicochemical properties of NPs, such as their small size and their large surface to volume ratio allow the host of a large quantity of AIs. Several AIs present drawbacks hampering their administration, such as low solubility, strong tendency to crystallize or lack of stability in biological media. In this context, NPs can act as shields for the AIs preventing their degradation. NPs can load high drug amounts, circumventing drug solubility problems together with avoiding crystallization. One of the most interesting ability of the nanocarriers is their accumulation specifically in pathogenic cells (targeting), where a higher amount of the drug is released in a controlled manner. Especially in the case of cancer treatment, nanovectors need to be specifically targeted only to the cancer cells without damaging the healthy tissues and organs, which could lead to undesirable side effects. Moreover, certain drug carriers may release their cargo upon internal or external stimuli (temperature, pH, light, molecular recognition, etc.) avoiding the uncontrolled premature release ('burst' release), before they successfully reach their target. Overall, protection of the AI, successful targeting and controlled release of the drug are some of the main parameters that should be taken into consideration in the design of a nanocarrier. Apart from these aspects, it is crucial to design biocompatible particles, which upon interaction with the living organism will not introduce any toxicity to it.

Each nanocarrier presents a different behavior, when is administered *in vivo*. For assessing its safety and efficacy, its activity inside the body should be carefully studied. The pathway that the nanovectors are following inside the body designates their pharmacokinetic profile, which is described through ADME (Absorption, Distribution, Metabolism, Excretion) concept in the section that follows.

### **Pharmacokinetics**

The acronym ADME (Absorption, Distribution, Metabolism, Excretion) describes the pharmacokinetic profile of an AI that is the effect the body has on drugs. ADME consists of four crucial steps, the absorption of the AI, its distribution in the body, its metabolization and finally the excretion from the organism, all of which will determine the biological activity or the *in vivo* fate of a chemical compound. The nanosystems carrying the AIs to the living organism for achieving a therapeutic effect will follow these four steps, which will now be described.<sup>8</sup>

## Absorption

Absorption is the process of a substance before entering the systemic circulation. This process depends strongly on the administration route of the drug. The main routes of administration are distinguished into two main categories, the enteral and the parenteral. The enteral administration describes the absorption of the AI via the gastrointestinal track, whereas the parenteral administration includes any route, which does not include the gastrointestinal system. Oral, rectal and sublingual or buccal administrations belong to the enteral category and intravenous, intramuscular, subcutaneous, transdermal, inhalation and topical administrations to the parenteral one. Some of the main administration routes are discussed below.

- *Oral administration*; the AI is administered orally in the organs, following the total circulation in the body that is the pass from the stomach and the intestinal system, then in the blood stream with a first pass in the liver and finally to other organs, kidneys, lungs, heart, brain, etc. Oral route is convenient and it is preferred from the patients, mainly because it improves their compliance. Therefore, more and more nanocarriers are increasingly being developed for oral delivery.<sup>9-12</sup>
- *Intravenous administration (i.v)*; the AI is administered by injection directly into the vascular space bypassing some barriers and metabolism mechanisms as compared to the oral administration. Among the other administration routes, the i.v one provides the highest drug availability with a minimum delay. Nowadays, delivery of antitumor drugs intravenously is the most common route of administration.<sup>13, 14</sup> However, one of its main limitations is the control of the particle size of the nanosystems. Small NPs are often aggregated during injections and they trigger embolism hampering the treatment.
- *Inhalation*; the AI is administered within the respiratory track by inhaling orally or nasally for systemic or local effect. The AIs are formulated and administered with Dry Powder Inhaler (DPI), metered-dose inhaler (MDI) or nebulizers.<sup>15</sup> In this case, inhalation therapies are among the optimal solutions for improvement and therapy of lung diseases, such as cystic fibrosis<sup>16</sup> or chronic cases, such as asthma.<sup>17</sup>
- *Transdermal administration* is taking place through the skin. The AI is slowly diffused by the external layer of the skin (stratum corneum), passes the viable epidermis and ends up to dermis, which contains capillary loops for systemic administration.<sup>18</sup> The last years, more and more nanodevices have been designed for

transdermal delivery.<sup>19, 20</sup>

- *Subcutaneous route* is a pathway to administer a substance into the fatty tissue between the skin and the muscle by an injection. Insulin and some hormones, but also pain medications, such as morphine and hydromorphone (Dilaudid) are commonly given as subcutaneous injections.<sup>21</sup>

## **Distribution**

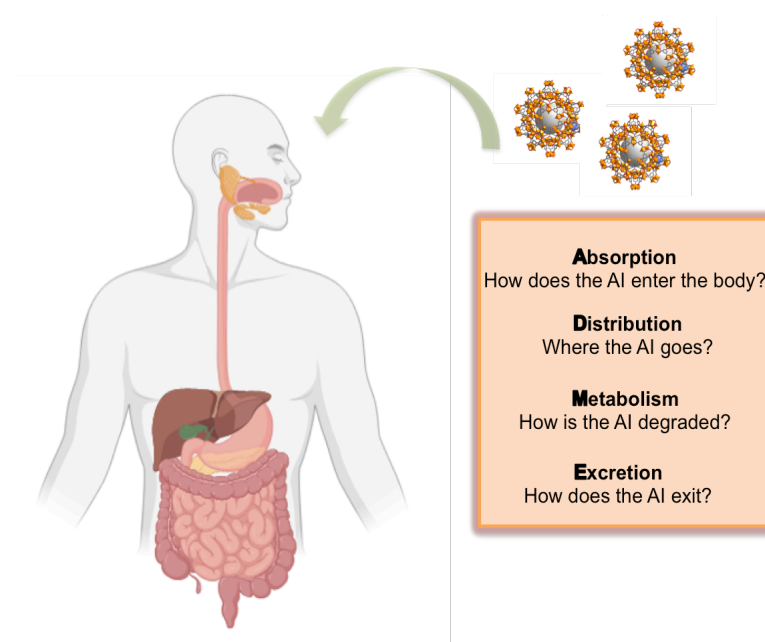
Distribution is the process of dispersion of the AI from the vascular space (blood vessels) to extravascular space (tissues, fat, cells, etc.) The biodistribution of nanocarriers to organs strongly depends on their physicochemical parameters and especially their size and shape.<sup>22-24</sup>

## **Metabolism**

Metabolism or biotransformation of the drug mainly occurs in the liver by the enzymatic system Cytochrome P450. Drugs undergo reactions like oxidation, hydrolysis and hydroxylation, in order to become polar and be excreted from the organism. Metabolism is a major process in determining toxicity of the compound.

## **Excretion**

The excretion of the drug from the organism by urine or feces mainly happens through the renal system (kidneys). There are also other ways for the metabolites to get eliminated, such as the sweat, bile, tears, breast milk, etc.

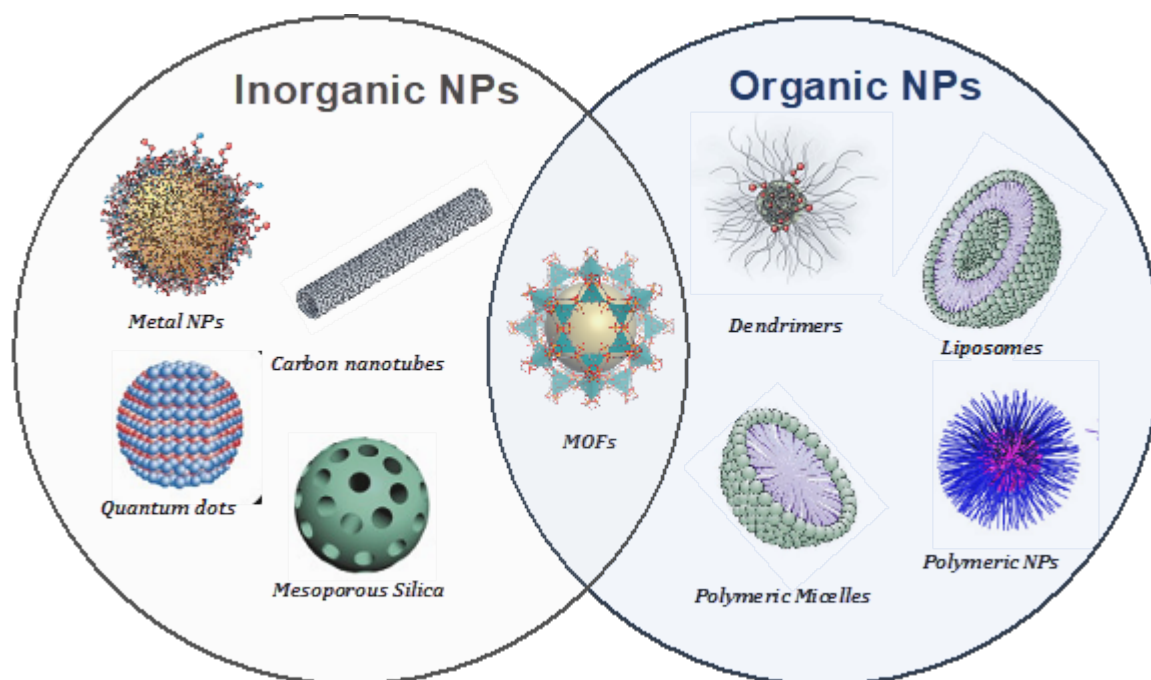


**Figure 1-2.** Schematic representation of NPs pharmacokinetics through the ADME concept. Figure created by Biorender and Diamond.

To sum up, nanocarriers are administered inside the organism to deliver AIs and act as therapeutic agents until their final elimination. To notice, during their travel in the body, they are biotransformed into different species, which are or can potentially be toxic for the organism. Drug fate in the organism is related to its ADME and it is of a great importance that the degraded products of the NPs are excreted by the organism and should not induce any toxicity. During the last decades various types of materials have been developed to produce nanocarriers and their potential use in nanomedicine has been studied. A core incorporating and protecting the AI and a shell that interacts with the living environment composes the majority of drug nanocarriers. Some of the most studied drug delivery systems (DDS) will be summarized in the next section.

## **B. Types of drug carriers**

Since their first discovery in the early seventies, a large diversity of DDS has been reported and still nowadays it is a very active domain particularly with the development of the material science and bioengineering (**Figure 1-3**).



**Figure 1-3.** Representation of the main drug delivery systems (DDS) based on their inorganic and organic composition. Adapted from <sup>25-28</sup>

Giving a fully accurate picture of all these systems is challenging. Therefore, we will focus on the most commonly reported carrier systems highlighting their main advantages and drawbacks. We will discriminate them based on their composition (organic, inorganic) and describe the most suitable ones in terms of biodegradability and cytotoxicity based on *in vitro* and *in vivo* studies reported to date.

## Liposomes

Liposomes discovered by Bangham in early 60's are vastly used in nanomedicine as drug carriers.<sup>29</sup> They are defined as microscopic spherical particles consisting of an internal aqueous core surrounded by a double lipidic layer (glycerophospholipids). Drug molecules can be either entrapped in the aqueous core or solubilized in the lipid bilayers, depending on their physicochemical properties. The limited toxicity that liposomes present, in reason of their biodegradable character is one of the main advantages of these drug carriers. To mention, Doxil liposomal formulation was the first approved formulation by FDA for the treatment of Kaposi's sarcoma<sup>30</sup> and since then more than 20 liposomal and lipid-based formulations have already been approved by regular authorities.<sup>31</sup> Vyxeos (Jazz Pharmaceuticals) is another liposomal formulation of daunorubicin and cytarabine for

treatment of acute myeloid leukaemia (AML) recently approved by FDA.<sup>32</sup> On the other hand, the inefficient drug loadings and the limited stability of liposomes are some of their main limitations. Indeed, diffusion of hydrophilic drugs from the liposome cores out of the lipid layer can severely decrease the loading efficiency of these molecules and make difficult to control the release. Furthermore, the hydrolysis and/or oxidation reactions of the phospholipids and the leakage and fusion of liposomes due to the defects in their membrane sometimes might lead to stability issues.<sup>33</sup>

One recent example of lipid NPs that were formulated to encapsulate the vaccine component, messenger RNA (mRNA), became the first approved vaccine against coronavirus 2 (SARS-CoV-2) hitting clinical use in the context of the pandemic declared in March 2020. The new class of DNA- and RNA-based vaccines deliver the genetic sequence of specific viral proteins to the host cells using lipid-based nanotechnology platforms.

## Polymeric NPs

Polymers in bioapplications date back to 1960s with pioneer research from different groups. Speiser et al. studied polyacrylic beads for oral administration and NPs for drug delivery and mainly for vaccination purposes.<sup>34, 35</sup> Folkman and Langer were the first who demonstrated the controlled release for the delivery of macromolecules from polymers.<sup>36</sup> Couvreur et al. studied release of doxorubicin from biodegradable acrylic NPs.<sup>37</sup> A very important study that opened the pathway for the development of nanocarriers and their access to the market was the attachment of poly(ethylene glycol) (PEG) chains to PLA/PLGA NPs which increased blood circulation half-time and influenced their biodistribution.<sup>38, 39</sup> Polymeric NPs can be distinguished into two major categories according to the choice of the polymer source: natural or synthetic. Natural polymer based NPs include protein-based polymers, such as collagen, albumin, gelatin and polysaccharides, such as agarose, alginate, hyaluronic acid, dextran, chitosan and cyclodextrins. Synthetic polymeric NPs include polyesters (PLA, PGA, PLGA polymers, PLGA-PEG copolymers), poly (alkyl cyanoacrylates), poly (ortho esters), polyanhydrides, polyamides, poly (ester amides) and poly(phosphoesters).<sup>40</sup> Hydrolytic degradation of polymeric NPs *in vivo* leads to biodegradable products without inducing toxicity to the living organism. As an example, PLGA NPs degrade via hydrolysis of their ester bonds into lactic and glycolic acid monomers. The nature and the properties of polymers (crystallinity, solubility, glass transition) and the drug incorporation/release determine the *in vivo* fate of the material and the type of application. For example, in the case of hyaluronic acid (HA), its high hydrophilicity and its ability to absorb water result to an expansion up to 1000 times its solid volume, leading to a loose hydrated network that makes HA attractive for hydrogel-based drug delivery.<sup>41-43</sup>

Another case is chitosan based NPs for oral drug delivery. Chitosan based NPs can overpass to some extent the barriers of the gastrointestinal tract, have good stability in acidic environment (gastric area) and thus can improve the drug permeability in intestinal tract.<sup>44, 45</sup> Biodegradability of polymeric NPs has rendered them promising candidates for drug delivery, a fact that is proved by their entrance in the market. Abraxane based on human serum albumin NPs containing paclitaxel, it was firstly approved for the treatment of metastatic breast cancer.<sup>46</sup> Nowadays, it is also indicated for advanced non-small lung cancer, for pancreatic cancer and very recently for triple negative breast cancer.<sup>47-49</sup> Another formulation approved recently, named Patisiran/ONPATRO, is a siRNA-delivering lipid-based NP suitable for the therapy of transthyretin amyloidosis.<sup>50</sup> It is of a great importance to note, that this formulation constitutes the first approval of an RNAi therapeutic agent.

Drug loading of AIs into polymeric NPs is achieved by covalent bonding to the polymeric backbone, by physical adsorption to the polymeric surface or by encapsulation in the polymeric matrix.<sup>51</sup> Biocompatibility and versatility are two of the main advantages of polymeric NPs. However, they have key limitations such as their difficulty to entrap hydrophilic drugs inside their structures resulting in poor drug loadings.<sup>52, 53</sup>

### **Polymeric micelles**

Spherically-shaped polymeric micelles are made of hydrophilic and hydrophobic units which self-assemble in aqueous solutions. Hydrophobic molecules can be incorporated in the hydrophobic core either by physical entrapment or by chemical conjugation whereas the hydrophilic shell interacts with the biological environment and provides micelles with steric stability. The main preparation methods are dialysis and emulsification.<sup>54</sup> Based on the type of intermolecular interactions, polymeric micelles were classified by Kapse *et al.* into the following three types.<sup>55</sup>

- Conventional polymeric micelles or block copolymer micelles, based on block copolymers consisting of two or more homopolymeric blocks of different hydrophilicity.
- Polyionic complex polymeric micelles, forming from two or more oppositely charged ionic polymers that self-assemble, due to the combination of electrostatic and hydrophobic interactions.
- Noncovalently joined polymeric micelles, which are noncovalently bonded to macromolecules such as homopolymers, random copolymer, graft copolymer, or oligomers.



The three types of polymeric micelles, as well as their advantages and limitations in drug delivery procedure were recently discussed by Kaspé et al.<sup>55</sup>

Polymeric micelles share some of the limitations of polymeric NPs described in Section B, such as the poor drug loadings. In addition, another important drawback of these drug carriers is their chemical and thermal instability. The formation of polymeric NPs is a self-assembly procedure inseparably linked to the critical micellar concentration (CMC) of the polymer, which is an indicator of micellar stability and micellization ability. The lower the CMC value, the easier the preparation of the micelles and higher their stability.<sup>56</sup> Due to the extreme dilution when the polymeric micelles are administered by the i.v. route, they are prone to disassemble leading to premature drug leakage.<sup>57</sup> Another major issue faced by polymeric micelles is the scalability of their production. Whereas it is possible to produce micelles with good drug loading and stability at the laboratory scale, it is more delicate to extrapolate the procedures at large scale and variability often occurs in the preparations because of the impact of many physical factors.<sup>58</sup>

## Dendrimers

Dendrimers were first reported in 1985 by Tomalia and Newcome.<sup>59</sup> They are synthetic polymers presenting terminal groups in the form of branching points, starting from an initial core. They are highly monodisperse particles with a size in the range of 1-100 nm. Dendrimers present internal cavities, known as 'dendritic boxes', which allow them to operate as vessels or hosts for other molecules.<sup>60</sup> Hydrophilic and hydrophobic molecules can be encapsulated by adsorption, ionic interactions or covalently bonded in the internal nanostructure. The low polydispersity, high functionality and the exponential growth in branches and surface groups are some of the main benefits of dendrimers for drug delivery applications. Since their first discovery, several types of dendrimers have been studied and they are grouped in 5 different families depending on their composition; phosphorus dendrimers (CPD), carbosilane dendrimers (CBS), polypropyleneimine dendrimers (PPI), poly (amidoamine) (PAMAM) dendrimers and poly(lysine) and poly(L-ornithine) dendrimers.<sup>61</sup> Some of them have already been approved or they are in preclinical and clinical trials.<sup>62</sup> The main limitations of dendrimeric drug carrier systems are the high cost of production and important concerns about toxicity. Toxicity of dendrimers is related to the nature of the core and their terminal groups, their small size and most importantly to their surface charge. Specifically, the amino groups and associated cationic charge on dendrimers hinder their use in bioapplications, as they might cause hemolytic toxicity.<sup>63</sup> Therefore, surface engineering (PEGylation, acetylation, carbohydrate and peptide conjugation) is crucial for the decrease of

potential toxicity.<sup>64</sup> Hemolytic studies of bare and coated dendrimeric systems (either with the carbohydrate galactose or with the hydrophilic polymer polyethylene glycol) showed a drastic reduction of hemolysis, due to the shielding of the cationic surface moieties.<sup>65, 66</sup>

### **Mesoporous Silica NPs (MSNs)**

Mesoporous Silica was first reported in the 1990s by Mobil Oil Scientists in USA.<sup>67</sup> But it was only in 2001 that mesoporous silica NPs (MSN) were first proposed as potential candidates for drug delivery.<sup>68</sup> The same group succeeded to synthesize mesoporous silica structures down to the nanoscale.<sup>69</sup> MSNs belong to the category of inorganic particles of ordered pores with homogeneous sizes (2-50 nm), high surface area (up to  $\approx 1000 \text{ m}^2/\text{g}$ ) and convenient functionalization of their external surface, because of the presence of silanol groups. MSNs in the range of 10-300 nm were able to incorporate mainly hydrophobic drugs by physical adsorption in their internal surface or by covalent bonding on their external surface.<sup>70</sup>

Degradation of MSNs is based on a dissolution mechanism of silica particles into orthosilicic acid in biological media. More precisely, MSNs consist of a  $\text{SiO}_2$  matrix that can undergo a nucleophilic attack by hydroxyl ions from water in aqueous media, leading to the hydrolytic breakdown of the network and the release of orthosilicic acid as by-product, which is biocompatible and excreted through the urine.<sup>71</sup> Many *in vitro* and *in vivo* toxicological tests have been performed to probe the fate of MSNs. However some toxicity concerns were raised for MSNs.<sup>72</sup>

### **Multifunctional DDS**

Recent studies have discussed the solutions to overcome current limitations of drug delivery systems, such as lack of stability, poor drug loadings and/or uncontrolled drug release through the preparation of mixed delivery nanocarriers.<sup>73</sup>

Paclitaxel is a mitotic inhibitor widely used in chemotherapy. Its poor solubility and relevant side effects make its administration problematic. To overcome these problems, polymeric micelle formulation for paclitaxel encapsulation (Genexol-PM) and a polymeric nanoparticle formulation (Xyotax) have been developed.<sup>74</sup> In another study, paclitaxel was loaded into a lipid dendrimer mixed system, presenting some important advantages, such as higher drug payloads, reduction of the size of the vesicle due to strong interactions of the phosphate headgroup to dendrimer and improvement in the anticancer potency of paclitaxel as it was revealed by *in vitro* and *in vivo* studies.<sup>75</sup>

Polymer lipid nanocarriers is another type of mixed DDS with potential benefits compared to the bare liposomes or polymeric NPs. The polymeric part improves the stability and enables a controlled release of the therapeutic substance. Synthetic polymers, such as PEG and PLGA, are vastly used for the formation of lipid-polymer vesicles<sup>76</sup> but many natural polymers, such as chitosan and cyclodextrins, have also been studied.<sup>77, 78</sup> Dave et al. have described a few examples of applications of these hybrid systems in addition to their synthetic methods.<sup>79</sup>

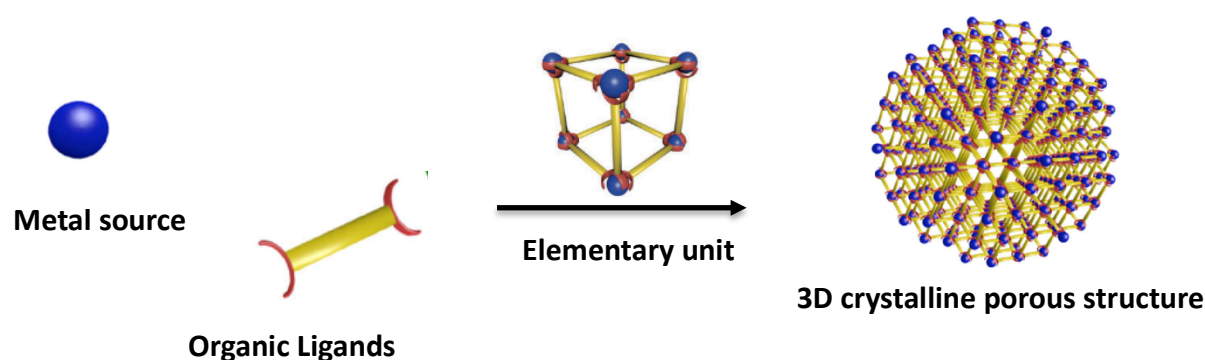
Finally, multifunctional nanoplatfroms constructed from both contrast agents and biodegradable nanomaterials hosting AIs, have been widely used for simultaneous treatment and imaging (theragnostics).<sup>80, 81</sup> For instance, folic acid was covalently bonded to superparamagnetic iron oxide NPs coated with PEG and PEI polymers for the targeted delivery of the anticancer agent doxorubicin.<sup>82</sup> The application of a magnetic field enabled the effective targeting of doxorubicin to the tumor site, as followed by *in vitro* and *in vivo* studies.

If one carefully analyse the literature, it appears that each type of drug carrier exhibits its own advantages and limitations. It is obvious that there is no “ideal” or universal drug delivery system. As already mentioned, various types of DDS, including porous particles, polymers, lipids, dendrimers, etc. can act as therapeutic agents. Some challenges remain to be addressed such as poor drug loadings, stability issues, biocompatibility and uncontrolled drug release. Besides, surface modification which shells and/or ligands is often complicated and requires several synthesis steps. Moreover, in post case each type of DDS is adapted to type of drug (hydrophilic or hydrophobic, charged or not etc) for a given administration route. Thus, NPs able to efficiently (co)incorporate drugs with a wide range of physicochemical properties for diverse administration routes are still scarce.

In this context, ordered porous hybrid NPs emerged as versatile DDS candidates. In the following section, these porous solids, named Metal Organic Frameworks (MOFs) will be discussed with a special emphasis to their potential as nanovectors of AIs compared to systems previously reported (Section B).

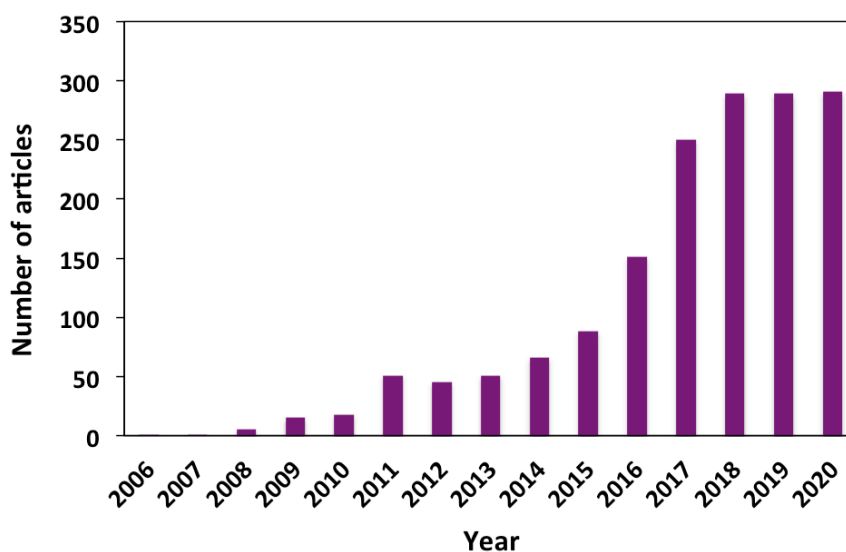
## C. Metal Organic Frameworks (MOFs)

Metal Organic Frameworks (MOFs) is a recent class of hybrid ordered porous materials consisting of inorganic blocks and organic bridging ligands that self-assembled into 3D network with a well-defined porosity (**Figure 1-4**). Their high internal surface areas (up to almost 8000 m<sup>2</sup>/g)<sup>83, 84</sup> and tunable pore sizes (micro to meso-pores)<sup>85</sup>, the almost unlimited combination of building blocks (metal, ligand) and finally the control of their particle sizes have made MOFs ideal candidates for several applications, such as gas storage and separation<sup>86, 87</sup>, catalysis<sup>88</sup> and the last decade in bioapplications.<sup>89</sup> Some of the pioneering groups in this field are those of Yaghi, Kitagawa and Férey that reported benchmark structures such as MOF-5, PCPs and the MIL-n families, respectively.<sup>90-92</sup>



**Figure 1-4.** Scheme of Metal Organic Frameworks (MOFs) formation through self-assembly of inorganic and organic building blocks. Adapted from<sup>93</sup>

However, it was only in the late 2000's that biodegradable and biocompatible nanoscale MOFs were proposed for drug delivery and revealed all their potential to entrap a large variety of AIs.<sup>94</sup> MOFs as DDS were introduced for the first time in 2006 using the model Cr-based mesoporous MOFs by entrapping successfully the analgesic and anti-inflammatory ibuprofen up to an unprecedented loading of 1.4 g of the AI per gram of the MOF.<sup>95</sup> However, chromium presents a high toxicity. For this reason, its non toxic iron based analogue MIL-100(Fe) was reported.<sup>96</sup> Since their first use in biomedicine, MOFs have increasingly been studied as DDS, as highlighted by the growth of the scientific publications of the last fifteen years (**Figure 1-5**).



**Figure 1-5.** Number of publications of MOFs for drug delivery in the period 2005-2020. Data from Web of Science.

**Figure 1-5** has been obtained by extracting data from Web of Science after crossing the terms ‘Metal-Organic Frameworks’ and ‘drug delivery’. Herein, if using other platforms such as Scopus or Google Scholar, the results could slightly change. Yet, the growing tendency remains, revealing the strong interest of the scientific community for these hybrid porous systems as drug carriers.

Nevertheless, the studies outlined in this figure do not distinguish studies based on micron-sized or nanoscaled particles. Although micron-sized particles can be used in biomedicine *via* specific administration routes, such as oral or nasal route, it is also of utmost importance to design nanosized MOFs (nanoMOFs) as drug nanocarriers, especially when intravenous administration is required, e.g. for cancer therapy.

## NanoMOFs

One important step for the use of nanoMOFs in biomedicine is their synthesis via ‘green’ routes.

One of the most common synthetic strategy to obtain crystalline hybrid porous particles is the solvothermal/hydrothermal route, which takes place in closed vessels under autogenous pressure above the boiling point of the solvent.<sup>97</sup>

Other alternative routes include the microwave (MW)-assisted solvothermal/hydrothermal, electrochemical, thermomechanical or sonochemical synthesis. To date several MOFs have also been produced via green reactions at ambient pressure and room temperature in a view of bioapplications.<sup>98-100</sup>

MW-assisted nanoMOF synthesis attracted great interest in biomedicine typically because of the possibility to produce more homogenous NPs with controlled sizes. MW heating relies on the interaction of electromagnetic waves with mobile electric charges. It enables an efficient and homogeneous heating with a precise monitor of temperature and pressure during the reaction and thus lead to a more precise control of reaction conditions. The faster heating is also a convenient way to isolate kinetic phases and/or to solubilize more rapidly poorly soluble ligands. The resulting faster nucleation leads also to smaller crystals compared to conventional heating. The first report of MOF synthesis through MW irradiation was obtained with MIL-100(Cr)<sup>101</sup> and later for MIL-101(Cr)<sup>102</sup>, MOF-5<sup>103</sup>, HKUST-1<sup>104</sup>, MIL-53(Fe)<sup>105</sup> etc.

In most cases, growth inhibitors such as acetic acid, hydroxybenzoic acid, pyridine and/or acido-basic agents are typically used for a better control of the nucleation/growth process and thus the final crystallinity as well as the colloidal stability of the nanoMOFs.<sup>106, 107</sup> Moreover, depending on the MOF, different solvents can be used for their preparation (H<sub>2</sub>O, EtOH, DMF, etc.). However, "green" solvents and less hazardous reactants shall be privileged for biomedical applications. Finally, one shall take into account the activation step of the nanoMOFs to take full benefit from the porosity of the MOF.<sup>108</sup>

The quasi-infinite choice of primary building blocks (metal sources and organic ligands), the optimization of the existing synthetic routes or the development of new ones have led to large diversity of MOFs structures. To date, almost 100 000 MOFs structures can be found in the Cambridge Structural Database (CSD), a number that has increased by a factor of 1.5 during the last three years.<sup>109, 110</sup> It is obvious, that selecting a MOF among this huge database for a given application is not straightforward. Nonetheless, for biomedicine, this choice is guided by (i) the stability in biological media and (ii) the *in vivo* biocompatibility. Keeping these criteria in mind, the most appropriate MOFs for bioapplications will be highlighted, in the next part. Finally, the case of biologically active MOFs, prepared either from endogenous organic ligands or exogenous ligands with therapeutic activity, named bioMOFs, will be presented.

## Biodegradable nanoMOFs

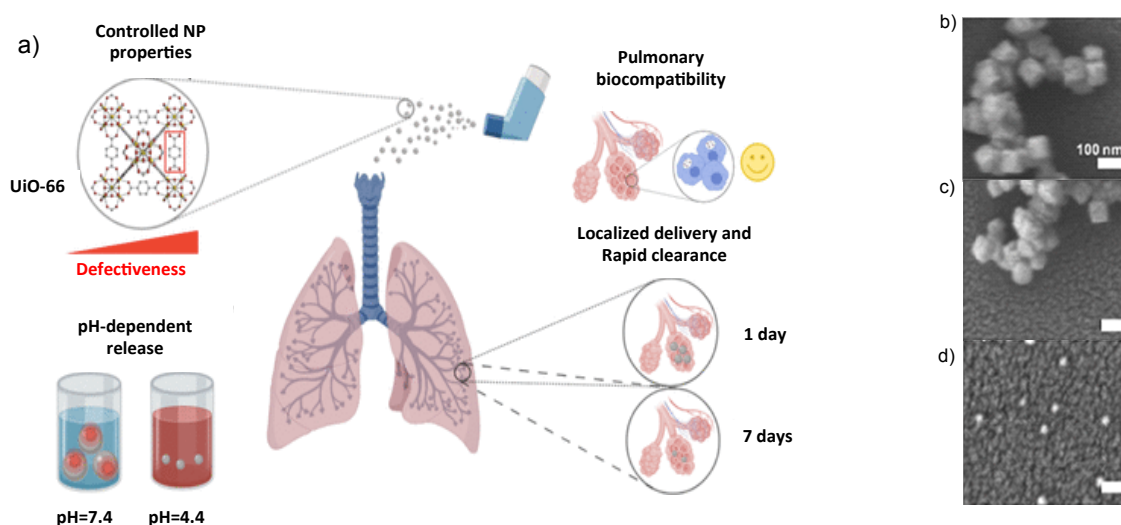
Numerous MOF structures have been reported as candidates for biomedical applications. The first step to design biocompatible MOFs is the choice of the constitutive parts of the framework. Regarding the metal species, it is compulsory to use endogenous metals (Fe, Ca, Zn..) or metals endowed with specific medical purposes (Eu, Gd ..). However, the daily uptake, administration route and biodistribution should also be considered for the evaluation of the toxicity. The median lethal dose (LD<sub>50</sub>) is an indication of the potential toxicity, which represents the dose of the substance required to kill half the members of the tested population after the end of the specific test.<sup>111</sup>

Zirconium, like titanium, is not an endogenous metal but is considered as biocompatible due to its inertness. Zr based MOFs have therefore been proposed as DDS. In general, these MOFs can be highly porous, exhibit good chemical stabilities in water and can host large amounts of drugs.<sup>112</sup> The UiO series (University of Oslo), the PCN-n series (Porous Coordination Network) and the NU family (Northwestern University) include large pores Zr-based MOFs that have gained a great interest in biomedicine.

UiO-66 and its larger analogues (UiO-67 and UiO-68) is a zirconium-based MOF reported by K.P. Lillerud et al. UiO-66 is built up from Zr<sub>6</sub>O<sub>4</sub>(OH)<sub>4</sub> oxo-clusters connected by 1,4-benzenedicarboxylates (BDC) delimiting a cubic network of tetrahedral and octahedral microporous cages.<sup>104</sup> The good stability of this framework results from bonds formed between the cluster and the carboxylates.

Like most metal carboxylate MOFs, the stability of UiO-66 was tested under physiological conditions (PBS pH=7.4), where a very rapid degradation of the framework was observed.<sup>113</sup> Phosphate ions replaced the terephthalic ligands leading to a total collapse of the framework.

In a recent study Jarai et al. used UiO-66 NPs as carriers for pulmonary delivery through inhalation.<sup>114</sup> Bared and loaded NPs were incubated both in neutral PBS and in artificial lysosomal fluid (ALF) pH=4.4, which mimics extracellular and intracellular conditions respectively. According to the stability tests, the NPs were rapidly degraded at lower pH, because of the protonation of the carboxylate ligands that weaken the previously strong metal-carboxylate bonds (**Figure 1-6**).



**Figure 1-6.** a) UiO-66 NPs for pulmonary drug delivery. Scanning electronic microscopic images (SEM) of UiO-66 NPs in PBS after b) 0 h, c) 48 h and d) in ALF after 48 h. Adapted from <sup>114</sup>

Porous Coordination Network (PCN) series, mainly developed by Zhou's group, are constructed from  $Zr_6$  oxo-clusters connected by porphyrin tri- or tetra-carboxylate ligands.<sup>115-117</sup> This leads to rather stable structures. Substitution of zirconium atoms by other metals, such as  $Fe^{II}$ ,  $Co^{II}$ ,  $Ni^{II}$  or  $Mn^{II}$  has also led to the formation of new PCNs with different stabilities and potential applications.<sup>118</sup>

A Zr porphyrinic MOF, PCN-224, was further studied as DDS for the anticancer drug methotrexate (MTX).<sup>119</sup> Upon incubation in PBS buffer solutions (pH 7.4 and 2.0 at 37 °C), the drug release was faster upon incubation in neutral pH. The authors attributed this release to the host-guest interactions in combination with the changes of the pH values.

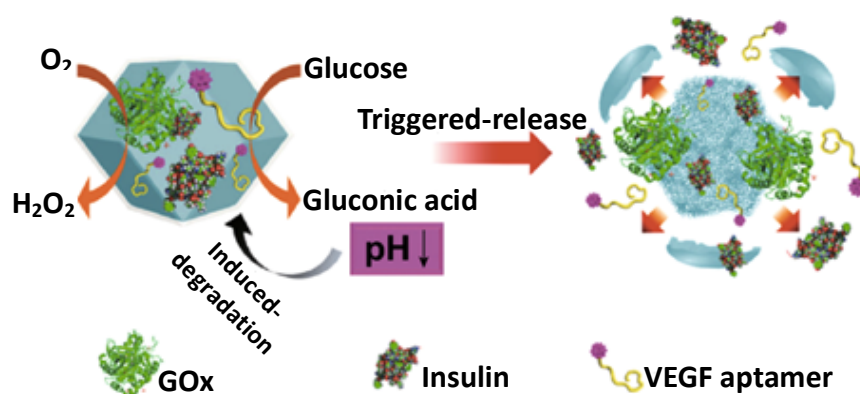
NPs of a controllable size of PCN-224 were also considered as a platform for targeted photodynamic therapy.<sup>120</sup> The researchers followed the stability of PCN-224 by PXRD for one week upon incubation in buffer (0.1 M HEPES, pH 7.4, 37 °C) and, remarkably, no degradation was observed in the first 48 hours, confirming the robustness of the framework. It was highlighted that PCN-224 particles did not degrade in neutral medium except, in the presence of phosphates. In these conditions, PCN-224 faced a rapid degradation, similarly to UiO-66, which is also constructed by  $Zr_6$  clusters, as previously discussed. Therefore, we can conclude that the stability of the framework is a result of the pH together with the composition of the degradation medium.



Moreover, the mesoporous zirconium MOF, NU-1000 (Northwestern University), was studied as an insulin carrier under harsh acidic conditions, which simulated the stomach environment, and under neutral physiological conditions which mimicked the bloodstream.<sup>121</sup> A protection of the insulin into the framework for the first conditions was evidenced, associated with a stability of the MOF, while the release of the protein occurred in the presence of phosphates as a consequence of the framework degradation.

Another candidate of interest is the zinc imidazolate framework ZIF-8, constructed from  $Zn^{2+}$  ions and 2-methylimidazolate linkers. Although this MOF exhibits narrow pores, it possesses a high loading capacity of a large variety of drugs or biomolecules, due to the very mild synthesis conditions (RT, water or alcohol, neutral pH) of this MOF enabling a direct encapsulation of the molecules that are in most cases 'embedded' within the MOF nanocrystals. This material also enables an on-demand release in the presence of an external stimulus such as the pH.<sup>122</sup> The protonation of the imidazolate linker under acidic conditions results in the progressive disassembly of the framework and the release of the cargo, making ZIF-8 an interesting vehicle for drug delivery applications. For instance, the anticancer drug doxorubicin was successfully encapsulated into ZIF-8 NPs via one pot synthesis and released during one week.<sup>123</sup> The system remained on the whole stable under physiological conditions at pH 7.4 and disassembled under acidic conditions (pH=5.0). Similarly, Sun et al. studied the incorporation and the release of 5-Fu for cancer treatment. 5-Fu@ZIF-8 NPs were stable at PBS pH=7.4, whereas they were rapidly degraded after immersion in acetate buffer at pH=5.0.<sup>122</sup>

In another study, insulin or the vascular endothelial growth factor (VEGF) aptamer were released from ZIF-8 in a controlled manner, upon local acidification of the microenvironment caused by the co-immobilization of glucose oxidase (GOx), as presented in **Figure 1-7**.<sup>124</sup>



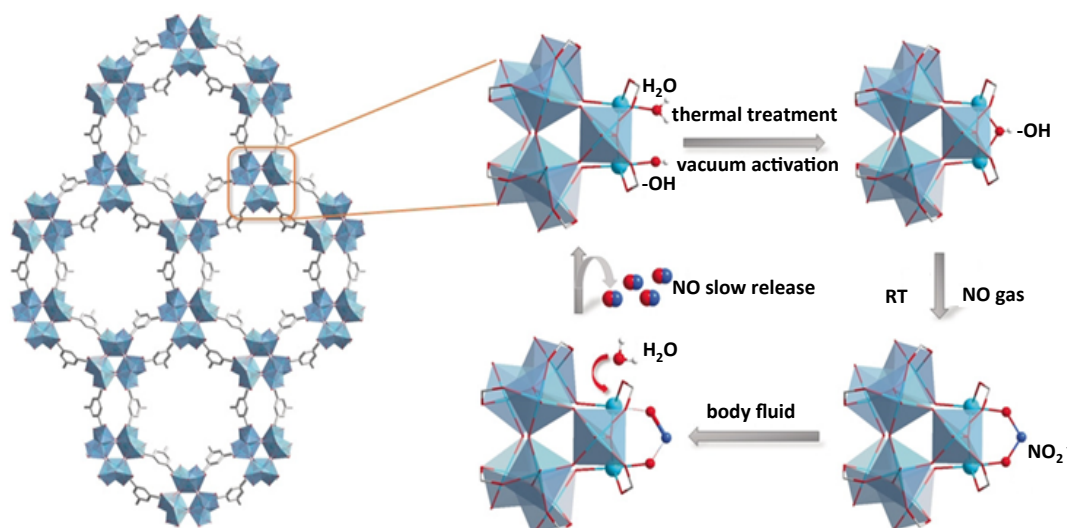
**Figure 1-7.** Triggered release of insulin and VEGF aptamer from ZIF-8 particles. Adapted from <sup>124</sup>

In a recent study, Luzuriaga et al. investigated the degradation mechanism stability of micron-sized ZIF-8 particles for bioapplications.<sup>125</sup> Particles of ca. 1  $\mu\text{m}$  were incubated in different media and their crystallinity, composition and morphology were assessed at different time points. Their stability in neutral conditions (PBS 10 mM pH=7.4) was demonstrated, whereas they degraded in acidic ones. This is in agreement with the previously studies by Sun et al. and Zheng et al.<sup>122</sup>

A similar work has been carried on by Falcaro et al, who studied the degradation mechanism of both nano and microparticles in physiological conditions. In contradiction with the previous reports, they showed that both type of particles rapidly degraded in PBS at pH 7.4, leading to the formation of zinc phosphate products.<sup>126</sup> Such discrepancies have been attributed to different degradation conditions used in the reported studies, especially MOF concentrations varied by a factor of ten.<sup>125, 127</sup>

Among the vast series of MOFs from the MIL-n family (MIL stands for Materials of Lavoisier Institut) those built from iron(III) and polycarboxylic acid ligands are of a particular interest in biomedicine, thanks to their biodegradable character and lack of toxicity. The stability and *in vivo* toxicity of a series of three different iron carboxylate nanoMOFs was thoroughly evaluated.<sup>94</sup> It was first shown that the MOFs were stable in water and under simulated stomachal acidic conditions, while PBS (pH 7.4) led to the degradation of the MOFs with a progressive release of their constitutive ligands. Noteworthy, the *in vivo* toxicity study (rats) demonstrated that these nanoMOFs were non toxic even at highest injectable concentrations of around 250 mg/mL, and that both iron and ligands were excreted through urines and feces.

Very recently, a new microporous Ti-based carboxylate MOF, named MIP-177 (MIP stands for Materials of Institut of Porous Materials of Paris) has been reported as a promising candidate for nitric oxide (NO) adsorption, a gas related to therapeutic applications, such as wound healing.<sup>128</sup> Remarkably MIP-177 (Ti) was shown to be highly stable in biological media, while its open metal sites enabled the formation of nitrites that were further released as NO upon exposure to PBS, as shown in **Figure 1-8**. This release of NO was accompanied by a migration of cells, mimicking the mechanism in play for wound healing.



**Figure 1-8.** Schematic representation of NO adsorption/release mechanism from MIP-177(Ti). Adapted from <sup>128</sup>

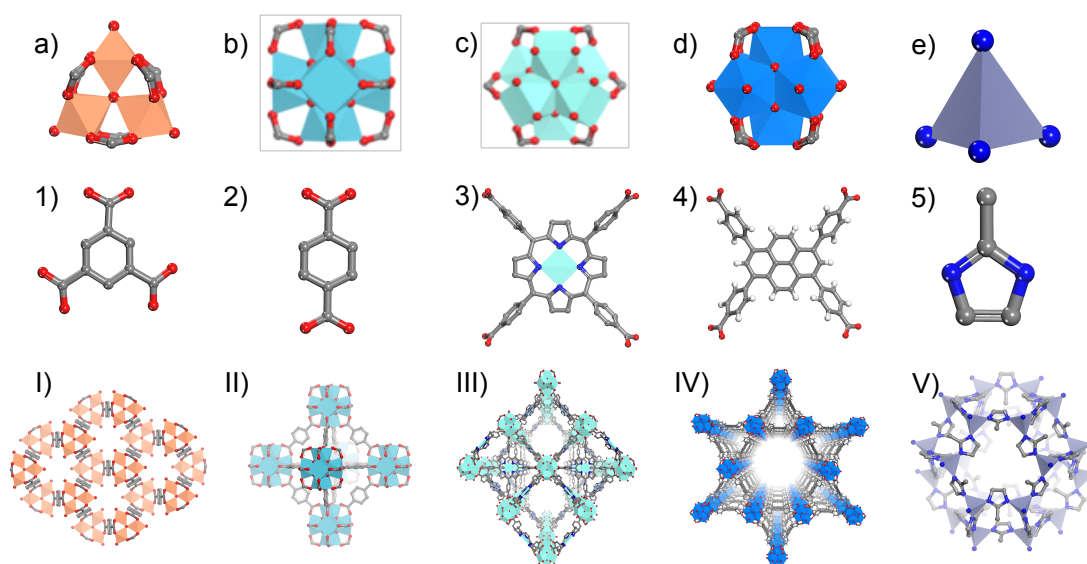
## BioMOFs

BioMOFs also known as Metal Biomolecules Frameworks are constructed from metal ions linked to endogenous organic molecules or AIs. This allows reaching exceptional drug loadings, as the AI is a constitutive part of the framework. It also decreases the risk of toxicity related to the use of exogenous ligands. Besides, one can also take envision the co-delivery of bioactive molecules is possible through an encapsulation of another drug inside the pores together with the bioactive ligand from the framework. Several biomolecules were used for the construction of bioMOFs, such as amino acids, peptides and proteins, nucleobases, saccharides, porphyrins and also drugs and bioactive molecules.<sup>129-131</sup>

The first example of bioMOF was bioMIL-1, an iron based MOF built up from trimeric Fe<sub>3</sub>N<sub>3</sub>O<sub>13</sub> units linked together via nicotinate molecules.<sup>132</sup> Although the framework presents a high drug payload (the AI consists part of the structure), it was rapidly degraded in the presence of simulated body fluid (within an hour).  $\gamma$ -cyclodextrin MOFs ( $\gamma$ -CD-MOFs) both as micron- and nanosized particles were later synthesized for drug delivery applications.<sup>133, 134</sup> Rosseinsky's group has also extensively studied peptide and porphyrin-based bioMOFs, most of these materials prepared, however, using toxic solvents and being not water stable.<sup>135-137</sup>

Although bioMOFs have gained an increasing interest, they present some important limitations attributed either to their poor stability in body fluids, the use of toxic solvents, lack of porosity to host drugs, while the complex structure of some biomolecules (e.g. proteins) prevent from a rational design once combined with metal ions to construct a new BioMOF. Of note, some important studies show the controllable supramolecular assembly of proteins by choosing the appropriate ligands' sizes for the construction of highly ordered structures.<sup>138-140</sup> Overall, we should keep in mind that these systems have been recently introduced in bioapplications and thus constitute a promising research topic associated with important challenges.

To sum up, a large number of MOF candidates have been developed and studied in a view of bioapplications. Depending on their structure, composition and stability, these can be of interest for different applications. Researchers have to carefully decide, case by case, which MOF looks the most appropriate candidate for each application. **Figure 1-9** summarizes the most studied MOFs series, as discussed in this Section.



**Figure 1-9.** Schematic illustration of building blocks, ligands and tridimensional porous structures of some MOFs appropriate for bioapplications.

**SBUs:** **a)** μ<sub>3</sub>-oxo trimer **b)** [Zr<sub>6</sub>O<sub>4</sub>(OH)<sub>4</sub>] octahedron cluster, **c)** [Zr<sub>6</sub>O<sub>4</sub>(OH)<sub>8</sub>(H<sub>2</sub>O)<sub>4</sub>]<sub>4</sub>, **d)** [Zr<sub>6</sub>O<sub>16</sub>H<sub>16</sub>]<sup>8+</sup> **e)** Zn<sup>2+</sup> ions connected with four N atoms of the ligands.

**Ligands:** **1)** Benzene-1,3,5-tricarboxylic acid **2)** 1,4-benzene-dicarboxylic acid, **3)** tetrakis(4-carboxyphenyl)porphyrin (TCPP) **4)** 1,3,6,8-tetrakis(p-benzoate) pyrene, H<sub>4</sub>TBAPy, **5)** 2-methylimidazole

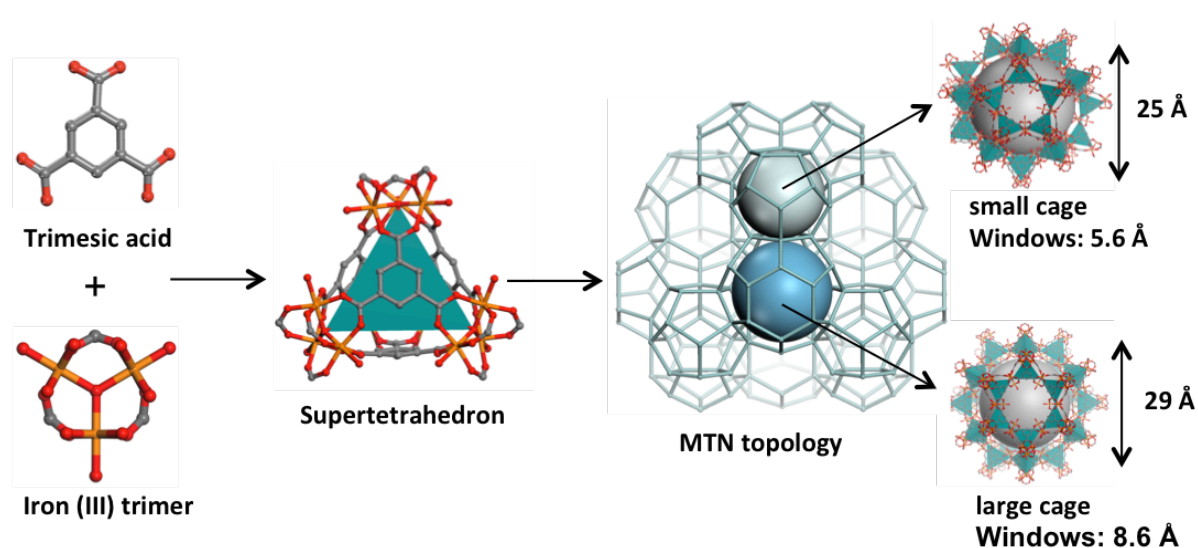
**3D structures: I).** MIL-88B(Fe) mesoporous large cage, 8 Å, **II).** UiO-66 (Zr) octahedral cage, 12 Å, **III).** PCN-224 (Zr) channel, 19 Å, **IV).** NU-1000 (Zr) mesoporous, 31 Å, hexagonal channel and microporous 12 Å triangular channels, **V).** ZIF-8 (Zn) large cage, 11.6 Å

C atoms in grey ; O atoms in red ; N atoms in blue ; H atoms are omitted for clarity. Structures made with Material Studio.

Among several MOFs structures presented in this Section (Section C) an iron-based carboxylate MOF, named MIL-100(Fe) is the MOF of interest in our study. In the next sub-chapter the composition and the main properties of MIL-100(Fe) will be presented and continuously some of the most important studied considering drug loading, surface coating and *in vitro/in vivo* studies will be highlighted.

### MIL-100(Fe)

MIL-100(Fe), MIL stands for the Materials of Institut Lavoisier, is a mesoporous iron(III) carboxylate MOF built up from trimers iron(III) octahedra linked by trimesates.<sup>96</sup> The two moieties, iron trimers and organic ligands, assemble into supertetrahedra units, which leads to the formation of the mesoporous architecture with the MTN (Mobil Thirty Nine) topology. Its porosity is reachable through two different types of cages, a small cage of 25 Å and a large cage of 29 Å, accessible through microporous windows of 5.5 and 8.6 Å respectively (**Figure 1-10**).



**Figure 1-10.** Representation of MIL-100(Fe) structure after self-assembly of iron supertetrahedra. Two cages of 25 Å and 29 Å (small and large cage) are accessible through microporous pentagonal windows of 5.6 Å and microporous hexagonal windows of 8.6 Å. Structures designed with Material Studio.

The main advantages of this MOF for drug delivery applications will now be presented. To begin with, its high surface area ( $\sim 2000 \text{ m}^2/\text{g}$ ), large pore volume ( $\approx 1 \text{ cm}^3 \cdot \text{g}^{-1}$ ) and open metal sites<sup>141</sup>, is ideal for the efficient loading of a variety of AIs in its structure.<sup>94</sup> Moreover, the presence of two types of mesoporous cages, accessible through microporous windows of different sizes, opens the possibility for the co-encapsulation of molecules and the delivery of these synergetic combinations in the organism.<sup>142</sup> In addition, this MOF can be produced at the nanoscale by “green” methods, through ambient pressure or microwave assisted routes, while several (green) protocols of surface functionalization have been reported not only to improve the colloidal stability, but also to confer the nanoMOFs targeting and imaging properties (theranostics).<sup>143-145</sup> Finally, as stated above, this MOF is biodegradable and non toxic.<sup>146</sup>

However, the degradation of a drug carrier shall not induce any side toxicity. This depends not only on the nature of the constitutive metal and linker, but also on other factors such as the particle size, drug loading, drug aggregation inside the pores, surface coating and naturally the nature and composition of the release media. In the following section, we will analyse the main parameters that play a key role in the *in vivo* fate of the drug carriers.

### **Particle size and morphology**

As discussed previously, the particle size and morphology of the nanoMOF are two key parameters influencing the drug loading and release processes.

The particle size of MIL-100(Fe) can vary from less than 100 nm until few microns.<sup>94, 96</sup> Once in neutral PBS, small particles degrade fast in less than 6 hours, against more than one week for the micro-particles.<sup>147</sup> Thus, depending on their size, MIL-100(Fe) can be considered for any administration route, including intravenous administration.

### **Surface charge**

When the nanoMOFs are administered by the intravenous route, not only their size but also their surface charge plays a key role by determining their blood circulation time, accumulation in various organs, cellular uptake, and more generally, *in vivo* fate. Several studies have investigated the role of the external surface charge of the particles and their phagocytic uptake.<sup>111, 148</sup> Once the particles are administered in the body, they come in contact with various components of the physiological media (proteins, enzymes, ions, etc). Protein binding of the NPs (opsonization) and subsequent NP uptake by macrophages or other cells of the immune systems strongly depends on the value of their  $\zeta$ - potential (or surface charge), together with the type and thickness of the coating.

In the case of MIL-100(Fe) nanoMOF, the external surface charge of MIL-100(Fe) is driven by the pending carboxylic acid and Fe-OH or Fe-H<sub>2</sub>O groups that terminate the external surface of the particle; this will determine their colloidal stability and impact their *in vivo* fate.<sup>149</sup>

It should be mentioned that high absolute values of zeta potential (positive or negative) were shown to provoke massive NP uptake by macrophages.<sup>150</sup> Surface coating of the external surface with biodegradable moieties could change these values and prolong circulation, improve colloidal stability and reduce NP cellular recognition and internalization, making them potentially “stealthy”.

### Surface coating

A variety of strategies for the surface coating of MIL-100(Fe) have been reported so far, including non-covalent or covalent approaches, such as direct grafting methods, coating of MOFs by polymer adsorption, *in situ* polymerization of the coatings onto MOFs particles. PEGylation is one of the most common approaches for surface coating in biomedicine. Hydrophilic PEG chains are FDA approved and are appropriate for improving the colloidal stability of NPs, prolonging the circulation of the drug carriers in the bloodstream. However, PEG chains can also penetrate MOFs’ cavities and consequently block the porosity. Recently, two studies have reported the successful PEG coating of MIL-100(Fe) NPs by GraftFast method<sup>151</sup> and a novel family of engineered coating (copolymers made by click chemistry consisting of dextran grafted with PEG and alendronate moieties).<sup>152</sup> Another approach is the coating of the external surface with moieties bulkier than the MOF’s windows, such as biocompatible cyclodextrin derivatives. Agostoni et al. studied the coating of the outer surface of MIL-100(Fe) with phosphated  $\beta$ -CD *via* coordination of the phosphates with the unsaturated iron sites on the external MOF surfaces.<sup>153</sup> In other studies, MIL-100(Fe) has been coated with biodegradable polysaccharides, such as dextran, biotin, heparin and chitosan, with lipids, sodium alginate, or silica.<sup>154</sup>

### Drug loading

The incorporation of AIs in the pores of MIL-100(Fe) was accomplished in most cases by impregnation methods, where preformed NPs acted as molecular sponges by soaking AIs from aqueous solutions. High drug loadings were reported together with high encapsulation efficiencies for both hydrophilic and hydrophobic drugs, which could enter into the internal porosity of the framework through the mesoporous windows of the MOF.<sup>94, 155-157</sup> AIs are encapsulated in the pores of MOFs either by covalent bonds via coordination with the metal nodes or the unsaturated sites of the organic ligands or by non-covalent interactions.

Interestingly, in some cases, encapsulated drugs self-associated inside the pores, in a “ship-in-a-bottle” manner, leading to a dramatic increase of the stability of the MOFs upon degradation.<sup>158</sup> Alternatively, drug molecules were covalently linked to the MOF structures or inserted in their composition (BioMOFs reviewed in section C).

In previous studies, the encapsulation of phosphorylated antiviral drugs azidothymidine 5'-monophosphate (AZT-MP) and azidothymidine 5'-triphosphate AZT-TP as well as the anticancer drug gemcitabine monophosphate (Gem-MP) revealed the coordination of the phosphate groups with the unsaturated iron sites of the framework.<sup>156, 157</sup> This binding of the drug onto the metal sites led, particularly for AZT-TP, to a prolonged drug release despite the strong hydrophilic character of the drug.

In another study, the hydrophilic drug topotecan (TPT) was efficiently encapsulated in MIL-100(Fe) NPs after step by step impregnation with a final loading of 12 wt %.<sup>158</sup> Topotecan formed aggregates by  $\pi$ - $\pi$  stacking interactions inside the nanoMOF matrix, resulting in the stabilization of the NPs upon degradation possibly by hindering the penetration of ions from the degrading outer media.

Overall, the controlled release of a drug was strongly related both to the state of the drug (individualized molecules or aggregates) and to the nature and strength of interactions between the AI and the unsaturated metal sites and/or ligands of the framework.

### ***In vitro/In vivo studies***

Toxicity of NPs is governed by several parameters, such as composition, size, surface charge, incorporation of AIs and surface functionalization, as we have commented previously. In this context, MIL-100(Fe) is composed by iron(III) and trimesic acid that induced no toxicity in the organism upon degradation.<sup>146</sup> However, this parameter is not an absolute condition for the avoidance of the *in vivo* toxicity. Numerous stability tests and characterization techniques are needed to gain a clear picture, continuously by *in vitro* studies and finally by *in vivo* tests in living organism, before nanosized MOFs are considered safe for medical applications.

*In vitro* studies are rapid and low cost tests performed with cells, microorganisms or biological molecules outside their normal biological context, but they are of a great importance in understanding NPs interaction with biological systems and their degradation mechanism. On the other hand, *in vitro* studies cannot give an integral information about cytotoxicity, as it is the case with *in vivo* studies. NanoMOFs are relatively new materials in the domain of drug delivery and *in vitro/in vivo* toxicological tests are still in their infancy. In



this part, we will summarize some of the most important studies having reported for nano-sized MIL-100(Fe).

There are numerous *in vitro* studies to date for the cytotoxicity of bare, loaded or coated nano-sized MIL-100(Fe). The choice of different cell lines according to the chosen application makes difficult a general categorization of these studies.

*In vitro* tests based on various cell lines for loaded nano-sized MIL-100(Fe) (busulfan, AZT-TP, doxorubicin) demonstrated the protection of the AIs inside the pores and their integral accumulation in the cells.<sup>159</sup>

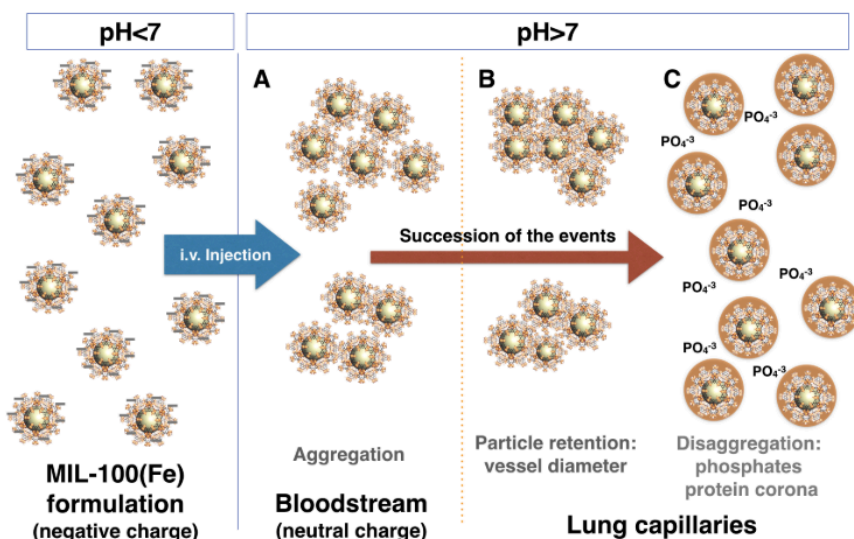
Wuttke et al. studied the cellular response of bared NPs and coated NPs with lipid bilayers by three different cell lines. Interestingly, in lung epithelial cells, biocompatibility of NPs was improved thanks to the lipid functionalization.<sup>160</sup> In another study, NPs were coated with heparin moieties via coordination of the iron metal sites with the sulfates of heparin. *In vitro* studies revealed that the heparin coating significantly slowed down the internalization process at early stages of incubation providing NPs with “stealth” properties.<sup>161</sup>

Although several *in vitro* studies for nanoMOFs have been performed, only few *in vivo* have been reported. The first was described in 2013 after intravenous administration of up to 220 mg Kg<sup>-1</sup> of bare NPs upon one month in Wistar rats.<sup>146</sup> Pharmacokinetic profiles revealed particle accumulation mainly in liver and spleen and histological studies demonstrated no toxicity of the degraded products (iron and trimesate ligand). The lack of toxicity has been confirmed in an early-stage (24 hours) experiment.<sup>162</sup>

Interestingly, another *in vivo* test performed for both bare and loaded NPs with the antineoplastic drug Busulfan, concluded that the pharmacokinetic profile dramatically changed in the presence of an AI. More precisely, empty NPs were excreted more rapidly than the loaded ones, possibly due to a change of the surface charge after drug incorporation.<sup>163</sup>

Furthermore, a large series of nanoMOFs were tested in terms of their *in vitro* and *in vivo* behavior by using as model Zebrafish embryos.<sup>164</sup> Both studies were in good correlation. The variety of NPs that were used for this study revealed that the degraded products upon physiological media differ for each kind of nanoMOF and strongly depends on its composition. Another important conclusion was that a lower toxicity was observed for the particles that were degraded slower.

Recently, the *in vivo* fate of loaded NPs for specific targeting in lungs was reported.<sup>165</sup> The behavior of MIL-100(Fe) NPs was studied as a function of their pH-responsiveness to trigger the accumulation of the loaded anticancer drug gemcitabine monophosphate (Gem-MP) in the lung tumor. A mechanism of aggregation/disaggregation of the NPs related to their surface charge, the pH and the phosphate ions present in the biological media was proposed (**Figure 1-11**).



**Figure 1-11.** Aggregation-disaggregation mechanism of MIL-100(Fe) NPs in the presence of phosphate ions and proteins upon intravenous administration for lung targeting. Adapted from<sup>165</sup>

Precedently, we attempted to summarize the most important parameters, which influence the degradation mechanism of DDS, and a special emphasis to iron(III) carboxylate MOFs was given. The nature of its components, the pKa of the ligands and the oxidation state of the metal in addition with the strength of the metal-oxo bonding and the hydrophilicity/hydrophobicity of the framework are the main factors for the determination of its stability.

We aimed to combine information from different investigations methods to gain deeper understanding on the degradation mechanism of MOF particles with different sizes and loaded or not with drugs. To achieve that, advanced characterization techniques are essential.

## D. Characterization techniques

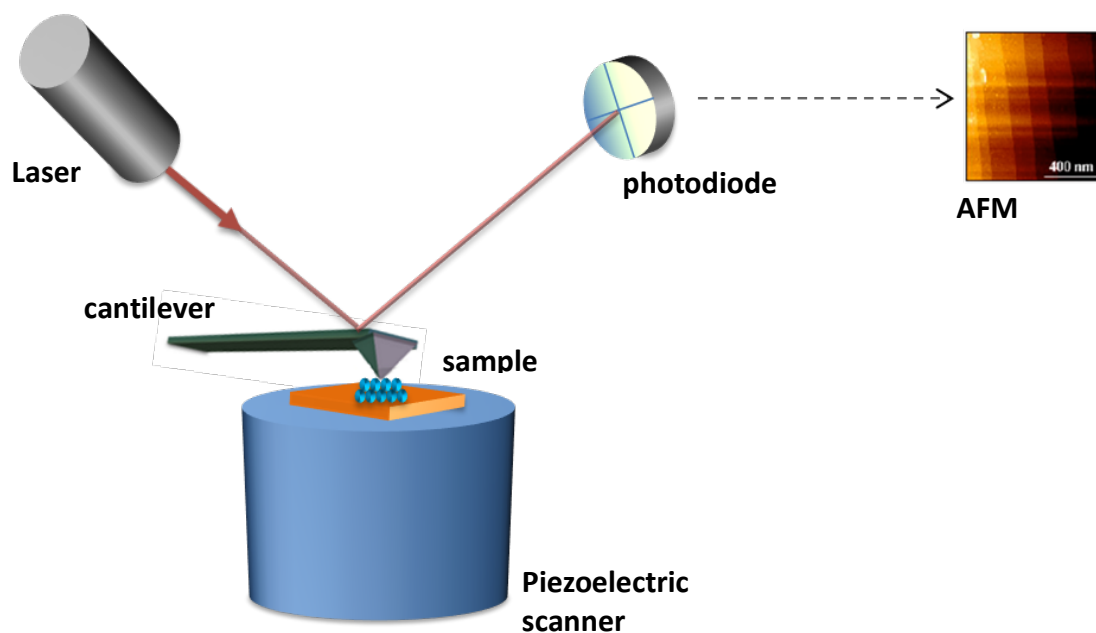
A panel of techniques have been used for the characterization of bare, loaded and coated nano-sized MIL-100(Fe) as well as their final structure upon degradation. In this section, we will present some of the main techniques that have been used in the context of this study with a focus on the methods developed in the frame of this thesis and used for the first time in the field of MOFs.

Powder X-Ray Diffraction (PXRD) provides information about the crystallinity of the sample, the nature of the phases and lattice parameters for the intact synthesized NPs and also the changes of them upon loading and/ or coating and after degradation. Nitrogen porosimetry (at 77 K) is a well-established technique for the determination of the surface area and the pore volume of porous materials. Moreover, it provides indirect qualitative data about the existence of AIs inside the internal porosity by comparing the loaded NPs with the preformed reference NPs. Particle size and size distribution are some of the main parameters that should be determined for the NPs used in biomedical application. Scanning and Transmission Electronic Microscopy (SEM/TEM) are important direct techniques to assess the size and the morphology of the NPs. Moreover, Dynamic Light Scattering (DLS) measures the hydrodynamic diameter of particles in suspensions in addition to the colloidal stability. Information concerning the strength and nature of bonds and specific functional groups is given by Fourier-transformed infrared spectroscopy (FT-IR), with wavelengths within the mid-infrared region ( $4000\text{-}400\text{ cm}^{-1}$ ). For the thermal stability and the composition of NPs Thermal Gravimetric Analysis (TGA) is suitable. Solid state Nuclear Magnetic Resonance (ssNMR) is another technique that provides information about the composition and the structural determination of NPs. Finally, High Performance Liquid Chromatography (HPLC) enables the evaluation of the degradation and release kinetics by determining the release of the ligand and of the drug, respectively. It also allows the determination of the drug payload and the drug-loaded NP stability upon storage.

All the techniques presented above are essential for studying the drug nanocarriers. In addition, we will present here two other techniques of particular interest, which have been used in our study. Atomic Force Microscopy and Spectroscopic Ellipsometry have both been used widely in the domain of material science to investigate the properties of various nanomaterials. However, to our knowledge, these have not been used so far for the evaluation of the degradation mechanism of nano-sized MIL-100(Fe) as a potential drug carrier inside miniaturized liquid cells upon incubation in physiological biological media. In the following section, the principles and the challenges of these two techniques will be discussed and finally some important studies of MOFs by *in situ* AFM and ellipsometry will be highlighted.

## Atomic Force Microscopy

Atomic Force Microscopy (AFM) is a microscopic technique invented in 1986 by Binnig, Quate and Gerber used widely to study the surface properties of materials such as the morphology, the size and the mechanical properties, with tens of nanometer spatial resolution.<sup>166</sup> AFM works with a sharp probe tip attached to a cantilever, which deflects upon interaction with the surface according to Hooke's law. A laser beam is used to detect the deflections of the cantilever (induced by the force of tip-substrate interaction) relative to the surface. Any movement of the cantilever changes the direction of the reflected beam and these changes are recorded by PSD (position-sensitive photodiode), which makes it possible to obtain a topographic map of the sample under study (**Figure 1-12**).

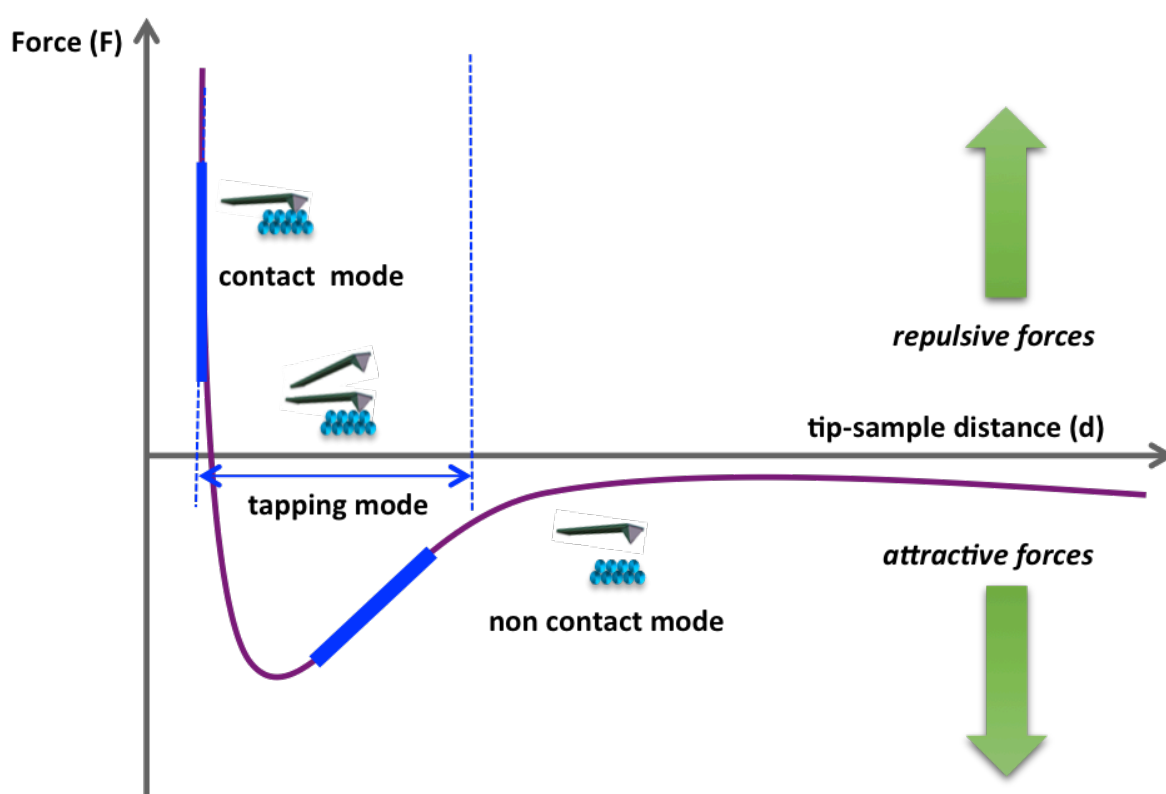


**Figure 1-12.** Schematic representation of Atomic Force Microscopy principle.

There are three main modes of operation for the AFM; the contact mode, the non-contact mode and the tapping mode.

In the contact mode the tip is continuously in physical contact with the surface of the sample during the scanning procedure. In non-contact mode, the tip is setted slightly away from the sample. Tapping mode is the combination of the two previous modes. In tapping mode, the tip contacts intermittently the surface of the sample.

When the tip is retracted from the surface of the sample, no interactions forces exist. In contrast, when the tip is in contact with the sample (contact mode), repulsive interactions occur. When it is not in contact with sample (non-contact mode), attractive forces occur. When tapping mode is used, approach and retraction forces appear depending on the distance between the tip and the sample. The competition between the attractive and the repulsive interactions that occur between the tip and the sample according to the operating mode that is chosen are summarized in a force-distance curve shown in **Figure 1-13**.



**Figure 1-13.** Graph summarizes the three main modes of Atomic Force Microscopy.

Each operational mode differs and it is chosen according to the needs of the study. The contact mode presents the highest resolution compared to the other two modes. However, two main drawbacks of this operational mode are the possible damage of the sample due to the direct contact with the tip and also the difficulty to detect single atoms, small molecules or defects along the surface of soft materials. The non-contact mode, on the other hand, protects the sample without changing its properties (ideal to avoid contamination of biological

samples). Nonetheless, the low resolution of this mode does not make it an ideal candidate. In tapping mode, the cantilever briefly touches sample's surface only at the top of each oscillation cycle. To ensure successful imaging without affecting the surface structure, tapping mode is preferable.

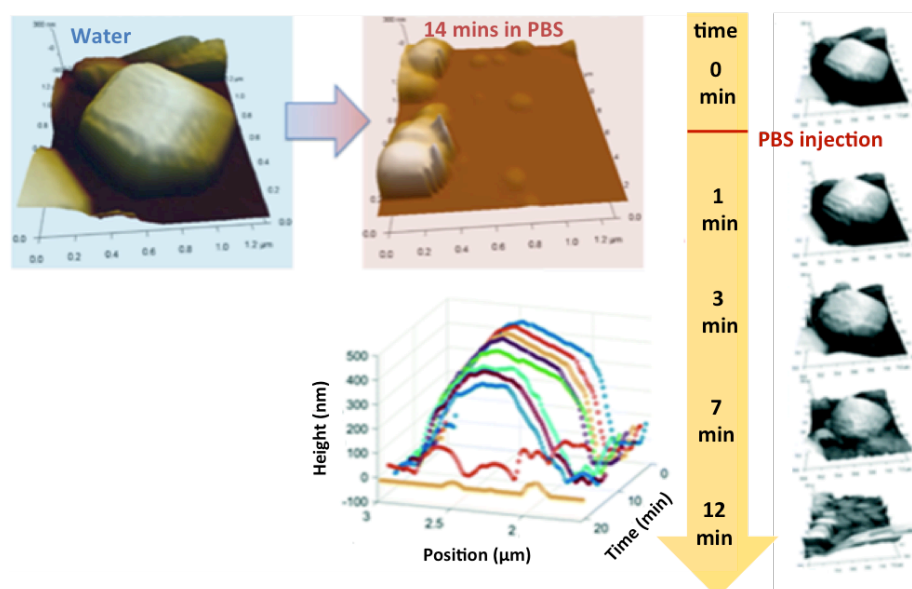
### ***In situ* Atomic Force Microscopy**

*In situ* AFM is a powerful tool used to obtain information about local morphological and mechanical changes of samples in liquids. The main advantage of *in situ* techniques is the direct observation of the studied sample and its possible changes in real time upon modification of external parameters such as the composition of the medium. Therefore, *in situ* AFM has been widely used to determine structural and mechanical changes in biological samples, such as biomolecules or cells.<sup>167</sup> It is worth mentioning, that although there are no limitations in the nature of the liquid or the sample for the measurement, the medium should be transparent for successful detection (laser light used in AFM). Another challenge for the *in situ* studies is the preparation of the sample in the liquid cell. More importantly, the measured sample should present a sufficient adhesion on the substrate, in order to be scanned by the tip. Finally, it is necessary to perform the measurements in absolutely clean media to avoid contamination of the tip and the sample.

### ***In situ* AFM and MOFs**

AFM is nowadays a common technique widely used for various types of materials, among which are the MOFs. Especially, *in situ* AFM has been employed in several studies to determine the mechanical properties of MOFs/composites, the crystal growth process and the behavior of MOFs in presence of other molecules. In 2008, *in situ* AFM monitored for the first time the crystallization growth of HKUST-1.<sup>168</sup> This study revealed a spiral or a two-dimensional surface nucleation crystal growth mechanism that started from multiple defects already presented on the initial substrate surface. Moreover, this technique could give valuable information for the intermediate structures during the crystal growth process. The same group investigated the crystal growth of the same MOF grown this time in an oriented manner on gold substrates functionalized with self-assembled monolayers (SAMs).<sup>169</sup> In this study, the growth steps emerged from this single nucleation point and spread across the entire exposed crystal face. In a similar study about crystal growth, MOF-5 was studied.<sup>170</sup> Cubillas et al. studied the crystal growth of a MOF via a SBU-type approach by *in situ* AFM. Another interesting study for the cadmium 2-ethylimidazolate MOF CdIF-4, determined for the first time the preassembled nucleating units that provoke the nucleation and the crystal growth of the framework.<sup>171</sup> In a different aspect, this technique has been used to capture in "real" time

the transformation process of a porous material in the presence of guest molecules.<sup>172</sup> More precisely, the flexible porous coordination polymer (PCP) named  $(\text{Zn}_2(1,4\text{-ndc})_2(\text{dabco}))_n$  and the guest molecule biphenyl was chosen for the study. Interestingly, the initial tetragonal lattice of the framework underwent a change to a rhombic shape in the presence of the biphenyl. More importantly, the same study provided information about the degradation mechanism of the framework, as it observed the delamination process of layer-by-layer exfoliation of the framework. In the same frame, a recent study of the degradation mechanism of ZIF-8 in PBS, a degrading medium that mimics the biological environment, monitored the behavior of a micron-sized particle by *in situ* AFM.<sup>173</sup> According to this study, the initial morphology of the particle changed instantly in the presence of PBS (within 3 minutes) and in less than 15 minutes a total dissolution of the crystal was observed (**Figure 1-14**).



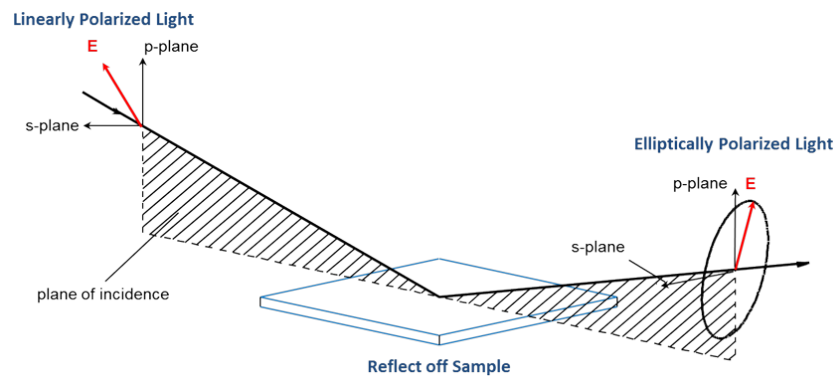
**Figure 1-14.** Degradation of ZIF-8 crystal (2  $\mu\text{m}$ ) in the presence of PBS 10 mM studied by *in situ* AFM. Adapted from<sup>173</sup>

All in all, with the exception of the most recent study concerning the degradation of ZIF-8 in PBS<sup>173</sup>, the majority of studies using *in situ* AFM have focused on the crystal growth of MOFs. Compared to these studies, in the context of the thesis, *in situ* AFM was used for the first time for the study of degradation mechanism of MIL-100(Fe). The novelty of this study does not consist only to measurements in liquid phase, but also to the *in situ* change of the pH in a wide range (from acidic to basic). As it has already mentioned in Section C, the pH of the media has a key role to the degradation mechanism of MOFs particles for drug delivery

applications. Of note, MIL-100(Fe) particles of different crystallinity rates were studied by *in situ* AFM for exploring their impact on particles stability under physiological conditions. The conclusions of this study have been proved valuable for the better understanding of the degradation mechanism of nanoMOFs, which have been further explored by another innovative technique; *in situ* ellipsometry.

## Spectroscopic Ellipsometry

Spectroscopic Ellipsometry (SE) is an optical measurement technique that uses light to characterize thin films, surfaces and materials microstructures. SE measures the change in polarization that occurs when a light beam is reflected from a surface (**Figure 1-15**). Professor Paul Drude team firstly reported this technique in 1887<sup>174</sup>, which however gained ground in early 1990s thanks to the commercialization of SE instruments. Ellipsometry determines the optical constants of a film (refractive index), its thickness and any modification of them. Moreover, other properties, such as the porosity, composition, roughness, and conductivity can also be determined through the optical modelling of the film properties. SE is a non-destructive method with high sensitivity to thin films (sub nanometers to several tens of microns). Additionally, no special preparation of the sample and no ‘calibration’ are needed. On the other hand, some of the limitations of ellipsometry are that data analysis is model dependent and that the studied sample has to be of a reasonable optical quality.<sup>175</sup>



**Figure 1-15.** Illustration of ellipsometric measurement. The emitted light is reflected on sample’s surface from the left and the changes of polarized light is detected on the right. Adapted from<sup>176</sup>



### ***In situ* ellipsometry**

Ellipsometry can be performed within any transparent medium. As a consequence, *In situ* ellipsometry can be performed with samples embedded in liquids or gases at a constant flow or even under ultra-high vacuum and uses large chambers or small liquid flow cells depending on the requirements of the process. The measurement in the changes of the optical properties in real time offers the unique opportunity to measure the sample without destroying it (only the light beam passes through the cell). This approach replaces the use of many films by the continuous monitoring of one single film. This technique is mostly used for the study of semiconductor growth and process control, optical coatings and multi-layer structures, photovoltaics and nanostructured devices and finally biomaterials and bio-interfaces.<sup>177</sup> In a recent study, degradation mechanism of mesoporous silica nanovectors were studied by *in situ* ellipsometry under simulated biological media (also in the presence of bovine serum albumin) in undersaturated conditions.<sup>178</sup> Bindini *et al.* showed that the dissolution kinetics of the silica NPs depends strongly on their accessible surface area by comparing bare and coated NPs. Furthermore, it was demonstrated that upon incubation in a medium rich in proteins, the degradation was slowed down due to the diffusion of the proteins on the particles' surface. This result strengthened the point that the surface area and the degradation mechanism are firmly dependent.

As we have discussed in Section C, degradation mechanism of nanocarriers is governed by several parameters and it can be followed by *in vivo* studies. These studies are complex to be performed and acquire specialized trainings for obtaining successful results. When nanocarriers are injected intravenously in the bloodstream, they experience large dilutions (sink conditions), considering that the blood volume is around 5L for humans and in the case of animal studies, around 200 mL for rats. At the opposite, their successful vectorization will lead to high local concentration (in either extra and/or intracellular media). Studies of chemical stability performed *ex vivo* in laboratory and characterization techniques of the NPs (as described in Section D) are essential for the understanding of the degradation of nanocarriers. However, they are not sufficient to reach all conditions that exist inside the living organism. *In situ* ellipsometry is an appropriate tool to study the degradation mechanism of NPs in biological media that mimic closely real diluted conditions.

Therefore, in the frame of our study, *in situ* ellipsometry was used to study the degradation mechanism of MIL-100(Fe) nanoMOFs in diluted conditions, drawing conclusions on the influence of intrinsic/structural parameters of the nanoMOFs and exterior parameters (pH, temperature, presence of mobile ions and biomolecules).

To achieve this goal, *in situ* ellipsometry requires the absolute control of the conditions in liquid cell and also the fabrication of a thin film of optical quality.

## Optical films and MOFs

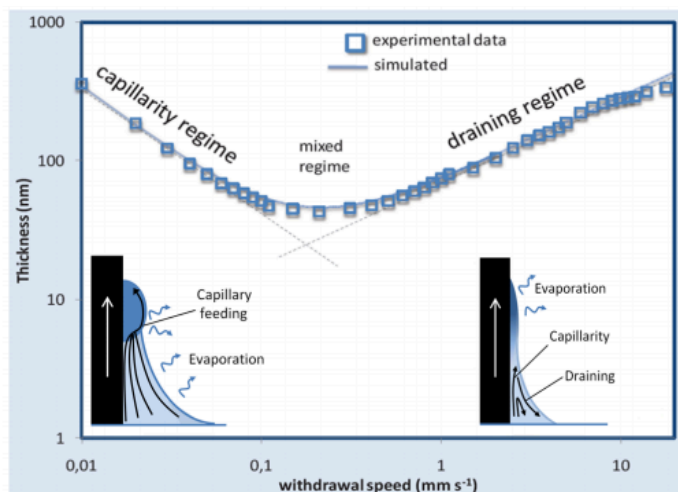
In the field of MOFs, several methods have been reported to obtain thin films of an optical quality, such as growth/deposition<sup>179</sup> or oriented growth from solvothermal methods<sup>180, 181</sup>, step-by-step liquid epitaxy (LPE)<sup>182</sup>, electrochemical synthesis<sup>183, 184</sup> and colloidal deposition methods (spin or dip coating). Dip coating was firstly applied in the field of MOFs for the MIL and ZIF family and their application as vapor sensors was studied<sup>185-187</sup>. MIL-89(Fe), MIL-101(Cr) and ZIF-8 were the three frameworks that were studied. Thin optical films of high quality were fabricated, using nanoMOFs made under mild conditions or microwave assisted hydrothermal route, by chemical solution deposition (CSD) also known as dip coating and continuously they were characterized by surface analysis techniques, such as WAXS, SEM, AFM and ellipsometry. The vapor sorption properties of MOFs associated to the pore sizes and the inter-particle mesoporosity of the frameworks were followed by environmental ellipsometry and revealed their unique properties, which made them good candidates as vapor sensors.

As far as we know, no studies involving *in situ* monitoring of MOF degradation by ellipsometry has been reported. In our case, the method of dip coating was used for the fabrication of a thin film of nano-sized MIL-100(Fe). It should be noted, that the elaboration of the optical film is a delicate procedure. The small nanosized particles of MIL-100(Fe) (around 50 nm), elaborated through a new synthesis protocol<sup>188</sup>, tend to aggregate at a certain concentration, leading to the formation of inhomogeneous films. Therefore, a good compromise between sample's concentration, colloidal stability, solvent evaporation speed and withdrawal speed during dip coating process of films is crucial for successful measurements.

## Dip coating

Dip coating designates the deposition of a thin film from a liquid medium onto a substrate. The dip coating steps can be summarized in the **Figure 1-16**. Different models for film deposition exist based on the nature of the system and the intended application. The formation and the thickness of the film are dominated by the substrate withdrawal speed according to Landau-Levich model (LL), the first theoretical model aiming at describing film formation.<sup>189</sup> Following this model, the thickness of the cast film increases with the increasing of the withdrawal speed due the combination of gravitational draining and viscous drag of the

solution. At ultralow withdrawal speeds, the formation of the film is explained by another model depending on solvent evaporation and the capillary force. Faustini et al. published a semi-empirical model that successfully combines both models, covering a broad withdrawal speed range (from 0.001 to 10 mm s<sup>-1</sup>).<sup>190</sup>



**Figure 1-16.** Schematic representation of the semi-empirical model. The schema demonstrates both the capillary and draining regime for the fabrication of an optical film by dip coating process. Adapted from<sup>190</sup>

To conclude, characterization techniques that have already been widely used to understand the degradation mechanism of MOFs, but also innovative *in situ* techniques for deeper investigation of NPs under biological media have been discussed in this Section (Section D). In previous sections, the use of MOFs and especially of MIL-100(Fe) as DDS was proven through several studies. The following section will describe the advances in that field.



## **E. Metal-organic frameworks for drug delivery: Degradation mechanism and *in vivo* fate**

In this part a comprehensive chapter dealing with the biodegradation of MOFs will be presented. It is a chapter upon invitation in the book ‘‘Metal-Organic Frameworks for Biomedical Applications’’ (Elsevier) and has been published in 2020.

In this chapter, first of all, the synthesis and the composition of various biodegradable MOFs are described. Secondly, an overview of different drugs incorporated in nanoscale MOFs is presented.

The chapter highlights the importance of gaining deep knowledge on MOF degradation and *in vivo* fate for biological applications.

A special emphasis is given to MIL-100(Fe), as one of the most promising candidates for bioapplications and for which solid data on *in vivo* applications have been presented. Moreover, engineering of the external MOFs’ surface and its role in biodegradation are highlighted. Finally, important *in vitro/in vivo* studies of MIL-100(Fe) are summarized to evaluate particles’ fate.

# *Metal-organic frameworks for drug delivery: Degradation mechanism and in vivo fate*

Ioanna Christodoulou<sup>a,b</sup>, Christian Serre<sup>b</sup>, Ruxandra Gref<sup>a</sup>

<sup>a</sup>National Center for Scientific Research (CNRS), Institute of Molecular Sciences, Paris-Sud University, Paris-Saclay University, Orsay, France <sup>b</sup>Institut des Matériaux Poreux de Paris, FRE 2000 CNRS, Ecole Normale Supérieure, Ecole Supérieure de Physique et de Chimie Industrielles de Paris, PSL Research University, Paris, France

## **21.1 Introduction**

More than 100 years ago, Paul Ehrlich, a Nobel Prize winner, was dreaming about “magic bullets”, or chemical compounds that could bind to specific pathogens in order to selectively destroy them. Inspired by this concept, scientists nowadays focus their efforts on engineering nanoscale drug carriers that could load drugs and transport them specifically to diseased tissues, thus acting as “magic bullets”.

However, to be used as nanocarrier, a particulate system has to fulfill a series of requirements:

- Biodegradability to avoid accumulation in the living organism
- Lack of toxicity and excretion of the degradation products
- High drug payloads and good incorporation yields of the active molecules
- Controlled release of the cargo
- Selective targeting of diseased cells or organs
- Possibilities of surface modifications to control in vivo fate and ensure stability
- Good detection by imaging techniques
- “Green”, reproducible, and scalable synthesis

A wide variety of drug nanocarriers has been developed in the field of nanomedicine, including liposomes, polymeric micelles, dendrimers, and nanoparticles. Each system presents advantages and disadvantages, in terms of stability, toxicity, and capacity to incorporate drugs with specific properties. For instance, organic carriers such as liposomes discovered in the mid-1960s attracted high interest because of their composition based on natural phospholipids [1]. On the other hand, drug payloads were often low, especially for hydrophobic

## 468 Chapter 21

molecules, and the vesicular structures were fragile in complex media. While liposomes were adapted to incorporate hydrophilic drugs into their inner aqueous compartment, polymeric micelles were mainly used for the delivery of lipophilic drugs and they could readily disassemble, depending on their critical micellar concentration [2]. Dendrimers have also been studied as drug carriers, but the cost of their synthesis is relatively elevated [3]. Polymeric nanoparticles are generally endowed with good shelf stability, but due to the hydrophobic nature of the biocompatible materials, most hydrophilic drugs were difficult to be incorporated [4].

In this context, recently, a new family of hybrid porous particles, named metal-organic frameworks (MOFs), was discovered and proposed for drug delivery. Contrary to the organic particles described above, MOFs are hybrid porous materials, consisting of metal nodes connected to organic bridging ligands [5–7]. Traditionally, they are used in applications such as gas storage, adsorption, and catalysis [8–10]. MOFs are also used as molecular sieves for the separation of gases or larger molecules. In 2006, Férey and coworkers presented for the first time the use of a Cr-based MOF, as a potential system for drug delivery, by successfully encapsulating the analgesic and antiinflammatory drug ibuprofen into its pores [11]. Later on, the first nanoscale biocompatible Fe-based MOF was used to incorporate a series of drugs with either hydrophilic or hydrophobic character [12].

MOFs appeared as ideal candidates for biomedical applications. Their open porosity was expressed by unprecedented surface areas (they can reach 7839 m<sup>2</sup>/g) [13]. Drug payloads reached 25% wt or more [12, 14–16]. MOFs' intrinsic amphiphilic microenvironment was adapted to host both hydrophilic and hydrophobic active molecules. Finally, the possibility to produce MOFs using a practically unlimited variety of metals and organic ligands ends up to a boundless combination of them, which in turn generates new structures of MOFs.

On the other hand, as always, there are two sides to every coin. To begin with, MOFs were first used in the domains of energy and storage, where a significant stability is required. However, in the domain of biomedicine, the carriers should be stable during the loading and the coating procedures and also during their circulation in the living organism, until they reach their target. However, they should eventually degrade and release their cargo. In a nutshell, a subtle balance between stability and degradation is needed to design effective MOFs for drug targeting purposes.

It should also be kept in mind that MOFs should possess engineered shells to reach their biological targets and that these coatings may in turn play a role in the degradation processes. Moreover, drugs in the MOF pores can either stabilize or destabilize the matrices, as they can interfere with the fluxes of water and ions from the outside media and with the diffusion of the degradation products.

At this point, it is worth to mention that MOFs are coordination polymers, and contrary to organic nanocarriers with strong chemical bonds (nanoparticles, micelles, dendrimers, etc.), they show peculiar features related to their degradation in various media.

It is, therefore, extremely challenging to control the chemical stability of the MOFs and simultaneously maintain their biodegradable character intact. Herein, we discuss these challenges based on recent literature on MOFs for biomedical applications.

## 21.2 Synthesis of biodegradable MOFs

To design biodegradable MOFs carriers, first metals and ligands with minimal toxicities should be chosen.  $\text{Fe}^{2,3+}$ ,  $\text{Ca}^{2+}$ ,  $\text{Zr}^{2+}$ ,  $\text{Co}^{2+}$ ,  $\text{Mn}^{2+}$ , and  $\text{Zn}^{2+}$  are some of the elements which are included already, in traces, in the composition of the human body.

Concerning the ligand compositions, two families are particularly appealing, the carboxylates and the imidazolates, because of their high polarity and their easy elimination from the human body [17]. The method and the reaction conditions are important factors to be taken into account in the design of MOFs. A wide variety of synthetic pathways has been developed, including hydrothermal/solvothermal, electrochemical, and microwave-assisted methods [18, 19]. Among them, one of the most appealing synthesis routes was the microwave irradiation one, as it leads to homogenous nanoparticles within short reaction times [20].

Independently of the synthesis procedure, it is highly recommended that nontoxic solvents and mild conditions (“green” synthesis) should be used. Whenever this is not possible, the organic solvents need to be totally removed from the final product. It is finally crucial to mention the possibility of scaling up the synthesis of the particles in an industrial level. BASF has already developed synthesis techniques and produces in ton scale a variety of MOFs named Basolite for energy applications and catalysis [21].

Named as MIL-family (Materials of Institute Lavoisier), the iron-carboxylate MOFs are considered as one of the most adapted groups of MOFs for bioapplications. Zinc-imidazolate MOFs and mainly ZIF-8 are also interesting candidates. Some other systems, UiO-66(Zr) (UiO stands for University of Oslo) or HKUST-1 (Hong Kong University of Science and Technology), are also used extensively in bioapplications. Last but not the least, a new group was developed, called bioMOFs, in which biomolecules were used as constitutive linkers. For example, BioMIL-5 synthesized from  $\text{Zn}^{2+}$  and azelaic acid was stable in aqueous solutions and, after degradation, azelaic acid was released [22]. All these materials are gathered in Table 21.1, showing the large variety of ligands and possibility to reach pore sizes up to 34 Å.

Obviously, the unlimited combination of different metals and ligands leads to the formation of new porous materials with different sizes and properties, some of which are suitable for bioapplications. However, the stability of these materials remains still an important issue and the most studied one, MIL-100(Fe), was considered one of the most promising candidates [23]. MIL-100 is a mesoporous MOF consisting of iron trimers connected by trimesic acid ligands, which reproduce a crystalline structure with two different types of cages (25 and 29 Å),



Table 21.1 Overview of biodegradable MOFs.

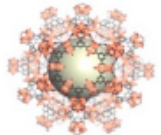
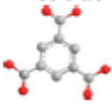
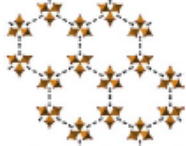
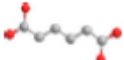
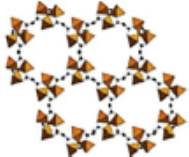
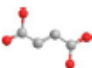
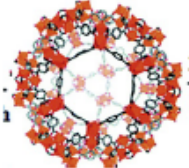
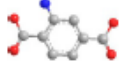
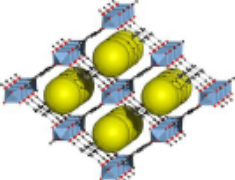

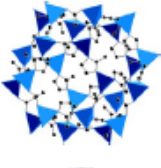
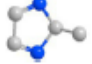
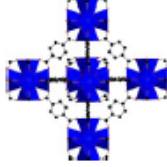

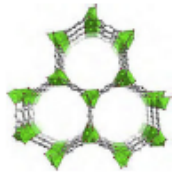
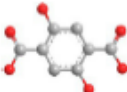
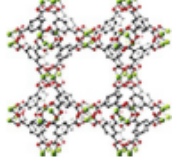
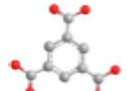
MOF name	Structure	Organic ligand	Pore size (Å)	References
MIL-100(Fe)		Trimesic acid 	25 29	[12]
MIL-89(Fe)		Muconic acid 	11	[12]
MIL-88A(Fe)		Fumaric acid 	13.9	[12]
MIL-101_NH2		Aminoterephthalic acid 	29 34	[12]
MIL-53		Terephthalic acid 	8.5	[12]
ZIF-8		2-Methyl imidazole 	11.6	[63]
UiO-66(Zr)		Terephthalic acid 	12	[64]

Table 21.1 Overview of biodegradable MOFs—cont'd

MOF name	Structure	Organic ligand	Pore size (Å)	References
CPO-27-Co/Ni		2,5-Dihydroxyterephthalic acid 	11	[65]
HKUST-1		Trimesic acid 	9	[66]

accessible through pentagonal (5.6 Å) and hexagonal windows (8.6 Å) [24]. MIL-100(Fe) advantageously presented high drug loadings and good stability by maintaining simultaneously its biodegradable character [25].

### 21.3 Drug loading and release

A wide variety of active molecules have been incorporated in the pores of MOFs, such as anticancer, antiviral and antiinflammatory drugs, or antibiotics. Recently, oligopeptides, nucleic acids, and proteins were also encapsulated inside the MOFs' pores [26] and even hydrogen for cancer therapy [27]. Ibuprofen was successfully encapsulated into the pores of MIL-100(Cr) and MIL-101(Cr) [24]. However, the toxicity issues of the chromium metal was an important issue and this metal could be successfully replaced by iron leading to the formation of MIL-53(Fe), a flexible MOF structure that by the effect of its "breathing" phenomenon could adsorb into its pores the drug ibuprofen [28]. In 2010, a wide range of nanosized iron-carboxylate MOFs, adapted for intravenous administration, was described [12]. By this way, it was demonstrated that the loading capacity was related to the pore and window sizes, as well as the nature of the constitutive ligands. Of note, a variety of drugs, hydrophobic, hydrophilic, and amphiphilic, were successfully incorporated [14, 29].

In another example, M-CPO-27 (where M= Ni or Co) adsorbed significant amounts of NO, a biological active gas, of interest for its antibacterial, antithrombotic, and wound healing applications [30]. HKUST-1 was the guest of different molecules (ibuprofen, anethole, and guaiaicol) with a loading of more than 30 wt% [32]. Lin et al. synthesized a Tb<sup>3+</sup>-based MOF coated with Silica for platinum-based anticancer drug delivery [33]. Moreover, Gd<sup>3+</sup>-based MOFs were developed as contrast agents for MRI [34, 35]. In another study, Mn<sup>2+</sup> nanorods

## 472 Chapter 21

were proposed for the same imaging purpose, in order to avoid the toxicity issues raised from the use of  $Gd^{3+}$  [34, 35]. In conclusion, increasing interest is dedicated to the use of MOFs for drug incorporation and/or imaging purposes. Table 21.2 summarizes the different families of active molecules incorporated in nanoscale MOFs.

Table 21.2 Loadings of different active molecules.

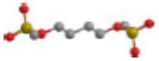
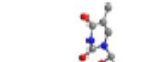
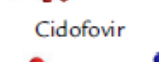
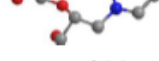
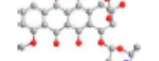
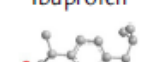
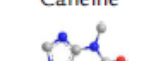
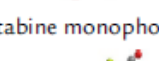
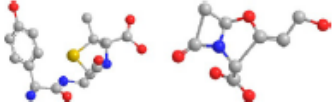
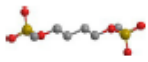
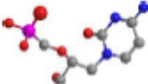
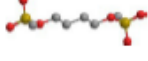
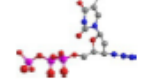
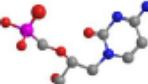
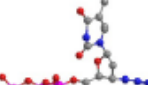
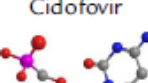
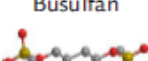
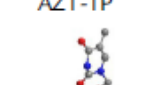
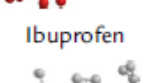
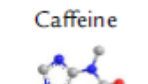
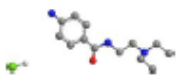
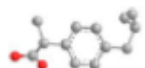
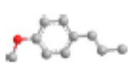
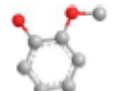
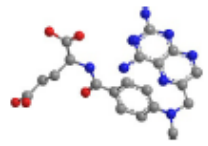
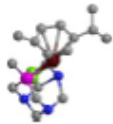
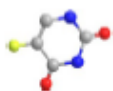
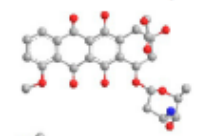
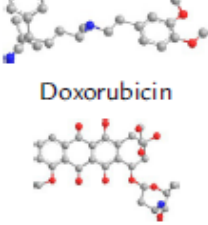
MOF	Active molecule	Drug loading (wt%)	References
MIL-100(Fe)	Busulfan 	25.5	[12]
	AZT-TP 	21.2	[12]
	Cidofovir 	16.1	[12]
	Doxorubicin 	9.1	[12]
	Ibuprofen 	33	[12]
	Caffeine 	24.2	[12]
	Gemcitabine monophosphate 	30	[36]
	Topotecan 	11.6	[41]
	Amoxicillin/cluvalanate 	13/22	[42]

Table 21.2 Loadings of different active molecules—cont'd

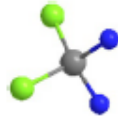
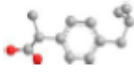
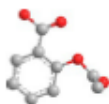
MOF	Active molecule	Drug loading (wt%)	References
MIL-89(Fe)	Busulfan 	9.8	[12]
	Cidofovir 	14	[12]
MIL-88A (Fe)	Busulfan 	8.0	[12]
	AZT-TP 	0.6	[12]
	Cidofovir 	2.6	[12]
MIL-101_NH2	AZT-TP 	42.0	[12]
	Cidofovir 	41.9	[12]
MIL-53	Busulfan 	14.3	[12]
	AZT-TP 	0.24	[12]
	Ibuprofen 	22	[12]
	Caffeine 	23.1	[12]

*Continued*

Table 21.2 Loadings of different active molecules—cont'd

MOF	Active molecule	Drug loading (wt%)	References
bio-MOF-1	Procainamide hydrochloride 	22	[42a]
HKUST-1	Ibuprofen 	34	[31, 32]
	Anethole 	38	[31, 32]
	Guaicacol 	40	[31, 32]
PCN-221	MTX 	40	[42b]
CPO-27-Ni/Co	RAPTA-C 	100	[67]
ZIF-8	5-Fluorouracil 	45.4	[16]
	Doxorubicin/verapamil 	8.9/32	[68]
UiO-66(Zr)	Doxorubicin 	The amount of DOX loadable into UiO-66 was calculated to be 1 mg DOX/mg UiO-66	[31, 32]

**Table 21.2** Loadings of different active molecules—cont'd

MOF	Active molecule	Drug loading (wt%)	References
	Cisplatin 	29.8	[68a]
	Ibuprofen 	35.5	[68b]
	Aspirin 	25.5	[68b]

It is of main importance that the MOF carrier doesn't alter its properties during and after the drug loading procedure and also that the loading efficiency is high enough. The most common loading procedures consist of impregnations of MOF particles in aqueous or ethanolic drug solutions, during which the active molecules are incorporated into the pores of the MOFs by diffusion and coordinate with the metal sites and/or organic ligands. Some of the most studied active molecules are the phosphorylated drugs, such as the anticancer drug Gemcitabine monophosphate or the azidothymidine triphosphate (AZT-TP), which were incorporated in MIL-100(Fe) with yields close to 100% [36, 37]. It was found that azidothymidine monophosphate (AZT-MP) was released faster from the MOFs as compared to AZT-TP, as a result of its weaker interaction with the nanoparticles [37] (Fig. 21.1).

After drug loading, the release of the cargo was typically studied in different media, such as PBS (phosphate buffer saline), Tris (containing sulfates), and biological mediums with or without serum [38]. In PBS, the most investigated release medium, a competition for the metal sites of the framework, was observed between the phosphates, the linker, and the active molecule. As shown in Fig. 21.2, the phosphates in the release media triggered both drug and ligand releases, whereas no drug release was observed in Tris buffer or in water [39]. In another study, the degradation mechanism of MOF particles loaded with the antibiotic gentamicin was investigated in different media [40]. The release of the constitutive ligand was both influenced by the presence of the incorporated drug and the nature of the release media.

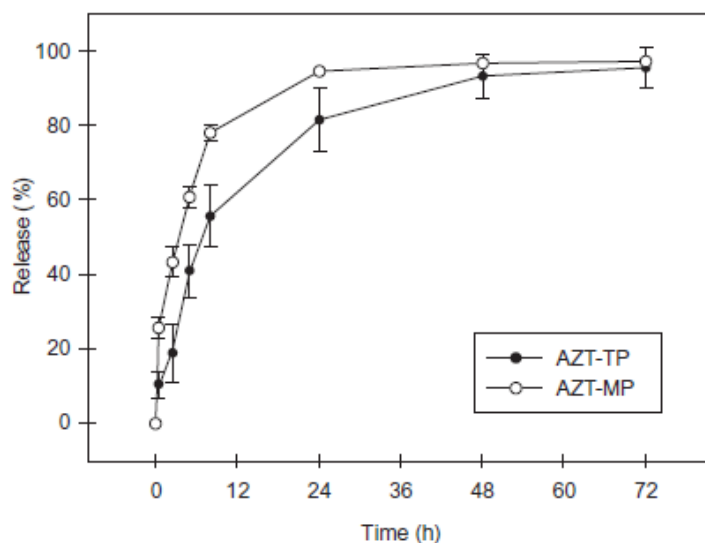


Fig. 21.1

Degradation of loaded MOFs with two different phosphorylated drugs: release of AZT-MP and AZT-TP in PBS at 37°C. Reproduced with permission from V. Agostoni, et al., *Impact of phosphorylation on the encapsulation of nucleoside analogues within porous iron(III) metal-organic framework MIL-100(Fe) nanoparticles*, *J. Mater. Chem. B* 1 (34) (2013) 4231–4242, copyright 2013, *J. Mater. Chem. B*.

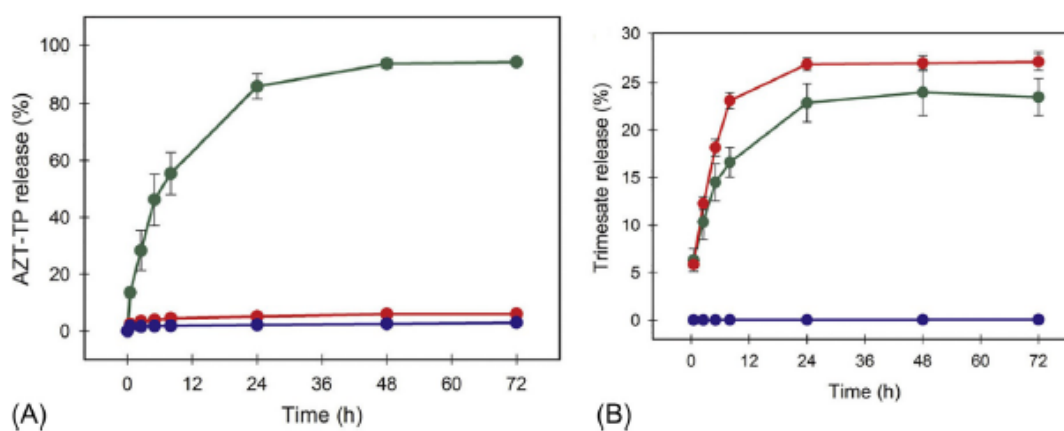


Fig. 21.2

Release of the drug and the constitutive ligand in different mediums: (A) release of AZT-TP in PBS (green line), Triss buffer (red line), and H<sub>2</sub>O (blue line). (B) Release of trimesic acid in PBS (green line), Triss buffer (red line), and H<sub>2</sub>O (blue line). Reproduced with permission from V. Agostoni, et al., *Towards an improved anti-HIV activity of NRTI via metal-organic frameworks nanoparticles*, *Adv. Healthc. Mater.* 2 (12) (2013) 1630–1637, copyright 2013, *Advanced Healthcare Materials*.

As a consequence, it is logic to assume that the presence and the nature of molecules entrapped into the pores of the MOFs affect the degradation kinetics, either by accelerating or by slowing it down. This has been demonstrated in the case of the topotecan, an anticancer drug entrapped in MIL-100(Fe) nanoparticles [41].

Topotecan has the particularity of forming aggregates in solution and  $\pi$ - $\pi$  stacking interactions in solid state. It could be efficiently loaded inside the MOF pores after step by step impregnations (“ship in a bottle” method). By this way, impregnation took place in diluted drug solution, where the molecules were not aggregated and could pass through the MOF windows (Fig. 21.1). However, once in the pores, topotecan molecules aggregated forming clusters and the final loading reached 12 wt%. In this case, around 14 topotecan molecules were packed inside each cage of the framework. Interestingly, this clustering effect dramatically reduced the degradation of the MOFs, possibly by avoiding the penetration of the outer medium in the pores (Fig. 21.3).

More recently, it was shown that two different molecules could be co-incorporated inside MIL-100(Fe) nanoparticles [42]. The antibiotics amoxicillin (AMOX) and potassium clavulanate (CL) were co-encapsulated reaching a total drug loading close to 35 wt%. As already mentioned, MIL-100(Fe) is a mesoporous material with two different types of cages (25 and 29 Å) accessible through pentagonal and hexagonal windows (5.5 and 8.6 Å). CL was preferentially packed inside the small cages, whereas AMOX was located in the large ones. Of interest, the loaded nanoparticles penetrated inside infected macrophages releasing their drug cargo in the vicinity of the intracellular pathogen. It was demonstrated that the MOFs degraded inside the cells, within a few hours. However, the mechanism of intracellular degradation was not investigated.

In a nutshell, the degradation mechanism of the MOF carriers was found to be related to the amount and nature of the incorporated active molecules, their location (large and/or small cages), capacity to form aggregates inside the pores, as well as nature of the degradation medium and concentration of ion species. Therefore, it would be of great interest to perform a systematic study of the degradation mechanism of the loaded particles in different media.

## **21.4 Degradation**

The stability of the MOF particles depends on several parameters, such as their constitutive ligands and metal ions, the medium, the temperature, and the pH. In addition, the presence of loaded molecules in the cores or an outer coating shell also affects MOF suspensions’ stabilities and degradation.

As an example, a series of zirconium-based MOFs were studied after modifications of their constitutive ligands in different media and their chemical and thermal stability was reported [43].



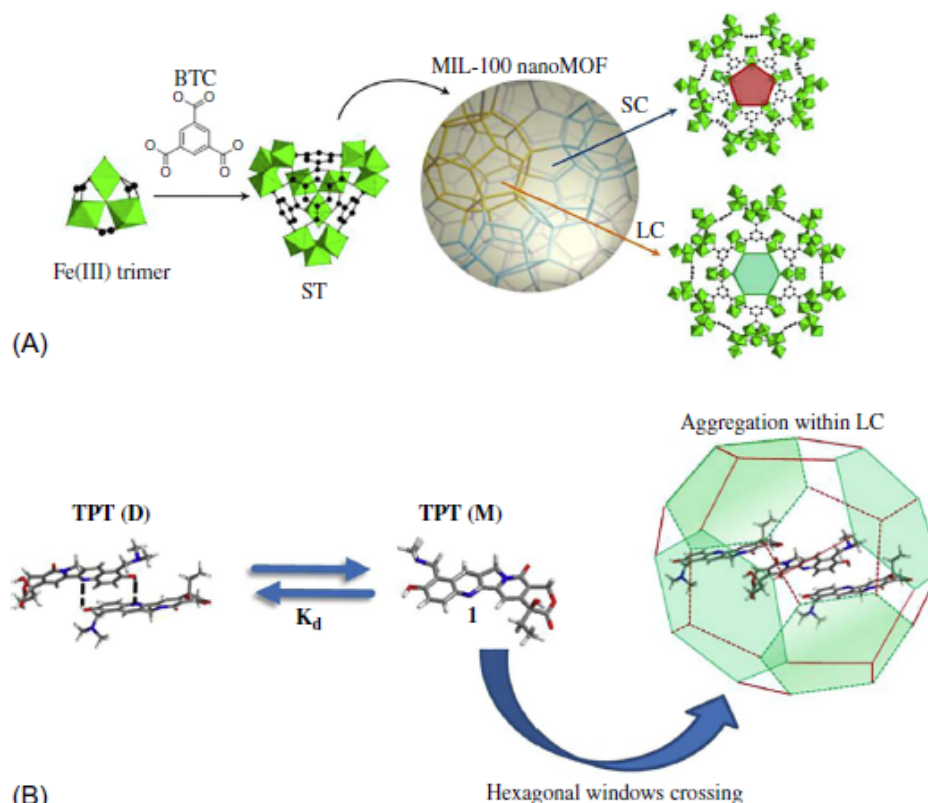


Fig. 21.3

Self-assembly of MIL-100(Fe) and loading of Topotecan: (A) Schematic representation of the synthesis of MIL-100(Fe). Formation of supertetrahedra by the ligand (trimesic acid) and the metal (iron) and self-assembly into the final mesoporous MOF, MIL-100(Fe). MIL-100 consists of two cages, small and large ones, which can be accessed by hexagonal and/or pentagonal windows. (B) Dissociation of the dimers of topotecan into monomers and their entrapment selectively in the large cages (LC) of the MIL-100. Once the monomers are entrapped, they are prone to aggregate by  $\pi$ - $\pi$  interactions inside the pores. *Reproduced with permission from M.R. Di Nunzio, et al., A "ship in a bottle" strategy to load a hydrophilic anticancer drug in porous metal organic framework nanoparticles: efficient encapsulation, matrix stabilization, and photodelivery, J. Med. Chem. 57 (2) (2014) 411–420, copyright 2014, Journal of Medicinal Chemistry.*

The length of the ligand chain, as well as the attachment of functional groups (amino and nitrogen atoms) and finally their impregnation in various chemical solvents altered the stability of the MOFs, as it was proven by a series of complementary techniques (PXRD, FTIR, TGA, etc.).

In other studies, the influence of the medium on the degradation mechanism of a Mg-gallate MOF was investigated [44]. The constitutive ligand of this MOF is a natural active molecule (gallic acid) with a remarkable antioxidant activity once it is released inside the organism. It was shown that the release of the ligand was provoked by the degradation of the framework

itself, but the kinetics of the release were influenced by the medium. More precisely, the stability of the particles was tested in water and in RPMI and a lower stability was observed in RPMI, probably due to the presence of phosphates in this medium.

Recently, the degradation mechanism of two different iron-carboxylate MOFs, MIL-100(Fe) and MIL-53(Fe), was deeply studied under two different conditions [45]. The behavior of both particles was investigated in boiling water (100°C) and after the adjustment of the pH to 7 by addition of NaOH. Interestingly, it was shown that during degradation in boiling water, the XRD patterns remained unchanged, whereas microscopic techniques revealed the formation of small aggregates of 3–4 nm consisting of  $\alpha$ -Fe<sub>2</sub>O<sub>3</sub> in the case of MIL-100(Fe) together with a well-crystallized product (goethite), or hematite in the case of MIL-53(Fe). In contrast, at pH 7, both studied material became amorphous and partially degraded into an iron (oxo)hydroxide material, ferrihydrite (Fig. 21.4).

The above study revealed the partial degradation of the MOFs and the formation of different products at elevated temperatures or after pH modifications. However, these studies referred only to the degradation of the particles in water and not in a buffer, nor a biological media.

Another study investigated the degradation mechanism of large MIL-100(Fe) crystals and the effect of incorporated anticancer drugs after 8 days of incubation in PBS by using Raman microscopy [46]. Advantageously, the method enabled studying the morphological features of thousands of particles during their degradation and to take Raman spectra on selected ones.

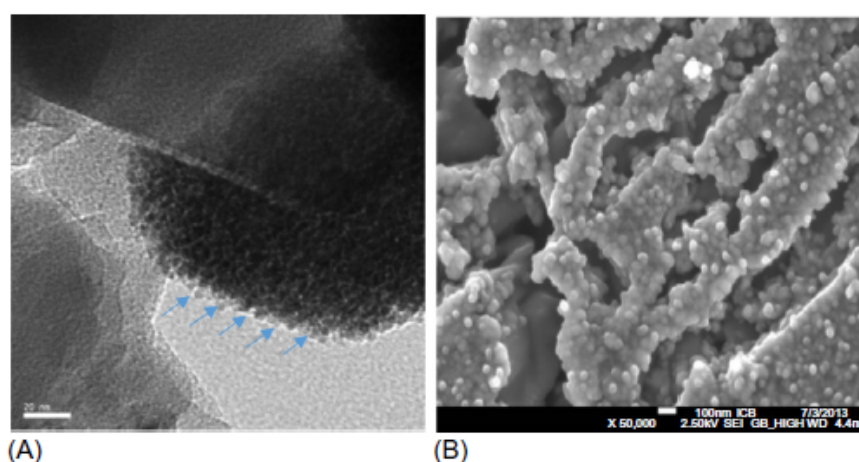


Fig. 21.4

Morphology of MIL-100(Fe) and MIL-53(Fe) after reflux in water 100°C: (A) TEM image of MIL-100(Fe) sample after reflux in water at 100°C for 48 h. (B) SEM image of MIL-53(Fe) after reflux in water at 100°C for 8 h. *Reproduced with permission from I. Bezverkhyy, et al., Degradation of fluoride-free MIL-100(Fe) and MIL-53(Fe) in water: effect of temperature and pH, Microporous Mesoporous Mater. 219 (2016) 117–124, copyright 2015, Microporous and Mesoporous Materials.*

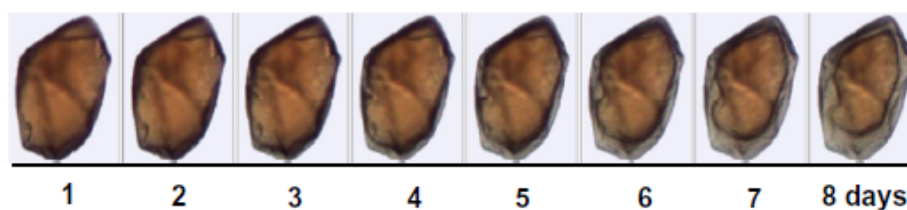


Fig. 21.5

Incubation in PBS of a micron-sized MIL-100(Fe) crystal. Taken by Raman microscopy of a micron-sized MIL-100(Fe) crystal during 8 days. Reproduced with permission from X. Li, et al., *New insights into the degradation mechanism of metal-organic frameworks drug carriers*, *Sci. Rep.* 7 (1) (2017) 13142, copyright 2017, *Scientific Reports*.

Even after 8 days of incubation in PBS, the global morphology and the size of the particles remained unaffected. However, an eroded amorphous shell around a practically intact crystalline core could be clearly visualized when following an individual MOF crystal over several days (Fig. 21.5).

On the contrary, neither drug loading nor coating did affect the integrity of the MOF crystals. These findings are in agreement with studies performed with nanoscale MIL-100(Fe) particles, for which neither loading with the anticancer drug Gemcitabine monophosphate nor the coating with phosphated cyclodextrins induced degradation [36, 47].

Of interest, Mossbauer spectroscopy and Energy Dispersive X-Ray Analysis revealed that, upon degradation in phosphate buffer saline, the final degradation product of MOFs presumably contained iron phosphate [46]. Indeed, phosphates from the degradation media could coordinate with iron sites, leading to the release of the trimesate constitutive ligands and thus to the amorphization of the material.

It can be expected that the composition of the degraded material is related to the nature of the complexing molecules in the degradation medium. This would need further investigations. Indeed, when a biodegradable polymer such as poly (lactic-*co*-glycolic) acid (PLGA) degrades, the final products are always lactic acid and glycolic acid. In the particular case of MOFs, the nature of the degraded products would depend strongly on the degradation medium and its ability to complex iron sites to release trimesate linkers. This highlights the importance of studying in depth the degradation of each type of MOF in different experimental conditions.

### 21.5 Surface engineering

Surface engineering is generally performed to improve nanoparticle colloidal stability and for targeting diseased organs and tissues. Appropriate surface modification of highly porous MOFs should

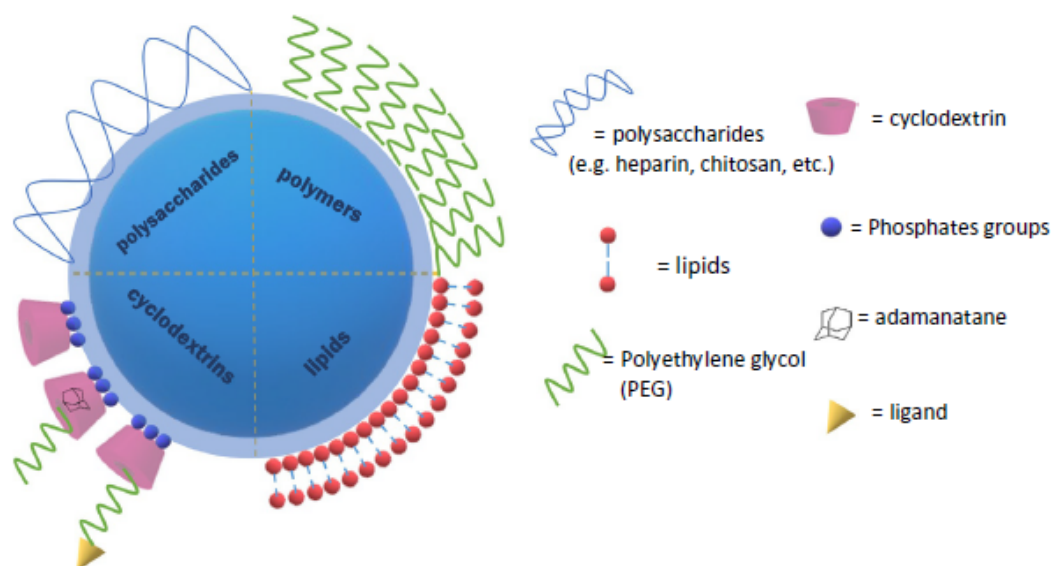


Fig. 21.6  
Surface modifications.

- Not degrade the carrier during the coating procedure
- Be anchored on the external surface of the particles and not affect the internal porosity of the particles
- Have a biodegradable character without side toxic effects
- Undergo an easy and “green” procedure

Several approaches, schematically represented in Fig. 21.5, were described to modify the surface of nanoscale MOFs (Fig. 21.6).

First attempts of MOF surface modification consisted in grafting silica shells in order to avoid rapid dissolution [34, 35]. Interestingly, the drug release was controlled by varying the silica thickness. The silica coating stabilized the particles against degradation ( $t_{1/2} = 1.2$ h for the uncoated ones and  $t_{1/2} = 16$  h for the silica-coated MOFs).

As mentioned, surface modification should not alter the internal porosity of the particles. Polyethylene glycol (PEG) is a hydrophilic polymer used in biochemistry for modifying a variety of biomolecules and it is one of the most common used polymers, approved by the US Food and Drug Administration (FDA). PEGylation is the process of grafting PEG on the surface of the nanocarriers, in order to improve their pharmacokinetics and to avoid their aggregation. Gupta et al. studied the influence of the coating with PEG chains on the drug release of drug-conjugated MIL-101(Fe) particles [48]. Firstly, the particles were functionalized with amino groups, followed by ibuprofen loading and surface coating by PEG chains. The surface-modified particles were incubated in PBS at different pHs and their degradation mechanism was explored. It was shown that the release of the drug cargo was strongly dependent on the pH.

## 482 Chapter 21

The acidic pH provoked a faster release of the drug as compared to neutral pH. It was also discovered that the release was slowed down after surface modifications, mainly because of the protection of the particles by the PEG corona, which prohibited the penetration of the phosphates from the release media into the core to erode it.

In another study, Zr-based MOFs were considered for surface modifications [49]. Because of a lower pKa of fumaric acid as compared to terephthalic acid, the fumarate analog was more stable than the terephthalate one during incubation in PBS 10 mM at pH=7.4. Moreover, after PEGylation, the stability of the Zr-fumarate particles was further increased, indicating that the coating plays an important role on the stability.

An innovative system was engineered for Positron Emission Tomography (PET) imaging coupled with tumor targeting [31]. UiO-66 (Zr) MOFs loaded with Doxorubicin and the isotope  $^{89}\text{Zr}$  were coated by a series of molecules in a “Lego” manner and they were studied both *in vitro* and *in vivo* as drug carriers and theragnostic agents. It was shown that the release of DOX in simulated physiological conditions was pH-dependent. The released drug amounts were higher in acidic conditions. Here again, surface modification significantly improved the stability of the MOF particles, by establishing strong  $\pi$ - $\pi$  interactions with the bridging organic ligands of the MOFs.

However, in the case of MIL-100 (Fe) nanoparticles, it was shown that PEG coating can easily penetrate inside the open MOF porosity, which makes the coating of these materials particularly challenging [47]. Indeed, PEG is able to fill the pores leading to a dramatic loss of the incorporated drugs. To address this issue, a strategy was to coat the outer surface of the MOFs with bulky materials, by keeping their porosity unaffected [47]. Thus, MIL-100(Fe) nanoparticles were covered by phosphated cyclodextrins, biocompatible molecules that efficiently coordinated to the CUS sites at the surface of the nanoMOFs, leading to stable coatings in biological media, despite their noncovalent nature.

Bulky enough, cyclodextrins were anchored only on the MOFs’ external surface. By a simple incubation with aqueous nanoMOF suspensions, an efficient coating was achieved by coordination of phosphates with iron sites at the surface, and it could be further functionalized with PEG chains and targeting moieties, such as mannose by a Lego-type methodology. To do so, PEG chains were grafted with adamantane which formed inclusion complexes with cyclodextrins, maintaining PEG at the surface and avoiding its penetration inside the MOF pores. Of note, the coating procedure did not degrade the MOFs nor induce drug leakage.

More recently, three different phosphated cyclodextrins (CD-P) were used to coat MIL-100(Fe) nanoparticles and their influence on the release of AZT-TP was studied [50]. Moreover, polymeric cyclodextrins were used and it was demonstrated that the drug release was better controlled in this case, as compared to monomeric cyclodextrins. Indeed, the thicker shell could afford better interactions with the drug, slowing down its release. This study is an evidence that

the nature of the coating material and the encapsulated active molecule can both affect the degradation of the MOF particles and the release patterns.

$\beta$ -CD was also used to coat an iron-based MOF (MOF-235), significantly increasing their stability, because of the external shell [51]. Another versatile method for MOF surface modifications was the noncovalent bonding of biomolecules such as chitosan and heparin [52, 53]. Both macromolecules were used for the coating of MIL-100(Fe) nanoparticles. Heparin is a polysaccharide large enough ( $8.2 \times 8.9 \text{ \AA}$ ) not to penetrate within the MIL-100(Fe) porosity. It also has various functional groups (i.e., sulfate, carboxylic, and hydroxyl) prone to interact with MOF surface. As for cyclodextrins [47, 50], MOF coating was performed in aqueous solutions by simple impregnation. The degradation of the nanoparticles was not influenced by the presence of the heparin coating.

In a similar manner, MIL-100(Fe) nanoparticles were coated with chitosan, a biocompatible polysaccharide. The stability of the coating was evaluated using chitosan grafted with a fluorescent dye. In parallel, the degradation profile of coated and uncoated nanoparticles was investigated by quantifying the release of the organic ligand trimesate at  $37^\circ\text{C}$  in different media. Interestingly, in the case of PBS the release of the ligand was around 30 wt% for the uncoated and less than 7 wt% for the coated particles, indicating that chitosan hinders the degradation of the nanoparticles and improved their chemical stability, probably because of the slower penetration inside the cores of the degrading phosphates from the suspension media due to the presence of the shell.

Lipid coating is also another convenient method for MOF coating and stabilization. Nanoscale coordination polymers (NCPs) based on  $\text{Zn}^{2+}$ ,  $\text{Zr}^{4+}$ , and  $\text{Gd}^{3+}$  ions and containing methotrexate (MTX) as bridging ligand were synthesized and they were further encapsulated in a functionalized lipid bilayer for the delivery of MTX into cancer cells.  $\text{Zn}^{2+}$  metal ions were first chosen because of their biocompatibility. However, the nanoparticles were not stable enough to be coated by the lipid layer. Therefore, the more stable tetravalent metal ion  $\text{Zr}^{4+}$  was chosen and the lipid coating was successfully achieved. However, the resulting nanoparticles were unstable in PBS and in simulated body fluid (SBF). Finally,  $\text{Gd}^{3+}$ -based MOFs were most stable during and after coating. In the same context, Wuttke et al. successfully synthesized MOFs lipid nanocarriers, using as a lipid layer DOPC (1,2-dioleoyl-sn-glycero-3-phosphocholine) for the hostage of dye molecules [53a]. According to the *in vitro* studies performed by these authors, it was proved that the coating of the particles by lipid layer prevented the fast release of their cargo.

More recently, a GraftFast polymerization procedure was developed to coat MIL-100 nanoparticles with a PEG or a polysaccharide shell [54]. Specifically, MIL-100(Fe) and MIL-100(Al) were coated with different polymers (480 Da, 2 and 5 kDa acryl-PEGs and acryl-hyaluronic acid grafted with PEG). Acrylate polymerization occurred at the outer MOF surface preserving its porosity and without degradation. Of note, degradation of the coated particles was reduced as

---

**484 Chapter 21**

---

compared to uncoated ones. More precisely, 50 wt% of the trimesate was released in PBS after 24 h incubation for the uncoated particles and 43 and 38 wt% for the particles coated with PEG<sub>2kDa</sub> and PEG<sub>5kDa</sub>, respectively. This result shows not only that the chemical stability of the nanoparticles was improved by coating, but also that it depends on the molecular weight of the coating polymer.

From the above studies, it can be concluded that after coating, MOF degradation can either be unaffected or be significantly reduced. Indeed, some coating procedures and materials can protect MOFs against degradation. It would be of high interest to establish a relationship between the nature of the coating and the degradation patterns. This would pave the way toward the design of engineered coatings that will not alter the MOF physico-chemical properties, but improve their colloidal stability and control the degradation in biological media.

### **21.6 Toxicity and in vivo fate**

One of the major concerns with in vivo administration of the nanocarriers is their potential toxicity after degradation/metabolism inside the body. The degradation mechanism of the MOF particles is difficult to be mimicked in vitro, as body fluids contain thousands of different ions, proteins, and cells. Moreover, depending on their administration route, the MOFs get in contact with different media.

There is still a lot of research to be performed to unravel the in vivo degradation mechanism of MOFs as only scarce studies mention the biodegradability of these relatively novel drug carriers inside the body. Some of these studies were mainly focused on biodistribution of nanoMOFs after intravenous administration and their lack of toxicity [55].

In one of the first attempts to investigate the in vivo fate of MOF nanoparticles in a living organism, Baati et al. performed in vivo toxicity tests in Wistar rats using three different Fe-based nanocarriers: MIL-88A, MIL-88B-CH<sub>3</sub>, and MIL-100 [25]. All of the particles were neither loaded nor coated, and one month after intravenous administration of 220 mg/kg of MOFs, no evident sign of toxicity was detected. In another study, nanoscale MOFs were loaded with the antineoplastic drug busulfan, leading to dramatic pharmacokinetic changes as compared with unloaded nanoparticles [56]. The degradation profile of the particles appeared to be affected by drug loading and the loaded particles were eliminated faster from the organism than the unloaded ones [56]. In a more recent study, MIL-89 nanosized MOFs were evaluated in vivo for their ability to treat pulmonary arterial hypertension (PAH) [57]. Uncoated and PEGylated particles were investigated and none of them induced toxicity after intravenous administration. Interestingly, it was shown that the coated particles were more stable than the uncoated ones.

More recently, MIL-100 particles loaded with the anticancer drug Gemcitabine-monophosphate were intravenously administered to treat lung cancer in a mice model [58]. Interestingly, the nanoparticles immediately aggregated after injection and contact with blood, and the

---

aggregates were sequestered into the lungs. This strategy enabled delivering locally their active anticancer drug cargo to kill cancer cells. Interestingly, aggregates rapidly disassembled and the animals tolerated the treatment. It was shown that this aggregation/disaggregation mechanism was related to the nanoparticles' surface charge and to the pH of the suspension media. Moreover, it was hypothesized that the fast degradation of the particles in the presence of phosphates from blood could trigger the disassembly of the aggregates.

In a complementary study, the behavior *in vitro* and *in vivo* of a large series of MOFs was studied by using as model Zebrafish embryos [59]. A strong correlation between *in vitro* and *in vivo* studies was found. Interestingly, a lower toxicity was observed for the particles that were degraded slower. After cell internalization or *in vivo* administration, each nanoMOF was degraded showing different degradation products and patterns.

In different fields than drug delivery, a copper-based MOF used as a catalyst was synthesized, in order to perform localized drug synthesis in mitochondria [60]. The catalytic activity and stability of this complex were indicated by using the localized synthesized resveratrol-derived drug, and most importantly, the *in vivo* tests performed in *C. elegans* and mice models proved the biocompatibility of the catalyst.

In another study, MOFs were used as radio-sensitizers to improve the performance of radiotherapy [61]. MOF nanoparticles synthesized from the heavy metal hafnium ( $\text{Hf}^{4+}$ ) and a porphyrin ligand were coated by PEG chains and studied *in vitro* and *in vivo* as potential candidates for radiotherapy treatments. After 30 days of exposure in mice models, their biocompatibility was proved, mainly because of the successful excretion of the nanoparticles from the organism. Even further, a new treatment strategy combining local Photodynamic Therapy Treatment and Immunotherapy by using MOF nanoparticles was introduced [62]. A chlorin-based nanoMOF loaded with the immunotherapy agent that inhibits indoleamine 2,3-dioxygenase (IDO) was studied *in vivo* showing that both primary-treated and distant-untreated tumors were shrunked, because of the synergistic effect of the therapy.

After taking into consideration the previously reported pharmacokinetics and biodistribution data, it can be concluded that the presence and the nature of a drug molecule inside the MOF framework affect their degradation behavior. Each MOF shows a different degradation mechanism, which is strongly related to the composition of the release media. This is one of the main reasons that each drug-loaded MOF material designed for biomedical applications should be examined individually in terms of stability and consequently of biodegradability

### ***21.7 Conclusions and future outlook***

In reason of their versatility in terms of sizes, composition and surface modification, biodegradability, and biocompatibility, MOFs engineered for biomedical applications demonstrated their usefulness for drug delivery applications. They were able to load



## 486 Chapter 21

unprecedented amounts of drugs with various physico-chemical properties. However, the stability of nanoscale MOFs in vitro (biological media) and in vivo (after intravenous administration) remains still challenging to be controlled.

Furthermore, the intriguing effects of drug clustering in cages on the stability of MOFs are another interesting observation to be exploited. Shells were shown to stabilize MOFs against degradation and aggregation and this research field is expected to be in constant growth.

While polymeric nanoparticles typically degrade forming oligomers and further monomers of well-known chemical structures, MOF end-degradation products are dependent on the degradation media. This peculiar behavior incites to perform exhaustive studies to unravel the MOF degradation behavior as well as to identify the nature of the degraded material in relation with its elimination from the body. One strategy reviewed here was the investigation of the degradation of individual large MOF particles, with focus on the chemical composition of different regions on a same particle as a function of degradation time. Such studies could be carried on with a series of particles with different compositions and sizes.

With a deep knowledge on the degradation mechanism of MOFs, their peculiar aggregation/disaggregation behavior in complex media could be further exploited to engineer novel MOFs for biomedical applications.

## References

- [1] G. Gregoriadis, Liposomes in drug delivery: how it all happened, *Pharmaceutics* 8 (2) (2016) 19.
- [2] A.P. Clark, et al., Liposomes as drug delivery systems, *Cancer Pract.* 6 (4) (1998) 251–253.
- [3] E. Kahraman, et al., Potential enhancement and targeting strategies of polymeric and lipid-based nanocarriers in dermal drug delivery, *Ther. Deliv.* 8 (11) (2017) 967–985.
- [4] B.L. Banik, P. Fattahi, J.L. Brown, Polymeric nanoparticles: the future of nanomedicine, *Wiley Interdiscip. Rev. Nanomed. Nanobiotechnol.* 8 (2) (2016) 271–299.
- [5] M. Eddaoudi, et al., Modular chemistry: secondary building units as a basis for building units as a basis for robust metal-organic carboxylate frameworks, *Acc. Chem. Res.* 34 (4) (2001) 319–330.
- [6] G. Férey, Hybrid porous solids: past, present, future, *Chem. Soc. Rev.* 37 (1) (2008) 191–214.
- [7] S. Kitagawa, et al., Functional porous coordination polymers, *Angew. Chem. Int. Ed.* 43 (18) (2004) 2334–2375.
- [8] A.G. Wong-foy, et al., Exceptional H<sub>2</sub> saturation uptake in microporous metal-organic frameworks, *JACS Commun.* 128 (11) (2006) 3494–3495.
- [9] T. Grant Glover, et al., MOF-74 building unit has a direct impact on toxic gas adsorption, *Chem. Eng. Sci.* 66 (2) (2011) 163–170.
- [10] E. Soubeyrand-Lenoir, et al., How water fosters a remarkable 5-fold increase in low-pressure CO<sub>2</sub> uptake within mesoporous MIL-100(Fe), *J. Am. Chem. Soc.* 134 (24) (2012) 10174–10181.
- [11] P. Horcajada, et al., Metal-organic frameworks as efficient materials for drug delivery, *Angew. Chem. Int. Ed.* 45 (36) (2006) 5974–5978.
- [12] P. Horcajada, et al., Porous metal-organic-framework nanoscale carriers as a potential platform for drug delivery and imaging, *Nat. Mater.* 9 (2) (2010) 172–178.
- [13] S. Raschke, et al., Balancing mechanical stability and ultrahigh porosity in crystalline framework materials, *Angew. Chem. Int. Ed.* 57 (42) (2018) 13780–13783.

- [14] M. Giménez-Marqués, et al., Nanostructured metal-organic frameworks and their bio-related applications, *Coord. Chem. Rev.* 307 (2016) 342–360.
- [15] F.R.S. Lucena, et al., Induction of cancer cell death by apoptosis and slow release of 5-fluoracil from metal-organic frameworks Cu-BTC, *Biomed. Pharmacother.* 67 (8) (2013) 707–713.
- [16] C.Y. Sun, et al., Zeolitic imidazolate framework-8 as efficient pH-sensitive drug delivery vehicle, *Dalton Trans.* 41 (23) (2012) 6906–6909.
- [17] P. Horcajada, et al., Metal-organic frameworks in biomedicine, *Chem. Rev.* 112 (2012) 1232–1268.
- [18] Y. Lee, et al., Synthesis of metal-organic frameworks: a mini review, *Korean J. Chem. Eng.* 30 (9) (2013) 1667–1680.
- [19] N. Stock, et al., Synthesis of metal-organic frameworks (MOFs): routes to various MOF topologies, morphologies, and composites, *Chem. Rev.* 112 (2) (2012) 933–969.
- [20] J. Klinowski, et al., Microwave-assisted synthesis of metal-organic frameworks, *Dalton Trans.* 40 (2) (2011) 321–330.
- [21] P. Silva, et al., Multifunctional metal-organic frameworks: From academia to industrial applications, *Chem. Soc. Rev.* 44 (19) (2015) 6774–6803.
- [22] C. Tamames-Tabar, et al., A Zn azelate MOF: combining antibacterial effect, *CrystEngComm* 17 (2) (2014) 456–462.
- [23] E. Bellido, et al., Understanding the colloidal stability of the mesoporous MIL-100(Fe) nanoparticles in physiological media, *Langmuir* 30 (20) (2014) 5911–5920.
- [24] P. Horcajada, et al., Synthesis and catalytic properties of MIL-100(Fe), an iron(III) carboxylate with large pores, *Chem. Commun.* 100 (27) (2007) 2820–2822.
- [25] T. Baati, et al., In depth analysis of the in vivo toxicity of nanoparticles of porous iron(III) metal-organic frameworks, *Chem. Sci.* 4 (4) (2013) 1597–1607.
- [26] J. Zhuang, A.P. Young, C.K. Tsung, Integration of biomolecules with metal-organic frameworks, *Small* 13 (32) (2017) 1–14.
- [27] G. Zhou, et al., Porphyrin-palladium hydride MOF nanoparticles for tumor-targeting photoacoustic imaging-guided hydrogenothermal cancer therapy, *Nanoscale Horiz.* 4 (2019) 1185–1193.
- [28] P. Horcajada, et al., Flexible porous metal-organic frameworks for a controlled drug delivery, *J. Am. Chem. Soc.* 130 (21) (2008) 6774–6780.
- [29] C. He, et al., Nanomedicine applications of hybrid nanomaterials built from metal-ligand coordination bonds: nanoscale metal-organic frameworks and nanoscale coordination polymers, *Chem. Rev.* 115 (19) (2015) 11079–11108.
- [30] A.C. McKinlay, et al., Multirate delivery of multiple therapeutic agents from metal-organic frameworks, *APL Mater.* 2 (12) (2014) 124108-1–124108-8.
- [31] D. Chen, et al., In vivo targeting and positron emission tomography imaging of tumor with intrinsically radioactive metal-organic frameworks nanomaterials, *ACS Nano* 11 (4) (2017) 4315–4327.
- [32] Q. Chen, et al., Controlled release of drug molecules in metal-organic framework material HKUST-1, *Inorg. Chem. Commun.* 79 (2017) 78–81.
- [33] W.J. Rieter, et al., Nanoscale coordination polymers for platinum-based anticancer drug delivery, *J. Am. Chem. Soc.* 130 (35) (2008) 11584–11585.
- [34] K.M.L. Taylor, et al., Surfactant-assisted synthesis of nanoscale gadolinium metal-organic frameworks for potential multimodal imaging, *Angew. Chem. Int. Ed.* 47 (40) (2008) 7722–7725.
- [35] K.M.L. Taylor, et al., Manganese-based nanoscale metal-organic frameworks for magnetic resonance imaging, *J. Am. Chem. Soc.* 130 (44) (2008) 14358–14359.
- [36] V. Rodríguez-Ruiz, et al., Efficient “green” encapsulation of a highly hydrophilic anticancer drug in metal-organic framework nanoparticles, *J. Drug Target.* 23 (7–8) (2015) 759–767.
- [37] V. Agostoni, et al., Impact of phosphorylation on the encapsulation of nucleoside analogues within porous iron(III) metal-organic framework MIL-100(Fe) nanoparticles, *J. Mater. Chem. B* 1 (34) (2013) 4231–4242.
- [38] S. Rojas, et al., Nanoscaled zinc pyrazolate metal-organic frameworks as drug-delivery systems, *Inorg. Chem.* 55 (5) (2016) 2650–2663.

## 488 Chapter 21

- [39] V. Agostoni, et al., Towards an improved anti-HIV activity of NRTI via metal-organic frameworks nanoparticles, *Adv. Healthc. Mater.* 2 (12) (2013) 1630–1637.
- [40] X. Unamuno, et al., Biocompatible porous metal-organic framework nanoparticles based on Fe or Zr for gentamicin vectorization, *Eur. J. Pharm. Biopharm.* 132 (2018) 11–18.
- [41] M.R. Di Nunzio, et al., A “ship in a bottle” strategy to load a hydrophilic anticancer drug in porous metal organic framework nanoparticles: efficient encapsulation, matrix stabilization, and photodelivery, *J. Med. Chem.* 57 (2) (2014) 411–420.
- [42] X. Li, et al., Compartmentalized encapsulation of two antibiotics in porous nanoparticles: an efficient strategy to treat intracellular infections, *Part. Part. Syst. Charact.* 36 (3) (2019) 1800360.
- [42a] J. An, S.J. Geib, N.L. Rosi, Cation-triggered drug release from a porous zinc-adeninate metal-organic framework, *J. Am. Chem. Soc.* 131 (2009) 8376–8377, <https://doi.org/10.1021/ja902972w>.
- [42b] W. Lin, et al., A porphyrin-based metal-organic framework as a pH-responsive drug carrier, *J. Solid State Chem.* 237 (2016) 307–312, <https://doi.org/10.1016/j.jssc.2016.02.040>.
- [43] J.B. Decoste, et al., Stability and degradation mechanisms of metal-organic frameworks containing the  $Zr_6O_4(OH)_4$  secondary building unit, *J. Mater. Chem. A* 1 (18) (2013) 5642–5650.
- [44] L. Cooper, et al., A biocompatible porous Mg-gallate metal-organic framework as an antioxidant carrier, *Chem. Commun.* 51 (27) (2015) 5848–5851.
- [45] I. Bezverkhyy, et al., Degradation of fluoride-free MIL-100(Fe) and MIL-53(Fe) in water: effect of temperature and pH, *Microporous Mesoporous Mater.* 219 (2016) 117–124.
- [46] X. Li, et al., New insights into the degradation mechanism of metal-organic frameworks drug carriers, *Sci. Rep.* 7 (1) (2017) 13142.
- [47] V. Agostoni, et al., A “green” strategy to construct non-covalent, stable and bioactive coatings on porous MOF nanoparticles, *Sci. Rep.* 5 (2015) 1–7.
- [48] V. Gupta, et al., Development of biocompatible iron-carboxylate metal organic frameworks for pH-responsive drug delivery application, *J. Nanosci. Nanotechnol.* 19 (2) (2018) 646–654.
- [49] I. Abánades Lázaro, et al., Surface-functionalization of Zr-fumarate MOF for selective cytotoxicity and immune system compatibility in nanoscale drug delivery, *ACS Appl. Mater. Interfaces* 10 (37) (2018) 31146–31157.
- [50] A. Aykaç, et al., A non-covalent “click chemistry” strategy to efficiently coat highly porous MOF nanoparticles with a stable polymeric shell, *Biochim. Biophys. Acta Gen. Subj.* 1861 (4) (2017) 1606–1616.
- [51] X. Mao, et al.,  $\beta$ -Cyclodextrin functionalization of metal-organic framework MOF-235 with excellent chemiluminescence activity for sensitive glucose biosensing, *Talanta* 188 (April) (2018) 161–167.
- [52] E. Bellido, et al., Heparin-engineered mesoporous iron metal-organic framework nanoparticles: toward stealth drug nanocarriers, *Adv. Healthc. Mater.* 4 (8) (2015) 1246–1257.
- [53] T. Hidalgo, et al., Chitosan-coated mesoporous MIL-100(Fe) nanoparticles as improved bio-compatible oral nanocarriers, *Sci. Rep.* 7 (January) (2017) 1–14.
- [53a] A. Zimpel, T. Preiß, R. Röder, H. Engelke, M. Ingrisch, M. Peller, J.O. Rädler, E. Wagner, T. Bein, U. Lächelt, S. Wuttke, Imparting functionality to MOF nanoparticles by external surface selective covalent attachment of polymers, *Chem. Mater.* 28 (10) (2016) 3318–3326, <https://doi.org/10.1021/acs.chemmater.6b00180>.
- [54] M. Giménez-Marqués, et al., GraftFast surface engineering to improve MOF nanoparticles furtiveness, *Small* 14 (40) (2018) 1–11.
- [55] T. Simon-Yarza, et al., Nanoparticles of metal-organic frameworks: on the road to in vivo efficacy in biomedicine, *Adv. Mater.* 30 (37) (2018) 1–15.
- [56] M.T. Simon-Yarza, et al., Antineoplastic busulfan encapsulated in a metal organic framework nanocarrier: first in vivo results, *J. Mater. Chem. B* 4 (4) (2016) 585–588.
- [57] N.A. Mohamed, et al., Chemical and biological assessment of metal organic frameworks (MOFs) in pulmonary cells and in an acute in vivo model: relevance to pulmonary arterial hypertension therapy, *Pulm. Circ.* 7 (3) (2017) 643–653.

- [58] T. Simon-Yarza, et al., A smart metal–organic framework nanomaterial for lung targeting, *Angew. Chem. Int. Ed.* 56 (49) (2017) 15565–15569.
- [59] A. Ruyra, et al., Synthesis, culture medium stability, and in vitro and in vivo zebrafish embryo toxicity of metal-organic framework nanoparticles, *Chem. Eur. J.* 21 (6) (2015) 2508–2518.
- [60] F. Wang, et al., A biocompatible heterogeneous MOF–Cu catalyst for in vivo drug synthesis in targeted subcellular organelles, *Angew. Chem. Int. Ed.* 58 (21) (2019) 6987–6992.
- [61] J. Liu, et al., Nanoscale metal-organic frameworks for combined photodynamic & radiation therapy in cancer treatment, *Biomaterials* 97 (2016) 1–9.
- [62] K. Lu, et al., Chlorin-based nanoscale metal-organic framework systemically rejects colorectal cancers via synergistic photodynamic therapy and checkpoint blockade immunotherapy, *J. Am. Chem. Soc.* 138 (38) (2016) 12502–12510.
- [63] K.S. Park, et al., ZIFs - first synthesis, *Proc. Natl. Acad. Sci. USA* 103 (27) (2006) 10186–10191.
- [64] K.P. Lillerud, et al., A new zirconium inorganic building brick forming metal organic frameworks with exceptional stability, *J. Am. Chem. Soc.* 130 (42) (2008) 13850–13851.
- [65] P.D.C. Dietzel, et al., An in situ high-temperature single-crystal investigation of a dehydrated metal-organic framework compound and field-induced magnetization of one-dimensional metal-oxygen chains, *Angew. Chem. Int. Ed.* 44 (39) (2005) 6354–6358.
- [66] S.S.-Y. Chui, et al., A chemically functionalizable nanoporous material  $[\text{Cu}_3(\text{TMA})_2(\text{H}_2\text{O})_3]_n$ , *Science* 283 (1999) 1148–1150.
- [67] E. Quartapelle Procopio, et al., Study of the incorporation and release of the non-conventional half-sandwich ruthenium(ii) metalodrugs RAPTAC on a robust MOF, *Chem. Commun.* 47 (42) (2011) 11751–11753.
- [68] H. Zhang, et al., Rational design of metal organic framework nanocarrier-based codelivery system of doxorubicin hydrochloride/verapamil hydrochloride for overcoming multidrug resistance with efficient targeted cancer therapy, *ACS Appl. Mater. Interfaces* 9 (23) (2017) 19687–19697.
- [68a] K.A. Mocniak, I. Kubajewska, D.E.M. Spillane, G.R. Williams, R.E. Morris, Incorporation of cisplatin into the metal-organic frameworks UiO66-NH<sub>2</sub> and UiO66-encapsulation vs. conjugation, *RSC Adv.* 5 (102) (2015) 83648–83656.
- [68b] S. Rojas, I. Colinet, D. Cunha, T. Hidalgo, F. Salles, C. Serre, N. Guillou, P. Horcajada, Toward understanding drug incorporation and delivery from biocompatible metal-organic frameworks in view of cutaneous administration, *ACS Omega* 3 (3) (2018) 2994–3003, <https://doi.org/10.1021/acsomega.8b00185>.

### **Further reading**

- S. Braig, et al., MOF nanoparticles coated by lipid bilayers and their uptake by cancer cells, *Chem. Commun.* 51 (87) (2015) 15752–15755.
- H. Zheng, et al., One-pot synthesis of metal-organic frameworks with encapsulated target molecules and their applications for controlled drug delivery, *J. Am. Chem. Soc.* 138 (3) (2016) 962–968.

## F. Conclusions

The first chapter of the manuscript included the theoretical background of our study concerning hybrid porous materials (MOFs) as carriers of AIs in bioapplications.

In a first stage, we defined the term of nanotechnology and we presented its main advantages for both the AI and the living organism in pharmacokinetics. The AI is protected and distributed inside the body by a controlled manner via biodegradable carriers, named drug delivery systems (DDS). We mentioned some of these systems (liposomes, micelles, polymeric NPs, dendrimers, mesoporous silica), highlighting their benefits and their limitations. Poor drug payloads and stability issues are the main disadvantages to design a performable system.

We, therefore, introduced a relevant recent class of drug carriers, the Metal Organic Frameworks (MOFs). MOFs are hybrid porous particles with unprecedented high surface areas, pore volumes, together with an amphiphilic microenvironment, which can host a variety of AIs in large quantities. Yet, the abundant combination of building blocks for the formation of MOFs combined to their relative new entrance in biomedical field leads to a great need for better understanding of their biodegradability. One of the most promising candidate is the mesoporous iron(III) trimesate MOF denoted MIL-100(Fe), which is the material of interest in our study. In the first chapter, we explored the intrinsic and the extrinsic parameters affecting MIL-100(Fe) degradation and we cited some of the most important *in vitro* and *in vivo* studies that have been published.

To explore particles' degradation a sum of characterization techniques is demanded. In the fourth subchapter, we outlined some of them by emphasizing in two innovative techniques, the Atomic Force Microscopy and the ellipsometry. As we have already mentioned, both techniques were used for the *in situ* study of the degradation mechanism of micron- and nanosized particles respectively. These methods are direct and give us valuable information about the changes of the particles in real time, which is of a great importance in bioapplications.

Overall, MIL-100(Fe) seems a very promising MOF for drug delivery applications. Still, its stability under physiological media needs to be further explored and this challenging study will be presented in the next part of the manuscript.

## G. References

1. Goldberg, M. S. Improving cancer immunotherapy through nanotechnology. *Nat. Rev. Cancer* **19**, 587–602 (2019).
2. Kyeremateng, N. *et al.* Microsupercapacitors as miniaturized energy-storage components for on-chip electronics. *Nat. Nanotechnol.* **12**, 7–15 (2017).
3. Nasrollahzadeh, M. *et al.* *Applications of Nanotechnology in Daily Life. Interface Science and Technology* **28**, 113-143 (2019).
4. Alvarez, P. J. J. *et al.* Emerging opportunities for nanotechnology to enhance water security. *Nat. Nanotechnol.* **13**, 634–641 (2018).
5. Duhan, J. S. *et al.* Nanotechnology: The new perspective in precision agriculture. *Biotechnol. Reports* **15**, 11–23 (2017).
6. Tang, Z. *et al.* Insights from nanotechnology in COVID-19 treatment. *Nano Today* **36**, 101019 (2021).
7. ISO/TR 18401:2017(en), Nanotechnologies — Plain language explanation of selected terms from the ISO/IEC 80004 series. <https://www.iso.org/obp/ui/#iso:std:iso:tr:18401:ed-1:v1:en>.
8. Su, C. *et al.* Absorption, distribution, metabolism and excretion of the biomaterials used in Nanocarrier drug delivery systems. *Adv. Drug Deliv. Rev.* **143**, 97–114 (2019).
9. Damge, C. *et al.* New approach for oral administration of insulin with polyalkylcyanoacrylate nanocapsules as drug carrier. *Diabetes* **37**, 246–251 (1988).
10. Ensign, L. M. *et al.* Oral drug delivery with polymeric nanoparticles: The gastrointestinal mucus barriers. *Adv. Drug Deliv. Rev.* **64**, 557–570 (2012).
11. Griffin, B. T. *et al.* Pharmacokinetic, pharmacodynamic and biodistribution following oral administration of nanocarriers containing peptide and protein drugs. *Adv. Drug Deliv. Rev.* **106**, 367–380 (2016).
12. Homayun, B. *et al.* Challenges and recent progress in oral drug delivery systems for biopharmaceuticals. *Pharmaceutics* **11**, 129 (2019).
13. Pillai, G. *Nanotechnology Toward Treating Cancer. Applications of Targeted Nano Drugs and Delivery Systems* 221- 256 (Elsevier Inc., 2019).
14. Goldman, E. *et al.* Nanoparticles target early-stage breast cancer metastasis *in vivo*. *Nanotechnol.* **28**, 43LT01 (2017).
15. Praphawatvet, T. *et al.* Inhaled nanoparticles—An updated review. *Int. J. Pharm.* **587**, 119671 (2020).
16. D’Angelo, I. *et al.* Improving the efficacy of inhaled drugs in cystic fibrosis: Challenges and emerging drug delivery strategies. *Adv. Drug Deliv. Rev.* **75**, 92–111 (2014).
17. Wadhwa, R. *et al.* *Nanoparticle-based drug delivery for chronic obstructive pulmonary disorder and asthma. Nanotechnology in Modern Animal Biotechnology: Concepts and Applications* 59-73 (Elsevier Inc., 2019).
18. Prausnitz, M. R. *et al.* Current status and future potential of transdermal drug delivery. *Nat. Rev. Drug Discov.* **3**, 115–124 (2004).
19. Lee, H. *et al.* Device-assisted transdermal drug delivery. *Adv. Drug Deliv. Rev.* **127**, 35–45 (2018).
20. Waghule, T. *et al.* Microneedles: A smart approach and increasing potential for transdermal drug delivery system. *Biomed. Pharmacother.* **109**, 1249–1258 (2019).
21. Banerjee, A. *et al.* Treatment of insulin resistance in obesity-associated type 2 diabetes mellitus through adiponectin gene therapy. *Int. J. Pharm.* **583**, 119357 (2020).
22. De Jong, W. H. *et al.* Particle size-dependent organ distribution of gold nanoparticles after intravenous administration. *Biomaterials* **29**, 1912–1919 (2008).

23. Hillyer, J. F. *et al.* Gastrointestinal persorption and tissue distribution of differently sized colloidal gold nanoparticles. *J. Pharm. Sci.* **90**, 1927–1936 (2001).
24. Duan, X. *et al.* Physicochemical characteristics of nanoparticles affect circulation, biodistribution, cellular internalization, and trafficking. *Small* **9**, 1521–1532 (2013).
25. Van Rijt, S. H. *et al.* Medical nanoparticles for next generation drug delivery to the lungs. *Eur. Respir. J.* **44**, 765–774 (2014).
26. Hyeon, T. *et al.* Nanomedicine themed issue and therapy. *Chem. Soc. Rev.* **41**, 2885–2911 (2012).
27. Lee, J. S. *et al.* Recent advances in quantum dots for biomedical applications. *J. Pharm. Investig.* **48**, 209–214 (2018).
28. He, Q. *et al.* A pH-responsive mesoporous silica nanoparticles-based multi-drug delivery system for overcoming multi-drug resistance. *Biomaterials* **32**, 7711–7720 (2011).
29. Bangham, A. D. *et al.* The surface properties of some neoplastic cells. *Biochem. J.* **84**, 513–517 (1962).
30. Daemen, T. *et al.* Liposomal doxorubicin induced toxicity: Depletion and impairment of phagocytic activity of liver macrophages. *Int. J. Cancer* **61**, 716–721 (1995).
31. Anselmo, A. C. *et al.* Nanoparticles in the clinic: An update. *Bioeng. Transl. Med.* **4**, 1–16 (2019).
32. Blair, H. A. Daunorubicin/Cytarabine Liposome: A Review in Acute Myeloid Leukaemia. *Drugs* **78**, 1903–1910 (2018).
33. Sercombe, L. *et al.* Advances and challenges of liposome assisted drug delivery. *Front. Pharmacol.* **6**, 1–13 (2015).
34. Khanna, S.C. *et al.* Bead Polymerization Technique for Sustained-Release Dosage Form. *J. Pharm. Sci.* **5**, 614–618 (1970).
35. Birrenbach, G. *et al.* Polymerized micelles and their use as adjuvants in immunology. *J. Pharm. Sci.* **65**, 1763–1766 (1976).
36. Langer, R. *et al.* Polymers for the sustained release of proteins and other macromolecules. *Nature* **263**, 797–800 (1976).
37. Couvreur, P. *et al.* Adsorption of antineoplastic drugs to polyalkylcyanoacrylate nanoparticles and their release in calf serum. *J. Pharm. Sci.* **68**, 1521–1524 (1979).
38. Gref, R. *et al.* Biodegradable long-circulating polymeric nanospheres. *Science*. **263**, 1600–1603 (1994).
39. Gref, R. *et al.* The controlled intravenous delivery of drugs using PEG-coated sterically stabilized nanospheres. *Adv. Drug Deliv. Rev.* **16**, 215–233 (1995).
40. Kamaly, N. *et al.* Degradable controlled-release polymers and polymeric nanoparticles: Mechanisms of controlling drug release. *Chem. Rev.* **116**, 2602–2663 (2016).
41. Li, J. *et al.* Designing hydrogels for controlled drug delivery. *Nat. Rev. Mater.* **1**, 1–18 (2016).
42. Dosio, F. *et al.* Hyaluronic acid for anticancer drug and nucleic acid delivery. *Adv. Drug Deliv. Rev.* **97**, 204–236 (2016).
43. Trombino, S. *et al.* Strategies for hyaluronic acid-based hydrogel design in drug delivery. *Pharmaceutics* **11**, 1–17 (2019).
44. Chen, M. C. *et al.* Recent advances in chitosan-based nanoparticles for oral delivery of macromolecules. *Adv. Drug Deliv. Rev.* **65**, 865–879 (2013).
45. Lang, X. *et al.* Advances and applications of chitosan-based nanomaterials as oral delivery carriers: A review. *Int. J. Biol. Macromol.* **154**, 433–445 (2020).
46. Green, M. R. *et al.* Abraxane®, a novel Cremophor®-free, albumin-bound particle form of paclitaxel for the treatment of advanced non-small-cell lung cancer. *Ann. Oncol.* **17**, 1263–1268 (2006).
47. Von Hoff, D. D. *et al.* Increased Survival in Pancreatic Cancer with nab-Paclitaxel plus Gemcitabine. *N. Engl. J. Med.* **369**, 1691–1703 (2013).

## Chapter I

### Introduction

48. Paz-Ares, L. *et al.* Pembrolizumab plus Chemotherapy for Squamous Non–Small-Cell Lung Cancer. *N. Engl. J. Med.* **379**, 2040–2051 (2018).
49. Schmid, P. *et al.* Atezolizumab and Nab-Paclitaxel in Advanced Triple-Negative Breast Cancer. *N. Engl. J. Med.* **379**, 2108–2121 (2018).
50. Adams, D. *et al.* Patisiran, an RNAi Therapeutic, for Hereditary Transthyretin Amyloidosis. *N. Engl. J. Med.* **379**, 11–21 (2018).
51. Kumari, A. *et al.* Biodegradable polymeric nanoparticles based drug delivery systems. *Colloids Surfaces B Biointerfaces* **75**, 1–18 (2010).
52. Couvreur, P. Nanoparticles in drug delivery: Past, present and future. *Adv. Drug Deliv. Rev.* **65**, 21–23 (2013).
53. Liu, Z. *et al.* Polysaccharides-based nanoparticles as drug delivery systems. *Adv. Drug Deliv. Rev.* **60**, 1650–1662 (2008).
54. Cabral, H. *et al.* Block Copolymer Micelles in Nanomedicine Applications. *Chem. Rev.* **118**, 6844–6892 (2018).
55. Kapse, A. *et al.* Polymeric micelles: A ray of hope among new drug delivery systems, In: *Drug Delivery Systems*, 235-289 (2020).
56. Wakaskar, R. R. Polymeric Micelles and their Properties. *J. Nanomed. Nanotechnol.* **8**, 433 (2017).
57. Yokoyama, M. Polymeric micelles as drug carriers: Their lights and shadows. *J. Drug Target.* **22**, 576–583 (2014).
58. Gothwal, A. *et al.* Polymeric Micelles: Recent Advancements in the Delivery of Anticancer Drugs. *Pharm. Res.* **33**, 18–39 (2016).
59. Newkome, G. R. *et al.* Cascade Molecules: A New Approach to Micelles. *J. Org. Chem.* **50**, 2003–2004 (1985).
60. Jansen, J. F. G. A. *et al.* Encapsulation of guest molecules into a dendritic box. *Science.* **266**, 1226–1229 (1994).
61. Pedziwiatr-Werbicka, E. *et al.* Dendrimers and hyperbranched structures for biomedical applications. *Eur. Polym. J.* **119**, 61–73 (2019).
62. Chauhan, A. *et al.* *Therapeutic dendrimers. Pharmaceutical Applications of Dendrimers* (Elsevier Inc., 2020).
63. Duncan, R. *et al.* Dendrimer biocompatibility and toxicity. *Adv. Drug Deliv. Rev.* **57**, 2215–2237 (2005).
64. Santos, A. *et al.* Dendrimers as pharmaceutical excipients: Synthesis, properties, toxicity and biomedical applications. *Materials.* **13**, 65 (2020).
65. Bhadra, D. *et al.* PEGylated dendritic nanoparticulate carrier of fluorouracil. *Int. J. Pharm.* **257**, 111–124 (2003).
66. Bhadra, D. *et al.* Glycodendrimeric nanoparticulate carriers of primaquine phosphate for liver targeting. *Int. J. Pharm.* **295**, 221–233 (2005).
67. Kresge, C. T. *et al.* Ordered mesoporous molecular sieves synthesized by a liquid-crystal template mechanism. *Nature* **359**, 710–713 (1992).
68. Vallet-Regí, M. *et al.* A new property of MCM-41: Drug delivery system. *Chem. Mater.* **13**, 308–311 (2001).
69. Vallet-Regí, M. *et al.* Bioceramics: From bone regeneration to cancer nanomedicine. *Adv. Mater.* **23**, 5177–5218 (2011).
70. Maleki, A. *et al.* Mesoporous silica materials: From physico-chemical properties to enhanced dissolution of poorly water-soluble drugs. *J. Control. Release* **262**, 329–347 (2017).



71. Manzano, M. *et al.* Mesoporous Silica Nanoparticles for Drug Delivery. *Adv. Funct. Mater.* **30**, 3–5 (2020).
72. Li, L. *et al.* Biodistribution, excretion, and toxicity of mesoporous silica nanoparticles after oral administration depend on their shape. *Nanomedicine Nanotechnology, Biol. Med.* **11**, 1915–1924 (2015).
73. Mohammadi, M. *et al.* Hybrid Vesicular Drug Delivery Systems for Cancer Therapeutics. *Adv. Funct. Mater.* **28**, 1–18 (2018).
74. Chou, P. L. *et al.* Improvement of paclitaxel-associated adverse reactions (ADRs) via the use of nano-based drug delivery systems: A systematic review and network meta-analysis. *Int. J. Nanomedicine* **15**, 1731–1743 (2020).
75. Liu, Y. *et al.* Lipid-dendrimer hybrid nanosystem as a novel delivery system for paclitaxel to treat ovarian cancer. *J. Control. Release* **220**, 438–446 (2015).
76. Chan, J. M. *et al.* PLGA-lecithin-PEG core-shell nanoparticles for controlled drug delivery. *Biomaterials* **30**, 1627–1634 (2009).
77. Mady, M. M. *et al.* Effect of chitosan coating on the characteristics of DPPC liposomes. *J. Adv. Res.* **1**, 187–191 (2010).
78. Versluis, F. *et al.* Coiled coil driven membrane fusion between cyclodextrin vesicles and liposomes. *Soft Matter* **10**, 9746–9751 (2014).
79. Dave, V. *et al.* Lipid-polymer hybrid nanoparticles: Synthesis strategies and biomedical applications. *J. Microbiol. Methods* **160**, 130–142 (2019).
80. Indoria, S. *et al.* Recent advances in theranostic polymeric nanoparticles for cancer treatment: A review. *Int. J. Pharm.* **582**, 119314 (2020).
81. Shetty, A. *et al.* Inorganic hybrid nanoparticles in cancer theranostics : understanding their combinations for better clinical translation. *Mater. Today Chem.* **18**, 100381 (2020).
82. Huang, Y. *et al.* Superparamagnetic iron oxide nanoparticles conjugated with folic acid for dual target-specific drug delivery and MRI in cancer theranostics. *Mater. Sci. Eng. C* **70**, 763–771 (2017).
83. Farha, O. K. *et al.* Metal-organic framework materials with ultrahigh surface areas: Is the sky the limit? *J. Am. Chem. Soc.* **134**, 15016–15021 (2012).
84. Hönicke, I. M. *et al.* Balancing Mechanical Stability and Ultrahigh Porosity in Crystalline Framework Materials. *Angew. Chemie - Int. Ed.* **57**, 13780–13783 (2018).
85. Feng, L. *et al.* The chemistry of multi-component and hierarchical framework compounds. *Chem. Soc. Rev.* **48**, 4823–4853 (2019).
86. Li, H. *et al.* Recent advances in gas storage and separation using metal–organic frameworks. *Mater. Today* **21**, 108–121 (2018).
87. Ding, M. *et al.* Carbon capture and conversion using metal-organic frameworks and MOF-based materials. *Chem. Soc. Rev.* **48**, 2783–2828 (2019).
88. Dhakshinamoorthy, A. *et al.* Catalysis and photocatalysis by metal organic frameworks. *Chem. Soc. Rev.* **47**, 8134–8172 (2018).
89. Yang, J. *et al.* Metal–Organic Frameworks for Biomedical Applications. *Small* **16**, 1–24 (2020).
90. Li, H. *et al.* Design and synthesis of an exceptionally stable and highly porous metal-organic framework. *Nature* **402**, 276–279 (1999).
91. Kondo, M. *et al.* Three-Dimensional Framework with Channeling Cavities for Small Molecules: {[M<sub>2</sub>(4,4'-bpy)<sub>3</sub>(NO<sub>3</sub>)<sub>4</sub>]·xH<sub>2</sub>O}<sub>n</sub> (M = Co, Ni, Zn). *Angew. Chemie (International Ed. English)* **36**, 1725–1727 (1997).
92. Barthelet, K. *et al.* A breathing hybrid organic-inorganic solid with very large pores and high magnetic characteristics. *Angew. Chemie - Int. Ed.* **41**, 281–284 (2002).

## Chapter I

### Introduction

93. Wuttke, S. *et al.* Positioning metal-organic framework nanoparticles within the context of drug delivery – A comparison with mesoporous silica nanoparticles and dendrimers. *Biomaterials* **123**, 172–183 (2017).
94. Horcajada, P. *et al.* Porous metal-organic-framework nanoscale carriers as a potential platform for drug delivery and imaging. *Nat. Mater.* **9**, 172–178 (2010).
95. Horcajada, P. *et al.* Metal-organic frameworks as efficient materials for drug delivery. *Angew. Chemie - Int. Ed.* **45**, 5974–5978 (2006).
96. Horcajada, P. *et al.* Synthesis and catalytic properties of MIL-100(Fe), an iron(III) carboxylate with large pores. *Chem. Commun.* **100**, 2820–2822 (2007).
97. Stock, N. *et al.* Synthesis of metal-organic frameworks (MOFs): Routes to various MOF topologies, morphologies, and composites. *Chem. Rev.* **112**, 933–969 (2012).
98. Kaur, H. *et al.* Synthesis and characterization of ZIF-8 nanoparticles for controlled release of 6-mercaptopurine drug. *J. Drug Deliv. Sci. Technol.* **41**, 106–112 (2017).
99. Sánchez-Sánchez, M. *et al.* Synthesis of metal-organic frameworks in water at room temperature: Salts as linker sources. *Green Chem.* **17**, 1500–1509 (2015).
100. Dai, S. *et al.* One-Step Room-Temperature Synthesis of Metal (IV) Carboxylate Metal-Organic Frameworks. *Angew. Chemie - Int. Ed.* **60**, 4282–4288 (2021).
101. Sung, H. J. *et al.* Microwave synthesis of a nanoporous hybrid material, chromium trimesate. *Bull. Korean Chem. Soc.* **26**, 880–881 (2005).
102. Jhung, S. H. *et al.* Microwave synthesis of chromium terephthalate MIL-101 and its benzene sorption ability. *Adv. Mater.* **19**, 121–124 (2007).
103. Choi, J. S. *et al.* Metal-organic framework MOF-5 prepared by microwave heating: Factors to be considered. *Microporous Mesoporous Mater.* **116**, 727–731 (2008).
104. Schlesinger, M. *et al.* Evaluation of synthetic methods for microporous metal-organic frameworks exemplified by the competitive formation of [Cu<sub>2</sub>(btc)<sub>3</sub>(H<sub>2</sub>O)<sub>3</sub>] and [Cu<sub>2</sub>(btc)(OH)(H<sub>2</sub>O)]. *Microporous Mesoporous Mater.* **132**, 121–127 (2010).
105. Taylor-Pashow, K. M. L. *et al.* Postsynthetic modifications of iron-carboxylate nanoscale metal-organic frameworks for imaging and drug delivery. *J. Am. Chem. Soc.* **131**, 14261–14263 (2009).
106. Morris, W. *et al.* Role of modulators in controlling the colloidal stability and polydispersity of the UiO-66 metal-organic framework. *ACS Appl. Mater. Interfaces* **9**, 33413–33418 (2017).
107. Canossa, S. *et al.* Overcoming Crystallinity Limitations of Aluminium Metal-Organic Frameworks by Oxalic Acid Modulated Synthesis. *Chem. - A Eur. J.* **26**, 3564–3570 (2020).
108. Zhang, X. *et al.* A historical overview of the activation and porosity of metal-organic frameworks. *Chem. Soc. Rev.* **49**, 7406–7427 (2020).
109. Moghadam, P. Z. *et al.* Development of a Cambridge Structural Database Subset: A Collection of Metal-Organic Frameworks for Past, Present, and Future. *Chem. Mater.* **29**, 2618–2625 (2017).
110. Moghadam, P. Z. *et al.* Targeted classification of metal-organic frameworks in the Cambridge structural database (CSD). *Chem. Sci.* **11**, 8373–8387 (2020).
111. Tamames-Tabar, C. *et al.* Cytotoxicity of nanoscaled metal-organic frameworks. *J. Mater. Chem. B* **2**, 262–271 (2014).
112. Abánades Lázaro, I. *et al.* Application of zirconium MOFs in drug delivery and biomedicine. *Coord. Chem. Rev.* **380**, 230–259 (2019).
113. Cunha, D. *et al.* Rationalization of the entrapping of bioactive molecules into a series of functionalized porous zirconium terephthalate MOFs. *J. Mater. Chem. B* **1**, 1101–1108 (2013).

114. Jarai, B. M. *et al.* Evaluating UiO-66 Metal-Organic Framework Nanoparticles as Acid-Sensitive Carriers for Pulmonary Drug Delivery Applications. *ACS Appl. Mater. Interfaces* **12**, 38989–39004 (2020).
115. Jiang, H. L. *et al.* An exceptionally stable, porphyrinic Zr metal-organic framework exhibiting pH-dependent fluorescence. *J. Am. Chem. Soc.* **135**, 13934–13938 (2013).
116. Feng, D. *et al.* Construction of ultrastable porphyrin Zr metal-organic frameworks through linker elimination. *J. Am. Chem. Soc.* **135**, 17105–17110 (2013).
117. Feng, D. *et al.* A highly stable porphyrinic zirconium metal-organic framework with shp-a topology. *J. Am. Chem. Soc.* **136**, 17714–17717 (2014).
118. Feng, D. *et al.* Zirconium-Metalloporphyrin PCN-222: Mesoporous Metal-Organic Frameworks with Ultrahigh Stability as Biomimetic Catalysts. *Angew. Chemie* **124**, 10453–10456 (2012).
119. Lin, W. *et al.* A porphyrin-based metal-organic framework as a pH-responsive drug carrier. *J. Solid State Chem.* **237**, 307–312 (2016).
120. Park, J. *et al.* Size-Controlled Synthesis of Porphyrinic Metal-Organic Framework and Functionalization for Targeted Photodynamic Therapy. *J. Am. Chem. Soc.* **138**, 3518–3525 (2016).
121. Chen, Y. *et al.* Acid-Resistant Mesoporous Metal-Organic Framework toward Oral Insulin Delivery: Protein Encapsulation, Protection, and Release. *J. Am. Chem. Soc.* **140**, 5678–5681 (2018).
122. Sun, C. Y. *et al.* Zeolitic imidazolate framework-8 as efficient pH-sensitive drug delivery vehicle. *Dalt. Trans.* **41**, 6906–6909 (2012).
123. Zheng, H. *et al.* One-pot Synthesis of Metal-Organic Frameworks with Encapsulated Target Molecules and Their Applications for Controlled Drug Delivery. *J. Am. Chem. Soc.* **138**, 962–968 (2016).
124. Chen, W. H. *et al.* Glucose-responsive metal-organic-framework nanoparticles act as ‘smart’ sense-and-treat carriers. *ACS Nano* **12**, 7538–7545 (2018).
125. Luzuriaga, M. A. *et al.* ZIF-8 degrades in cell media, serum, and some—but not all—common laboratory buffers. *Supramol. Chem.* **31**, 485–490 (2019).
126. Velásquez-Hernández, M. D. J. *et al.* Degradation of ZIF-8 in phosphate buffered saline media. *CrystEngComm* **21**, 4538–4544 (2019).
127. Hoop, M. *et al.* Biocompatibility characteristics of the metal organic framework ZIF-8 for therapeutical applications. *Appl. Mater. Today* **11**, 13–21 (2018).
128. Pinto, R. V. *et al.* Tuning Cellular Biological Functions Through the Controlled Release of NO from a Porous Ti-MOF. *Angew. Chemie - Int. Ed.* **59**, 5135–5143 (2020).
129. Rojas, S. *et al.* Metal organic frameworks based on bioactive components. *J. Mater. Chem. B* **5**, 2560–2573 (2017).
130. Cai, H. *et al.* Biological metal–organic frameworks: Structures, host–guest chemistry and bio-applications. *Coord. Chem. Rev.* **378**, 207–221 (2019).
131. Wang, H. S. *et al.* Development of biological metal-organic frameworks designed for biomedical applications: From bio-sensing/bio-imaging to disease treatment. *Nanoscale Adv.* **2**, 3788–3797 (2020).
132. Miller, S. R. *et al.* Biodegradable therapeutic MOFs for the delivery of bioactive molecules. *Chem. Commun.* **46**, 4526–4528 (2010).
133. Smaldone, R. A. *et al.* Metalorganic frameworks from edible natural products. *Angew. Chemie - Int. Ed.* **49**, 8630–8634 (2010).
134. Furukawa, Y. *et al.* Nano- and micro-sized cubic gel particles from cyclodextrin metal-organic frameworks. *Angew. Chemie - Int. Ed.* **51**, 10566–10569 (2012).
135. Martí-Gastaldo, C. *et al.* Sponge-Like Behaviour in Isoreticular Cu(Gly-His-X) Peptide-Based Porous Materials. *Chem. - A Eur. J.* **21**, 16027–16034 (2015).

## Chapter I

### Introduction

136. Marti-Gastaldo, C. *et al.* Enhanced stability in rigid peptide-based porous materials. *Angew. Chemie - Int. Ed.* **51**, 11044–11048 (2012).
137. Paquin, F. *et al.* Multi-phase semicrystalline microstructures drive exciton dissociation in neat plastic semiconductors. *J. Mater. Chem. C* **3**, 10715–10722 (2015).
138. Sakai, F. *et al.* Protein crystalline frameworks with controllable interpenetration directed by dual supramolecular interactions. *Nat. Commun.* **5**, 1–8 (2014).
139. Yang, G. *et al.* Precise and Reversible Protein-Microtubule-Like Structure with Helicity Driven by Dual Supramolecular Interactions. *J. Am. Chem. Soc.* **138**, 1932–1937 (2016).
140. Yang, G. *et al.* Highly Ordered Self-Assembly of Native Proteins into 1D, 2D, and 3D Structures Modulated by the Tether Length of Assembly-Inducing Ligands. *Angew. Chemie - Int. Ed.* **56**, 10691–10695 (2017).
141. Wuttke, S. *et al.* Discovering the active sites for C3 separation in MIL-100(Fe) by using operando IR spectroscopy. *Chem. - A Eur. J.* **18**, 11959–11967 (2012).
142. Li, X. *et al.* Compartmentalized Encapsulation of Two Antibiotics in Porous Nanoparticles: an Efficient Strategy to Treat Intracellular Infections. *Part. Part. Syst. Charact.* **36**, 1–9 (2019).
143. Agostoni, V. *et al.* ‘Green’ fluorine-free mesoporous iron(III) trimesate nanoparticles for drug delivery. *Green Mater.* **1**, 209–217 (2013).
144. Zimpel, A. *et al.* Imparting Functionality to MOF Nanoparticles by External Surface Selective Covalent Attachment of Polymers. *Chem. Mater.* **28**, 3318–3326 (2016).
145. Sene, S. *et al.* Maghemite-nanoMIL-100(Fe) Bimodal Nanovector as a Platform for Image-Guided Therapy. *Chem* **3**, 303–322 (2017).
146. Baati, T. *et al.* In depth analysis of the in vivo toxicity of nanoparticles of porous iron(iii) metal–organic frameworks. *Chem. Sci.* **4**, 1597–1607 (2013).
147. Li, X. *et al.* New insights into the degradation mechanism of metal-organic frameworks drug carriers. *Sci. Rep.* **7**, 1–11 (2017).
148. Grall, R. *et al.* In vitro biocompatibility of mesoporous metal (III; Fe, Al, Cr) trimesate MOF nanocarriers. *J. Mater. Chem. B* **3**, 8279–8292 (2015).
149. Bellido, E. *et al.* Understanding the colloidal stability of the mesoporous MIL-100(Fe) nanoparticles in physiological media. *Langmuir* **30**, 5911–5920 (2014).
150. He, C. *et al.* Effects of particle size and surface charge on cellular uptake and biodistribution of polymeric nanoparticles. *Biomaterials* **31**, 3657–3666 (2010).
151. Giménez-Marqués, M. *et al.* GraftFast Surface Engineering to Improve MOF Nanoparticles Furtiveness. *Small* **14**, 1–11 (2018).
152. Cutrone, G. *et al.* Comb-like dextran copolymers: A versatile strategy to coat highly porous MOF nanoparticles with a PEG shell. *Carbohydr. Polym.* **223**, 115085 (2019).
153. Agostoni, V. *et al.* A ‘green’ strategy to construct non-covalent, stable and bioactive coatings on porous MOF nanoparticles. *Sci. Rep.* **5**, 1–7 (2015).
154. Qiu, J. *et al.* *Carbohydrates in metal organic frameworks: Supramolecular assembly and surface modification for biomedical applications. Metal-Organic Frameworks for Biomedical Applications* 445–465 (Elsevier Inc., 2020).
155. Anand, R. *et al.* Host-guest interactions in Fe(III)-trimesate MOF nanoparticles loaded with doxorubicin. *J. Phys. Chem. B* **118**, 8532–8539 (2014).
156. Rodriguez-Ruiz, V. *et al.* Efficient ‘green’ encapsulation of a highly hydrophilic anticancer drug in metal-organic framework nanoparticles. *J. Drug Target.* **23**, 759–767 (2015).

157. Agostoni, V. *et al.* Impact of phosphorylation on the encapsulation of nucleoside analogues within porous iron(III) metal-organic framework MIL-100(Fe) nanoparticles. *J. Mater. Chem. B* **1**, 4231–4242 (2013).
158. Di Nunzio, M. R. *et al.* A ‘ship in a bottle’ strategy to load a hydrophilic anticancer drug in porous metal organic framework nanoparticles: Efficient encapsulation, matrix stabilization, and photodelivery. *J. Med. Chem.* **57**, 411–420 (2014).
159. Chalati, T. *et al.* Porous metal organic framework nanoparticles to address the challenges related to busulfan encapsulation. *Nanomedicine* **6**, 1683–1695 (2011).
160. Wuttke, S. *et al.* Validating Metal-Organic Framework Nanoparticles for Their Nanosafety in Diverse Biomedical Applications. *Adv. Healthc. Mater.* **6**, 1–11 (2017).
161. Bellido, E. *et al.* Heparin-Engineered Mesoporous Iron Metal-Organic Framework Nanoparticles: Toward Stealth Drug Nanocarriers. *Adv. Healthc. Mater.* **4**, 1246–1257 (2015).
162. Simon-Yarza, T. *et al.* In vivo behavior of MIL-100 nanoparticles at early times after intravenous administration. *Int. J. Pharm.* **511**, 1042–1047 (2016).
163. Simon-Yarza, M. T. *et al.* Antineoplastic busulfan encapsulated in a metal organic framework nanocarrier: First in vivo results. *J. Mater. Chem. B* **4**, 585–588 (2016).
164. Ruyra, A. *et al.* Synthesis, culture medium stability, and in vitro and in vivo zebrafish embryo toxicity of metal-organic framework nanoparticles. *Chem. - A Eur. J.* **21**, 2508–2518 (2015).
165. Simon-Yarza, T. *et al.* A Smart Metal–Organic Framework Nanomaterial for Lung Targeting. *Angew. Chemie - Int. Ed.* **56**, 15565–15569 (2017).
166. Binnig, G. *et al.* Atomic Force Microscope. *Phys. Rev. Lett.* **56**, 930–934 (1986).
167. Li, M. *et al.* Nanoscale imaging and force probing of biomolecular systems using atomic force microscopy: From single molecules to living cells. *Nanoscale* **9**, 17643–17666 (2017).
168. Shoaee, M. *et al.* Crystal growth of the nanoporous metal-organic framework HKUST-1 revealed by in situ atomic force microscopy. *Angew. Chemie - Int. Ed.* **47**, 8525–8528 (2008).
169. John, N. S. *et al.* Single layer growth of sub-micron metal-organic framework crystals observed by in situ atomic force microscopy. *Chem. Commun.* **2**, 6294–6296 (2009).
170. Cubillas, P. *et al.* Crystal growth of MOF-5 using secondary building units studied by in situ atomic force microscopy. *CrystEngComm* **16**, 9834–9841 (2014).
171. Wagia, R. *et al.* Determination of the Preassembled Nucleating Units That Are Critical for the Crystal Growth of the Metal-Organic Framework CdIF-4. *Angew. Chemie* **128**, 9221–9225 (2016).
172. Hosono, N. *et al.* Highly responsive nature of porous coordination polymer surfaces imaged by in situ atomic force microscopy. *Nat. Chem.* **11**, 109–116 (2019).
173. Velásquez-Hernández, M. D. J. *et al.* Degradation of ZIF-8 in phosphate buffered saline media. *CrystEngComm* **21**, 4538–4544 (2019).
174. Drude, P. On the laws of reflection and refraction of light at the interface to absorbing crystals. *Ann. Phys.* **268**, 584–625 (1887).
175. Garcia-Caurel, E. *et al.* Application of spectroscopic ellipsometry and mueller ellipsometry to optical characterization. *Appl. Spectrosc.* **67**, 1–21 (2013).
176. Ellipsometry FAQ - J.A. Woollam. <https://www.jawoollam.com/resources/ellipsometry-faq>.
177. Hilfiker, J. N. *In situ spectroscopic ellipsometry (SE) for characterization of thin film growth. Situ Charact. Thin Film Growth* 99–151 (Elsevier Inc., 2011).
178. Bindini, E. *et al.* Following in Situ the Degradation of Mesoporous Silica in Biorelevant Conditions: At Last, a Good Comprehension of the Structure Influence. *ACS Appl. Mater. Interfaces* **12**, 13598–13612 (2020).

## Chapter I

### Introduction

179. Hermes, S. *et al.* Selective nucleation and growth of metal-organic open framework thin films on patterned COOH/CF<sub>3</sub>-terminated self-assembled monolayers on Au(111). *J. Am. Chem. Soc.* **127**, 13744–13745 (2005).
180. Biemmi, E. *et al.* Oriented growth of the metal organic framework Cu<sub>3</sub>(BTC) 2(H<sub>2</sub>O)<sub>3</sub>·xH<sub>2</sub>O tunable with functionalized self-assembled monolayers. *J. Am. Chem. Soc.* **129**, 8054–8055 (2007).
181. Zacher, D. *et al.* Deposition of microcrystalline [Cu<sub>3</sub>(btc)<sub>2</sub>] and [Zn<sub>2</sub>(bdc)<sub>2</sub>(dabco)] at alumina and silica surfaces modified with patterned self assembled organic monolayers: Evidence of surface selective and oriented growth. *J. Mater. Chem.* **17**, 2785–2792 (2007).
182. Shekhah, O. *et al.* Step-by-step route for the synthesis of metal-organic frameworks. *J. Am. Chem. Soc.* **129**, 15118–15119 (2007).
183. U. Mueller, H. *et al.* BASF Aktiengesellschaft, (2007).
184. Zhang, X. *et al.* Electrochemical deposition of metal-organic framework films and their applications. *J. Mater. Chem. A* **8**, 7569–7587 (2020).
185. Horcajada, P. *et al.* Colloidal route for preparing optical thin films of nanoporous metal-organic frameworks. *Adv. Mater.* **21**, 1931–1935 (2009).
186. Demessence, A. *et al.* Elaboration and properties of hierarchically structured optical thin films of MIL-101(Cr). *Chem. Commun.* **101**, 7149–7151 (2009).
187. Demessence, A. *et al.* Adsorption properties in high optical quality nanoZIF-8 thin films with tunable thickness. *J. Mater. Chem.* **20**, 7676–7681 (2010).
188. Borzehandani, M. Y., Basyaruddin, M. & Rahman, A. Development of Metal-Organic Frameworks for Biomedical Applications – A Review. **6**, 105–116 (2019).
189. Landau, L. *et al.* Dragging of a Liquid By a Moving Plate. *Collect. Pap. L.D. Landau* **42**, 355–364 (1965).
190. Faustini, M. *et al.* Preparation of sol-gel films by dip-coating in extreme conditions. *J. Phys. Chem. C* **114**, 7637–7645 (2010).

## **Chapter II**

Degradation mechanism of porous metal-organic frameworks by in situ Atomic Force Microscopy

## Chapter II

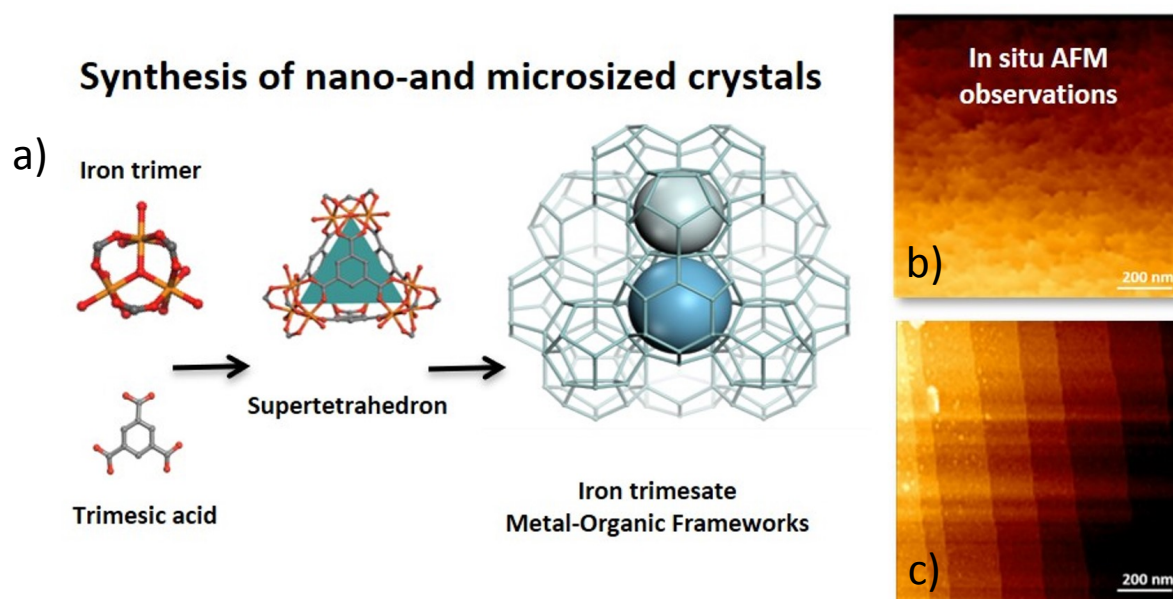
Degradation mechanism of porous metal-organic frameworks by *in situ* Atomic Force Microscopy



## General objectives

This chapter focuses on the study of the degradation mechanism of MIL-100(Fe) micron-sized particles (microMOFs). As already mentioned, particles of submicronic scale (nanoMOFs) are rapidly degraded under simulated physiological conditions. More specifically, nanoMOFs can lose practically the totality of their constitutive ligand within a few hours in phosphate buffer saline (PBS), due to the fast diffusion of phosphate ions into their internal porosity and their strong coordination with the iron (III) acid Lewis sites of the framework.<sup>1</sup> In addition to the composition of the degrading media, pH is another key parameter of particles' stability.<sup>1,2</sup> Previous studies have indicated that nanoMOFs are more stable in acidic environments compared to neutral ones.<sup>3</sup> Recently, microMOFs particles synthesized by "green" methods, were incubated in neutral PBS for more than one week and the final product consisted of an inorganic iron phosphate corona around the MOF particles. Noteworthy, despite their dramatic changes in composition, the MOFs maintained their initial size and shape.<sup>4</sup> Based on these findings, we performed further studies to explore the parameters that determine the degradation of MIL-100(Fe) particles.

This work is presented in the format of a research article recently published in the journal *Nanomaterials*. The main goal of this work was the deeper understanding of MIL-100(Fe) particles for their optimization as therapeutic vectors in the biomedical field. *In situ* AFM was the technique of choice, aimed to unravel the morphological, dimensional and mechanical changes of the external surface of microMOFs upon degradation. This technique was selected, because of its capacity to follow the degradation of individual particles in real time together with a very high resolution down to the nanoscale. MIL-100(Fe) microMOFs of different crystal qualities were synthesized, to compare their degradation by *in situ* AFM. Of note, to complete the study, nanoMOFs of around 200 nm were also prepared *via* a microwave-assisted "green" method and were observed using a high-resolution electronic microscope, Scanning TEM with High Annular Dark Field (STEM-HAADF). This study demonstrated that MOF's surfaces respond within minutes to changes in the composition of the media there are in contact with and that their degradation process depends on the size and the crystallinity of the studied material. These results are of importance for the wider comprehension of the *in vivo* fate of nanoMOFs.



**Figure 2-1:** a) Schematic representation of MIL-100(Fe) assembly and AFM images of microMOFs crystals during their degradation b) in PBS pH 7.4 and c) in PBS pH 5.4.

## References

1. Bellido, E. *et al.* Understanding the colloidal stability of the mesoporous MIL-100(Fe) nanoparticles in physiological media. *Langmuir* **30**, 5911–5920 (2014).
2. Agostoni, V. *et al.* Towards an Improved anti-HIV Activity of NRTI via Metal-Organic Frameworks Nanoparticles. *Adv. Healthc. Mater.* **2**, 1630–1637 (2013).
3. Simon-Yarza, T. *et al.* A Smart Metal–Organic Framework Nanomaterial for Lung Targeting. *Angew. Chemie - Int. Ed.* **56**, 15565–15569 (2017).
4. Li, X. *et al.* New insights into the degradation mechanism of metal-organic frameworks drug carriers. *Sci. Rep.* **7**, 1–11 (2017).



## Article

# Degradation Mechanism of Porous Metal-Organic Frameworks by In Situ Atomic Force Microscopy

Ioanna Christodoulou <sup>1,2</sup>, Tom Bourguignon <sup>1</sup>, Xue Li <sup>1</sup>, Gilles Patriarche <sup>3</sup> , Christian Serre <sup>2</sup> , Christian Marlière <sup>4</sup> and Ruxandra Gref <sup>1,\*</sup>

- <sup>1</sup> Institute of Molecular Sciences, UMR CNRS 8214, Université Paris Saclay, 91400 Orsay, France; ioanna.christodoulou@universite-paris-saclay.fr (I.C.); tom.bourguignon@universite-paris-saclay.fr (T.B.); xue.li@universite-paris-saclay.fr (X.L.)
- <sup>2</sup> Institut des Matériaux Poreux de Paris, UMR 8004, Ecole Normale Supérieure, ESPCI Paris, CNRS, PSL University, 75005 Paris, France; christian.serre@ens.psl.eu
- <sup>3</sup> Center for Nanoscience and Nanotechnology, UMR 9001, CNRS, Université Paris Saclay, 75000 Palaiseau, France; gilles.patriarche@c2n.upsaclay.fr
- <sup>4</sup> Laboratoire de Physique des Solides, UMR CNRS 8502, Université Paris Saclay, 91400 Orsay, France; christian.marliere@universite-paris-saclay.fr
- \* Correspondence: ruxandra.gref@universite-paris-saclay.fr



**Citation:** Christodoulou, I.; Bourguignon, T.; Li, X.; Patriarche, G.; Serre, C.; Marlière, C.; Gref, R. Degradation Mechanism of Porous Metal-Organic Frameworks by In Situ Atomic Force Microscopy. *Nanomaterials* **2021**, *11*, 722. <https://doi.org/10.3390/nano11030722>

Academic Editor: Pablo del Pino

Received: 19 January 2021

Accepted: 11 March 2021

Published: 13 March 2021

**Publisher's Note:** MDPI stays neutral with regard to jurisdictional claims in published maps and institutional affiliations.



Copyright © 2021 by the authors. Licensee MDPI, Basel, Switzerland. This article is an open access article distributed under the terms and conditions of the Creative Commons Attribution (CC BY) license (<https://creativecommons.org/licenses/by/4.0/>).

**Abstract:** In recent years, Metal-Organic Frameworks (MOFs) have attracted a growing interest for biomedical applications. The design of MOFs should take into consideration the subtle balance between stability and biodegradability. However, only few studies have focused on the MOFs' stability in physiological media and their degradation mechanism. Here, we investigate the degradation of mesoporous iron (III) carboxylate MOFs, which are among the most employed MOFs for drug delivery, by a set of complementary methods. In situ AFM allowed monitoring with nanoscale resolution the morphological, dimensional, and mechanical properties of a series of MOFs in phosphate buffer saline and in real time. Depending on the synthetic route, the external surface presented either well-defined crystalline planes or initial defects, which influenced the degradation mechanism of the particles. Moreover, MOF stability was investigated under different pH conditions, from acidic to neutral. Interestingly, despite pronounced erosion, especially at neutral pH, the dimensions of the crystals were unchanged. It was revealed that the external surfaces of MOF crystals rapidly respond to in situ changes of the composition of the media they are in contact with. These observations are of a crucial importance for the design of nanosized MOFs for drug delivery applications.

**Keywords:** metal organic frameworks; in situ AFM; degradation; bio applications

## 1. Introduction

Metal Organic Frameworks (MOFs) are a recent class of tunable hybrid materials crafted from metal connecting points and organic bridging ligands. The nanosized MOFs (nanoMOFs) have emerged as promising candidates for biomedical applications such as drug delivery [1–3]. Their high and modular porosity and internal amphiphilic microenvironment allow the incorporation of a variety of drug molecules with various physicochemical properties (hydrophobic, hydrophilic, and amphiphilic) reaching high drug loadings up to 20–70 wt% and yields close to 100% [4,5]. The drugs penetrated through the nanoMOFs accessible porosity, while versatile strategies were developed to functionalize the nanoMOFs' external surfaces with cyclodextrins, (co)polymers, lipids, or silica shells [6,7]. In recent years, the design and synthesis of MOFs for biomedical applications has attracted a growing interest. However, only few studies have focused on the MOFs' stability in physiological media and their degradation mechanism with the exception of a few recent studies [8–10]. These aspects determine the biological fate of the nanoMOFs after their intravenous administration. On one hand, the nanoMOFs should present a good

stability when circulating in the bloodstream, to ferry their cargo to the biological targets. On the other hand, they should also degrade to release their cargo and avoid accumulation inside the body. Therefore, the design of nanoMOFs should take into consideration the subtle balance between stability and biodegradability. This calls for a better understanding of the mechanisms involved in MOF degradation and their optimization as drug carriers.

Numerous MOF structures have been reported as candidates for biomedical applications. Zr based MOFs have been proposed as drug delivery systems. In general, these MOFs are highly porous, exhibit good chemical stability in water, and can host large quantities of drugs [5]. The UiO series (University of Oslo), the PCN-n series (Porous Coordination Network) and the NU family (Northwestern University) include large-pore Zr-based MOFs that have attracted great interest in biomedicine. Another example is the zinc imidazolate framework ZIF-8, constructed from  $Zn^{2+}$  ions and 2-methylimidazolate linkers. This material enables an on-demand release in the presence of an external stimulus such as the pH [11]. MOFs belonging to MIL-n series (MIL stands for Material of the Institute Lavoisier) have also been studied for drug delivery applications, thanks to their versatility and their biocompatibility [12]. Among the family of MOFs candidates for biomedical applications, the mesoporous iron (III) carboxylate MIL-100(Fe) accounts for one of the most studied materials for drug incorporation and release. This material has been selected here in reason of its numerous advantages for drug delivery applications: (i) Biofriendly composition (Fe is an endogenous metal and the trimesate ligand is non toxic) [13,14]; (ii) its mesoporosity, enabling the hostage of various drugs reaching high payloads and/or synergetic co-encapsulations [12,15]; (iii) its chemical stability in water; (iv) its "green" preparation [16,17]; (v) the numerous possibilities of surface modification [18,19], and (vi) its proven biodegradability and lack of toxicity both *in vitro* and *in vivo* [20–22].

MIL-100(Fe) nanoMOFs could host a variety of drugs including the anticancer drugs doxorubicin, gemcitabine monophosphate, or busulfan [23–25], anti-inflammatory drugs such as ibuprofen [26], a series of nucleoside reverse transcriptase inhibitors (NRTIs) for anti-HIV therapy [27], a combination of antibiotics [15], and very recently two co-encapsulated drugs used in skin disorders azelaic acid as antibiotic, and nicotinamide as anti-inflammatory drug [28]. MIL-100(Fe) nanoMOFs were shown to be stable in aqueous and ethanolic solutions, but degraded rapidly upon incubation in simulated biological media, such as PBS enriched or not with proteins, simulated intestinal fluid (SIF) supplemented or not with pancreatin and cell culture media (DMEM or RPMI), and serum, releasing an important amount of their carboxylate ligands [14,29,30]. It was shown that the degradation of MIL-100(Fe) nanoMOFs depends mainly on its interaction with specific components of the release media. More precisely, complexing ions diffuse in the matrix and coordinate with the unsaturated iron (III) sites, leading to a progressive loss of the MOF constitutive ligands (trimesic acid) [29,31]. A previous study in our group indicated that degradation of larger microparticles of MIL-100(Fe) in PBS was associated with the progressive formation of an inorganic fragile corona around the MOFs. Interestingly, the microparticles maintained their initial size and morphology despite a massive loss of their constitutive ligands [10].

In another work, it was shown that MIL-100(Fe) nanoMOFs have the tendency to reversibly aggregate depending on the pH and the ionic strength of the suspension media [24]. More precisely, the nanoMOFs remained colloidally stable in acidic conditions and experienced aggregation in neutral ones. The authors attributed this phenomenon to the changes of the  $\zeta$ -potential of the particles related to their surface charge. Taking advantage of this phenomenon, these nanoMOFs were used to passively target tumors in the lungs. Immediately after administration, the nanoMOFs aggregated at the neutral pH of the blood and ended up in the lungs where they released the drug cargo to the tumor. Eventually, the nanoMOFs disassembled again and it was hypothesized that this was due to surface erosion.

In this context, it is important to better understand the degradation of MIL-100(Fe) MOFs and more particularly their surface erosion by an *in situ* method. Atomic Force

Microscopy (AFM) is an *in situ* microscopic technique of choice, widely used to study the surface properties of (bio)materials. It accounts for subtle height variations at any point on the surface of the observed specimen with nanoscale resolution, as well as for the surface mechanical properties.

Here we show the application of AFM to study the surface erosion and degradation of MIL-100(Fe) MOFs, both nano- and micron-scale particles. Micron-scale particles were selected, because of their slower degradation compared to the nanoMOFs, facilitating, in this manner, the exploration of the mechanism. Moreover, the AFM technique used for this study, could be performed only with particles of larger sizes. AFM is advantageously applicable to studies in liquid phase, which mimic the interaction of the crystalline material with the degradation medium as a function of its composition and pH. PBS solution was chosen, as it is one of the most common media used to maintain physiological pH and osmolarity for biomedical applications in cell culture and protein chemistry [32,33]. Neutral pH (PBS 7.4) was chosen to mimic the physiologic conditions, whereas acidic conditions (PBS 5.4) were selected to approach the pathogenic conditions and the pH in some intracellular compartments. *In situ* AFM allows real-time monitoring of the degradation of individual MOF particles in terms of morphology, size variations, and mechanical properties with submicron resolution. Moreover, it has the advantage over other methods “bulk” such as PXRD, FT-IR spectroscopy, and porosimetry to enable individual particle characterization, giving insights on the homogeneity of the samples. Conversely, electron microscopy techniques allow investigating the morphological changes of individual particles during their degradation but obtaining three dimensional information is challenging and there are no possibilities to follow changes in mechanical properties. Therefore, *in situ* AFM was selected to investigate the erosion mechanism of MOFs (morphological, dimensional, and mechanical properties) in real time and with nanometric resolution.

So far, *in situ* AFM has been used mainly to investigate the mechanical properties of MOFs/composites, the crystal growth process, and the behavior of MOFs in the presence of other molecules [34–38]. Recently, two groups reported the *in situ* degradation of MOF microparticles. Hosono et al. synthesized flexible porous coordination polymer (PCP) crystals suitable for separation and storage applications and followed their dissolution *in situ*. Degradation occurred by a delamination process consisting in a layer-by-layer exfoliation of the framework [39]. In another study, a zinc-based imidazolate MOF, ZIF-8 (ZIF stands for Zeolitic Imidazolate Framework) was incubated in PBS, and its behavior was monitored by *in situ* AFM [9]. The morphology of the particles was immediately modified upon contact with PBS and the crystals totally dissolved in less than 15 min.

Microparticles of MIL-100(Fe) have been analyzed here by AFM for the first time to reveal their morphology, dimensional, and stiffness changes upon interaction with various media. Furthermore, liquid AFM enabled the *in situ* monitoring of the major parameters that drive MOF degradation: The composition and the pH of the medium in contact with the particles. In addition, the analysis of different individual crystals enabled assessing their homogeneity in terms of surface properties and degradation behavior.

To complete the study, both nano- and micron-sized MOFs were produced to assess the impact of the particle size on the degradation mechanism. In addition to the particle size, special attention was given to the quality of the MOF crystals since the synthetic route is known to affect the crystal quality (defects) and thus potentially impact the degradation mechanism. It was found indeed that the degradation kinetics depend on the synthesis method and the purification method. Three synthesis pathways were employed. First, hydrofluoric acid (HF) was used as mineralizing agent to promote MOF crystal growth [40] to obtain high-quality large particles named microMOFs (+). Despite the fact that it provided the best crystalline materials, HF is corrosive, difficult to handle, and several purification steps are needed. Alternative HF-free synthesis methods were employed leading to the formation of crystalline particles named microMOFs (–) [10] of around 20–70 microns and nanoMOFs of around 200 nm [10,16,17].

The surface topography and mechanical rigidity of the microMOFs in contact with various liquid media was studied by AFM showing that small defects onto the microMOFs (–) surface contributed to their degradation. On the opposite, well-defined crystalline planes were observed on the microMOFs (+), which were eventually eroded at a specific pH. Complementary insights were obtained by Scanning TEM with High Annular Dark Field Mode (STEM-HAADF) enabling to unravel the structure and composition of nanoMOFs upon degradation.

## 2. Materials and Methods

### 2.1. Materials and Reagents

The chemicals iron (0), 1,3,5-benzenetricarboxylic acid (BTC) and HF were purchased from Sigma-Aldrich (Saint-Quentin-Fallavier, France). Iron (III) chloride hexahydrate (98%) was purchased from Alfa Aesar (Kandel, Germany). Nitric acid, potassium hydroxide, absolute EtOH, and Dulbecco's Phosphate Buffer Saline DPBS (1X, pH = 7.4) were purchased from Thermo Fischer Scientific (Les Ulis, France). DPBS contains 1.47 mM  $\text{KH}_2\text{PO}_4$ , 8.59  $\text{Na}_2\text{HPO}_4 \cdot 7\text{H}_2\text{O}$ , 137 mM NaCl, and 2.66 mM KCl. Milli-Q water was obtained from a Millipore apparatus equipped with a 0.22  $\mu\text{m}$  filter (18.2 M $\Omega$  cm). All reagents and solvents were used without further purification.

#### 2.1.1. Synthesis of microMOFs (–)

MicroMOFs were synthesized according to previous reported methods [10]. Briefly, a reaction mixture composed of 2.7 g iron (III) chloride hexahydrate (10.00 mmol) and 2.1 g trimesic acid (10.00 mmol) in 50 mL of water, was placed in a large Teflon bomb under magnetic stirring for 15 minutes. The Teflon reactor was encased in a metal bomb with controlled pressure, before being placed in an autoclave with a 1 hour heating ramp to 130 °C, and held at this temperature for 72 h. The product was cooled before being filtered and was then washed by heating under reflux, first in 700 mL of ethanol at 75 °C for 2 h and finally in 700 mL of water at 90 °C for 2 h. Finally, the resulting crystals were collected by filtration under vacuum and stored as powder after being dried in air.

#### 2.1.2. Synthesis of microMOFs (+)

Micron-sized MIL-100(Fe) crystals were successfully prepared by a hydrothermal method as previously reported [40]. This solid was isolated as a crystalline powder from a reaction mixture composed of 1.0 Fe<sup>0</sup>:0.66 1,3,5-BTC:2.0 HF:1.2 HNO<sub>3</sub>:280 H<sub>2</sub>O (1,3,5-BTC = benzene tricarboxylic or trimesic acid) that was held at 150 °C in a Teflon-lined autoclave for 6 days with an initial heating ramp of 12 h and a final cooling ramp of 24 h. The product was recovered by filtration and washed with deionized water.

#### 2.1.3. Synthesis of nanoMOFs

NanoMOFs were obtained by microwave-assisted hydrothermal synthesis as previously reported [10]. A mixture of iron chloride (8.97 mmol) and BTC (4.02 mmol) was placed in Teflon sealed autoclave reactors with 20 mL of deionized water and heated for 6 min at 130 °C under stirring. The applied power was 800 Watts (Mars-5, CEM, US) and pressure was fixed at 800 Watts. When temperature reached 90 °C, the reactors were placed in an ice bath for 10 min for stopping the nucleation. The resulting nanoMOFs were recovered by centrifugation (10,000 rpm, 15 min) and were washed with absolute ethanol 6 times to remove the residual non-reacted organic acid. A last centrifugation at 4000 rpm (2000× g) was performed during 1 min in absolute ethanol to sediment the largest particles and recover the supernatants as a suspension of monodisperse nanoparticles. NanoMOFs were stored in absolute ethanol until final use.

#### 2.1.4. Degradation of Nano and Micron Sized MOFs

For degradation studies, MIL-100(Fe) nanoMOFs were incubated under gentle stirring for 2 days in PBS 10 mM at 37 °C at a concentration of 0.25 mg/mL. Kinetic studies

were carried out until achieving a total degradation of the frameworks. In the case of microMOFs, degradation studies lasted one month, as their kinetics were much slower. At each time point during degradation, nano/microMOFs were separated from their supernatant by centrifugation and were extensively washed with Milli-Q water, in order to stop the degradation process and to remove the remaining salts. Finally, the degraded particles were either kept in Milli-Q water or dried under vacuum according to their further characterization method.

### 2.2. Experimental Techniques

The changes in crystallinity upon degradation were performed by powder X-ray diffraction (PXRD) analysis in a D8 Advance Bruker Diffractometer in Debye–Scherrer geometry, in the  $2\theta$  range  $2\text{--}40^\circ$ . The diffractometer was equipped with a Ge (111) monochromator producing Cu  $K\alpha_1$  radiation ( $\lambda = 1.540598 \text{ \AA}$ ) and a LynxEye detector. The size and the morphologies of the microparticles were determined by optical microscopy (Keyence VHX-7000). It was equipped with a motorized rotary turret of 4 high-resolution objectives covering a magnification of  $20\times\text{--}6000\times$  and with a 4k camera. The microscope was equipped with an illumination system in reflection (dark and bright field) and an illumination in transmission. Keyence's VHX software (7000, Kyoto, Japan) was used to reconstruct images without blurred areas and to perform measurements.

TEM/STEM studies were performed on a Titan Themis microscope (Palaiseau, France) corrected for spherical aberrations on the probe. The observations were made at 200 kV with a sufficiently low probe current, i.e., around 40 to 50 pA, so as not to degrade the sample and with an acquisition time of approximately 15 to 20 min. For the HAADF-STEM images acquisition, the half-angle of convergence of the probe was 17 mrad and the collection half-angle of the Annular Dark Field detector was 69 mrad (inner angle) and 200 mrad (outer angle).

For the TEM grid preparation, a 2  $\mu\text{L}$  drop of the solution was placed on a 200 mesh copper grid covered with a pure carbon membrane (from Ted Pella).

To study the composition and the coordination of phosphates after degradation process, Infrared spectra were measured with a Nicolet iS5 FTIR ThermoFisher spectrometer (Courtaboeuf, France) between 400 and  $4000 \text{ cm}^{-1}$ .

Porosity was evaluated by  $\text{N}_2$  sorption isotherms obtained at 77 K using a Micromeritics Tristar apparatus (Martignas, France). Before the analysis, around 30 mg of sample powder were activated by heating at  $150^\circ\text{C}$  under secondary vacuum for 5 h.

Ligand release was studied by a reversed-phase High Performance Liquid Chromatography analysis (HPLC), as previously reported [41]. Waters Alliance e2695 Separations Module (Waters, Milford, MA) equipped with a UV-Vis detector Waters 2998 was used. A SunFire-C18 reverse-phase column ( $5 \mu\text{m}$ ,  $4.6 \times 150 \text{ mm}^2$ , Waters) was employed. For the analysis of BTC, a mobile phase A consisting of a buffer solution (0.04 M,  $\text{pH} = 2.5$ ) and a mobile phase B MeCN (50:50) were used. The injection volume was 50  $\mu\text{L}$  and the detection wavelength was set at 225 nm. The column temperature was fixed at  $25^\circ\text{C}$  [41].

For buffer preparation,  $\text{NaH}_2\text{PO}_4$  (2.4 g, 0.02 mol) and  $\text{Na}_2\text{HPO}_4$  (2.84 g, 0.02 mol) were dissolved in 1 L of Milli-Q water. The pH was then adjusted to 2.5 with  $\text{H}_3\text{PO}_4$ .

### 2.3. Atomic Force Microscopy

AFM works with a sharp probe tip attached to a cantilever, which deflects upon interaction with the surface according to Hooke's law. A laser beam is used to detect the deflections of the cantilever induced by the force of tip–substrate interaction. Any movement of the cantilever changes the direction of the reflected beam and these changes are recorded by PSPD (position-sensitive photodiode), which makes it possible to obtain a topographic map of the sample under study. Force curves measure the sum of attractive and repulsive interactions between the cantilever and the sample as a function of distance and give valuable information about morphological deformations, dimensional changes (height measurements), and mechanical properties (stiffness) of the sample.

AFM studies were performed using a Bruker-JPK Instruments Nanowizard III (JPK Instruments AG, Berlin, Germany) and an electrochemical cell (ECCell Bruker-JPK Instruments). This equipment was associated with an inverted optical microscope (Axio Observer Z1 Zeiss, Göttingen, Germany). The entire system was placed on an anti-vibration table (Figure S1). AFM measurements were performed using a fast-speed approach/retract mode (Quantitative Imaging (QI) mode). At each pixel of the image, a complete force-distance curve, at a defined constant velocity, was acquired. The maximum force applied by the tip on the substrate was 2 nN, and the approach-retraction speed was constant at  $150 \mu\text{m}\cdot\text{s}^{-1}$ . The data were acquired on 128 00D7 128 pixel images and processed by OriginPro (Origin Corporation, Northampton, MA, USA) and Matlab (MathWorks, Natick, MA, USA). Stiffness data were calculated from the slope of the force-distance curves at different points as selected from the obtained topographic images.

#### Sample Preparation for AFM

Borosilicate glass substrates coated by a thin layer of an indium-tin-oxide (ITO) were used for the deposition of the sample. The substrates were carefully rinsed with Milli-Q water and then dried with the flow of a dry dust suppressant (Jel'R 99.9). One hundred and fifty microliters of microMOF sample were deposited to the ITO substrate and left to air dry for 10 min. The sample was then placed at the bottom of the liquid cell where it was washed six to eight times in a row with 600  $\mu\text{L}$  of Milli-Q water to remove any particles not adhered to the substrate. First, studies were carried on in Milli-Q water. Then, investigations were performed in PBS. To do so, 600  $\mu\text{L}$  of PBS pH = 7.4 were poured into the liquid cell and the MOF particles were visualized by an inverted optical microscope. When needed, the pH of the liquid medium was modified *in situ* by drop-wise addition of potassium hydroxide (KOH) 0.01M.

### 3. Results and Discussion

#### 3.1. Synthesis and Characterization of MOF Crystals

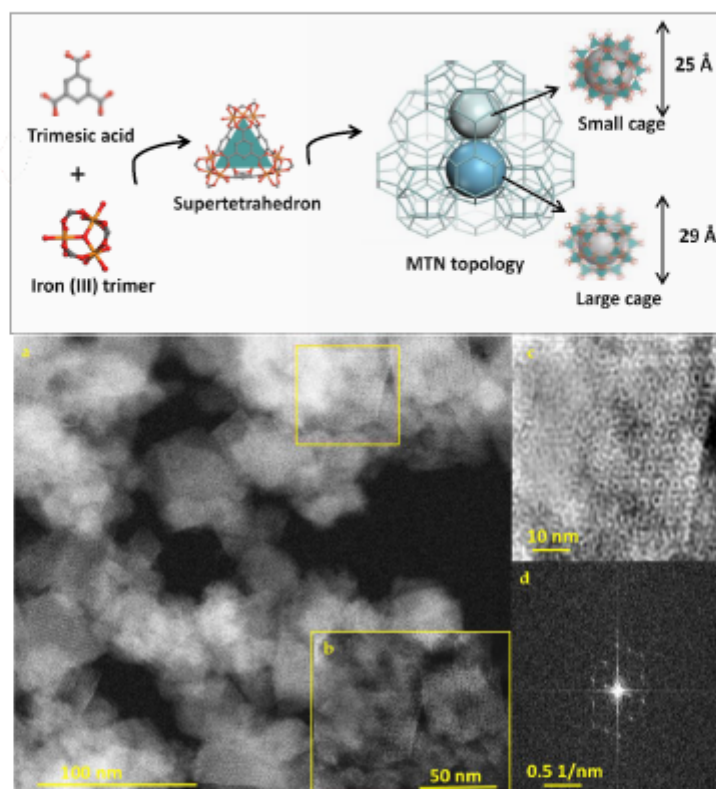
MIL-100(Fe) is a highly crystalline porous material, resulting from the self-assembly of iron trimers and tricarboxylic ligands, leading to a 3D mesoporous structure with MTN topology. This structure has two types of cages (25 and 29 Å) accessible through microporous windows (5.5 and 8.6 Å) and exhibits Lewis acid sites able to bind various molecules (drugs, gases, vapors) [8,12,42]. Nano(micro)MOFs crystals were successfully synthesized, as determined by a series of complementary investigations. Their structure is schematized in Figure 1 (upper panel).

First, STEM-HAADF, an *ex situ* advanced microscopic technique, was employed as a powerful tool for imaging local structures with atomic precision without damaging the samples. Highly ordered mesoporous cages were identified in agreement with the structure of MIL-100(Fe) by STEM-HAADF (Figure 1). Additionally, Fast Fourier Transform pattern (FFT) clearly confirms the crystalline character of the nanoMOFs.

However, STEM-HAADF cannot be used in the case of microMOFs due to their size above 20 microns. In contrast, these particles were visualized by optical microscopy (Figure S2). When stored in water, both types of microMOFs (+ and -) showed no detectable color or shape modifications.

PXRD patterns of synthesized micro and nanoMOFs were in agreement with previously reported data, confirming their crystalline structures [16,40] (Figure S3). Moreover, in line with published data [27,40],  $\text{N}_2$  sorption isotherms obtained at 77 K resulted in values of BET surface areas of  $1700 \pm 60 \text{ m}^2/\text{g}$  and  $2080 \pm 20 \text{ m}^2/\text{g}$  for microMOFs (-) and microMOFs (+), prepared as stated in introduction, by using HF or not, respectively. NanoMOFs surface area was  $1900 \pm 40 \text{ m}^2/\text{g}$ , in agreement with reported values [10,40] (Figure S4).





**Figure 1.** Upper panel: Schematic representation of the structure of MIL-100 (Fe) obtained by the self-assembly of iron supertetrahedra. Two cages 25 and 29 Å (small and large cage) are accessible through microporous pentagonal windows of 5 Å and microporous hexagonal windows of 8.6 Å. The structures were designed using Material Studio. Lower panel: Scanning TEM with High Annular Dark Field Mode (STEM-HAADF) images of MIL-100(Fe) nano Metal-Organic Frameworks (MOFs), (a) unprocessed image, (b) magnified image, (c) inverse FFT filtered STEM-HAADF image, and (d) FFT pattern which reveals the crystallinity of the particles. The ultrahigh resolution of STEM-HAADF shows the ordered porous structure of submicron particles.

### 3.2. MOF Degradation in PBS

In a comparative study, nanoMOFs were incubated under gentle stirring for 48 h in PBS (0.25 mg/mL) at pH = 5.4 and pH = 7.4 to study their degradation. First, they were visualized by STEM-HAADF to follow morphological changes. Interestingly, this technique evidenced that the well-formed nanoMOFs' crystalline planes remained intact in PBS in acidic environment (pH = 5.4) (Figure 2a,b) but they were lost during degradation in PBS in neutral conditions (pH = 7.4) (Figure 2d,e).

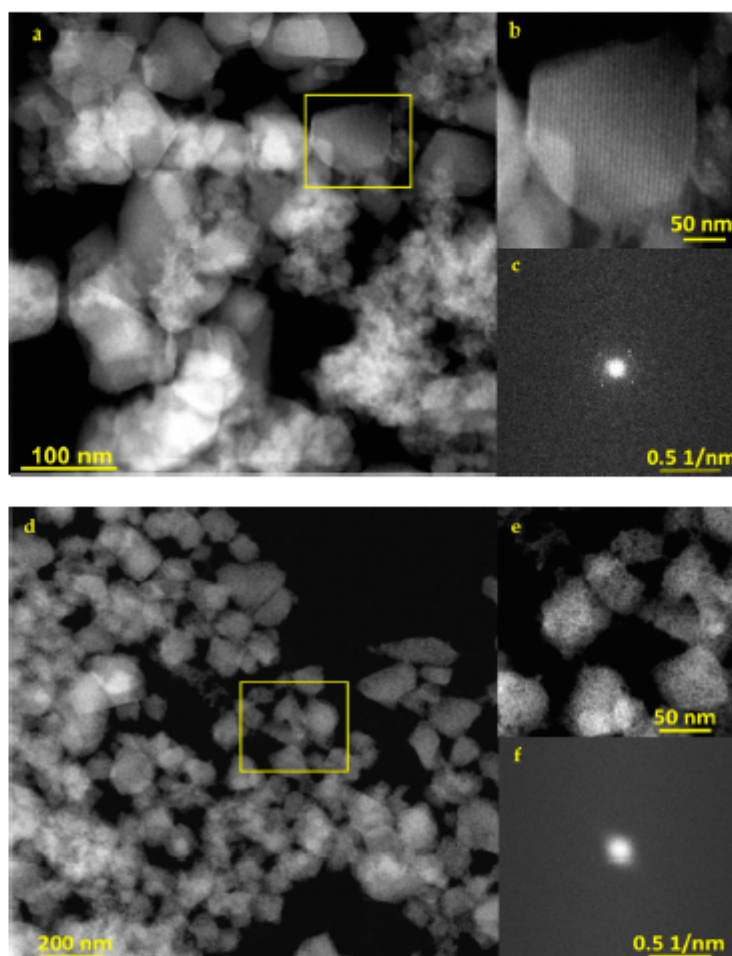


Figure 2. (a,b) STEM-HAADF images of degraded MIL-100(Fe) nanoMOFs in PBS (pH = 5.4) (d,e) in PBS (pH = 7.4) (c,f) FFT patterns of MIL-100(Fe) nanoMOFs in PBS pH = 5.4 and pH = 7.4, respectively.

More than 100 nanoMOF images were analyzed to measure the distance between their crystalline planes before any degradation, and the average value was found  $4.1 \pm 0.3$  nm (Figure S5a). When degraded at pH 5.4, the distance remained exactly the same ( $4.1 \pm 0.3$  nm) (Figure S5b). This value corresponds to [111] crystal planes of MIL-100(Fe), the main planes with an inter-reticular distance of 4.23 nm. Moreover, FFT patterns indicate that the nanoMOFs partially maintained their crystallinity in acidic conditions, whereas they lost it entirely in neutral ones (Figure 2c,f).

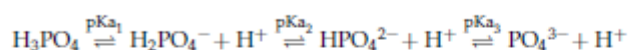
According to HPLC investigations, the nanoMOFs progressively released their constitutive ligand in neutral PBS with  $76 \pm 7$ ,  $95 \pm 8$ , and  $100 \pm 3$  wt% after 1.5, 6, and 48 h, respectively, whereas in acidic conditions (pH = 5.4), the degradation kinetics was much slower and partial with  $23 \pm 1$ ,  $30 \pm 1$  and  $38 \pm 1$  wt% loss at the same time points. Despite the erosion, the nanoMOFs' mean diameters were only slightly modified,  $140 \pm 37$  nm (intact) vs.  $130 \pm 11$  nm and  $125 \pm 11$  nm, upon 48 h degradation in PBS 5.4 and 7.4, respectively, as measured by STEM-HAADF. This moderate decrease in size is in agreement with previous reported data [10]. In contrast to STEM-HAADF, size measurements by DLS

were not possible in reason of the nanoMOF aggregation, especially in PBS and whatever the pH.

In the case of microMOFs, optical microscopy was employed to study MOF size and morphology upon degradation. After incubation in PBS pH = 7.4, the microMOFs progressively changed their color. Specifically, in the case of microMOFs (–), it was previously reported the formation of an amorphous inorganic shell and an intact crystalline core, with no size and morphological changes [10]. Interestingly, microMOFs (+) also lost their initial color (from orange to transparent), but contrary to the microMOFs (–), color faded homogeneously in the whole structure (Figure S6). These changes could be related to evolutions of both MOFs' composition and crystallinity upon degradation, the microMOFs (–), due to their higher defect content, being less homogenous than the microMOFs (+).

First, Fourier Transform Infrared spectroscopy (FTIR) demonstrated compositional changes attributed to the phosphates groups, which coordinated with the framework during degradation process. A typical example is given in Figure S7, showing the formation of a new (large) band at around  $1050\text{ cm}^{-1}$ , related to phosphate groups in the composition of the microMOFs upon their degradation in PBS. More specifically, this band corresponds to the asymmetrical P-O stretching [43,44]. Indeed, the degradation process follows a substitution mechanism. Firstly, the phosphates from the degradation media replace the bound water molecules, then they displace the organic linkers of the network which are released out.

Secondly, PXRD studies enabled to follow the evolution of the crystallinity of the particles upon degradation in PBS pH = 5.4 and pH = 7.4. After two days incubation in neutral PBS, nanoMOFs' peaks disappeared entirely, leading to an amorphous material. Interestingly, in the more acidic medium the nanoMOFs kept a significant part of their crystallinity. The same studies were performed for microMOFs particles at different time points (from one to eight days) (Figure S8). It was found that after eight days of incubation in PBS (5.4 and 7.4) the characteristic Bragg peaks of microMOFs (+) disappeared, due to their degradation. The main ions that participate in the MOF erosion process are the phosphate ions, due to their highest tendency to form complexes with the iron sites of the framework. PBS is a buffer containing orthophosphoric acid ( $\text{H}_3\text{PO}_4$ ), which exhibits three dissociation reactions.



In PBS at pH = 7.4,  $\text{H}_2\text{PO}_4^-$  and  $\text{HPO}_4^{2-}$  species are in equilibrium at similar concentrations (5 mM). On the contrary, in the range of pH = 4–6,  $\text{H}_2\text{PO}_4^-$  anions are the predominant species compared to  $\text{HPO}_4^{2-}$  (99:1 at pH 5.4). In both cases, phosphate ions diffuse into the MOFs and coordinate with the iron sites. It can therefore be hypothesized that the relative stability of the MOFs in acidic environment could be attributed to a predominant effect of  $\text{H}_2\text{PO}_4^-$  anions as compared to  $\text{HPO}_4^{2-}$  ones. Yet, the stability of the framework also depends on the iron metal sites of the structure. The Pourbaix diagram of Fe in water shows that in neutral environment, the metal is less stable, compared to the acidic conditions (Figure S9). In the present case, studies were carried on in PBS where the formation of iron phosphates is a predominant mechanism [10]. Therefore, the erosion process is the result of the combined effects of the phosphate ions of the PBS and the stability of Fe within the MOF framework.

In a nutshell, whatever their size and preparation method, MOFs rapidly degraded in neutral PBS with variations in their optical properties, crystallinity, particle size, and composition. However, PXRD and IR spectroscopy are not quantitative methods leading only to partial conclusions. Of particular interest was the apparition of core-shell structures observed upon degradation in the case of microMOFs (–) but not with microMOFs (+). To gain deeper understanding on the degradation mechanism, AFM investigations were performed *in situ* with a series of microMOFs after optimization of their deposition onto

the AFM ITO. However, liquid AFM is not adapted for nanoMOFs, which tend to detach from their support especially during degradation.

As a complement to characterization studies mentioned before, *in situ* AFM presents a particular interest, as it allowed visualizing local morphologies on the external surface of individual microcrystals, precisely calculating their dimensional changes and comparing their mechanical properties before and after degradation. It is also of great importance that these properties can be explored in real time, and not just on the final degraded product. Moreover, AFM allowed performing *in situ* changes of both composition and pH of the liquid media in contact with the MOFs, which is of man interest for the deeper understanding of their degradation mechanism. Based on these technical features, morphological, dimensional, and mechanical changes of the external surface of microMOFs (+) and microMOFs (-) were studied in water and in PBS.

### 3.3. *In Situ* AFM

#### 3.3.1. Morphology

To perform extensive *in situ* AFM studies and to be able to change the medium during the study, crystals' immobilization on ITO substrate is crucial. Firstly, particles were deposited as ethanolic dispersions, and after solvent evaporation and extensive washing, a good adhesion of the microMOFs on the substrate was observed (Figure S10). Afterwards, distilled water was added in the liquid cell and the external surface of intact particles was observed by *in situ* AFM (Figure 3). Topographic mapping of microMOFs (+) presented regular formed crystalline planes in agreement with the previous results of STEM-HAADF for nanoMOFs (Figure 2a). The same experiments were carried out for microMOFs (-). Globally, the morphology of the external surface of microMOFs (-) also consists of crystalline regions (parallel lines, Figure 3b) but with a significant number of defects (cracks). Noticeably, these features remained unchanged upon storage in the aqueous medium, proving the stability of particles in water (Figure 3a,b).

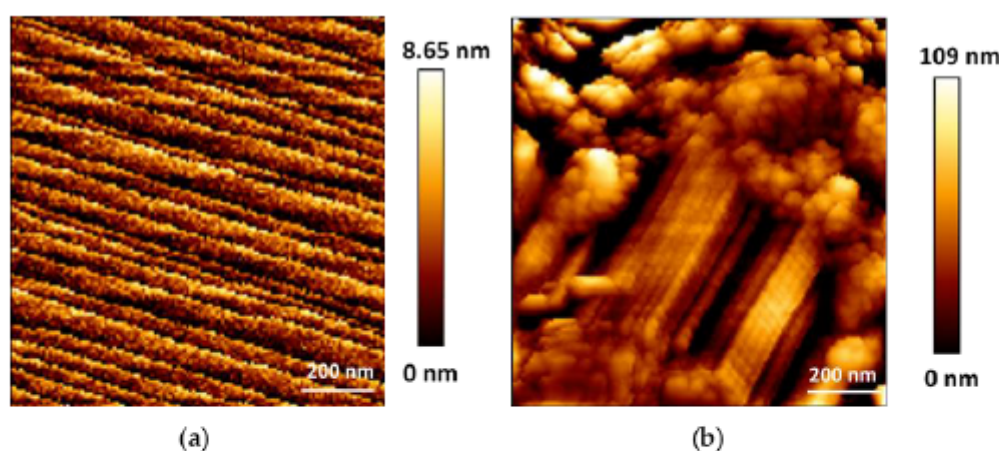


Figure 3. Topography of (a) microMOF (+) crystal and (b) a microMOF (-) crystal in water (128 pixels  $\times$  128 pixels). AFM mapping presents ordered crystalline planes typically observed for microMOFs (+) and some defects in the case of microMOFs (-).

To degrade microMOFs, water was gently removed from the liquid cell and was replaced by PBS. Firstly, *in situ* AFM unravelled the surface structure of microMOFs (+) incubated in PBS at pH 5.4. Noteworthily, the crystalline planes already observed in water (Figure 4a) remained unchanged in an acidic environment (Figure 4b). In the next step, the pH of the degrading medium was changed *in situ* from acidic to neutral. Immediately after

changing the pH to 7.4, erosion occurred, and irregular surfaces replaced the crystalline structures (Figure 4c).

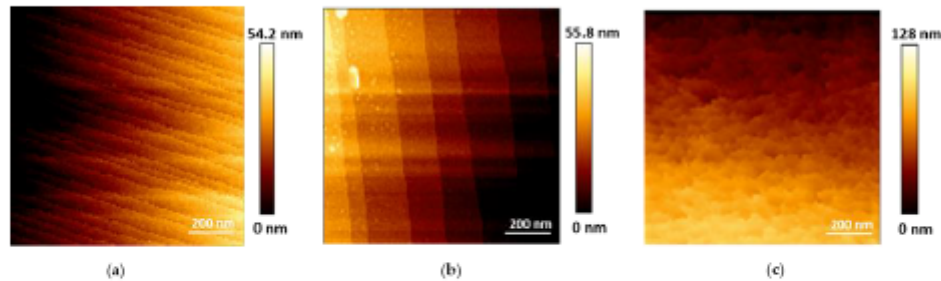


Figure 4. Topographic map of microMOFs (+) particles by *in situ* AFM (128 pixels  $\times$  128 pixels), in water (a), in PBS pH 5.4 (b) and in PBS pH 7.4 (c).

In the case of microMOFs (–), degradation started from the existing defects of around 80–170 nm on their external surface (Figure 5b, green circles). Once the medium was changed (from water to PBS pH = 7.4) and the particles were in contact with the phosphate ions, an immediate expansion of these defects was observed, revealing the degradation of the crystals (Figure 5c,d).

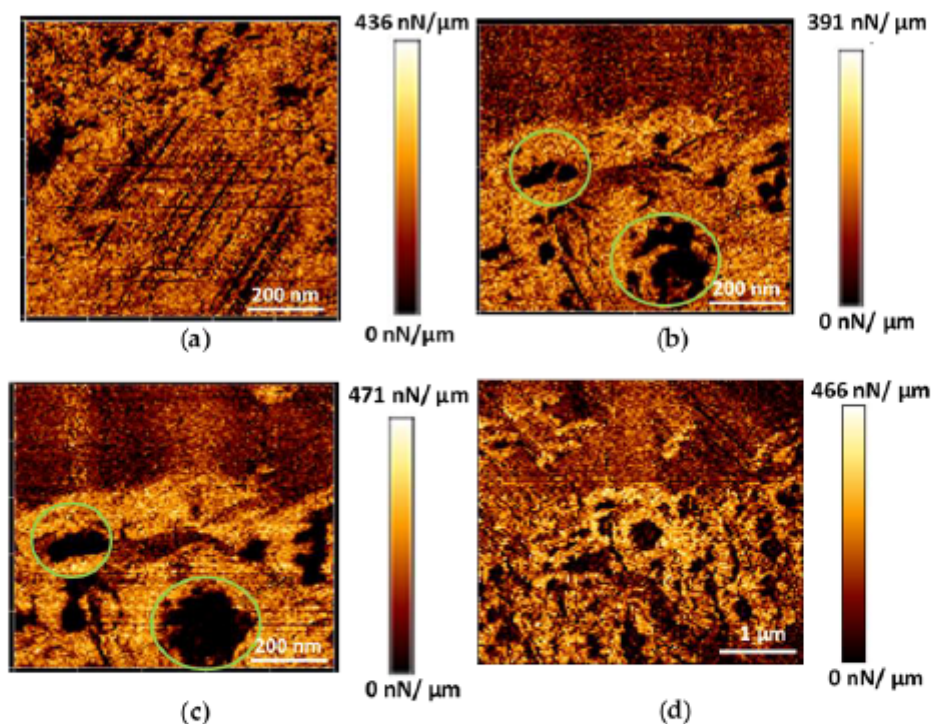


Figure 5. AFM images (stiffness map) (128 pixels  $\times$  128 pixels), of a microMOF (–) crystal in water at time 0 (a), in PBS pH = 7.4 at time 0 (b) and after 2 h at different magnifications (c,d). Defects that are progressively enlarging during degradation are surrounded with green circles.

In conclusion, microMOF (+) and (−) presented different morphologies strongly dependent on their initial defect content. The surface of microMOF (+) remained planar devoid of holes, whereas the initial defects on the external surface of microMOF (−) got larger and larger suggesting that these are the weakest regions to be degraded by phosphates from PBS, particularly at pH 7.4. Based on these findings, it was interesting to also investigate the dimensional changes of micron-sized particles upon degradation.

### 3.3.2. Height Measurements

In contrast to electron microscopy techniques that generate images of a sample surface in two dimensions, AFM can measure the vertical dimension (z-direction), enabling quantitatively accurate calculations of sample's height. To investigate dimensional changes of microMOFs upon degradation, height profiles were plotted. The typical profile is shown in Figure 6. In the case of microMOFs (−) (Figure 6a), regions were selected to include both crystalline regions and defects on the crystal. Surprisingly, the changes in height after 2 h of incubation in PBS at pH = 7.4, were less than 0.1% of the initial crystal size, indicating no dimensional changes. This result is in agreement with previous studies undertaken by Raman microscopy-spectroscopy showing no dimensional changes of microMOF (−) upon degradation in PBS at pH 7.4 [10]. This behaviour could be possibly attributed to the formation of a passivation layer. Following the height measurements for microMOFs (+), it was interesting to calculate the observed well defined crystal planes, in the presence of acidic PBS. The average value of plane distance was calculated and found at  $4.5 \pm 0.3$  nm. Remarkably, these values are in strong correlation with the results by STEM-HAADF for nanoMOFs, corresponding to the [111] crystal planes of MIL-100(Fe) of 4.23 nm.

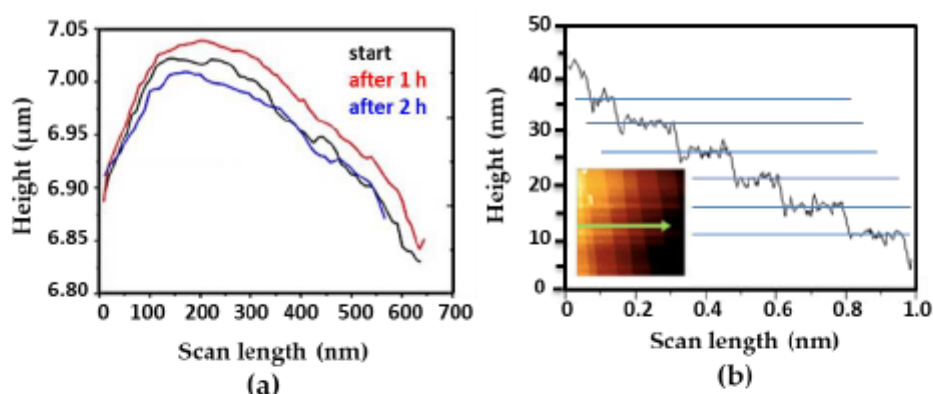


Figure 6. Typical height profiles of (a) a microMOF (−) crystal upon incubation in PBS pH = 7.4 up to 2 h and (b) a microMOF (+) crystal upon incubation in PBS pH = 5.4.

As previously mentioned, the crystalline planes of microMOF (+) disappear in PBS pH 7.4, leaving a rough irregular surface where height variations are difficult to be defined. In some rare cases, the formation of holes was observed (Figure S11). The height of the degraded region represented in this figure was calculated following the blue line. Interestingly, crystalline planes appeared at the edge of the observed hole at pH 5.4, whereas these were no longer observable on the surface of the crystal at pH = 7.4. However, the regularity in the spacing of these “steps” was lost: the differences in height from one plane to another are in most cases well over  $4.5 \pm 0.3$  nm. The different heights of these “steps” are approximate multiples of this interplanar distance obtained at pH = 5.4.

In conclusion, in the case of crystalline microMOFs (−) with initial defects on their surface, as it was demonstrated above, particles did not present any significant dimensional change even after 2 h of degradation in PBS. In the case of well-crystallized microMOFs

(+), the distances between the crystalline planes could be measured and remained constant upon incubation in acidic pH, where the crystals remained stable.

Although the crystal dimensions did not change, the progressive substitution of the organic ligand by phosphate ions led to a degraded product with different properties. In addition, we will show now that *in situ* AFM is a helpful tool to study the changes in the mechanical properties of microMOFs for both the degraded and non degraded regions of crystals, as well as their behavior after *in situ* change of the pH.

### 3.3.3. Mechanical Properties

The mechanical properties were measured for intact and degraded microMOFs. Figure 7 represents these changes in water (a) and in PBS at pH 7.4 (b) upon incubation for 2 h. The mechanical properties did not change upon storage in water (Figure 7a), which is in line with the previous results (Figure 1 and Figure S5a) showing that the morphology was unaltered in water and that there was practically no ligand release. On the contrary, in PBS, in the presence of phosphates, degradation occurred, and the slope profile dramatically changed. More precisely, the degraded regions of the particles presented a significant decrease (a factor of 4.4) in terms of surface's stiffness compared to the initially crystalline regions (Figure 7b). This indicates that the particles became more fragile upon contact with PBS. As expected, the stiffness of the natal default was low (green circles on Figure 7b), as a result of holes forming and growing.

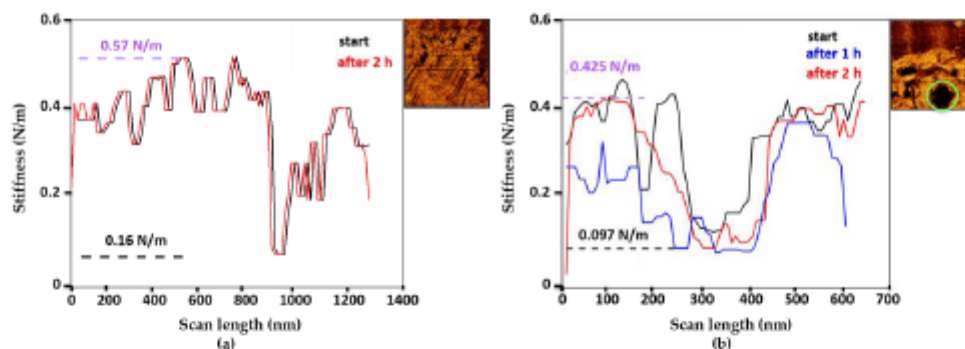


Figure 7. Stiffness profiles of a microMOF (–) particle upon incubation for 2 h in water (a) and in (b) PBS.

In the case of microMOFs (+), topographic images (Figure 4) showed regular crystalline planes in acidic conditions, which were no more visible in neutral ones (after *in situ* modification of the pH). Before studying the mechanical properties of the particles at different pH conditions, the properties of two crystals incubated in acidic PBS were measured. Thus, modifications of surface properties upon *in situ* change of the pH can be valid for the integrity of the sample. To perform this comparison, mechanical properties for different regions of each crystal were also measured.

Firstly, five different regions of the same particle were chosen. The stiffness average was around 0.575 N/m, with a standard deviation of 0.075 N/m, indicating that the measured stiffness is similar regardless of the region of the crystal analyzed (Figure 8a). Two more regions of a second crystal gave the same result in terms of stiffness (Figure 8b). It can therefore be concluded that each individual crystal has a similar measured stiffness and that the whole sample has, in average, the same characteristics in terms of measured stiffness. As a result, in PBS at pH 5.4, each crystal has comparable rigidity values over its entire surface and each crystal is similar to the rest of the sample from which it is derived. It is possible at any time to analyze a given region of a given crystal to study its rigidity to obtain significant results for the whole sample.

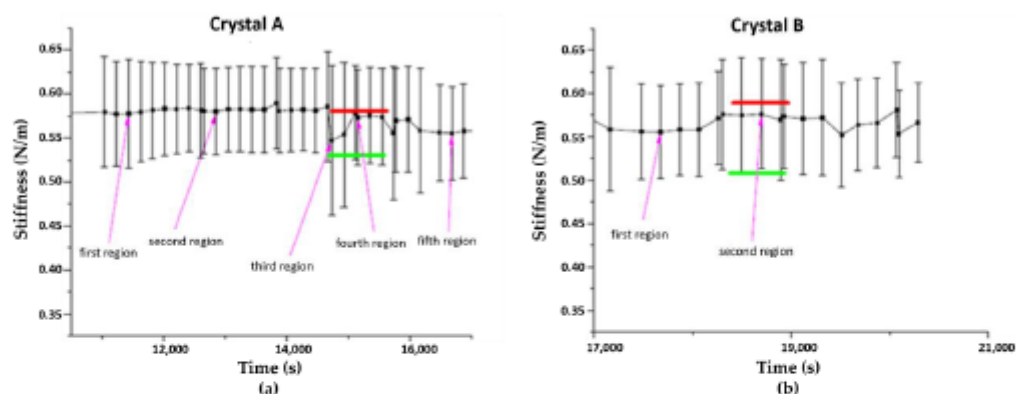


Figure 8. Comparison of the measured stiffnesses of different regions randomly chosen on two crystals named A (a) and B (b), in PBS at pH = 5.4. Results were averaged over regions of  $1 \mu\text{m}^2$ .

Therefore, we analyzed the surface stiffness of a crystal following an *in situ* pH change from 5.4 to 7.4. Immediately after the addition of a few drops of KOH, the stiffness values dropped rapidly (Figure 9) from 0.325 N/m (with a standard deviation of 0.05 N/m) at pH 5.4 to 0.20 N/m (with a standard deviation of 0.05 N/m) at pH 7.4. These results are in agreement with the loss of the crystalline planes and the formation of a degraded product.

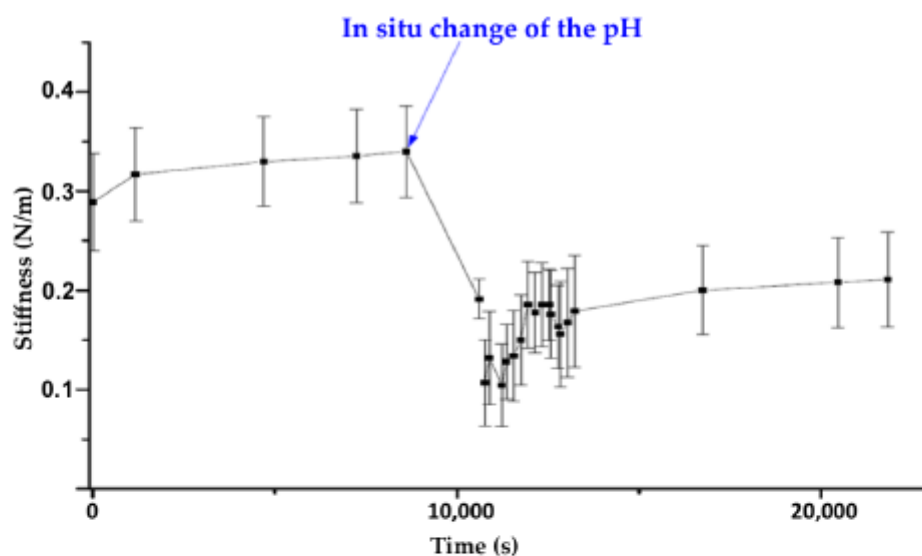


Figure 9. Stiffness profile of the evolution of the measured stiffness of a microMOF (+) particle following the addition of KOH.

#### 4. Conclusions

Depending on their synthetic methods, MOFs present different BET surface areas and degrees of crystallinity. AFM studies showed that the surface of large crystals has well-defined crystalline planes and might possess small crystal defects where degradation preferentially occurs, propagating then through the MOF material. The MOFs eroded mostly at neutral pH and not under acidic conditions. Noticeably, the MOF samples maintained their 3D structure without collapsing nor presenting dimensional changes,



possibly because of the formation of a passivation layer. In the case of well-crystallized MOFs, degradation occurred homogeneously over the entire surface of the material with the disappearance of the crystalline planes at the surface. Degradation occurred homogeneously also in nanoMOFs, which showed homogeneous compositions and morphologies over time. Initially very well crystallized, the nanoMOFs degraded without noticeable size modification. This study highlights the fast response of MOF materials to changes in the composition of the aqueous media they are in contact with. In contrast to microMOFs, nanoMOFs develop much larger surface areas where interactions take place. NanoMOFs are essentially developed for intravenous administration, also for pulmonary, ocular, or transdermal applications, whereas microMOFs could find applications as implants or for oral delivery of drugs. In all cases, the understanding of the changes in composition and mechanical properties is important. AFM studies showed that MOFs become very fragile upon degradation, but remarkably, without losing their initial shape. The MOF methodology presented here can open perspectives to study MOF degradation in more complex media, i.e., in the presence of proteins or serum. The results presented here are of utmost importance for a deeper understanding of the fate of MIL-100(Fe) MOFs administered *in vivo* where they experience rapid changes both in the pH and the composition of their surrounding media.

**Supplementary Materials:** The following are available online at <https://www.mdpi.com/2079-4991/11/3/722/s1>, Figure S1: Apparatus of AFM, Figure S2: Optical images of intact microMOFs (+). Figure S3: PXRD patterns ( $\lambda_{Cu} = 1.5406\text{\AA}$ ) of intact nanoMOFs and microMOFs (+) and their simulated pattern. Figure S4:  $N_2$  adsorption isotherms of intact nanoMOFs (blue) and of microMOFs (-)(red) at 77 K ( $P_0 = 1\text{ atm}$ ), Figure S5: Crystalline ordered planes of a) intact microMOFs (+) particles and b) upon incubation in acidic PBS by STEM-HAADF microscopy, Figure S6: Optical images of synthesized microMOFs (+) before (a) and after (b) degradation in neutral PBS for 1 month, Figure S7: FTIR spectra of microMOFs (+) upon incubation in PBS 10 mM pH = 5.4 and pH = 7.4. Figure S8: PXRD patterns of degraded nanoMOFs and microMOFs (+), Figure S9: Pourbaix diagram of iron. Figure S10: MOF crystal structure and cantilever-tip assembly visualized by inverted optical microscopy. Figure S11: Topographic image of a microMOF (+) degraded particle in PBS 7.4 and its plotted height profile as a function of sample's distance representing the loss of crystalline planes.

**Author Contributions:** The author(s) have made the following declarations about their contributions: Conceived and designed the experiments: R.G., I.C., and C.M.; performed the experiments: I.C., T.B., X.L., G.P., and C.M.; performed data analysis: I.C., T.B., X.L., G.P., C.S., C.M., and R.G.; wrote the paper: I.C. and R.G. All authors have read and agreed to the published version of the manuscript.

**Funding:** This research was funded by the Paris Ile-de-France Region–DIM Respire, grant number 'LS 167151'.

**Acknowledgments:** We are grateful to Samy Lahouel (Keyence) for help with optical microscopy investigations and to Antoine Tissot (IMAP, UMR 8004, ENS, ESPCI Paris, PSL university) for help with the preparation of microMOFs (+) samples. IC thanks the Paris Ile-de-France Region–DIM Respire for a PhD fellowship. This work was supported by a public grant overseen by the French National Research Agency (ANR) as part of the "Investissements d'Avenir" program (Labex NanoSaclay, reference: ANR-10-LABX-0035).

**Conflicts of Interest:** The authors declare no conflict of interest.

## References

1. Yang, J.; Yang, Y.W. Metal-Organic Frameworks for Biomedical Applications. *Small* **2020**, *16*, e1906846. [CrossRef] [PubMed]
2. Sun, Y.; Zheng, L.; Yang, Y.; Qian, X.; Fu, T.; Li, X.; Yang, Z.; Yan, H.; Cui, C.; Tan, W. Metal-Organic Framework Nanocarriers for Drug Delivery in Biomedical Applications. *Nano Micro Lett.* **2020**, *12*, 1–29. [CrossRef]
3. Horcajada, P.; Gref, R.; Baati, T.; Allan, P.K.; Maurin, G.; Couvreur, P.; Férey, G.; Morris, R.E.; Serre, C. Metal–Organic Frameworks in Biomedicine. *Chem. Rev.* **2012**, *112*, 1232–1268. [CrossRef] [PubMed]
4. Quijia, C.R.; Lima, C.; Silva, C.; Alves, R.C.; Frém, R.; Chorilli, M. Application of MIL-100 (Fe) in Drug Delivery and Biomedicine. *J. Drug Deliv. Sci. Technol.* **2020**, *100*, 102217. [CrossRef]
5. Abánades Lázaro, I.; Forgan, R.S. Application of Zirconium MOFs in Drug Delivery and Biomedicine. *Coord. Chem. Rev.* **2019**, *380*, 230–259. [CrossRef]

6. Qiu, J.; Li, X.; Gref, R.; Vargas-Berenguel, A. Carbohydrates in metal organic frameworks: Supramolecular assembly and surface modification for biomedical applications. In *Metal-Organic Frameworks for Biomedical Applications*, 1st ed.; Woodhead Publishing: Sawston, UK, 2020; ISBN 978-01-2816-985-8.
7. Simon-Yarza, T.; Mielcarek, A.; Couvreur, P.; Serre, C. Nanoparticles of Metal-Organic Frameworks: On the Road to In Vivo Efficacy in Biomedicine. *Adv. Mater.* **2018**, *30*, e1707365. [[CrossRef](#)]
8. Christodoulou, I.; Serre, C.; Gref, R. Metal-organic frameworks for drug delivery: Degradation mechanism and in vivo fate. In *Metal-Organic Frameworks for Biomedical Applications*, 1st ed.; Woodhead Publishing: Sawston, UK, 2020; ISBN 978-01-2816-985-8.
9. Velásquez-Hernández, M.D.J.; Ricco, R.; Carraro, F.; Limpoco, F.T.; Linares-Moreau, M.; Leitner, E.; Wiltse, H.; Rattenberger, J.; Schrötnner, H.; Frühwirth, P.; et al. Degradation of ZIF-8 in Phosphate Buffered Saline Media. *CrystEngComm* **2019**, *21*, 4538–4544. [[CrossRef](#)]
10. Li, X.; Lachmanski, L.; Safi, S.; Sene, S.; Serre, C.; Grenèche, J.M.; Zhang, J.; Gref, R. New Insights into the Degradation Mechanism of Metal-Organic Frameworks Drug Carriers. *Sci. Rep.* **2017**, *7*, 1–11. [[CrossRef](#)] [[PubMed](#)]
11. Sun, C.Y.; Qin, C.; Wang, X.L. Zeolitic imidazolate framework-8 as efficient pH-sensitive drug delivery vehicle. *Dalton Trans.* **2012**, *41*, 6906–6909. [[CrossRef](#)]
12. Horcajada, P.; Chalati, T.; Serre, C.; Gillet, B.; Sebrie, C.; Baati, T.; Eubank, J.F.; Heurtaux, D.; Clayette, P.; Kreuz, C.; et al. Porous Metal-Organic-Framework Nanoscale Carriers as a Potential Platform for Drug Delivery and Imaging. *Nat. Mater.* **2010**, *9*, 172–178. [[CrossRef](#)] [[PubMed](#)]
13. Wuttke, S.; Zimpel, A.; Bein, T.; Braig, S.; Stoiber, K.; Vollmar, A.; Müller, D.; Haastert-Talini, K.; Schaeske, J.; Stiesch, M.; et al. Validating Metal-Organic Framework Nanoparticles for Their Nanosafety in Diverse Biomedical Applications. *Adv. Healthc. Mater.* **2017**, *6*, 1600818. [[CrossRef](#)]
14. Grall, R.; Hidalgo, T.; Delic, J.; Garcia-Marquez, A.; Chevillard, S.; Horcajada, P. In vitro biocompatibility of mesoporous metal (III; Fe, Al, Cr) trimesate MOF nanocarriers. *J. Mater. Chem. B* **2015**, *3*, 8279–8292. [[CrossRef](#)] [[PubMed](#)]
15. Li, X.; Semiramo, N.; Hall, S.; Tafani, V.; Josse, J.; Laurent, F.; Salzano, G.; Foulkes, D.; Brodin, P.; Majlessi, L.; et al. Compartmentalized Encapsulation of Two Antibiotics in Porous Nanoparticles: An Efficient Strategy to Treat Intracellular Infections. *Part. Part. Syst. Charact.* **2019**, *36*, 1800360. [[CrossRef](#)]
16. García Márquez, A.; Demessence, A.; Platero-Prats, A.E.; Heurtaux, D.; Horcajada, P.; Serre, C.; Chang, J.S.; Férey, G.; De La Peña-O'Shea, V.A.; Boissière, C.; et al. Green Microwave Synthesis of MIL-100(Al, Cr, Fe) Nanoparticles for Thin-Film Elaboration. *Eur. J. Inorg. Chem.* **2012**, *100*, 5165–5174. [[CrossRef](#)]
17. Agostoni, V.; Horcajada, P.; Rodríguez-Ruiz, V.; Willaime, H.; Couvreur, P.; Serre, C.; Gref, R. 'Green' Fluorine-Free Mesoporous Iron(III) Trimesate Nanoparticles for Drug Delivery. *Green Mater.* **2013**, *1*, 209–217. [[CrossRef](#)]
18. Giménez-Marqués, M.; Bellido, E.; Berthelot, T.; Simón-Yarza, T.; Hidalgo, T.; Simón-Vázquez, R.; González-Fernández, Á.; Avila, J.; Asensio, M.C.; Gref, R.; et al. GraftFast Surface Engineering to Improve MOF Nanoparticles Furtiveness. *Small* **2018**, *14*, 1801900. [[CrossRef](#)] [[PubMed](#)]
19. Wuttke, S.; Braig, S.; Preiß, T.; Zimpel, A.; Sicklinger, J.; Bellomo, C.; Rädler, J.O.; Vollmar, A.M.; Bein, T. MOF Nanoparticles Coated by Lipid Bilayers and Their Uptake by Cancer Cells. *Chem. Commun.* **2015**, *51*, 15752–15755. [[CrossRef](#)] [[PubMed](#)]
20. Bellido, E.; Hidalgo, T.; Lozano, M.V.; Guillevic, M.; Simón-Vázquez, R.; Santander-Ortega, M.J.; González-Fernández, Á.; Serre, C.; Alonso, M.J.; Horcajada, P. Heparin-Engineered Mesoporous Iron Metal-Organic Framework Nanoparticles: Toward Stealth Drug Nanocarriers. *Adv. Healthc. Mater.* **2015**, *4*, 1246–1257. [[CrossRef](#)] [[PubMed](#)]
21. Tamames-Tabar, C.; Cunha, D.; Imbuluzqueta, E.; Ragon, F.; Serre, C.; Blanco-Prieto, M.J.; Horcajada, P. Cytotoxicity of Nanoscaled Metal-Organic Frameworks. *J. Mater. Chem. B* **2014**, *2*, 262–271. [[CrossRef](#)] [[PubMed](#)]
22. Ruyra, A.; Yazdi, A.; Espin, J.; Carné-Sánchez, A.; Roher, N.; Lorenzo, J.; Imaz, I.; Maspoch, D. Synthesis, Culture Medium Stability, and in Vitro and in Vivo Zebrafish Embryo Toxicity of Metal-Organic Framework Nanoparticles. *Chem. Eur. J.* **2015**, *21*, 2508–2518. [[CrossRef](#)]
23. Anand, R.; Borghi, F.; Manoli, F.; Manet, I.; Agostoni, V.; Reschiglian, P.; Gref, R.; Monti, S. Host-Guest Interactions in Fe(III)-Trimesate MOF Nanoparticles Loaded with Doxorubicin. *J. Phys. Chem. B* **2014**, *118*, 8532–8539. [[CrossRef](#)]
24. Simon-Yarza, T.; Giménez-Marqués, M.; Mrimi, R.; Mielcarek, A.; Gref, R.; Horcajada, P.; Serre, C.; Couvreur, P. A Smart Metal-Organic Framework Nanomaterial for Lung Targeting. *Angew. Chem. Int. Ed.* **2017**, *56*, 15565–15569. [[CrossRef](#)] [[PubMed](#)]
25. Simon-Yarza, M.T.; Baati, T.; Paci, A.; Lesueur, L.L.; Seck, A.; Chipier, M.; Gref, R.; Serre, C.; Couvreur, P.; Horcajada, P. Antineoplastic Busulfan Encapsulated in a Metal Organic Framework Nanocarrier: First in Vivo Results. *J. Mater. Chem. B* **2016**, *4*, 585–588. [[CrossRef](#)] [[PubMed](#)]
26. Horcajada, P.; Serre, C.; Maurin, G.; Ramsahye, N.A.; Balas, F.; Vallet-Regi, M.; Sebban, M.; Taulelle, F.; Férey, G. Flexible porous metal-organic frameworks for a controlled drug delivery. *J. Am. Chem. Soc.* **2008**, *130*, 6774–6780. [[CrossRef](#)] [[PubMed](#)]
27. Agostoni, V.; Chalati, T.; Horcajada, P.; Willaime, H.; Anand, R.; Semiramo, N.; Baati, T.; Hall, S.; Maurin, G.; Chacun, H.; et al. Towards an Improved Anti-HIV Activity of NRTI via Metal-Organic Frameworks Nanoparticles. *Adv. Healthc. Mater.* **2013**, *2*, 1630–1637. [[CrossRef](#)]
28. Taherzade, S.D.; Rojas, S.; Soleimannejad, J.; Horcajada, P. Combined Cutaneous Therapy Using Biocompatible Metal-Organic Frameworks. *Nanomaterials* **2020**, *10*, 2296. [[CrossRef](#)] [[PubMed](#)]
29. Bellido, E.; Guillevic, M.; Hidalgo, T.; Santander-Ortega, M.J.; Serre, C.; Horcajada, P. Understanding the Colloidal Stability of the Mesoporous MIL-100 (Fe) Nanoparticles in Physiological Media. *Langmuir* **2014**, *30*, 5911–5920. [[CrossRef](#)] [[PubMed](#)]

30. Hidalgo, T.; Giménez-Marqués, M.; Bellido, E.; Avila, J.; Asensio, M.C.; Salles, E.; Lozano, M.V.; Guillevic, M.; Simón-Vázquez, R.; González-Fernández, A.; et al. Chitosan-Coated Mesoporous MIL-100 (Fe) Nanoparticles as Improved Bio-Compatible Oral Nanocarriers. *Sci. Rep.* **2017**, *7*, srep43099. [[CrossRef](#)]
31. Agostoni, V.; Anand, R.; Monti, S.; Hall, S.; Maurin, G.; Horcajada, P.; Serre, C.; Bouchemal, K.; Gref, R. Impact of Phosphorylation on the Encapsulation of Nucleoside Analogues within Porous Iron (III) Metal-Organic Framework MIL-100 (Fe) Nanoparticles. *J. Mater. Chem. B* **2013**, *1*, 4231–4242. [[CrossRef](#)]
32. Prins, J. *Cell Biology: A Laboratory Handbook*, 2nd ed.; Academic Press: Cambridge, MA, USA, 1998.
33. Gupta, M.N. *Methods for Affinity-Based Separations of Enzymes and Proteins*; Springer: Basel, Switzerland, 2002; ISBN 978-3-0348-8127-2.
34. Moh, P.Y.; Cubillas, P.; Anderson, M.W.; Attfield, M.P. Revelation of the Molecular Assembly of the Nanoporous Metal Organic Framework ZIF-8. *J. Am. Chem. Soc.* **2011**, *133*, 13304–13307. [[CrossRef](#)]
35. Morris, R.E. How Does Your MOF Grow? *ChemPhysChem* **2009**, *10*, 327–329. [[CrossRef](#)] [[PubMed](#)]
36. Wagia, R.; Strashnov, I.; Anderson, M.W.; Attfield, M.P. Determination of the Preassembled Nucleating Units That Are Critical for the Crystal Growth of the Metal-Organic Framework CdIF-4. *Angew. Chem.* **2016**, *128*, 9221–9225. [[CrossRef](#)]
37. Moh, P.Y.; Brenda, M.; Anderson, M.W.; Attfield, M.P. Crystallisation of Solvothermally Synthesised ZIF-8 Investigated at the Bulk, Single Crystal and Surface Level. *Cryst EngComm* **2013**, *15*, 9672–9678. [[CrossRef](#)]
38. Shoaee, M.; Anderson, M.W.; Attfield, M.P. Crystal Growth of the Nanoporous Metal-Organic Framework HKUST-1 Revealed by *in Situ* Atomic Force Microscopy. *Angew. Chem. Int. Ed.* **2008**, *47*, 8525–8528. [[CrossRef](#)]
39. Hosono, N.; Terashima, A.; Kusaka, S.; Matsuda, R.; Kitagawa, S. Highly Responsive Nature of Porous Coordination Polymer Surfaces Imaged by *in Situ* Atomic Force Microscopy. *Nat. Chem.* **2019**, *11*, 109–116. [[CrossRef](#)] [[PubMed](#)]
40. Horcajada, P.; Surblé, S.; Serre, C.; Hong, D.Y.; Seo, Y.K.; Chang, J.S.; Grenèche, J.M.; Margiolaki, I.; Férey, G. Synthesis and Catalytic Properties of MIL-100 (Fe), an Iron (III) Carboxylate with Large Pores. *Chem. Commun.* **2007**, *100*, 2820–2822. [[CrossRef](#)] [[PubMed](#)]
41. Rojas, S.; Collinet, I.; Cunha, D.; Hidalgo, T.; Salles, E.; Serre, C.; Guillou, N.; Horcajada, P. Toward Understanding Drug Incorporation and Delivery from Biocompatible Metal-Organic Frameworks in View of Cutaneous Administration. *ACS Omega* **2018**, *3*, 2994–3003. [[CrossRef](#)]
42. Horcajada, P.; Serre, C.; Vallet-Regí, M.; Sebban, M.; Taulelle, F.; Férey, G. Metal-organic frameworks as efficient materials for drug delivery. *Angew. Chem. Int. Ed.* **2006**, *45*, 5974–5978. [[CrossRef](#)] [[PubMed](#)]
43. Barnes, D.H.; Jugdaosingh, R.; Kiamil, S. Shelf Life and Chemical Stability of Calcium Phosphate Coatings Applied to Poly Carbonate Urethane Substrates. *J. Biotechnol. Biomater.* **2011**, *1*, 2. [[CrossRef](#)]
44. Chávez, A.M.; Rey, A.; López, J.; Álvarez, P.M.; Beltrán, E.J. Critical aspects of the stability and catalytic activity of MIL-100 (Fe) in different advanced oxidation processes. *Sep. Purif. Technol.* **2020**, *255*, 117660. [[CrossRef](#)]



## Supplementary Materials

### Degradation Mechanism of Porous Metal-Organic Frameworks by In Situ Atomic Force Microscopy

Ioanna Christodoulou <sup>1,2</sup>, Tom Bourguignon <sup>1</sup>, Xue Li <sup>1</sup>, Gilles Patriarche <sup>3</sup>, Christian Serre <sup>2</sup>, Christian Marlière <sup>4</sup> and Ruxandra Gref <sup>1,\*</sup>

- <sup>1</sup> Institute of Molecular Sciences, UMR CNRS 8214, Université Paris-Saclay, 91400 Orsay, France; ioanna.christodoulou@universite-paris-saclay.fr (I.C.); tom.bourguignon@universite-paris-saclay.fr (T.B.); xue.li@universite-paris-saclay.fr (X.L.)
  - <sup>2</sup> Institut des Matériaux Poreux de Paris, UMR 8004, Ecole Normale Supérieure, ESPCI Paris, CNRS, PSL University, 75005 Paris, France; christian.serre@ens.psl.eu
  - <sup>3</sup> Center for Nanoscience and Nanotechnology, UMR 9001, CNRS, Université Paris Saclay, Palaiseau, France; gilles.patriarche@c2n.upsaclay.fr
  - <sup>4</sup> Laboratoire de Physique des Solides, UMR CNRS 8502, Université Paris Saclay, 91400 Orsay, France; christian.marliere@universite-paris-saclay.fr
- \* Correspondence: ruxandra.gref@universite-paris-saclay.fr

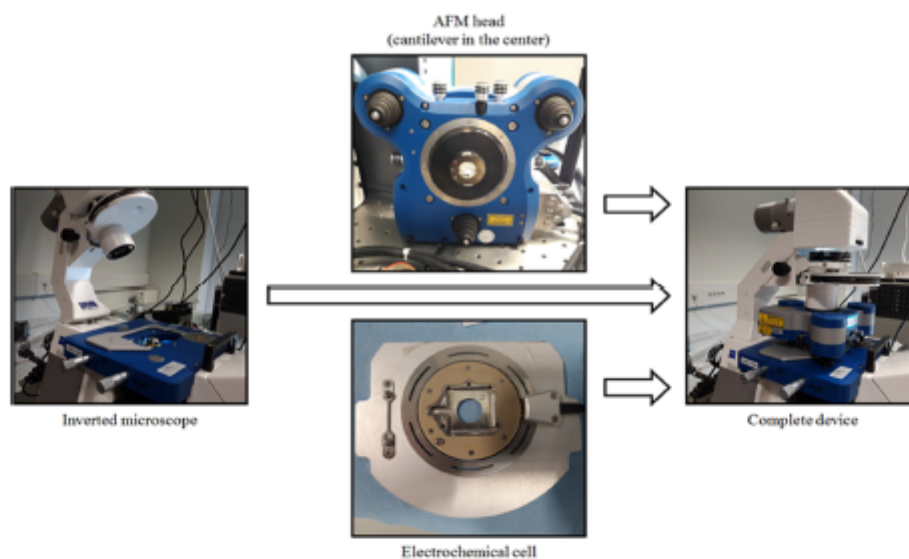


Figure S1. Apparatus used for AFM studies.

2 of 8

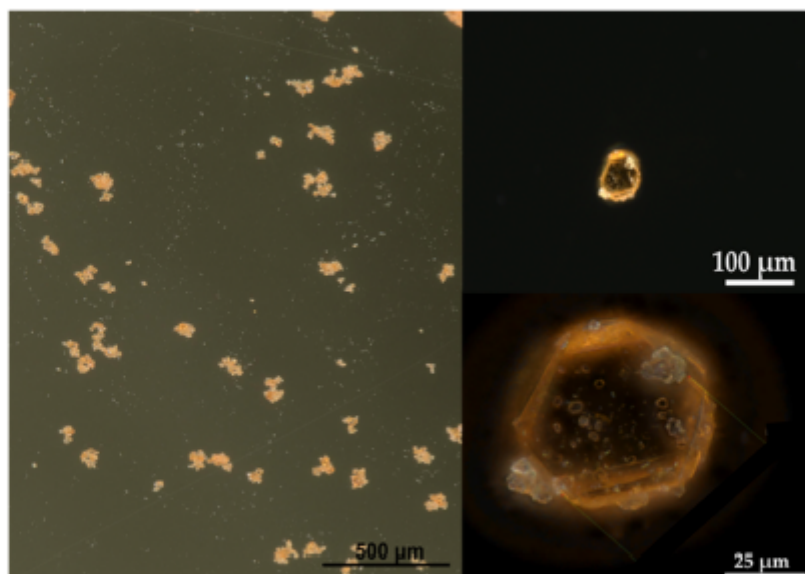


Figure S2. Optical images of intact microMOFs (+). The Fe-based particles present a typical intense orange color.

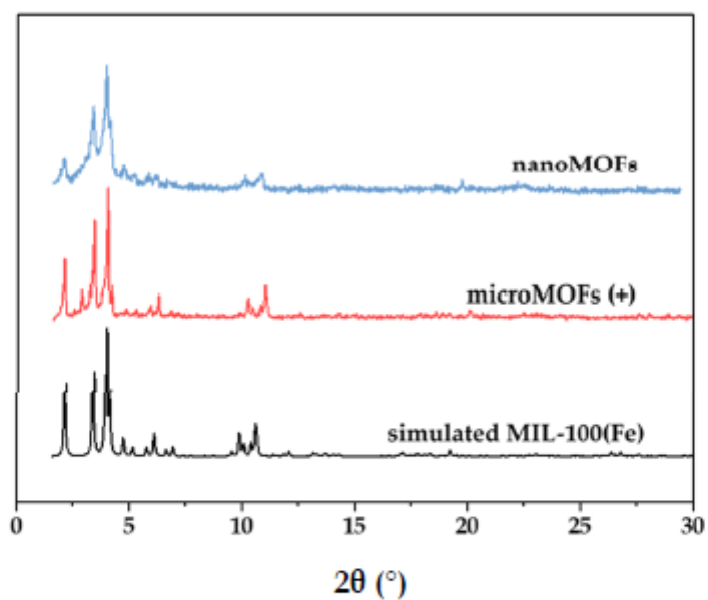


Figure S3. PXRD patterns ( $\lambda_{Cu}=1.5406\text{\AA}$ ) of intact nanoMOFs and microMOFs (+) and their simulated pattern.

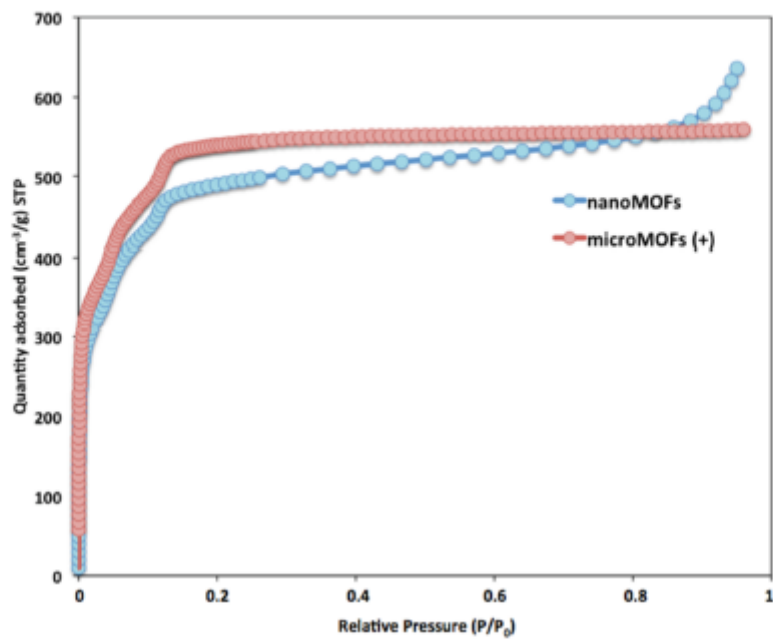
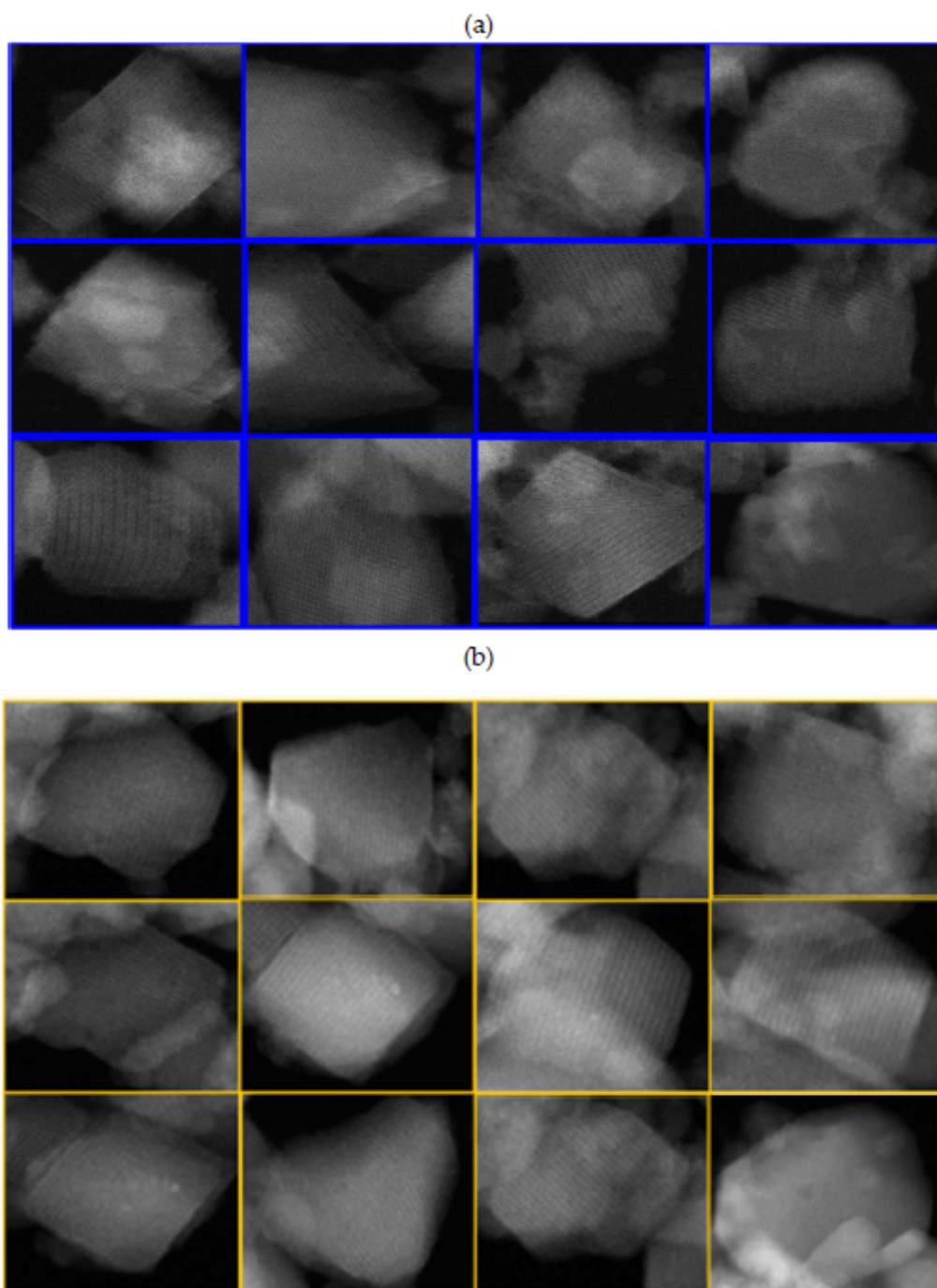


Figure S4. N<sub>2</sub> adsorption isotherms of intact nanoMOFs (blue) and of microMOFs (-) (red) at 77 K (P<sub>0</sub> = 1 atm).



**Figure S5.** STEM-HAADF of MIL-100(Fe) (a) intact and (b) after 48 hours incubation in PBS 10 mM pH = 5.4. The microscopic images present well formed crystalline planes of various nanoMOFs that remain in acidic conditions.

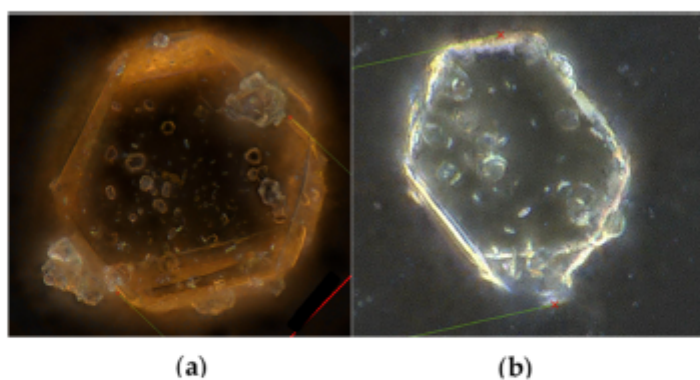


Figure S6. Optical images of synthesized microMOFs (+) before (a) and after (b) degradation under physiological conditions for 1 month.

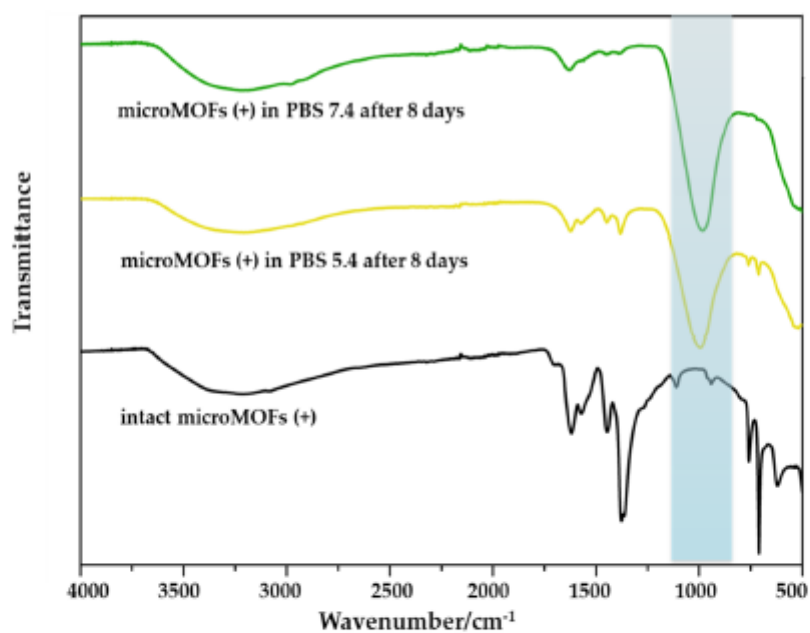
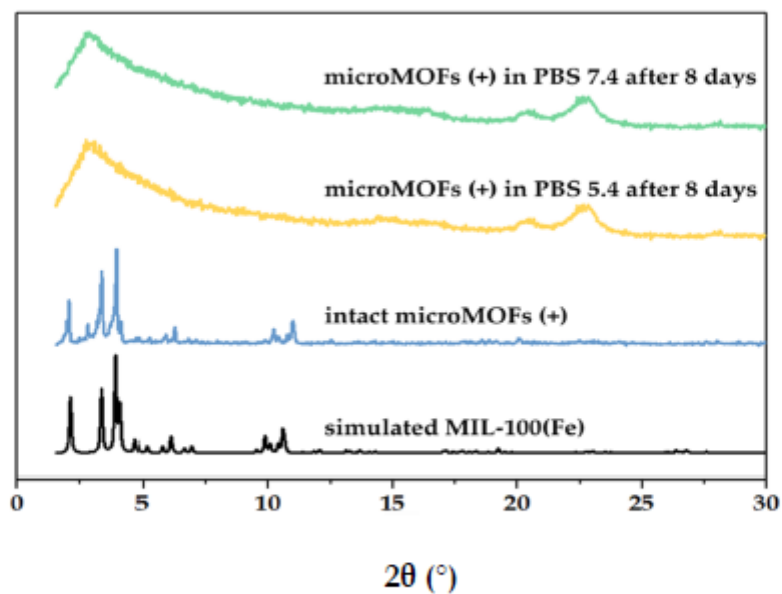
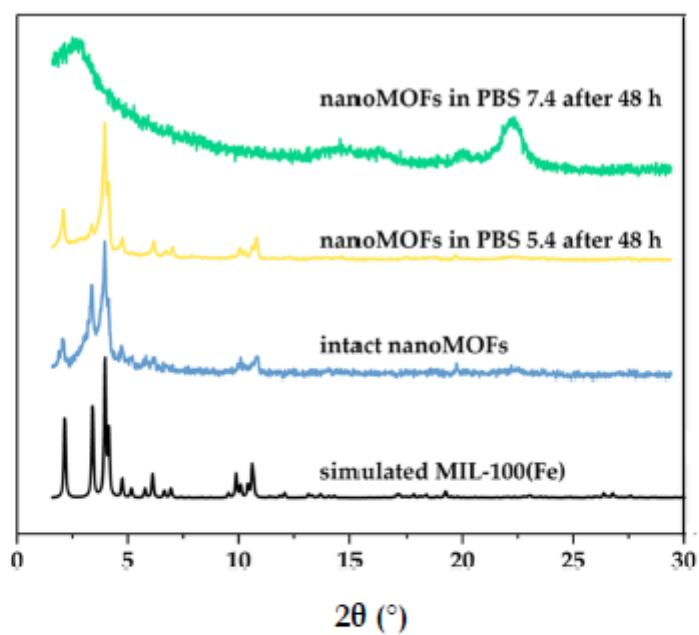


Figure S7. FTIR spectra of microMOFs (+) after 8 days incubation in PBS 10 mM pH = 5.4 (yellow) and in PBS 10 mM pH = 7.4 (green).





(a)



(b)

Figure S8. PXRD patterns of MIL-100(Fe) (a) microMOFs and (b) nanoMOFs before and after degradation in PBS pH=5.4 and 7.4.

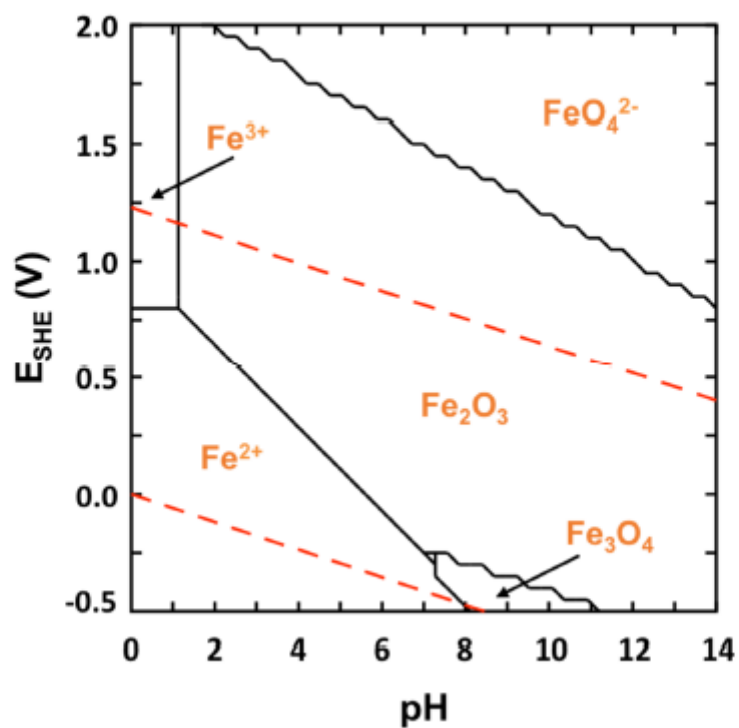


Figure S9. Pourbaix diagram of iron calculated for ionic concentrations of 1.0 mM at 25 °C, using the Hydra/Medousa software. Red dashed lines represent the redox couples  $O_2/H_2O$  and  $H_2O/H_2$ .

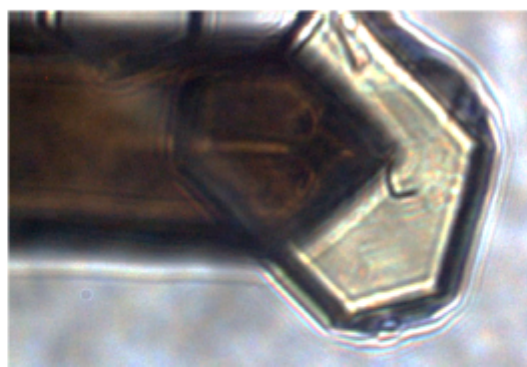


Figure S10. MOF crystal structure and cantilever-tip assembly visualized by inverted optical microscopy.

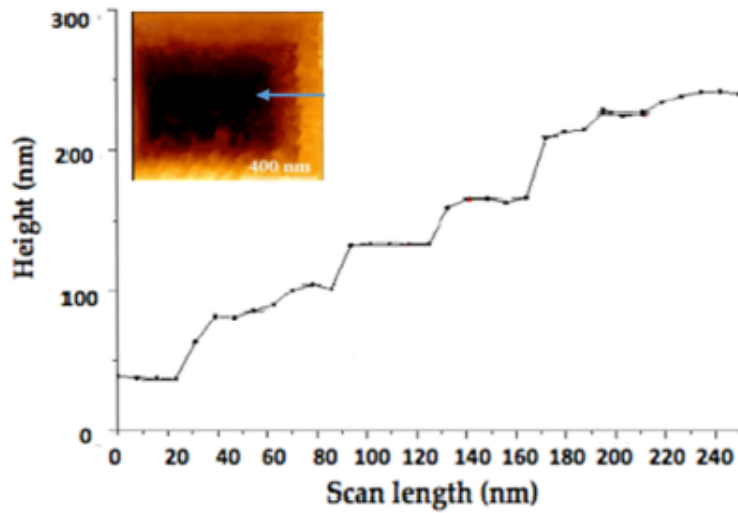


Figure S11. Topographic image of a microMOF (+) degraded particle in PBS 7.4 10 mM and its plotted height profile as a function of sample's distance representing the loss of crystalline planes.



© 2021 by the authors. Licensee MDPI, Basel, Switzerland. This article is an open access article distributed under the terms and conditions of the Creative Commons Attribution (CC BY) license (<http://creativecommons.org/licenses/by/4.0/>).



## **Chapter III**

Advanced characterization methodology to unravel MOF stability in extremely dilute conditions

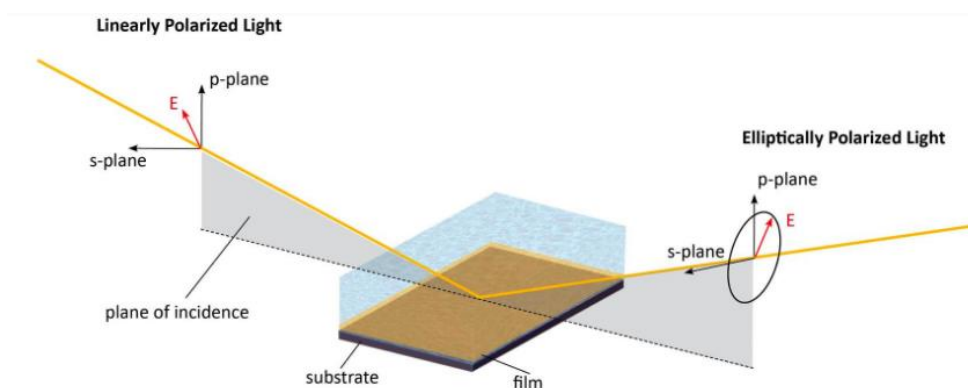
### Chapter III

Advanced characterization methodology to unravel MOF stability in extremely dilute conditions

## General objectives

Chapter 3 deals with the degradation mechanism of nanoMOFs and it is presented in the format of a research article, which will be submitted for publication in Journal of Colloids and Interface Science. This work highlights the importance of studying the degradation of nanoMOFs in extreme dilute conditions, in order to approach as much as possible the conditions of *in vivo* studies and distinguish the main parameters, which affect the MOFs' stability. Of main interest, we used an advanced methodology employing in a first approach high resolution STEM-HAADF, which allowed studying the nanoMOF crystalline features and composition, before and after degradation.

In addition, *in situ* ellipsometry was selected to study nanoMOFs degradation in extreme dilute conditions. To do so, nanoMOFs were prepared as homogeneous thin films, which were studied under flow of buffer solutions at different pH and containing or not a model protein. Changes in the optical properties of the films were continuously recorded (from the first minute to several hours) and attributed to the chemical transformation of nanoMOFs in the presence of phosphates. Complementary characterizations (PXRD, Infrared spectroscopy, HPLC) confirmed on their turn structural modifications of the nanoMOFs in agreement with ellipsometry measurements.



**Figure 3-1:** Schematic representation of *in situ* spectroscopic ellipsometry measurements. Polarized incident light (left) reflects off of the film made of dip coated nanoMOFs, embedded in a liquid and changes to elliptically polarized light (right). This technique allows the determination of the thickness and the optical properties of the film.

This work has been carried on in collaboration with Dr. C. Boissière in LCMCP and Dr. G. Patriarche in C2N.

### Chapter III

Advanced characterization methodology to unravel MOF stability in extremely dilute conditions



**Advanced characterization methodology to unravel MOF stability in extremely dilute conditions**

I. Christodoulou <sup>a,b</sup>, G. Patriarche <sup>c</sup>, C. Serre <sup>b</sup>, C. Boissière <sup>d\*</sup>, R. Gref <sup>a\*</sup>

<sup>a,b</sup> Institute of Molecular Sciences, UMR CNRS 8214, Université Paris-Sud, Université Paris-Saclay, 91400 Orsay, France ;

[ioanna.christodoulou@universite-paris-saclay.fr](mailto:ioanna.christodoulou@universite-paris-saclay.fr), [ruxandra.gref@universite-paris-saclay.fr](mailto:ruxandra.gref@universite-paris-saclay.fr)

<sup>b</sup> Institut des Matériaux Poreux de Paris, Ecole Normale Supérieure, ESPCI Paris, CNRS, PSL university, 75005 Paris, France ;

[christian.serre@espci.psl.eu](mailto:christian.serre@espci.psl.eu)

<sup>c</sup> Center for Nanoscience and Nanotechnology, C2N UMR 9001, CNRS, Université Paris Sud, Université Paris Saclay, Palaiseau, France ;

[gilles.patriarche@c2n.upsaclay.fr](mailto:gilles.patriarche@c2n.upsaclay.fr)

<sup>d</sup> Laboratoire Chimie de la Matière Condensée de Paris, UMR 7574, Sorbonne Université, 4 Place Jussieu 75005, Paris, France ;

[cedric.boissiere@sorbonne-universite.fr](mailto:cedric.boissiere@sorbonne-universite.fr)

**Abstract :** Iron carboxylates metal organic frameworks of submicronic size (nanoMOFs) attract a growing interest in the field of drug delivery in reason of their high drug payloads, excellent entrapment efficiencies and biodegradable character. However, to date only scarce studies have been dedicated to their degradation mechanism, which is key for their *in vivo* fate. Complementary methods have been used here to investigate the degradation mechanism of these nanoMOFs under neutral or acidic physiological simulated conditions, and in the presence of bovine serum albumin. High resolution STEM-HAADF coupled with EDX enabled monitoring the crystalline organization and the elemental distribution during degradation. NanoMOFs were also deposited onto silicon substrates by dip coating to form stable thin films of optical quality that were further investigated in terms of thickness and structural bands of the nanoMOFs by IR ellipsometry in order to approach the “sink conditions” of the *in vivo* studies. This approach is essential for the successful design of biocompatible nanovectors in extreme dilute conditions. It was revealed that while the presence of a protein coating layer did not impede the degradation process, the pH of the medium in contact with the nanoMOFs played a major role. The degradation of nanoMOFs occurred to the larger extent in neutral conditions, rapidly and homogeneously within the crystalline matrices and was associated with a departure of their constitutive organic ligands. Remarkably the nanoMOFs maintained their global morphology during degradation.

**Keywords :** nanoparticle, nanomedicine, degradation mechanism, metal organic frameworks, *in situ* ellipsometry

## 1. Introduction

Engineered drug nanocarriers are gaining increasing interest in the treatment of severe diseases such as cancer and resistant infections, by protecting the incorporated drugs and ferrying them to the target sites. Since the first design of a controlled-release drug delivery system, a great variety of nanoparticles have been developed and proposed as potential candidates to improve the drug bioavailability and reduce the side toxic effects [1], [2]. Among the recently developed systems, nanosized porous Metal Organic Frameworks (nanoMOFs) showed a high potential as drug carriers in reason of their important drug payloads, versatility in terms of composition and pore sizes and convenient surface functionalization [3], [4], [5]. Moreover, the biocompatible iron carboxylate nanoMOFs have caught great attention thanks to their biodegradability and lack of toxicity [6], [7].

In particular, one of the most studied materials is MIL-100(Fe) (MIL stands for Materials of the Institute Lavoisier), a mesoporous iron trimesate MOF, capable to encapsulate a variety of drugs with high payloads and yields close to 100% and also to release them often in a controlled manner [9], [10], [11], [12]. Some of the most important features of MIL-100(Fe) nanoMOFs are their biodegradability and their *in vitro* [13], [14], [15] and *in vivo* biocompatibility [6], [7]. Formed by the self-assembly of trimers of iron octahedra coordinated with trimesate ligands, they are chemically stable in aqueous and ethanolic solutions, but undergo degradation upon incubation in biological media. Once nanoMOFs are in contact with phosphate buffer saline (PBS), phosphate ions from the suspension media diffuse inside their pores and coordinate strongly with the iron metal sites, substituting the organic ligands and leading to a progressive disassembly of the crystalline MOF structure [3], [16], [17]. Recently, micron-sized MIL-100(Fe) particles were studied to gain a better understanding of their degradation mechanism [17]. Interestingly, the particles degraded in PBS without any significant size modification. It was found that degradation was initiated by the diffusion of phosphate ions from PBS into the matrix and that an inorganic shell made of iron phosphate was progressively formed around a crystalline core of MIL-100(Fe). In another study, the degradation of MIL-100(Fe) nanoMOFs was studied in PBS enriched with bovine serum albumin (BSA). BSA is the most abundant protein in the bloodstream with a molecular weight of approximately 66 kDa and dimensions of (140 x 40 x 40 Å) [18]. This bulky macromolecule could not penetrate inside the MOFs' porosity and remained adsorbed at their surface, forming a negatively charged protein corona of around 20 nm [16]. In the presence of BSA, the release of the constitutive trimesate ligands was slightly reduced, but the mechanism of degradation was not explored. More recently, it was shown that in the same PBS-BSA release medium, MIL-100(Fe) nanoMOFs decorated with Fe<sub>2</sub>O<sub>3</sub> maintained their global morphology without size changes [19].

In addition to its composition, the pH of the degrading media plays a key role in the degradation of the MIL-100(Fe) nanoMOFs. *In vivo* studies showed that they possess

unique pH-responsive properties. Once injected in the blood stream, they immediately aggregated at neutral pH and thus preferentially accumulated in the lungs where they released their drug content to eradicate the tumor [20]. Eventually, because of surface degradation, they disassembled and were thus well tolerated *in vivo*.

*In vivo* studies are crucial for the determination of the cytotoxicity and the biodistribution of the nanoMOFs in the living organism. Yet, these studies are complex as multiple phenomena occur simultaneously inside the body, hampering the deeper understanding of the degradation mechanism of the nanoMOFs. Conversely, *in vitro* conditions do not mimic the extreme dilution conditions corresponding to their injection into the blood stream. More generally, depending on the species, different amounts of nanoparticles are injected and blood volumes can differ on a large scale (for example, the volume of human blood is around 5 L, whereas in animal tests, volumes can reach around 200 mL for rats and only 5 mL for mice). Therefore, when nanoMOFs are injected in the bloodstream, they can reach undersaturated condition, which can affect their degradation kinetics.

In addition, even when performing *ex situ* characterization studies, the nanoMOF dilution conditions are different. Degradation and drug release are typically monitored with a MOFs concentration in the range of 0.5 to 1 mg mL<sup>-1</sup> [21]. Conversely, in the case of stability and degradation studies followed by Dynamic Light Scattering (DLS) measurements, the typical concentration is 0.1 mg mL<sup>-1</sup> [22]. As a result, different degradation kinetics are observed according to the experimental conditions. Moreover, when using *ex situ* techniques such as microscopies or chromatography, sample analysis at short times is complicated, as preparation of the samples (centrifugation, washings, dilutions) are commonly required before the measurements. Another constraint of *ex situ* techniques is that the studies are based on the final degraded products without exploring the possible intermediate steps.

To overcome these limitations, *in situ* ellipsometry was used here to study nanoMOF degradation in real time and in extremely dilute conditions to mimic the conditions corresponding to an intravenous administration. Ellipsometry is an optical technique based on the measurement of changes of polarization upon reflection or transmission for the investigation of the dielectric properties of the studied material. Thus, minute changes of the nanoMOFs optical properties arising from chemical transformations upon degradation can be followed over time. The main benefit of *in situ* ellipsometry is that it allows the use of very dilute conditions, mimicking the *in vivo* studies and with the additional advantage of attenuating the concentration gradients at the nanoMOFs surfaces. Furthermore, the geometric surface of the particles is fixed so that they cannot rearrange during the experiment time course. Consequently, artefacts due to the possible nanoMOF aggregation do not alter data. Last but not least, *in situ* ellipsometry presents a very good temporal resolution, allowing fast and precise measurements even at early times.

Some of us reported for the first time the use of *in situ* ellipsometry to study the

dissolution of hybrid organosilica nanoparticles in PBS at different temperatures and far from the saturation conditions [23]. It was found that the nanoparticle chemical composition was one of the main factors affecting the degradation kinetics. In a more recent study these authors prepared coated mesoporous silica-based films for *in situ* ellipsometry analysis in PBS with or without BSA [24]. The dissolution rate of silica nanoparticles was mainly controlled by their free accessible surface area, which regulated the accessibility of the diffused ions in the internal porosity of the particles.

Here, we propose for the first time an *in situ* analysis of the degradation mechanism of MIL-100(Fe) nanoMOFs using spectroscopical ellipsometry (SE). MIL-100(Fe) nanoMOFs of less than 100 nm were synthesized at room temperature (RT) to allow obtaining films of optical quality by dip-coating. Firstly, film's thickness was determined at room temperature by conventional spectroscopic ellipsometry and then film stability was evaluated in water and in PBS at 37°C. Then, degradation was studied as a function of the pH of the degrading medium in the presence or not of BSA, to assess its contribution to the mechanism. These studies were completed with morphological and composition *ex situ* investigations using STEM-HAADF coupled with EDX, to monitor the crystalline organization of the MOF and mapping their element distribution. This required the use of larger size nanoMOFs (140 nm) prepared through a microwave (MW)-assisted route to avoid aggregation issues with nanoMOFs of less than 100 nm in suspension. Finally, the release of the MOF ligand was followed by HPLC and showed that the size of the nanoMOFs did not much affect their degradation kinetics.

## 2. Materials and Methods

### 2.1. Materials

All reagents and solvents were purchased from commercial sources and used without any further purification. Iron(III) nitrate nine-hydrated ( $\text{Fe}(\text{NO}_3)_3 \cdot 9\text{H}_2\text{O}$ ) (Sigma-Aldrich), iron(III) chloride hexa-hydrated (98%, Alfa Aesar, France) and 1,3,5-benzene tricarboxylic acid (BTC or trimesic acid) (Sigma-Aldrich) were used for the synthesis of nanoMOFs. Dulbecco's Phosphate Buffer Saline (DPBS 1X, pH=7.4) was purchased from Thermo Fischer Scientific. It contains 1.47 mM  $\text{KH}_2\text{PO}_4$ , 8.59 mM  $\text{Na}_2\text{HPO}_4 \cdot 7\text{H}_2\text{O}$ , 137 mM NaCl and 2.66 mM KCl.  $\text{KH}_2\text{PO}_4$ ,  $\text{Na}_2\text{HPO}_4$ , NaCl and KCl (Sigma Aldrich) were used for the preparation of PBS pH=5.4. Bovine serum albumin (BSA) was also purchased from Sigma Aldrich. Milli-Q water (resistivity 18.2 M $\Omega$  cm) was obtained from a Millipore apparatus equipped with a 0.22  $\mu\text{m}$  filter. Silicon substrates were purchased by SolGelWay, Paris, France.

### 2.2. Synthesis of nanoMOFs

NanoMOFs were synthesized following two pathways. Firstly, MIL-100(Fe)

nanoMOFs with mean diameters of around 50 nm were synthesized from a mixture of 0.25 g of trimesic acid, 0.72 g of  $\text{Fe}(\text{NO}_3)_3 \cdot 9\text{H}_2\text{O}$  and 90 mL of water, which were mixed in a round bottom flask at room temperature under stirring for 48 h. The synthesized nanoMOFs were recovered by centrifugation (10000 rpm, 15 min) and purified by washing twice with distilled water and twice in absolute EtOH [25]. The nanoMOFs were stored as suspensions in absolute EtOH until final use. They are named nanoMOFs (RT).

Secondly, nanoMOFs of larger sizes (140 nm) were obtained using a microwave-assisted hydrothermal synthesis as previously reported [26], [27]. A mixture of iron chloride (8.97 mmol) and trimesic acid (4.02 mmol) was placed in Teflon sealed autoclave reactors with 20 mL of deionized water and heated for 6 min at 130 °C under stirring. The applied power was 800 Watts (Mars-5, CEM, US). The nucleation reaction was stopped by placing the reactors in an ice bath for 10 minutes. The resulting nanoMOFs were recovered by centrifugation (10000 rpm, 15 minutes) and were purified by washing with absolute EtOH 6 times to remove the residual non-reacted organic acid. A last centrifugation at 4000 rpm (2000 g) was performed during 1 min in absolute EtOH to sediment the largest particles and recover the supernatants as a suspension of monodisperse nanoparticles. NanoMOFs were stored wet in EtOH until final use. They are named nanoMOFs (MW).

### 2.3. Characterizations of nanoMOFs

The nanoMOFs were characterized before and after degradation in physiological conditions by a set of complementary techniques.

Powder X-ray diffraction (PXRD) analysis was carried out with a D8 Advance Bruker Diffractometer in Debye-Scherrer geometry, in the  $2\theta$  range of 2-40°. The diffractometer was equipped with a Ge (111) monochromator producing  $\text{Cu K}\alpha_1$  radiation ( $\lambda = 1.540598 \text{ \AA}$ ) and a LynxEye detector. Infrared spectra were collected using a Nicolet iS5 FT-IR (Thermo scientific, USA) from 4,000 to 400  $\text{cm}^{-1}$ . Porosity was evaluated by  $\text{N}_2$  sorption isotherms obtained at 77 K using a Micromeritics Tristar apparatus. Before the analysis, around 30 mg of nanoMOF samples were activated by heating at 150 °C under secondary vacuum for 5 hours. The size distribution and the polydispersity of nanoMOFs in suspension were determined by dynamic light scattering (DLS) and  $\zeta$ -potential measurements were performed using a Malvern Nano-ZS, Zetasizer Nano series. To do so, nanoMOFs from ethanolic suspensions were washed twice with Milli-Q water and finally resuspended in Milli-Q water at a concentration of 0.1  $\text{mg mL}^{-1}$ . Experiments were performed in triplicate at 25 °C.

The optical spectra of the nanoMOFs under the form of suspensions and in dried state were measured using a Varian Cary 300 Bio UV-Vis spectrometer equipped with an integration sphere in the diffuse reflectance mode. The release of the trimesate ligand was quantified using a reversed-phase high performance liquid chromatography

(HPLC) system (Waters Alliance e2695 Separations Module, Waters, Milford, MA) equipped with a UV-Vis detector (Waters 2998). The system was controlled by Agilent software. A SunFire-C18 reverse-phase column ( $5\ \mu\text{m}$ ,  $4.6 \times 150\ \text{mm}^2$ , Waters) was employed. For the analysis of BTC, a mobile phase A consisting of a buffer solution (0.04 M, pH=2.5) and a mobile phase B MeCN (50:50) were used. The buffer (phase A) was prepared by dissolving  $\text{NaH}_2\text{PO}_4$  (2.4 g, 0.02 mol) and  $\text{Na}_2\text{HPO}_4$  (2.84 g, 0.02 mol) in 1 L of Milli-Q water. The pH was then adjusted to 2.5 with  $\text{H}_3\text{PO}_4$  ( $\geq 85\%$ ). The injection volume was  $50\ \mu\text{L}$  and the detection wavelength was set at 225 nm. The column temperature was fixed at  $25\ ^\circ\text{C}$  [22].

The TEM/STEM studies were performed on a Titan Themis microscope corrected for spherical aberrations on the probe. The microscope was equipped with the "Super-X" analysis EDX system with 4 SDD detectors achieving a solid angle of 0.8 steradian. The observations were made at 200 kV with a sufficiently low probe current, ie around 40 to 50 pA, so as not to degrade the sample. The STEM-EDX chemical maps are carried out under the same conditions, for an acquisition time of approximately 15 to 20 minutes. For the HAADF-STEM images acquisition, the half-angle of convergence of the probe was 17 mrad and the collection half-angle of the Annular Dark Field detector was 69 mrad (inner angle) and 200 mrad (outter angle). For the TEM grid preparation, a  $2\ \mu\text{L}$  drop of the nanoMOF suspensions was placed on a 200 mesh copper grid covered with a pure carbon membrane (Ted Pella).

## 2.4. MIL-100(Fe) thin film deposition

An ethanolic dispersion of nanoMOFs ( $3.7\ \text{mg mL}^{-1}$ ) with mean diameters around 50 nm was dip-coated at room temperature on a silicon substrate with a withdrawal speed  $u$  of  $8\ \text{mm s}^{-1}$ . Relative humidity was measured at 50 %. The films were prepared by double coating with nanoMOF dispersions and after thermal treatment at  $130\ ^\circ\text{C}$  for 5 minutes, they were characterized by scanning electron microscopy (FEG-SEM Sigma HD, Zeiss) and their thickness and optical properties were determined by SE.

## 2.5. Spectroscopic Ellipsometry (SE)

SE experiments were performed using a J.A.Woolam M2000 spectroscopic ellipsometer equipped with a UV-IR detector in the 193 nm to 1690 nm spectral range. The acquisition time was 5 seconds for each point. Data were analyzed with CompleteEASE software. The imaginary part of the dispersion function of the film was modelled with a single Cody-Laurentz oscillator in 500-1700 nm wavelength range. Ellipsometric analyses in infrared angle were performed with a MARK II IR-VASE from Woolam within a closed cell flushed with dry air. MOFs films deposited onto Silicon wafer were analyzed at  $75^\circ$  incidence angle.

## 2.6. *In situ* ellipsometry

*In situ* dissolution experiments of nanoMOFs were performed with a thermostated ellipsometric liquid cell from Linkam. Data were collected every minute at 75° incidence using visible light wavelength range. The ellipsometer acquisition conditions were one measure of five seconds every minute. The experiments were performed at 37 °C, in order to mimic body's temperature and the media in contact with the films (100 mL total volumes) were circulated within the analysis cell at a flow rate of 10 mL min<sup>-1</sup>. The media used were Milli-Q water and PBS 10 mM containing or not BSA. The pH of the PBS medium was acidic (pH=5.4) or neutral (pH=7.4), whereas the concentration of BSA in PBS pH=7.4 was 3.7% w/v, to mimic albumin concentration in human blood.

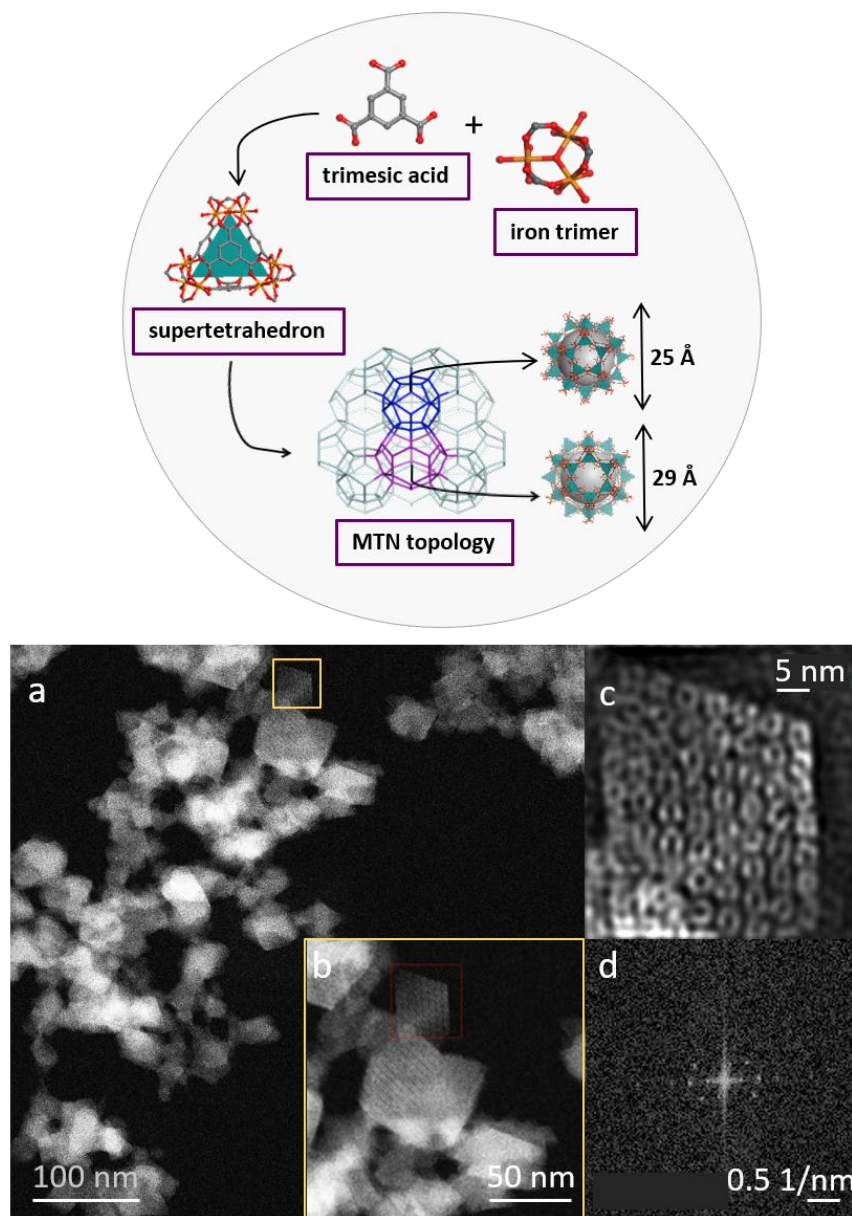
Data were analyzed with CompleteEASE software. The imaginary part of the dispersion function was modelled with a single Cody-Laurentz oscillator in the 400-900 nm wavelength range.

## 3. Results and Discussion

### 3.1. Characterization of nanoMOFs

MIL-100(Fe) presents a highly ordered mesoporous 3D structure resulting from the self-assembly of iron trimers with trimesate ligands. The zeotype architecture of a MTN topology, is composed of two types of interconnected mesoporous cages of 25 Å and 29 Å (Fig. 1 upper panel), the larger cages being accessible through microporous pentagonal and hexagonal windows of 5.6 Å and 8.6 Å, respectively, the small cages only through pentagonal windows (Fig. 1).





**Fig. 1: Upper panel:** Schematic representation of the structure of MIL-100(Fe) obtained by the self-assembly of BTC and iron, forming supertetrahedra and then 3D mesoporous cages of 25 and 29 Å accessible through microporous pentagonal windows of around 5 Å and microporous hexagonal windows of 8.6 Å.

**Lower panel:** Typical STEM-HAADF images of synthesized MIL-100(Fe) nanoMOFs.

(a) unprocessed image (b) magnified image (c) inverse FFT filtered HAADF-STEM image and (d) typical FFT pattern which reveals the crystallinity of the particles.

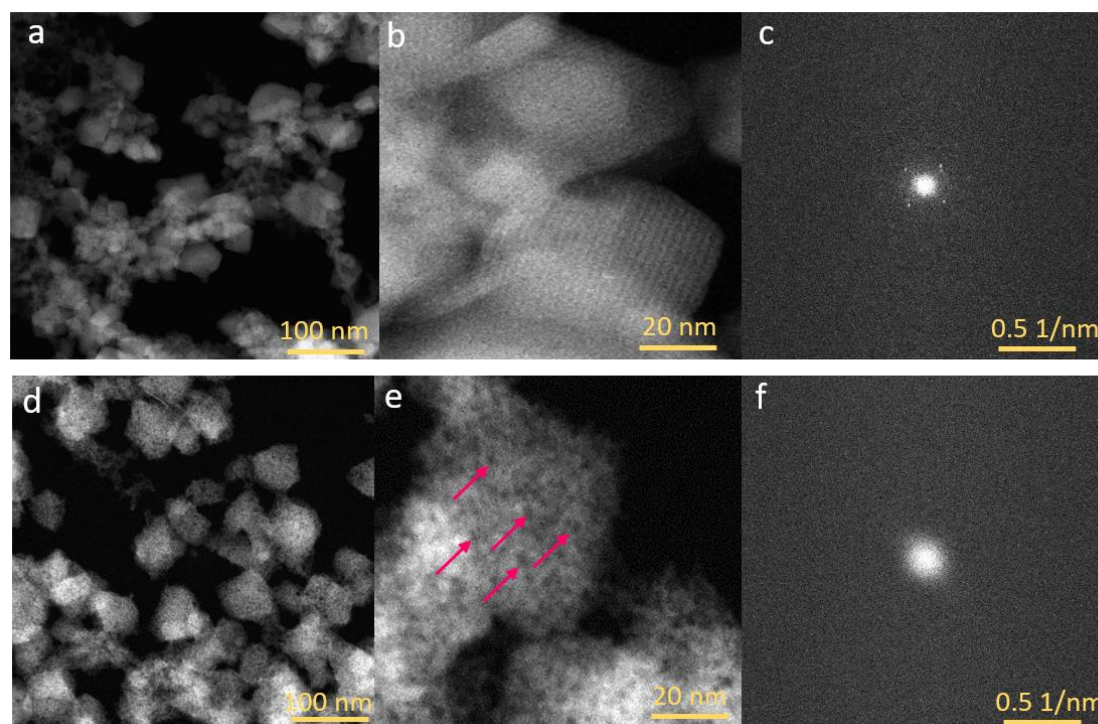
Whatever the synthesis method, crystalline MIL-100(Fe) nanoMOFs (nanoMOFs (RT) and nanoMOFs (MW)) were successfully obtained, as verified by a series of complementary investigations. First, due to its ultrahigh image resolution, STEM-HAADF performed first on the RT sample enabled the direct visualization of the mesoporous cages of MIL-100(Fe), as illustrated in Fig. 1a-c. A well-faceted octahedral morphology with an average diameter of  $60 \pm 10$  nm is observed while the crystalline

structure of individual particles was indicated by their Fast Fourier Transform (FFT) patterns (Fig. 1d). Yet, the nanoMOFs of ultrasmall sizes synthesized at RT were prone to aggregate rapidly in aqueous suspensions, as indicated by both SEM and DLS investigations (Fig. S1). To overcome this limitation, NanoMOFs (MW) exhibited average sizes of  $140 \pm 37$  nm measured by STEM-HAADF (Fig. S2) in the same order of magnitude as those determined by DLS ( $210 \pm 20$  nm), together with low polydispersity indices (0.07). In contrast to nanoMOFs (RT) they were more stable in aqueous media, possibly because of their lower specific surfaces. Both nanoMOFs (RT) and nanoMOFs (MW) exhibited a positive  $\zeta$ -potential of  $+26 \pm 2$  mV in acidic pH (3.5) and a negative  $\zeta$ -potential of  $-38 \pm 2$  mV at pH 7.4, in agreement with previously reported data [17], [19], [20]. The synthesized nanoMOFs were further characterized by PXRD, FT-IR spectroscopy and N<sub>2</sub> porosimetry. PXRD patterns were in agreement with data in the literature, showing the successful synthesis of a highly crystalline product (Fig. S3) [27], [28]. FT-IR spectroscopy allowed investigating the composition of the nanoMOFs. As shown in Fig. S4, the two bands at 1640 and 1380 cm<sup>-1</sup>, corresponding to the asymmetric  $\nu(\text{C-O})_{\text{as}}$  and symmetric  $\nu(\text{C-O})_{\text{s}}$  stretching modes of the C=O, indicate the coordination of the carboxylate ligands with the iron sites in the framework. The band at 1450 cm<sup>-1</sup> is related to the  $\nu(\text{OH})$  flexural vibrations. The spectra of MIL-100(Fe) display also two sharp bands at 760 and 710 cm<sup>-1</sup> attributed to the C-H stretching vibrations of the benzene rings [29]. The band at 620 cm<sup>-1</sup> is assigned to the  $\nu(\text{Fe}_3\text{O})$  vibration. Finally, the typical band of unreacted trimesic acid at 1710 cm<sup>-1</sup> was negligible, indicating that purification was successful to remove the unreacted ligand.[30], [31], [32]. N<sub>2</sub> adsorption resulted in a BET surface area of  $1450 \pm 60$  m<sup>2</sup>/g for nanoMOFs (RT) and  $1720 \pm 40$  m<sup>2</sup>/g for nanoMOFs (MW), respectively, in line with previous reported data [33], [34].

### 3.2. Degradation of nanoMOFs

NanoMOFs were allowed to degrade in acidic (pH 5.4) or neutral (pH 7.4) PBS at 37 °C. An incubation time of 48 hours was chosen to ensure a maximal degradation, according to previously published data [16], [17], [35], [36]. The degraded nanoMOFs were thoroughly washed to remove salts and were then investigated by STEM-HAADF to evaluate their morphological and dimensional changes. NanoMOFs (MW) were selected for these latter studies, in reason of their possible higher chemical stability as compared to nanoMOFs (RT) (Fig. S1).

NanoMOFs incubated in acidic PBS maintained their faceted crystalline structures, as shown by the presence of well-defined crystalline planes (Fig. 2b) and the FFT patterns (Fig. 2c). On the contrary, after exposure to neutral PBS, the nanoMOFs' crystallinity was lost, the crystalline planes disappeared in favor of an amorphous structure with large pores (Fig.2 d,e). Interestingly, despite losing more than 90% of their constitutive trimesate ligand, [3], [16], [36] the nanoMOFs (MW) mean diameter changes were only around 11% ( $140 \pm 37$  nm (intact) and  $125 \pm 11$  nm after degradation), in agreement with previous studies [17].



**Fig. 2:** a,b) STEM-HAADF images of MIL-100(Fe) nanoMOFs after 48 hours degradation in PBS at pH=5.4 and d,e) in PBS at pH=7.4. NanoMOFs concentration was  $0.25 \text{ mg mL}^{-1}$ . Red arrows show the apparition of large pores (yellow circles) indicating degradation. c,f) FFT patterns of degraded MIL-100(Fe) nanoMOFs indicate the loss of crystallinity.

STEM-HAADF coupled with X-Ray energy dispersive spectrometry (XEDS) allowed gaining further information about the degradation mechanism. Advantageously, it allows resolving the distribution of the nanoMOFs' constitutive elements. In particular, the atomic P/Fe ratio brings valuable insights on the evolution of the chemical composition. Noteworthy, Fe content in the nanoMOFs remains constant all over the degradation process, as it was not detected in the PBS release media at pH 7.4 [3], [12]. On the contrary, it was shown that phosphate ions from PBS progressively penetrate inside the matrix and coordinate to the iron sites. Therefore, determining the atomic P/Fe ratio is indicative of the nanoMOFs degradation.

It should be mentioned that although the nanoMOFs' trimesate constitutive ligand consists of carbon and oxygen atoms, tracking these elements is not a good option for STEM- XEDS studies. Indeed, sample holders contain carbon, making difficult to separate information arising from carbon atoms in the grids and in the analyzed samples. Besides, nanoMOFs contain a non-negligible amount of coordinated water molecules, which cannot be removed even under high vacuum conditions. Therefore, information on oxygen distribution arises both from coordinated water and trimesate ligands (Fig. S5).

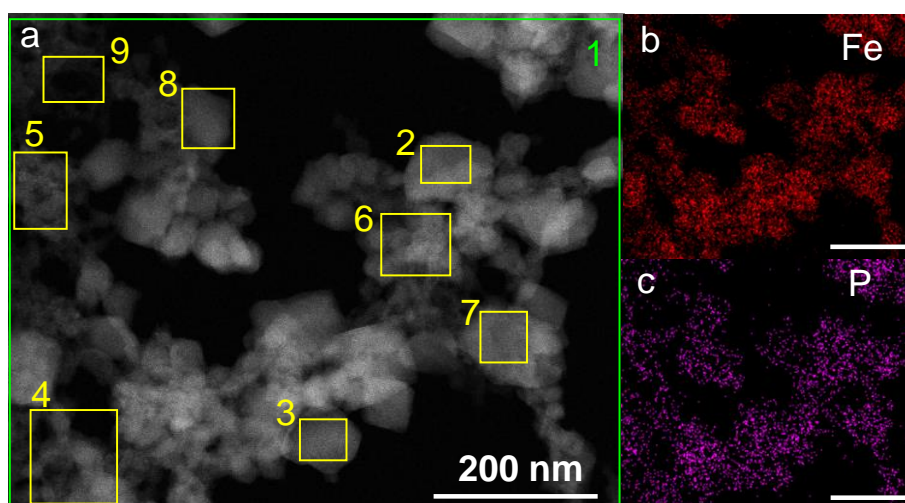
Thus, our attention was focused on the quantification of Fe and P atoms. Firstly, the

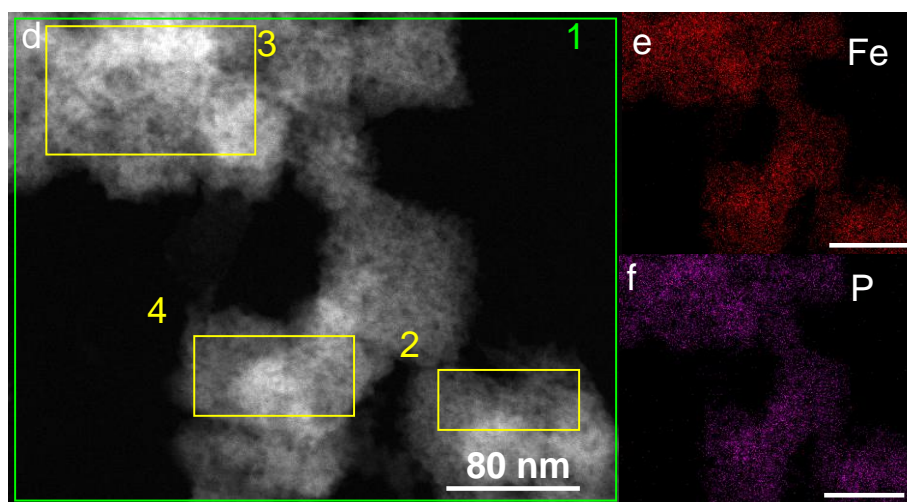
### Chapter III

#### Advanced characterization methodology to unravel MOF stability in extremely dilute conditions

distribution of P atoms within the nanoMOFs was homogeneous. In Fig. 3a and 3d, the selected regions of interest for the quantification of the elements are represented by yellow rectangles, while the green one represents the integral region (numbered 1). The normalized atomic percentage (at %) of P was calculated for each region. In the case of incubation in acidic PBS (Fig. 3a), regions numbered 2, 3 and 7 (indicating nanoMOFs structures), presented as P (at %)  $2.2 \pm 0.7$ ,  $2.4 \pm 0.8$  and  $2.5 \pm 0.7$ , respectively. For neutral environments P (at %) was  $7.5 \pm 0.4$ ,  $7.4 \pm 0.4$  and  $7.5 \pm 0.7$  for the regions 2, 3 and 4. These results confirm that P is evenly distributed with a much higher % in the case of pH=7.4. Secondly, the P/Fe atomic ratios were calculated for multiple regions of the nanoMOFs. The P/Fe ratio was found almost three times lower for particles degraded in pH=5.4 as compared to pH=7.4 ( $0.3 \pm 0.1$  as compared to  $0.7 \pm 0.4$ .) (Fig. 3). In a nutshell, these results suggest the lower degradation of the nanoMOFs in acidic conditions as compared to neutral ones.

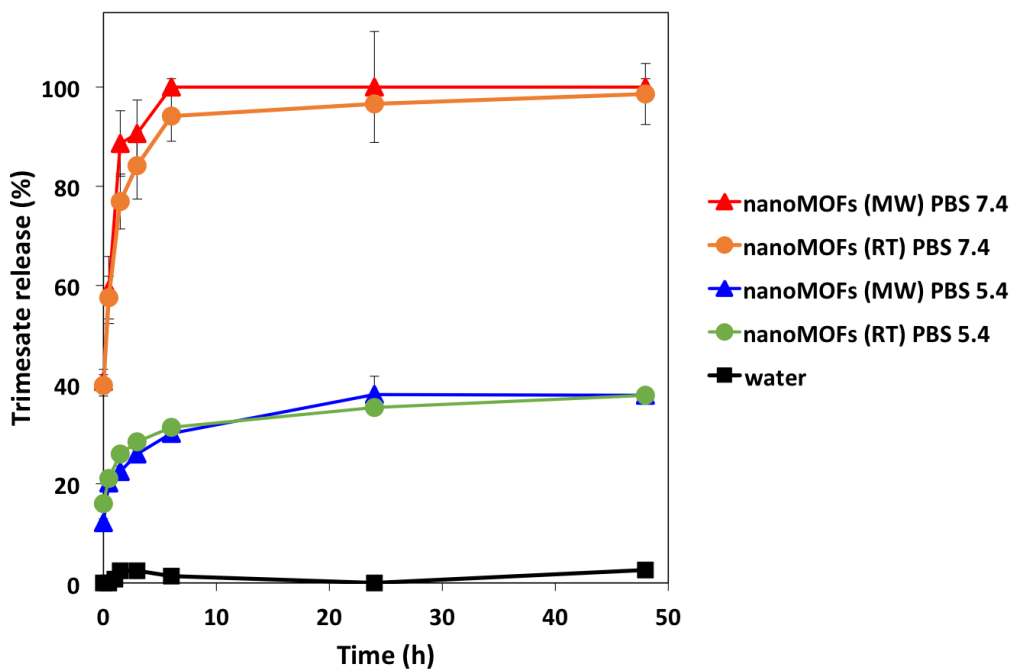
In addition, we took advantage of the STEM-HAADF methodology to assess the local P/Fe ratios and confirm that the degradation of the studied nanoMOFs was total after 48h (pH=7.4). To do so, further investigations were carried on with a longer degradation time of 72 hours (Fig. S6). Results showed that after this time, the P/Fe ratio remained stable ( $0.7 \pm 0.4$ ) and similar morphologies were obtained.





**Fig. 3:** a,d) STEM-HAADF images of MIL-100(Fe) nanoMOFs after 48 hours incubation in PBS at pH=5.4 and at pH=7.4 respectively. b,c,e,f) Elemental analysis reveals the homogeneous distribution of P after degradation. Yellow and green rectangles represent the selected regions by STEM-XEDS.

To complete the study, the amount of carboxylate ligand released from nanoMOFs (RT) and (MW) upon incubation in acidic and neutral PBS was measured at different time points by HPLC. In agreement with analysis at the microscopic level, the nanoMOFs (MW) progressively released their constitutive ligand in neutral PBS with  $76 \pm 7$ ,  $95 \pm 8$ ,  $100 \pm 3$  wt% after 1.5, 6 and hours, respectively, whereas in acidic conditions (pH=5.4) the degradation kinetics was much slower and partial with  $23 \pm 1$ ,  $30 \pm 1$  and  $38 \pm 1$  wt% loss at the same time points. Moreover, a plateau was reached after 24 hours degradation, corresponding to around  $38 \pm 1$  wt% ligand loss. To further assess the stability of the nanoMOFs in pure water, the trimesate release was also followed upon nanoMOF storage in water. Indeed, after 2 days incubation less than 2 wt% of the ligand was lost. This negligible loss could probably correspond to the unreacted residual ligand that remained trapped in the nanoMOFs pores after their synthesis. Interestingly, whatever the synthesis method (RT or MW) similar degradation patterns were observed, suggesting that in the studied range, nanoMOF size does not play a major role in this process (Fig. 4). Another important point, was the fast ligand release in the first minutes after the start of the degradation studies in both acidic and in neutral PBS ( $40 \pm 2$  wt% and  $12 \pm 1$  wt% respectively). This suggests that the degrading phosphate ions from PBS diffuse fast inside the nanoMOFs, coordinate with the unsaturated iron site and lead to ligand displacement.



**Fig. 4:** Trimesate release during MIL-100(Fe) nanoMOFs incubation in PBS (pH 7.4 and 5.4) and in water evaluated by HPLC. Sample concentration was  $0.5 \text{ mg mL}^{-1}$ .

As it has been discussed in a previous study, MIL-100(Fe) particles are more stable in acidic environments compared to the neutral ones. This observation can be explained by both the composition of PBS and the nature of iron metal of the framework. More precisely, at pH=5.4, 20 % of the ligands are monoprotonated and the rest 80% are deprotonated, while at pH=7.4, all the ligands are deprotonated. Also, the Pourbaix diagram of Fe in water shows that it presents different solubility state according to the pH range. At pH=7.4 the formation of iron oxide species is preferred. Moreover, the degrading medium is rich in phosphate ions, which present also a high complexing force with the metal. In PBS at pH=7.4,  $\text{H}_2\text{PO}_4^-$  and  $\text{HPO}_4^{2-}$  species are in equilibrium at similar concentration (5 mM). On the other hand, in the range of pH=4-6,  $\text{H}_2\text{PO}_4^-$  anions are the predominant species compared to  $\text{HPO}_4^{2-}$  (99 :1 at pH 5.4). At both studied pH, 5.4 and 7.4, phosphate ions diffuse into the nanoMOF porosity and coordinate with the iron sites. Thus, it can be hypothesized that the iron carboxylate species in the nanoMOFs have a tendency to degrade when the pH increases from 5.4 to 7.4, forming iron oxide and iron phosphates.

An additional indication of the nanoMOFs' degradation was the change of their surface charge, related to their  $\zeta$ -potential values, measured after 24 h incubation in PBS 5.4 and 7.4. The initial positive  $\zeta$ -potential value found for intact nanoMOFs ( $+26 \pm 2.1 \text{ mV}$ ) dramatically changed to negative in the case of degraded particles ( $-15 \pm 1.3 \text{ mV}$  and  $-37 \pm 2.1 \text{ mV}$  in PBS 5.4 and 7.4, respectively). This could be explained by the coordination of the phosphate ions with the unsaturated iron sites at the external

surface of the nanoMOFs and is in line with previously reported studies [16].

In agreement with these findings, PXRD patterns of nanoMOFs upon degradation in PBS 5.4 and 7.4 at different time points, demonstrated a rapid loss of crystallinity in neutral PBS (within 1 h) while a maintenance of the main characteristic Bragg peaks of MIL-100(Fe) in acidic PBS even after 2 days incubation was observed, in agreement with a more stable structure at pH 5.4 (Fig. S7).

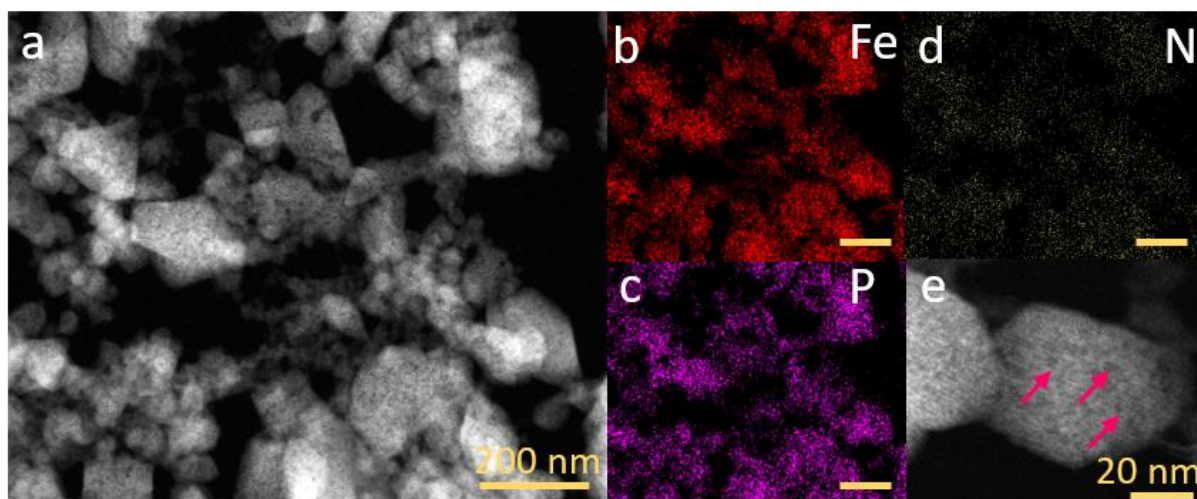
Moreover, FT-IR spectroscopy showed changes on the chemical composition of the nanoMOFs upon 48 h incubation in PBS (Fig. S8). In the presence of PBS, whatever the pH, a broad band at  $1050\text{ cm}^{-1}$  was observed, corresponding to asymmetrical P-O stretching [37], [38]. In a more acidic environment (PBS 5.4), the intensity of the stretching bands at  $1380$  and  $1640\text{ cm}^{-1}$  corresponding to the symmetric and asymmetric vibration of the trimesate was slightly decreased, but their shape and position was maintained. Thus, it can be concluded, that nanoMOFs kept partially their composition, in agreement to STEM-HAADF results. However, in neutral PBS, typical bands of the ligand were either broadened ( $1380$  and  $1450\text{ cm}^{-1}$ ), or totally disappeared ( $1640$ ,  $760$  and  $710\text{ cm}^{-1}$ ), suggesting the total release of the ligand and the formation of an amorphous degraded product. These observations are in line with the massive trimesate loss at pH 7.4, quantified by HPLC (Fig. 4).

$\text{N}_2$  adsorption isotherms for the degraded nanoMOFs revealed a decrease of their surface area upon degradation, which correlates to the loss of trimesate constitutive ligand and the phosphatation of the framework probably leading to some pores/windows clogging (Fig. S9). The initial BET surface area ( $1720 \pm 40\text{ m}^2/\text{g}$ ) decreased to  $960 \pm 20\text{ m}^2/\text{g}$  and to  $200 \pm 40\text{ m}^2/\text{g}$  for nanoMOFs degraded in PBS at pH 5.4 and 7.4, respectively.

To conclude, nanoMOFs lost partially or totally their structure in the presence of PBS, depending on the acidity of the medium. In a complementary study, PBS solution (pH=7.4) was enriched with BSA (3.7% w/v), to investigate its contribution to the degradation mechanism of nanoMOFs.

### 3.3. Degradation of nanoMOFs in the presence of a protein

NanoMOFs were immersed in neutral PBS containing BSA at a concentration corresponding to the standard one in blood [34]. Fig. 5 presents the morphology and the distribution of elements (Fe, P, N) as observed by STEM-HAADF-XEDS after 48 h incubation at  $37^\circ\text{C}$ . Of interest, nitrogen mapping is indicative of the location of BSA, as this element is only present in the protein.



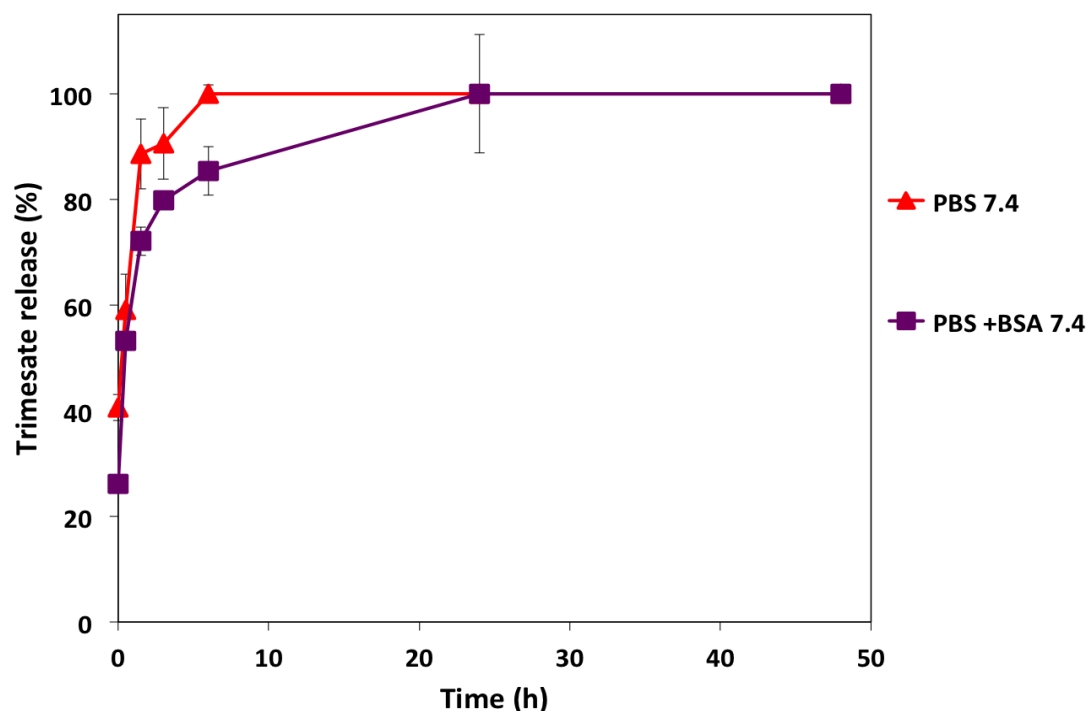
**Fig. 5:** a,e) STEM-HAADF images of MIL-100(Fe) nanoMOFs after 48 hours incubation in PBS-BSA at pH=7.4 ( $0.25 \text{ mg mL}^{-1}$ ). Formation of “holes” represented by red arrows suggest the degradation of the particles.

b,c,d) STEM-XEDS elemental analysis of Fe, P and N of nanoMOFs.

NanoMOFs kept their faceted structures (Fig. 5 a,e) and some of the initial crystalline planes (Fig. 5e), but “holes” in their structure similar to those observed in PBS 7.4 without BSA (Fig. 2e) also appeared (Fig. 5e). Fig. 5d shows an even distribution of N (BSA), which coincides with the nanoMOF location, suggesting that they were covered by this protein, after 48 h degradation. This is in line with data in the literature, showing that albumin readily adsorbs on nanoMOFs (MW) [34], [40].

These observations suggest that despite the BSA coating (ratio N/Fe was found at  $0.5 \pm 0.3$ ), nanoMOFs degradation still occurred (as indicating by elemental mapping), because phosphates were still present in high amounts (Fig. 5c). Indeed, calculated P/Fe ratios were  $0.7 \pm 0.3$ , as in the case of nanoMOFs degradation in PBS 7.4 without BSA, which most likely formed a non-compact corona around the external surface, leaving free pathways to the ions to diffuse in the core of the particles. To gain further understanding on the degradation process, constitutive trimesate loss was comparatively followed by HPLC in the case of nanoMOFs incubated in PBS with and without BSA. No significant differences in the degradation kinetics were observed in both cases (Fig. 6). This suggests that the protein corona is fully permeable to the degrading medium and is in agreement with STEM-HAADF results.





**Fig. 6:** Trimesate release during MIL-100(Fe) nanoMOFs incubation at 37°C in PBS pH=7.4 (red), and in PBS pH=7.4 enriched with BSA (violet) evaluated by HPLC. Sample concentration was 0.5 mg mL<sup>-1</sup>.

To sum up, nanoMOFs whatever their size, degrade under simulated physiological conditions by releasing the total amount of their constitutive ligand, regardless of the presence of BSA in the degradation medium, due to the rapid diffusion of phosphate ions in their porous structure.

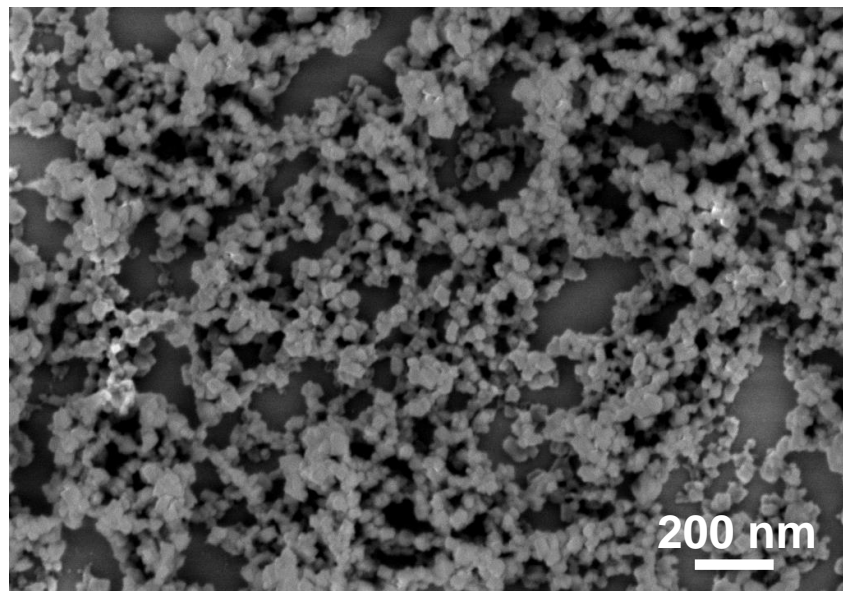
However, they globally maintained their shape and a certain amount of porosity whereas transforming into an inorganic matrix. These studies validate the possibility to further investigate the degradation of nanoMOFs deposited as films onto a silicone surface by *in situ* ellipsometry. This sensitive technique enables demonstrating the coordination of the phosphates to the nanoMOFs as well as the adsorption of BSA on the external surface of nanoMOFs *in situ*.

In a first step, thin films were prepared and then they were studied under well-controlled conditions (temperature and flow).

### 3.4. Film characterization

The thin films of optical quality were successfully prepared using an aqueous formulation of nanoMOFs (RT) by a dip coating process, showing a homogeneous and uniform coverage of the wafers as observed by SEM microscopy (Fig. 7). The presence of interparticular voids emerged from the ultra small size of nanoMOFs (62 ± 10 nm),

leading to partial aggregation. Similar voids have been also reported for coated of silicon substrates with larger nanoMOFs (MW) [23].



**Fig. 7:** SEM images of nanoMOFs (RT) thin films.

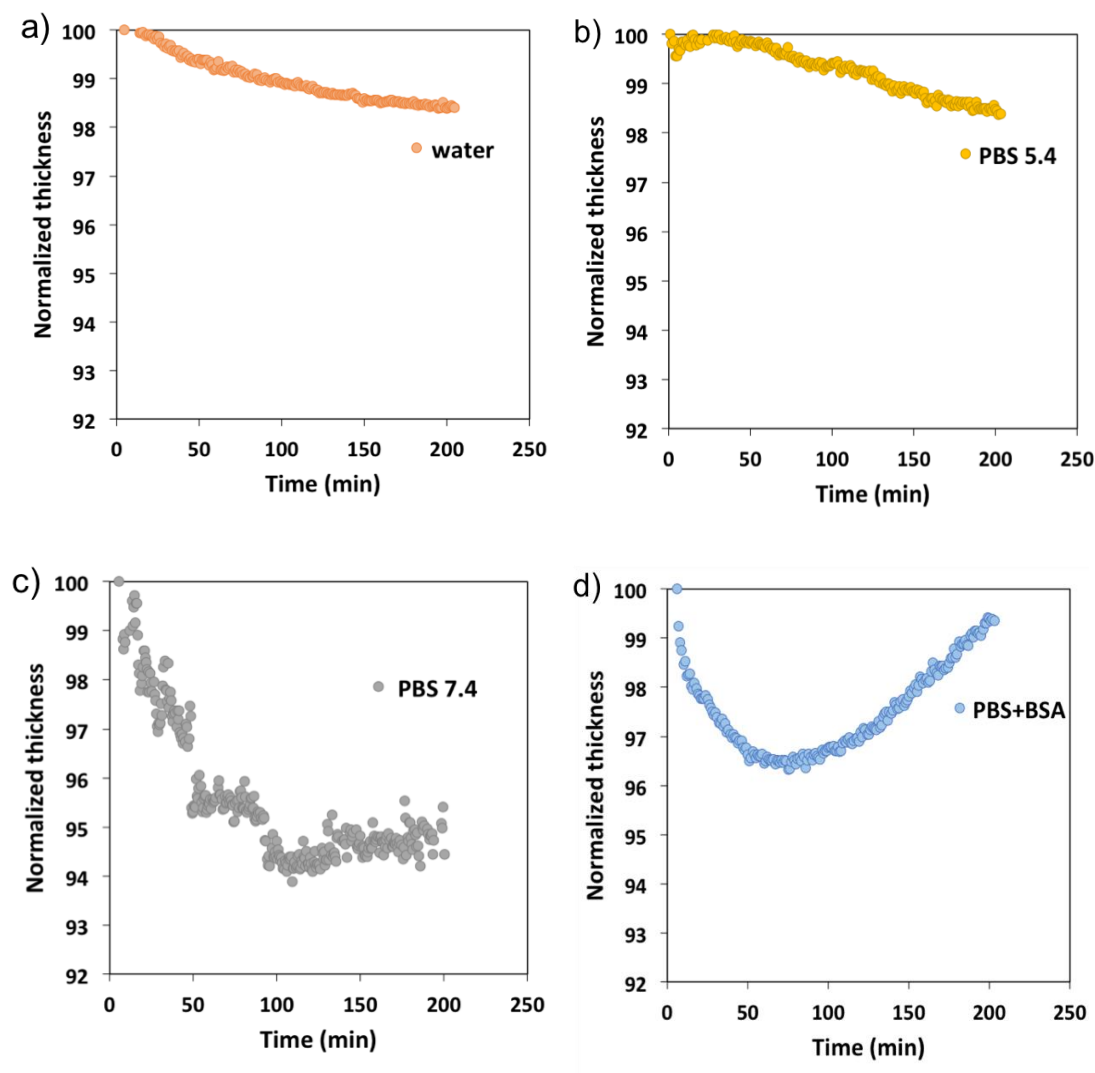
SE determined film thickness and its refractive index in a region (500-800 nm) at 0% relative humidity. The determination of these parameters is possible only when a film of optical quality is elaborated. Indeed, films were prepared more than ten times and the obtained mean film thickness was measured at  $200 \pm 20$  nm. The reproducibility of the films enabled further studies in solutions by *in situ* ellipsometry to compare their behavior in the presence of conditions triggering or not their degradation.

### 3.5. *In situ* ellipsometry

As a first experiment, the film was incubated in water (standard), for more than 3 hours, where very limited evolution occurred. Following thickness evolution as a function of time (Fig. 8a) a slow and progressive decrease attaining 1.5% after 200 minutes was observed, which can be either attributed to minor changes such as the departure of trace unreacted trimesate ligand and/or to the progressive packing of colloidal particles of the film. This result could be correlated with the HPLC results showing less than  $2 \pm 1$  wt % trimesate release, yet no definitive proof can be provided at this point. When similar tests were performed in PBS at pH=5.4 a similar progressive decrease of thickness was obtained (about 3 wt%). By contrast, the circulation of PBS at pH=7.4 led to a brutal decrease of 5 to 6% of the mean thickness of the colloidal layer then to its stabilization (Fig. 8b,c) confirming the rapid structural evolution of MIL-100(Fe) nanoMOFs described in the first part of this article. Similarly, to the previous conditions for the degradation of nanoMOFs, the final concentration of BSA was 37

Advanced characterization methodology to unravel MOF stability in extremely dilute conditions

mg/mL to mimic blood conditions. At early times (less than 1 hour), the thickness calculated by *in situ* ellipsometry exhibits the same tendency with PBS at pH=7.4 without the presence of BSA. After this point, a constant increase of the thickness was measured, most likely related to the adsorption of protein onto the particles' surface (Fig. 8d).



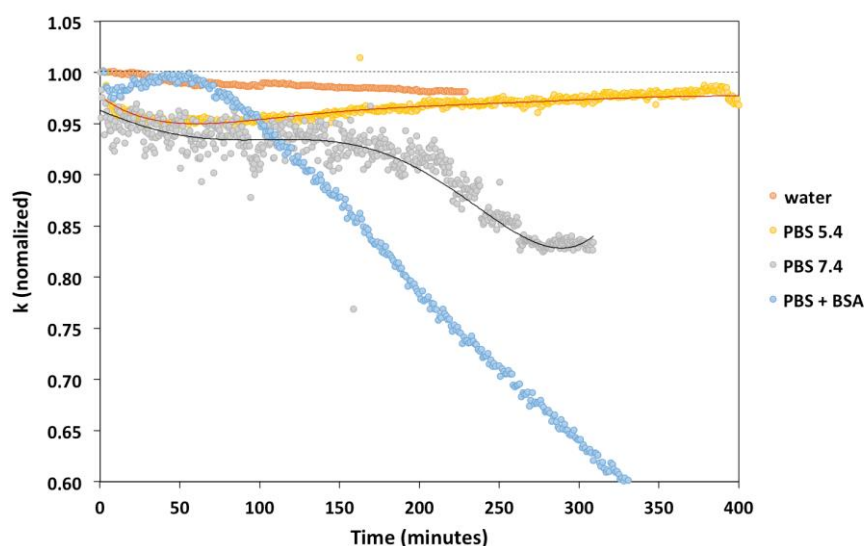
**Fig. 8:** Normalized thickness calculated by *in situ* ellipsometry for MIL-100(Fe) film incubated in a) water (orange), b) PBS 5.4 (yellow), c) PBS 7.4 (grey) and d) PBS+BSA (blue).

Changes in the thicknesses of the films certainly give us a strong indication about possible changes of nanoMOFs structure upon degradation, but cannot prove their chemical transformation. The resulted values can only be attributed to a mechanical contraction of the film or a physical rearrangement of the colloids to achieve a better stacking due to the constant flow of the liquid media.

To overcome these limitations, the imaginary part of refractive index model (that is the extinction coefficient  $k$ ), which quantifies the absorption of electric waves propagating

within the films, was measured. This parameter is proportional to the absorption coefficient, and shows modifications on the electronic environment of the iron metal. Herein, evolutions of  $k$  were followed, because UV-Vis absorption properties of the original MIL-100(Fe) powder presents two absorption peaks at 440 and 540 nm, while that of totally transformed material presents only one absorption shoulder at 440 nm followed by a smooth absorption decrease with increasing wavelength. (Fig. S10). The advantage of the ellipsometric measurement is that one can follow the exact same position of material and amount of matter with no need to use normalization procedures (such as Kuberka-Munk data treatment for example). This approach does not suffer from usual preparation bias of powders (grinding homogeneity of the powder, dispersion quality of grains within  $\text{BaSO}_4$ , ...) that make the estimation of the absolute absorption amplitude (thus the comparison of powders) sometimes difficult. On the other hand, the ellipsometric approach requires thin films with light absorption per volume unit strong enough for being able to model properly each absorption band of the spectrum.

When analyzing the films, models for all absorption contributions observed with diffuse reflectance of powders could sometimes be applied, but sometimes not. This problem arises from the fact that deposited MIL-100(Fe) colloids were poorly packed (Fig. 7). Forming highly porous films with low extinction coefficient values, results to an important loss of sensitivity, hampering the clear distinction of the two absorption contributions at 440 and 540 nm. By modelling only the absorption centered at 540 nm (omitting all wavelength below 500 nm), the evolution of  $k$  at 540 nm in different environments could be observed (Fig. 9).



**Fig. 9:** Evolution of extinction coefficient at 540 nm, normalised and taking into account the film thickness variations, calculated by *in situ* ellipsometry for MIL-100(Fe) film incubated in water (orange), PBS 5.4 (yellow), PBS 7.4 (grey) and PBS 7.4 containing BSA (blue). Fitted polynomials were superimposed onto PBS 5.4 and PBS 7.4 curves for easing their discrimination. They are only guides for the eyes.

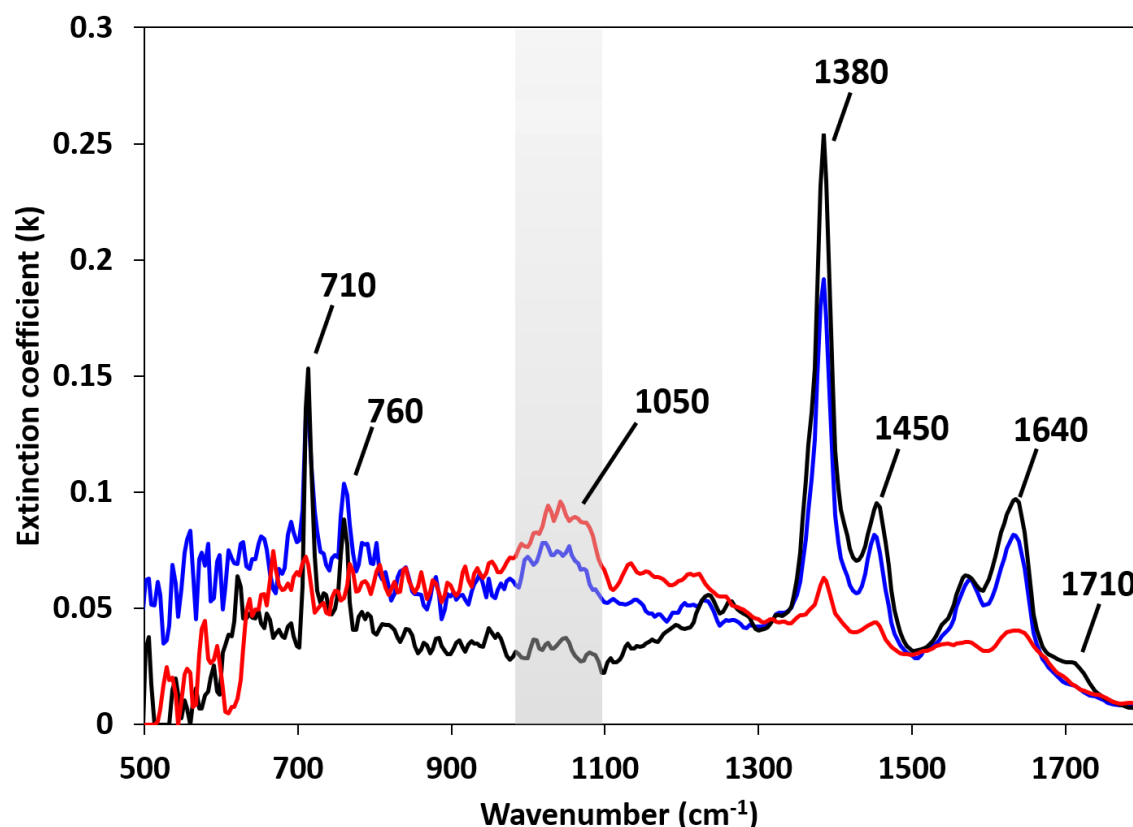
After normalization of the extinction coefficients, it was found that MIL-100(Fe) nanoMOFs on their support exhibited very little evolution in water. On the opposite, an immediate drop of  $k$  in the first 5 to 10 minutes in PBS at pH 7.4 was noticed. This fast response of optical absorption witnesses a change of iron center environment. As a consequence, it is likely due to the rapid chemisorption of phosphate anions on iron centers. By comparing the evolution of these curves with time, it was remarkably witnessed, that they diverge progressively. At pH 5.4,  $k$  values progressively converged through the curve of colloids in water and then stabilized, meaning that no drastic change seems to occur after the initial fast transformation. At pH 7.4,  $k$  values exhibited a slow decrease from 40 to 140 minutes and after that point, they decreased much faster. This is an indication of progressive structural transformation taking place in the immediate environment of iron sites. As most part of the ligand is released after two hours (about 70-80%), the fast optical transformation observed after 140 minutes may be related to the final displacement of trimesate ligands from the coordination sphere of iron centers, allowing a local rearrangement of the iron centers and phosphate anions. At this point, complementary data for describing this transformation in detail, such as a continuous monitoring of P/Fe molar ratio of the particles with time, would be essential for a better characterization of the degraded product. Finally, in presence of BSA, a moderate evolution of  $k$  during the first hour was noted. No sign of the short-time phosphate adsorption is visible in that case. Then a rapid acceleration of optical transformation, which reaches a  $k$  decrease rate similar to that of pure PBS 7.4, was observed. This last point suggests that PBS does not significantly change the final transformation rate of the colloids, in agreement with the *ex situ* studies, previously discussed for the degradation of nanoMOFs (STEM-HAADF, XEDS, HPLC, PXRD and FT-IR).

### 3.6. Characterization of the degraded films

After having explored the degradation mechanism of the thin films by *in situ* ellipsometry, Infrared spectroscopy was further applied to gain additional information on their chemical composition (Fig. 10). To note, the films incubated in PBS were washed three times in Milli-Q water to remove the excess of the remained salts which could recrystallize on the surface during drying process.

Upon incubation in aqueous media, where no degradation occurred, the spectrum of MIL-100(Fe) with the typical bands of the carbonyl group of the ligand coordinating with the iron sites of the framework was obtained. This spectrum is a strong indication of the successful coating of the substrate with nanoMOFs, as well as its stability upon incubation in water. When the film was in contact with PBS 5.4 (more than 2 hours), a new band appeared at around  $1050\text{ cm}^{-1}$ , denoting the anchoring of the phosphate ions within the framework. As for the FT-IR of nanoMOFs before deposition (Fig. S8), typical bands of the carboxylate ligand were found, showing that the vibrational structure of the MOFs remained mostly intact in this acidic environment in presence

of phosphate ions, even after 2 days incubation. In the case of neutral PBS, where a fast degradation was observed, IR spectroscopy was applied to a film which was in contact with PBS 7.4 for only 5 minutes. This time point was selected to study the influence of phosphates in the degradation mechanism of nanoMOFs at short times. Indeed, the band at  $1050\text{ cm}^{-1}$  corresponding to P-O stretching was found. Noteworthy, typical carbonyl bands of trimesate were severely decreased, designating the quasi instant chemical transformation of nanoMOFs.



**Fig. 10:** Infrared spectra of films after *in situ* measurements in water (black), PBS 5.4 (blue) and PBS 7.4 (red).

## 4. Conclusions

To assess the degradation mechanism of MIL-100(Fe) nanoMOF, *in situ* ellipsometry was successfully carried out based on optical quality thin films deposited onto silicon surfaces by dip coating. In addition to the stability of the nanoMOFs films, their thickness and their optical quality in extreme dilute conditions, in PBS with or without BSA, were also compared. In neutral conditions, it was found that the phosphate ions from PBS solutions instantly diffused in the framework and triggered the nanoMOF degradation by displacing their constitutive trimesate ligands. On the contrary, nanoMOFs partially maintained their global chemical composition in acidic conditions, compared to neutral ones despite the incorporation of phosphates in the internal

porosity of the nanoMOFs. The presence of a protein-coating layer did not impede the degradation process. *Ex situ* studies with a significant emphasis on STEM-HAADF microscopy further confirmed these findings.

The methodology presented here paves the way for numerous possible applications, such as the study of nanoMOFs degradation in more complex media such as serum and blood. It could also bring new insights in the case of nanoMOFs containing drugs inside their pores or with coating layers on their external surface.

**Funding:** “This research was funded by the Paris Ile-de-France Region – DIM Respire, grant number ‘LS 167151’

### Acknowledgments:

We are grateful to Dr. Antoine Tissot (FRE IMAP 2000, ENS, Paris) for help with solid UV-Vis spectroscopy and Dr. Farid Nouar for the synthesis of nanoMOFs at RT. We also acknowledge Dr. Francois Brisset for SEM microscopy. IC thanks the Paris Ile-de-France Region – DIM Respire for a PhD fellowship. This work was supported by a public grant overseen by the French National Research Agency (ANR) as part of the “Investissements d’Avenir” program (Labex NanoSaclay, reference: ANR-10-LABX-0035).

### References

- [1] R. Langer, J. Folkman, Polymers for the sustained release of proteins and other macromolecules, *Nature*. 263 (1976) 797–800. <https://doi.org/10.1038/263797a0>.
- [2] J.K. Patra, G. Das, L.F. Fraceto, E.V.R. Campos, M.D.P. Rodriguez-Torres, L.S. Acosta-Torres, L.A. Diaz-Torres, R. Grillo, M.K. Swamy, S. Sharma, S. Habtemariam, H.S. Shin, Nano based drug delivery systems: Recent developments and future prospects *J. Nanobiotechnology*. 16 (2018) 1–33. <https://doi.org/10.1186/s12951-018-0392-8>.
- [3] P. Horcajada, T. Chalati, C. Serre, B. Gillet, C. Sebrie, T. Baati, J.F. Eubank, D. Heurtaux, P. Clayette, C. Kreuz, J.S. Chang, Y.K. Hwang, V. Marsaud, P.N. Bories, L. Cynober, S. Gil, G. Férey, P. Couvreur, R. Gref, Porous metal-organic-framework nanoscale carriers as a potential platform for drug delivery and imaging, *Nat. Mater.* 9 (2010) 172–178. <https://doi.org/10.1038/nmat2608>.
- [4] J. Qiu, X. Li, R. Gref, A. Vargas-Berenguel, Carbohydrates in metal organic frameworks: Supramolecular assembly and surface modification for biomedical applications, Elsevier Inc., 2020. <https://doi.org/10.1016/b978-0-12-816984-1.00022-6>.
- [5] E. Ploetz, H. Engelke, U. Lächelt, S. Wuttke, The Chemistry of Reticular Framework Nanoparticles: MOF, ZIF, and COF Materials, *Adv. Funct. Mater.* 30 (2020) 1909062. <https://doi.org/10.1002/adfm.201909062>.
- [6] T. Baati, L. Njim, F. Neffati, A. Kerkeni, M. Bouttemi, R. Gref, M.F. Najjar, A. Zakhama, P. Couvreur, C. Serre, P. Horcajada, In depth analysis of the in vivo toxicity of nanoparticles of porous iron(III) metal-organic frameworks, *Chem. Sci.* 4 (2013) 1597–1607. <https://doi.org/10.1039/c3sc22116d>.
- [7] T. Simon-Yarza, T. Baati, F. Neffati, L. Njim, P. Couvreur, C. Serre, R. Gref, M.F. Najjar, A.

- Zakhama, P. Horcajada, In vivo behavior of MIL-100 nanoparticles at early times after intravenous administration, *Int. J. Pharm.* 511 (2016) 1042–1047. <https://doi.org/10.1016/j.ijpharm.2016.08.010>.
- [8] T. Simon-Yarza, A. Mielcarek, P. Couvreur, C. Serre, Nanoparticles of Metal-Organic Frameworks: On the Road to In Vivo Efficacy in Biomedicine, *Adv. Mater.* 30 (2018) 1–15. <https://doi.org/10.1002/adma.201707365>.
- [9] R. Anand, F. Borghi, F. Manoli, I. Manet, V. Agostoni, P. Reschiglian, R. Gref, S. Monti, Host-guest interactions in Fe(III)-trimesate MOF nanoparticles loaded with doxorubicin, *J. Phys. Chem. B.* 118 (2014) 8532–8539. <https://doi.org/10.1021/jp503809w>.
- [10] M.R. Di Nunzio, V. Agostoni, B. Cohen, R. Gref, A. Douhal, A “ship in a bottle” strategy to load a hydrophilic anticancer drug in porous metal organic framework nanoparticles: Efficient encapsulation, matrix stabilization, and photodelivery, *J. Med. Chem.* 57 (2014) 411–420. <https://doi.org/10.1021/jm4017202>.
- [11] V. Rodriguez-Ruiz, A. Maksimenko, R. Anand, S. Monti, V. Agostoni, P. Couvreur, M. Lampropoulou, K. Yannakopoulou, R. Gref, Efficient “green” encapsulation of a highly hydrophilic anticancer drug in metal-organic framework nanoparticles, *J. Drug Target.* 23 (2015) 759–767. <https://doi.org/10.3109/1061186X.2015.1073294>.
- [12] X. Li, N. Semiramoth, S. Hall, V. Tafani, J. Josse, F. Laurent, G. Salzano, D. Foulkes, P. Brodin, L. Majlessi, N.E. Ghermani, G. Maurin, P. Couvreur, C. Serre, M.F. Bernet-Camard, J. Zhang, R. Gref, Compartmentalized Encapsulation of Two Antibiotics in Porous Nanoparticles: an Efficient Strategy to Treat Intracellular Infections, *Part. Part. Syst. Charact.* 36 (2019) 1–9. <https://doi.org/10.1002/ppsc.201800360>.
- [13] C. Tamames-Tabar, D. Cunha, E. Imbuluzqueta, F. Ragon, C. Serre, M.J. Blanco-Prieto, P. Horcajada, Cytotoxicity of nanoscaled metal-organic frameworks, *J. Mater. Chem. B.* 2 (2014) 262–271. <https://doi.org/10.1039/c3tb20832j>.
- [14] R. Grall, T. Hidalgo, J. Delic, A. Garcia-Marquez, S. Chevillard, P. Horcajada, In vitro biocompatibility of mesoporous metal (III; Fe, Al, Cr) trimesate MOF nanocarriers, *J. Mater. Chem. B.* 3 (2015) 8279–8292. <https://doi.org/10.1039/c5tb01223f>.
- [15] S. Wuttke, A. Zimpel, T. Bein, S. Braig, K. Stoiber, A. Vollmar, D. Müller, K. Haastert-Talini, J. Schaeske, M. Stiesch, G. Zahn, A. Mohmeyer, P. Behrens, O. Eickelberg, D.A. Bölükbas, S. Meiners, Validating Metal-Organic Framework Nanoparticles for Their Nanosafety in Diverse Biomedical Applications, *Adv. Healthc. Mater.* 6 (2017) 1–11. <https://doi.org/10.1002/adhm.201600818>.
- [16] E. Bellido, M. Guillevic, T. Hidalgo, M.J. Santander-Ortega, C. Serre, P. Horcajada, Understanding the colloidal stability of the mesoporous MIL-100(Fe) nanoparticles in physiological media, *Langmuir.* 30 (2014) 5911–5920. <https://doi.org/10.1021/la5012555>.
- [17] X. Li, L. Lachmanski, S. Safi, S. Sene, C. Serre, J.M. Grenèche, J. Zhang, R. Gref, New insights into the degradation mechanism of metal-organic frameworks drug carriers, *Sci. Rep.* 7 (2017) 1–11. <https://doi.org/10.1038/s41598-017-13323-1>.
- [18] A.K. Wright, M.R. Thompson, Hydrodynamic structure of bovine serum albumin determined by transient electric birefringence, *Biophys. J.* 15 (1975) 137–141. [https://doi.org/10.1016/S0006-3495\(75\)85797-3](https://doi.org/10.1016/S0006-3495(75)85797-3).
- [19] S. Sene, M.T. Marcos-Almaraz, N. Menguy, J. Scola, J. Volatron, R. Rouland, J.M. Grenèche, S. Miraux, C. Menet, N. Guillou, F. Gazeau, C. Serre, P. Horcajada, N. Steunou, Maghemite-nanoMIL-100(Fe) Bimodal Nanovector as a Platform for Image-Guided Therapy, *Chem.* 3 (2017) 303–322. <https://doi.org/10.1016/j.chempr.2017.06.007>.
- [20] T. Simon-Yarza, M. Giménez-Marqués, R. Mrimi, A. Mielcarek, R. Gref, P. Horcajada, C. Serre, P. Couvreur, A Smart Metal–Organic Framework Nanomaterial for Lung Targeting, *Angew. Chemie - Int. Ed.* 56 (2017) 15565–15569. <https://doi.org/10.1002/anie.201707346>.
- [21] S. Rojas, I. Colinet, D. Cunha, T. Hidalgo, F. Salles, C. Serre, N. Guillou, P. Horcajada, Toward Understanding Drug Incorporation and Delivery from Biocompatible Metal-Organic Frameworks in View of Cutaneous Administration, *ACS Omega.* 3 (2018) 2994–3003. <https://doi.org/10.1021/acsomega.8b00185>.



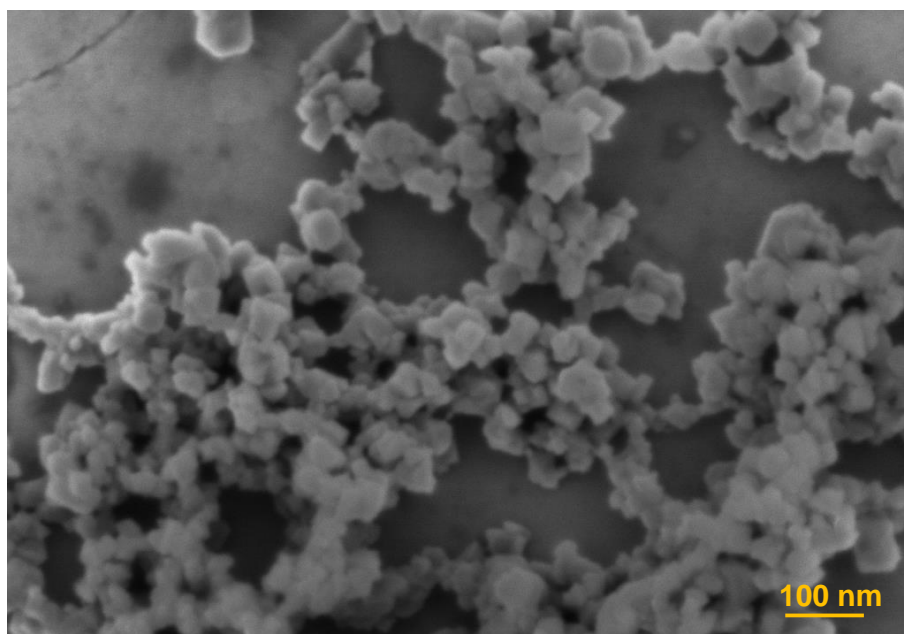
- [22] Size quality report for the Zetasizer Nano, Malvern Guid. 1–12.
- [23] T. Fontecave, C. Sanchez, T. Azaïs, C. Boissière, Chemical modification as a versatile tool for tuning stability of silica based mesoporous carriers in biologically relevant conditions, *Chem. Mater.* 24 (2012) 4326–4336. <https://doi.org/10.1021/cm302142k>.
- [24] E. Bindini, Z. Chehadi, M. Faustini, P.A. Albouy, D. Grosso, A. Cattoni, C. Chanéac, O. Azzaroni, C. Sanchez, C. Boissière, Following in Situ the Degradation of Mesoporous Silica in Biorelevant Conditions: At Last, a Good Comprehension of the Structure Influence, *ACS Appl. Mater. Interfaces.* 12 (2020) 13598–13612. <https://doi.org/10.1021/acsami.9b19956>.
- [25] M. Panchal, F. Nouar, C. Serre, M. Benzaqui, S. Sene, N. Steunou, M. Gimenez Marqués, Low Temperature Process For The Synthesis Of MOF Carboxylate Nanoparticles, EP3357929A1, 2017.
- [26] V. Agostoni, P. Horcajada, V. Rodriguez-Ruiz, H. Willaime, P. Couvreur, C. Serre, R. Gref, 'Green' fluorine-free mesoporous iron(III) trimesate nanoparticles for drug delivery, *Green Mater.* 1 (2013) 209–217. <https://doi.org/10.1680/gmat.13.00001>.
- [27] A. García Márquez, A. Demessence, A.E. Platero-Prats, D. Heurtaux, P. Horcajada, C. Serre, J.S. Chang, G. Férey, V.A. De La Peña-O'Shea, C. Boissière, D. Grosso, C. Sanchez, Green microwave synthesis of MIL-100(Al, Cr, Fe) nanoparticles for thin-film elaboration, *Eur. J. Inorg. Chem.* 100 (2012) 5165–5174. <https://doi.org/10.1002/ejic.201200710>.
- [28] P. Horcajada, S. Surblé, C. Serre, D.Y. Hong, Y.K. Seo, J.S. Chang, J.M. Grenèche, I. Margiolaki, G. Férey, Synthesis and catalytic properties of MIL-100(Fe), an iron(III) carboxylate with large pores, *Chem. Commun.* 100 (2007) 2820–2822. <https://doi.org/10.1039/b704325b>.
- [29] G. Mahalakshmi, V. Balachandran, FT-IR and FT-Raman spectra, normal coordinate analysis and ab initio computations of Trimesic acid, *Spectrochim. Acta - Part A Mol. Biomol. Spectrosc.* 124 (2014) 535–547. <https://doi.org/10.1016/j.saa.2014.01.061>.
- [30] H. Lv, H. Zhao, T. Cao, L. Qian, Y. Wang, G. Zhao, Efficient degradation of high concentration azo-dye wastewater by heterogeneous Fenton process with iron-based metal-organic framework, *J. Mol. Catal. A Chem.* 400 (2015) 81–89. <https://doi.org/10.1016/j.molcata.2015.02.007>.
- [31] S. Huang, K.L. Yang, X.F. Liu, H. Pan, H. Zhang, S. Yang, MIL-100(Fe)-catalyzed efficient conversion of hexoses to lactic acid, *RSC Adv.* 7 (2017) 5621–5627. <https://doi.org/10.1039/c6ra26469g>.
- [32] H. Leclerc, A. Vimont, J.C. Lavalley, M. Daturi, A.D. Wiersum, P.L. Llwellyn, P. Horcajada, G. Férey, C. Serre, Infrared study of the influence of reducible iron(iii) metal sites on the adsorption of CO, CO<sub>2</sub>, propane, propene and propyne in the mesoporous metal-organic framework MIL-100, *Phys. Chem. Chem. Phys.* 13 (2011) 11748–11756. <https://doi.org/10.1039/c1cp20502a>.
- [33] M.A. Simon, E. Anggraeni, F.E. Soetaredjo, S.P. Santoso, W. Irawaty, T.C. Thanh, S.B. Hartono, M. Yuliana, S. Ismadji, Hydrothermal Synthesize of HF-Free MIL-100(Fe) for Isoniazid-Drug Delivery, *Sci. Rep.* 9 (2019) 1–11. <https://doi.org/10.1038/s41598-019-53436-3>.
- [34] X. Li, G. Salzano, J. Qiu, M. Menard, K. Berg, T. Theodossiou, C. Ladavière, R. Gref, Drug-Loaded Lipid-Coated Hybrid Organic-Inorganic "Stealth" Nanoparticles for Cancer Therapy, *Front. Bioeng. Biotechnol.* 8 (2020) 1–12. <https://doi.org/10.3389/fbioe.2020.01027>.
- [35] D. Cunha, M. Ben Yahia, S. Hall, S.R. Miller, H. Chevreau, E. Elkaïm, G. Maurin, P. Horcajada, C. Serre, Rationale of drug encapsulation and release from biocompatible porous metal-organic frameworks, *Chem. Mater.* 25 (2013) 2767–2776. <https://doi.org/10.1021/cm400798p>.
- [36] I. Christodoulou, T. Bourguignon, X. Li, G. Patriarche, C. Serre, C. Marlière, R. Gref, Degradation mechanism of porous metal-organic frameworks by in situ atomic force microscopy, *Nanomaterials.* 11 (2021) 1–17. <https://doi.org/10.3390/nano11030722>.
- [37] X. Unamuno, E. Imbuluzqueta, F. Salles, P. Horcajada, M.J. Blanco-Prieto, Biocompatible porous metal-organic framework nanoparticles based on Fe or Zr for gentamicin vectorization, *Eur. J. Pharm. Biopharm.* 132 (2018) 11–18. <https://doi.org/10.1016/j.ejpb.2018.08.013>.
- [38] D.H. Barnes, R. Jugdaosingh, S. Kiamil, Shelf Life and Chemical Stability of Calcium Phosphate Coatings Applied to Poly Carbonate Urethane Substrates, *J. Biotechnol. Biomater.* 01 (2011) 1–11. <https://doi.org/10.4172/2155-952x.1000112>.
- [39] A.M. Chávez, A. Rey, J. López, P.M. Álvarez, F.J. Beltrán, Critical aspects of the stability and catalytic activity of MIL-100(Fe) in different advanced oxidation processes, *Sep. Purif. Technol.*

### Chapter III

#### Advanced characterization methodology to unravel MOF stability in extremely dilute conditions

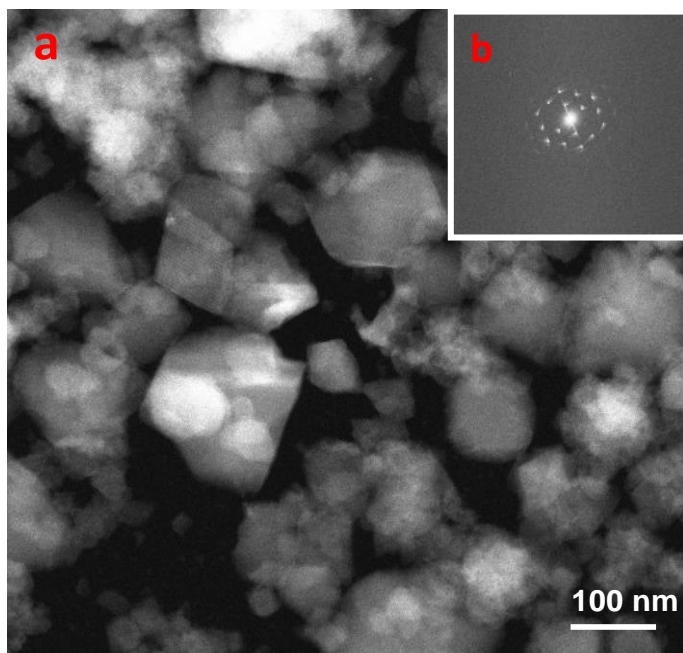
- 255 (2021) 117660. <https://doi.org/10.1016/j.seppur.2020.117660>.
- [40] G. Cutrone, X. Li, J.M. Casas-Solvas, M. Menendez-Miranda, J. Qiu, G. Benkovics, D. Constantin, M. Malanga, B. Moreira-Alvarez, J.M. Costa-Fernandez, L. García-Fuentes, R. Gref, A. Vargas-Berenguel, Design of engineered cyclodextrin derivatives for spontaneous coating of highly porous metal-organic framework nanoparticles in aqueous media, *Nanomaterials*. 9 (2019) 1–27. <https://doi.org/10.3390/nano9081103>.

## Supporting Information

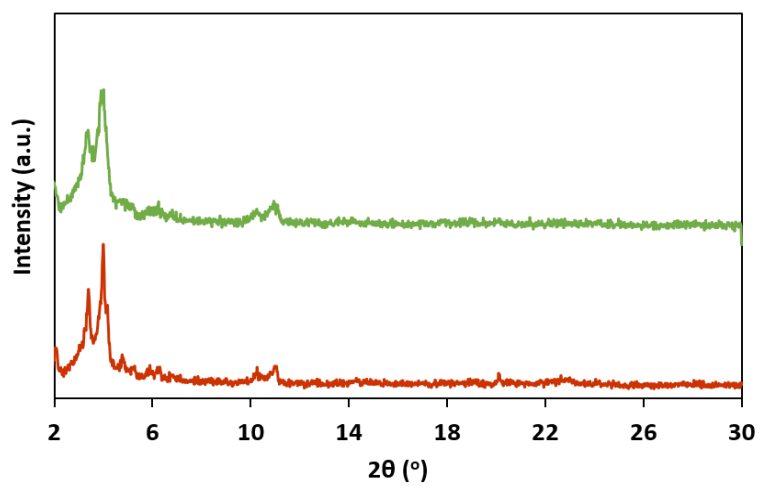


**Fig. S1:** SEM images of intact nanoMOFs synthesized at RT.

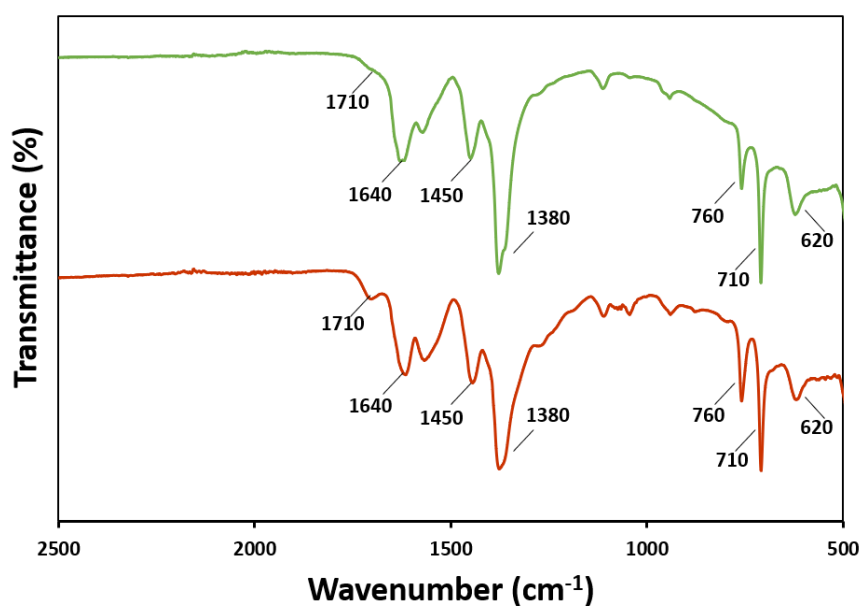
From the analysis of more than 100 nanoMOFs, mean diameters were estimated to  $60 \pm 10$  nm. However, these particles had a strong tendency to aggregate in water in reason of their small size. DLS measurements were impossible to be performed, as the average diameters reached  $700 \pm 40$  nm after 5 minutes.



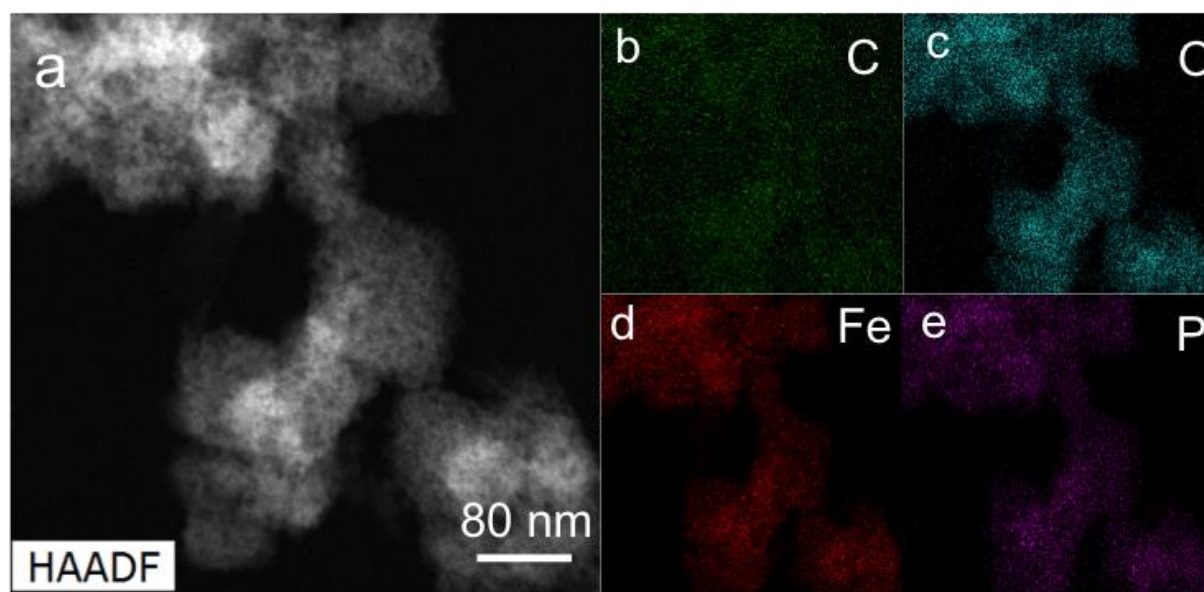
**Fig. S2:** a) STEM-HAADF and b) FFT pattern of intact nanoMOFs (MW).



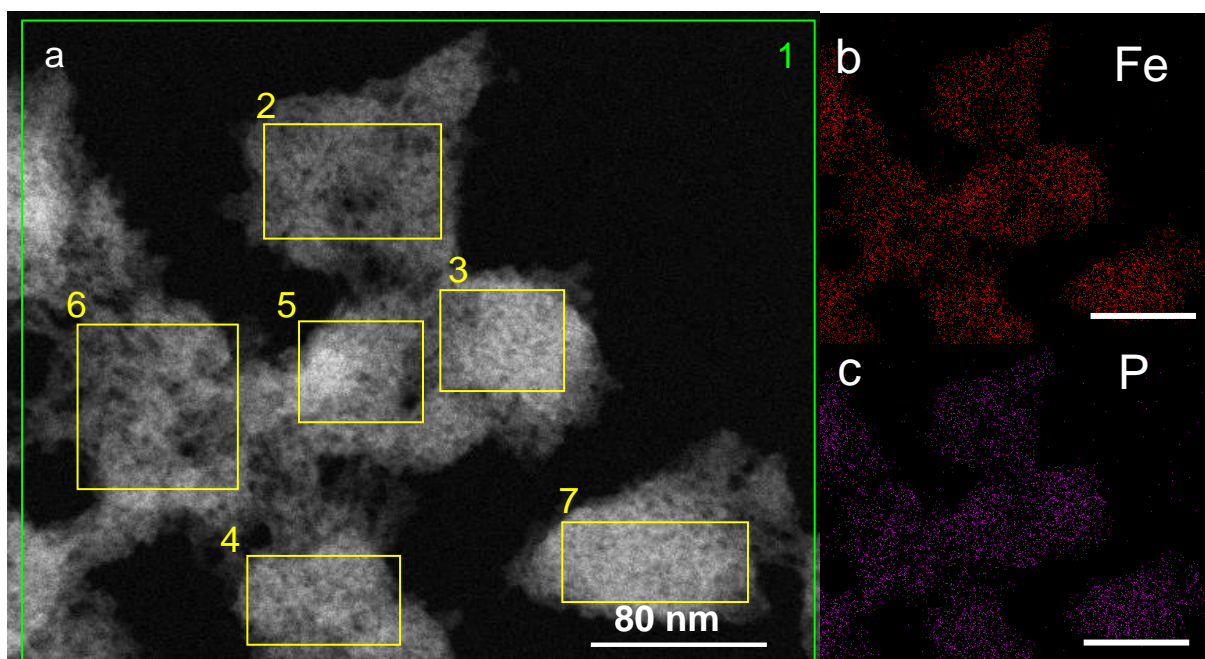
**Fig. S3:** PXRD pattern of intact nanoMOFs (MW) (red) and nanoMOFs (RT) (green).



**Fig. S4:** FT-IR spectrum of intact nanoMOFs (MW) (red) and nanoMOFs (RT) (green). The two bands at 1380 and 1640  $\text{cm}^{-1}$  indicate the successful coordination of the carboxylate ligand with the iron of the framework.

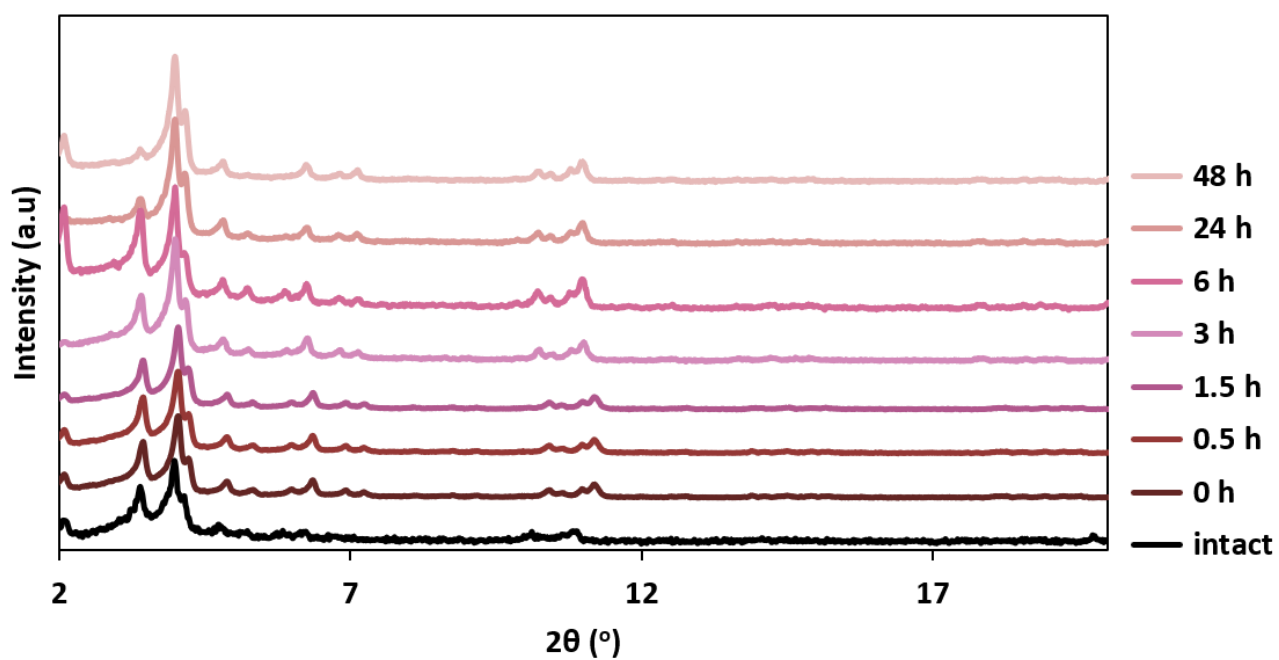


**Fig. S5:** a) STEM-HAADF images of MIL-100(Fe) nanoMOFs after 48 hours incubation in PBS at pH=7.4. b,c,d,e) STEM-XEDS elemental analysis of all the elements attributed to the sample.

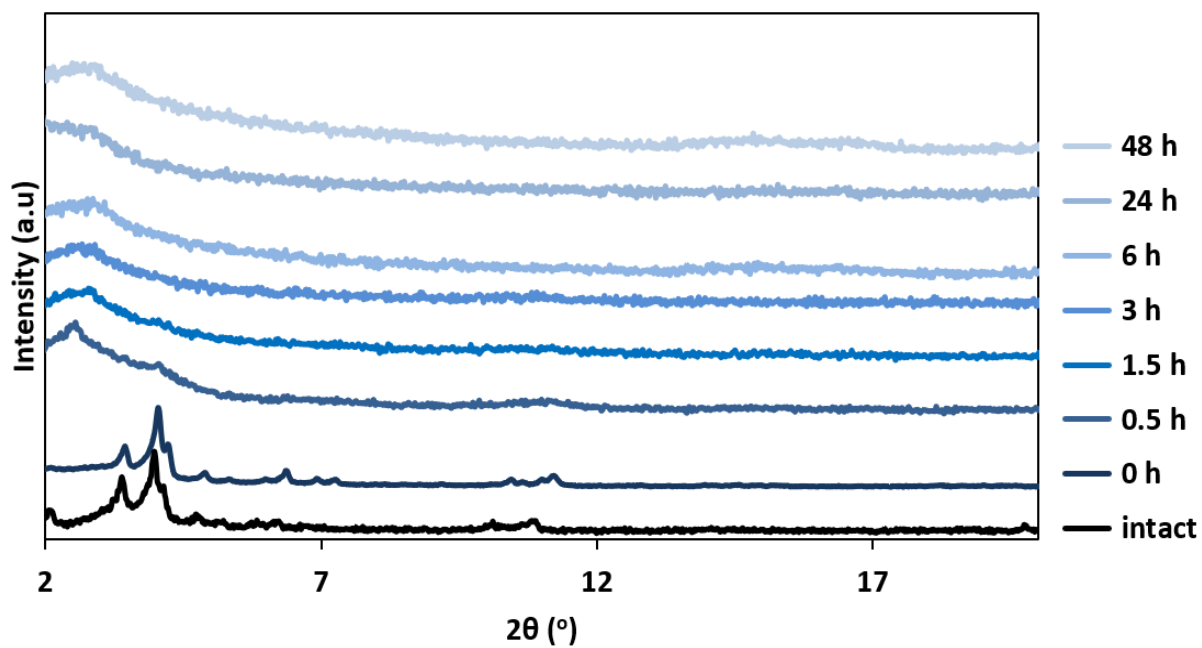


**Fig. S6:** a) STEM-HAADF images of MIL-100(Fe) nanoMOFs after 72 hours incubation in PBS 7.4. b,c) STEM-XEDS elemental analysis of all the elements attributed to the sample.

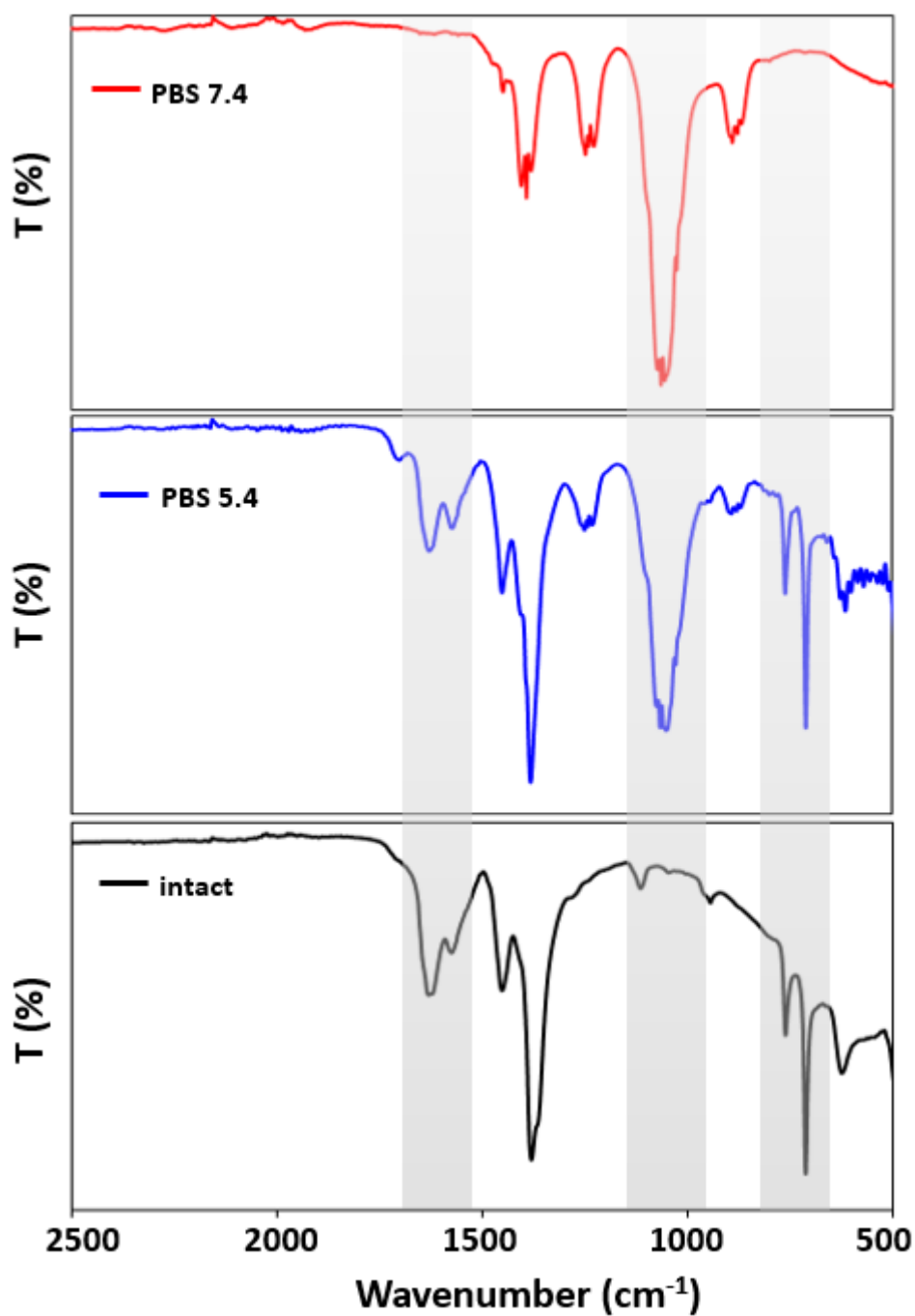
(a)



(b)

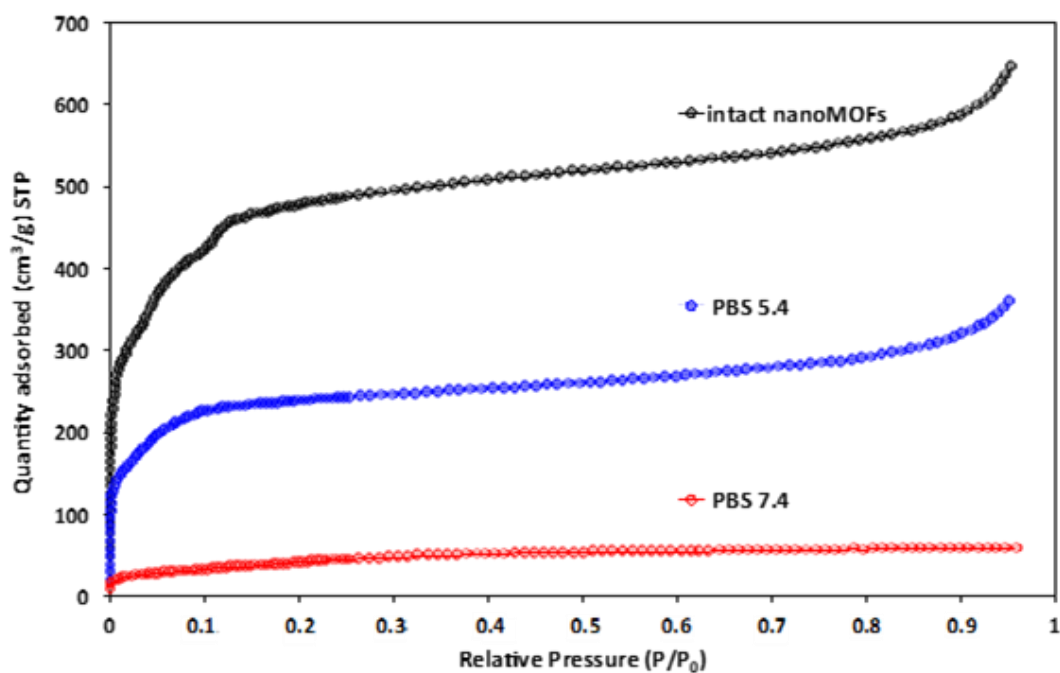


**Fig. S7:** PXRD patterns of degraded nanoMOFs (MW) at 37°C, in PBS 5.4 (a) and in PBS 7.4 (b) from time 0 to 48h. Sample concentration was 0.5. mg mL<sup>-1</sup>.

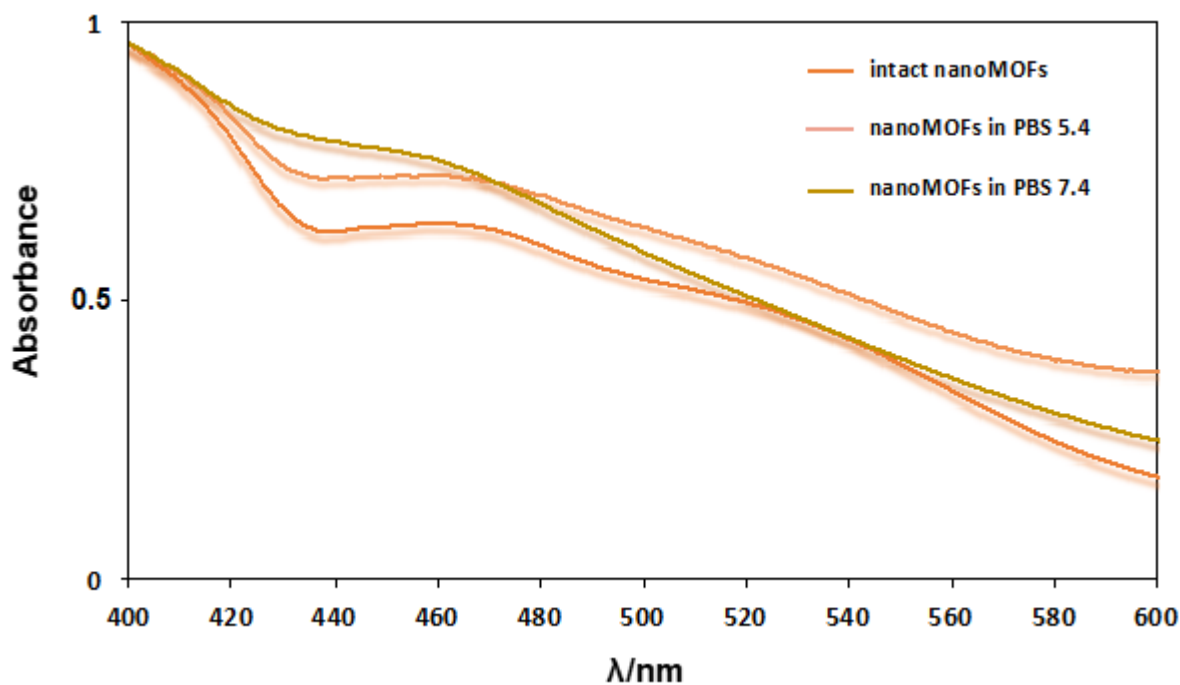


**Fig. S8:** FT-IR spectra of nanoMOFs (MW) upon 2 days incubation in PBS 5.4 and PBS 7.4.





**Fig. S9:** N<sub>2</sub> adsorption isotherms of intact nanoMOFs (MW) (black), nanoMOFs in PBS 5.4 (blue) and in PBS 7.4 (red) at 77 K (P<sub>0</sub>=1 atm).



**Fig. S10:** Solid state UV-Vis spectra collected at room temperature for MIL-100(Fe) nanoMOFs (RT) before (orange), and after incubation in PBS 5.4 (light orange) and in PBS 7.4 (brown).

### Chapter III

Advanced characterization methodology to unravel MOF stability in extremely dilute conditions

## **Chapter IV**

Drug loading in nanoscale MOFs and  
release kinetics: new insights from STEM-  
HAADF microscopy

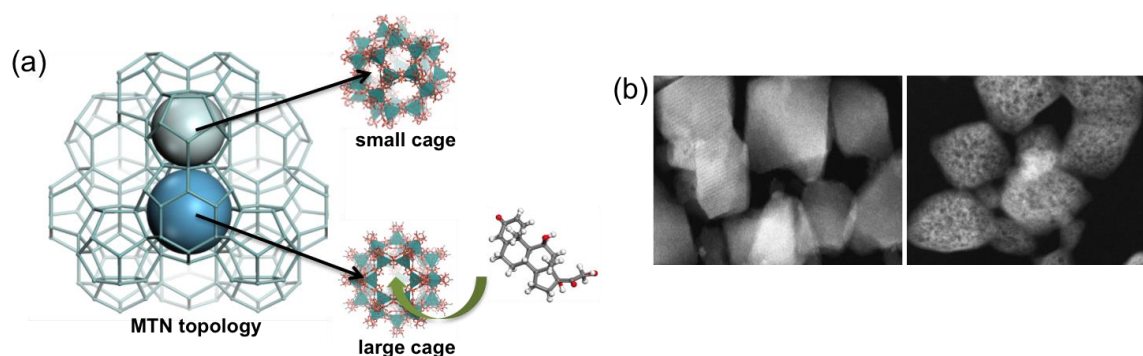
## Chapter IV

Drug loading in nanoscale MOFs and release kinetics: new insights from STEM-HAADF microscopy

## General objectives

This chapter focuses on the stability of nanoMOFs loaded with a family of active molecules in different degradation media. The chosen drugs belong to the corticosteroid family, comprising prednisolone bearing or not functional groups (sulfate, phosphate). These drugs were successfully encapsulated inside the nanoMOFs porosity and their release kinetics were followed upon incubation in PBS and/or in media containing sulfates, or in water. By this way, the competitive interactions drug/phosphates or sulfates for the iron sites could be evidenced. Different release kinetics were obtained for each studied case and were attributed to the different affinities of the active molecules with the framework. Molecular modelling studies were in good agreement with the experimental findings.

To complete the study, empty nanoMOFs were incubated in biological media (serum and blood), containing a large variety of ions, proteins and cells. STEM-HAADF investigations showed that the composition of the nanoMOFs rapidly evolved from a hybrid organic-inorganic to a more inorganic one, containing new elements, such as N and P (main elements) as well as traces of S, Mg, and Ca. These results suggest possible strong affinity of nanoMOF with proteins and other N-containing compounds from biological media, as well as with phosphate molecules. However, complementary investigations are needed to complete the study. Despite incubation in serum for 2 h, the nanoMOFs maintained their global shape but became very porous (**Figure 4.1**).



**Figure 4-1.** a) Schematic representation of prednisolone incorporation in nanoMOFs. The drug has access only to the large cages of the nanoMOFs. b) STEM-HAADF images of intact nanoMOFs (left) and degraded nanoMOFs after 2 h incubation in blood.

## Chapter IV

Drug loading in nanoscale MOFs and release kinetics: new insights from STEM-HAADF microscopy

This work has been carried on in collaboration with Dr. G. Maurin and Dr. P. Lyu in ICGM, Montpellier and Dr. G. Patriarche in C2N, Orsay, France. This work is presented under the form of an ongoing publication, with aspects, which are still under investigation.

## Drug loading in nanoscale MOFs and release kinetics: new insights from STEM-HAADF microscopy

Ioanna Christodoulou <sup>1,2</sup>, Pengbo Lyu <sup>3</sup>, Gilles Patriarche <sup>4</sup>, Christian Serre <sup>2</sup>, Guillaume Maurin <sup>3</sup>, Ruxandra Gref <sup>1,\*</sup>

<sup>1</sup> Institute of Molecular Sciences, UMR CNRS 8214, Université Paris-Sud, Université Paris-Saclay, 91400 Orsay, France;

[ioanna.christodoulou@universite-paris-saclay.fr](mailto:ioanna.christodoulou@universite-paris-saclay.fr), [ruxandra.gref@universite-paris-saclay.fr](mailto:ruxandra.gref@universite-paris-saclay.fr)

<sup>2</sup> Institut des Matériaux Poreux de Paris, CNRS Ecole Normale Supérieure, Ecole Supérieure de Physique et de Chimie Industrielles de Paris, PSL research university, 75005 Paris, France;

[christian.serre@ens.psl.eu](mailto:christian.serre@ens.psl.eu)

<sup>3</sup> Institut Charles Gerhardt Montpellier, UMR 5253 CNRS, UM, ENSCM, University of Montpellier, Montpellier, France;

[guillaume.maurin1@umontpellier.fr](mailto:guillaume.maurin1@umontpellier.fr), [pengbo.lyu@umontpellier.fr](mailto:pengbo.lyu@umontpellier.fr)

<sup>4</sup> Center for Nanoscience and Nanotechnology, C2N UMR 9001, CNRS, Université Paris Sud, Université Paris Saclay, Palaiseau, France;

[gilles.patriarche@c2n.upsaclay.fr](mailto:gilles.patriarche@c2n.upsaclay.fr)

#### **Abstract**

Metal-organic frameworks (MOFs) attract growing interest for biomedical applications. Among thousands of MOF structures, iron (III) carboxylate MIL-100 (MIL stands for Materials of Lavoisier Institute) is among the most studied MOF as drug nano-carrier, owing to its high porosity, biodegradability and lack of toxicity. Nanosized MIL-100(Fe) particles (nanoMOFs) readily coordinate with drugs leading to unprecedented payloads. Here we show how the functional groups of the drugs influence their interactions with the nanoMOFs and their release in various media. Molecular modelling enabled predicting the strength of interactions between prednisolone bearing or not phosphate or sulfate moieties (PP and PS, respectively). Noticeably, PP showed the highest interactions (loading up to 30 wt %, encapsulation efficiency >98%) and stabilized the nanoMOFs against degradation. This drug coordinated to the iron sites and was not displaced by other ions in the suspension media. On the contrary, PS was entrapped with lower efficiencies and was readily displaced by phosphates in the release media. Noticeably, the nanoMOFs maintained their faceted structures and morphologies after drug loading and after degradation, even in blood or serum. NanoMOFs lost almost the totality of their organic trimesic linkers, but their size was globally unchanged. Scanning Electron Microscopy with High Annular Dark Field (STEM-HAADF) in conjunction with Energy Dispersive X-Ray analysis (EDX) was a powerful tool enabling to unravel the main elements that enriched the nanoMOF structures during degradation and after drug loading. In a nutshell, nanoMOFs were not inert and their composition evolved as a function of the media they were in contact with.

**Keywords:** metal-organic frameworks, drug loading, stability, blood, biological media



## 1. Introduction

Nanomedicine provides the opportunity to organize matter at the nanometer scale, creating drug reservoirs with particular interest to treat severe diseases such as cancer and infections. Drug nanocarriers efficiently incorporate, protect towards degradation and ferry the active molecules from the administration site to their target, improving their pharmacokinetics.<sup>1</sup> A variety of natural and synthetic materials have been engineered at a nanoscopic level and explored for drug delivery. Liposomes, the first nanotechnology-based drug delivery system, were discovered early in the 1960s<sup>2</sup> and since many other types of drug nanocarriers have been developed, including organic or inorganic nanoparticles (NPs): polymeric and metal NPs, quantum dots, carbon nanotubes, micelles, nanogels, and dendrimers. Later, a report described the first application of hybrid organic- inorganic NPs for drug delivery applications.<sup>3</sup>

Among them, nanoscale iron trimesate metal–organic frameworks (MIL-100(Fe) nanoMOFs, MIL stands for Material of Institute Lavoisier) attract a growing interest due to their potential in the biomedical field.<sup>3,4</sup> They incorporated high payloads of a large variety of active ingredients (AIs), thanks to their highly porous structure and intrinsic amphiphilic microenvironment.<sup>5-8</sup> Additionally, MIL-100(Fe) nanoMOFs were shown to be biodegradable, non toxic both *in vitro* and *in vivo* and did not induce any adverse side effects even after repetitive administrations.<sup>9-15</sup> When nanoMOFs were in contact with media containing phosphate ions, a rapid degradation was observed due to the progressive replacing (within a few hours) of the constitutive trimesate ligands with the phosphates.<sup>16</sup> NanoMOFs presented higher stabilities in acidic pH, in gastric and simulated intestinal media.<sup>17</sup> Finally, it was shown that nanoMOFs were less degraded in serum than in PBS possibly because of the formation of a protein corona.<sup>9,12</sup> NanoMOFs were effective to avoid cancer metastases when administered in an animal model of mice bearing lung tumors.<sup>15</sup> The supposed mechanism was an instantaneous aggregation of the nanoMOFs in the lungs, followed by drug release and disaggregation due to degradation. *In vitro* studies showed that contrary to purely organic or inorganic NPs previously mentioned, hybrid nanoMOFs interact with their surrounding media by continuously changing their composition. For instance, phosphates from PBS coordinate with iron sites, and eventually erode the nanoMOFs leaving an inorganic skeleton.<sup>16,18</sup> However, the *in vivo* degradation mechanism of MIL-100(Fe) nanoMOFs is still not fully understood yet. Blood contains more than two thousands proteins and a variety of ions and other molecules, including phosphates. The erosion and composition of nanoMOFs in such a complex media is still unraveled

and is one main aim of this study. To do so, firstly, the interaction of nanoMOFs with single ions (phosphates and sulfates) was investigated. Molecular modelling was used to predict the strength of these simple interactions, whereas STEM-HAADF was used to image the nanoMOFs with atomic precision and without damaging them, before and after their degradation in various media, including blood and serum. Of main interest, STEM-HAADF coupled with Energy Dispersive X-Ray analysis (EDX) provided valuable information about the elements, which were irreversibly associated to the nanoMOFs after their incubation in the studied media.

In a similar manner, nanoMOFs interact with drugs that coordinate with their iron sites leading in some cases to strong binding and almost perfect encapsulation efficiencies. For instance, phosphorylated antiviral and anticancer drugs were successfully incorporated by soaking from aqueous solutions reaching loadings up to 35 wt %.<sup>6,19,20</sup> Agostoni *et al.*, characterized these interactions by successfully entrapping mono- and tri-phosphorylated derivatives of azidothymidine (AZT-MP and AZT-TP) into MIL-100(Fe) nanoMOFs and investigated their release kinetics under simulated physiological media.<sup>20</sup> The monophosphorylated AZT was released faster as compared to triphosphorylated AZT, due to its weaker interactions with the unsaturated iron (III) Lewis acid sites of the framework. In a further study, it was shown that the nanoMOFs loaded with AZT-TP presented a higher stability against degradation as compared to the ones loaded with AZT-MP.<sup>21</sup> Besides, the anticancer drug Gemcitabine monophosphate was encapsulated reaching a maximal loading of 30 wt % with an excellent encapsulation efficiency (>98%), validating once again the good affinity of phosphates for the iron sites.<sup>6</sup>

These studies suggest that the nanoMOFs' stability depends on the composition of the media they are in contact with and also on the presence of active molecules in their porosity. Yet, these studies focused only on nanoMOFs loaded with drugs bearing phosphate functional groups. To gain better insights on the interplay between the interactions drug-nanoMOFs-external media, in this study, a family of glucocorticoids (GCs) bearing or not functional groups (phosphates and sulfates) as used. Both moieties are prone to coordinate with the iron sites. GCs are synthetic analogues of natural steroid hormones presenting an anti-inflammatory and immunosuppressive activity.<sup>22</sup> In particular Prednisolone has been extensively studied for treatment of autoimmune diseases, such as rheumatoid arthritis,<sup>23</sup> allergies and asthma,<sup>24</sup> as well as cancer therapy to increase the effectiveness of chemotherapy and/or to reduce side effects.<sup>25</sup>

Yet, the systemic and long-term use of Prednisolone is hampered by severe side effects, low bioavailability and off-targeted biodistribution profile. To overcome these limitations, "smart" nanocarriers able to encapsulate GCs were developed for improving the therapeutic efficiency of Prednisolone and accomplish a sustained and controlled release.<sup>26</sup> PP is widely used for ocular anti-inflammatory therapy and several formulations have been already approved by U.S Food and Drug Administration (FDA).<sup>27</sup> Prednisolone and its phosphorylated and sulfated analogues (PP and PS) were incorporated for the first time in MIL-100(Fe) nanoMOFs. Density functional theory (DFT) calculations have been carried out to understand the affinities of Prednisolone and its derivatives with MIL-100(Fe). The drug-loaded nanoMOFs were allowed to degrade in media containing phosphates and/or sulfates, to analyze the competitive interactions. In parallel, release kinetics of the trimesate ligand was evaluated. We explored in a systematic manner the morphological and chemical stability of empty and loaded MIL-100(Fe) nanoMOFs in different media, using STEM-HAADF coupled to EDX.

## 2. Materials and Methods

### 2.1. Materials

Iron(III) chloride hexahydrate (98%, Alfa Aesar, France), and 1,3,5-benzenetricarboxylic acid (trimesate, 95%, Sigma Aldrich, France) were used for the synthesis of nanoMOFs. Absolute ethanol (99%, Carlo Erba, France) was used for the purification of nanoMOFs. Prednisolone (SigmaAldrich, France), Prednisolone phosphate (sodium salt) (Cayman Chemical, France) and methyl prednisolone sulfate (triethylamine salt) (Clearsynth, India) were the studied active molecules for drug encapsulation. Acetonitrile and methanol (HPLC grade) were purchased from Sigma-Aldrich (France) as organic mobile phases for detection of AIs and ligand. For the preparation of aqueous buffer solutions for HPLC measurements, ammonium acetate (99%, Alfa Aesar, France),  $\text{NaH}_2\text{PO}_4$  and  $\text{Na}_2\text{HPO}_4$  (Sigma Aldrich, France) were used. Ortho-phosphoric acid ( $\geq 85\%$ ) and potassium hydroxide (Sigma Aldrich, France) were used for the adjustment of the pH. DPBS (1X, pH=7.4) was purchased from Thermo Fischer Scientific. It contains 1.47 mM  $\text{KH}_2\text{PO}_4$ , 8.59  $\text{Na}_2\text{HPO}_4 \cdot 7\text{H}_2\text{O}$ , 137 mM NaCl and 2.66 mM KCl. Anhydrous sodium sulfate (99%, abcr, GmhB Germany) and sodium phosphate dibasic (Sigma Aldrich, France) were purchased for release studies.

Serum and blood were recovered from BALB/c mice after their sacrifice.

Milli-Q water was obtained from a Millipore apparatus equipped with a 0.22 $\mu$ m filter (18.2 M $\Omega$  cm). Reagents and solvents were used without further purification.

## 2.2. Synthesis of nanoMOFs

NanoMOFs were prepared by microwave-assisted hydrothermal synthesis from a mixture of iron chloride hexahydrate (8.97 mmol) and 1,3,5-benzenetricarboxylic acid (4.02 mmol) in 20 mL of deionized water, as previously described.<sup>8, 16</sup> The mixture was heated for 6 min at 130 °C under stirring (ramp time : 1.30 min, hold time : 4.30 min). The power applied was 800 Watts (Mars-5, CEM, US) with a power maximum output 800 and pressure at 800 Watts. At the end of the heating procedure, the reaction vessel the same quantity of water (20 mL) was added to the mixture and it was placed in an ice bath for 10 min, to stop the nucleation process. The synthesized nanoMOFs recovered by centrifugation (10000 rpm) and washed with absolute ethanol 6 times to remove the residual non-reacted trimesate. A last centrifugation was performed (4000 g, 1 min) to separate the smaller from the larger nanoMOFs. The final product was stored in ethanol until final use and the particles either were dried or re-suspended in aqueous media depending on the characterization technique.

## 2.3. Characterization of nanoMOFs

A series of characterization studies was used, to check the successful synthesis of MIL-100(Fe) nanoMOFs. Their morphology was observed by TEM/STEM studies, performed on a Titan Themis microscope corrected for spherical aberrations on the probe. The microscope was equipped with the "Super-X" analysis EDX system with 4 SDD detectors allowing to achieve a solid angle of 0.8 steradian.

The observations were made at 200 kV with a sufficiently low probe current, ie around 40 to 50 pA, so as not to degrade the sample. The STEM-EDX chemical maps were carried out under the same conditions, for an acquisition time of approximately 15 to 20 minutes.

For the HAADF-STEM images acquisition, the half-angle of convergence of the probe was 17 mrad and the collection half-angle of the Annular Dark Field detector was 69 mrad (inner angle) and 200 mrad (outer angle).

For the TEM grid preparation, a 2  $\mu$ L drop of the solution was placed on a 200 mesh copper grid covered with a pure carbon membrane (from Ted Pella).

Mean hydrodynamic diameter and size distribution were obtained by Dynamic Light

Scattering (DLS, Malvern Nano ZS, Zetasizer Nano series, France). Surface charge was evaluated by measuring the  $\zeta$ -potential with the Zetasizer NanoZS. Samples were prepared to a final concentration of  $0.1 \text{ mg mL}^{-1}$ , as recommended.<sup>28</sup>

The crystallinity of nanoMOFs was recorded on a D8 Advance Bruker Diffractometer in Debye-Scherrer geometry, in the  $2\theta$  range  $2\text{-}40^\circ$ . The diffractometer was equipped with a Ge (111) monochromator producing Cu  $K\alpha_1$  radiation ( $\lambda = 1.540598 \text{ \AA}$ ) and a LynxEye detector.

Infrared spectra showing chemical composition of the nanoparticles were evaluated with a Nicolet iS5 FT-IR ThermoFisher spectrometer between  $400$  and  $4000 \text{ cm}^{-1}$ .

## 2.4. Drug encapsulation

Drug loading was performed via a green procedure by simple impregnations of nanoMOFs into aqueous drug solutions. Before that, nanoMOFs ethanolic suspensions ( $0.5 \text{ mg mL}^{-1}$ ) were extensively washed with Milli-Q water. Continuously, they were re-dispersed in drug aqueous solutions ( $0.15 \text{ mg mL}^{-1}$ ). All the suspensions were gently mixed overnight at RT. After, they were centrifuged ( $17\,000 \text{ g}$ ,  $20 \text{ min}$ ) and supernatants were analysed by HPLC to quantify the amount of non-encapsulated drug.

The theoretical loading (TL) was defined using equation (1):

$$TL(\%) = \frac{\text{Drug solution (mg)}}{\text{nanoMOFs (mg)}} \times 100 \quad (1)$$

The drug loading (DL) and the encapsulation efficiency (EE) were calculated using equation (2) and (3) respectively:

$$DL(\%) = \frac{\text{Encapsulated drug (mg)}}{\text{nanoMOFs (mg)}} \times 100 \quad (2)$$

$$EE(\%) = \frac{\text{Encapsulated drug (mg)}}{\text{initial drug (mg)}} \times 100 \quad (3)$$

where "encapsulated drug" represents the amount (mg) of entrapped drug in nanoMOFs and "initial drug" represents the amount (mg) of total drug available in the starting solution.

## 2.5. Drug and Ligand release

To compare release studies in different media, the loaded pellets (0.5 mg) were re-suspended in 1 mL of each solution and incubated at 37 °C under continuous stirring. At different time points (0 h, 0.5 h, 1.5 h, 3 h, 6 h, 24 h, 48 h, 72 h) supernatants were recovered by centrifugation (17 000 g, 20 min) and analyzed by HPLC to quantify the released drug and the corresponding trimesate ligand.

## 2.6. HPLC measurement conditions

Drug content and release, as well as the release kinetics of the corresponding trimesate were followed by High Performance Liquid Chromatography (HPLC).

Different conditions were used for the quantification of the drugs and trimesic acid by HPLC.

### Determination of Prednisolone

The detection of Prednisolone was carried out in a reversed-phase HPLC system (Agilent 1100, USA) equipped with a Phenomenex C18 column (4.6 × 250 mm, 5 μm). Prednisolone was analyzed according to the official European Pharmacopoeia Method.<sup>29</sup> A flow rate of 1 mL min<sup>-1</sup> was used. The temperature was fixed at 40 °C and the injection volume was 10 μL. The mobile phase contained A (water):B (MeCN) (50:50 v/v) and the drug was detected through a gradient program, consisting of the following steps:

40 % of B was held for 14 minutes, then B was gradually increasing to 80 % until 20 minutes were reached and finally it was kept constant for 5 more minutes. The sample was monitored by UV absorbance at 254 nm. Retention time of Prednisolone was 8.7 min.

### Determination of PP

The detection of PP was carried out in a reversed-phase HPLC system Waters Alliance e2695 Separations Module (Waters, Milford, MA) equipped with a UV-Vis detector Waters 2998. The system was controlled by Agilent software. SunFire-C18 reverse-phase column (5 μm, 4.6 × 150 mm<sup>2</sup>, Waters) was employed and analysis method was adjusted, as previously reported.<sup>30</sup> More precisely, an isocratic method with a mobile

Drug loading in nanoscale MOFs and release kinetics: new insights from STEM-HAADF microscopy

phase containing A (acetate buffer 0.01 M, pH=7), B: ACN: C: MeOH (75:20:5 v/v/v) at a flow rate of 0.8 mL min<sup>-1</sup> was used. The temperature was fixed at 30 °C and the injection volume was 20 µL. The sample was monitored by UV absorbance at 254 nm. Retention time of Prednisolone sodium phosphate was 6.3 min.

### Determination of PS

The detection of PS was carried out in a reversed –phase HPLC system (Agilent 1100, USA) equipped with a Phenomenex C18 column (4.6 × 250 mm, 5 µm). The system was controlled by Agilent software. A flow rate of 1 mL min<sup>-1</sup> was used. The temperature was fixed at 25 °C and the injection volume was 50 µL. The mobile phase consisted of A: ammonium acetate buffer (0.01 M):B (ACN) (90:10) and the drug was detected through a gradient program, consisting of the following steps:

For the first 10 minutes, 10 % of B was gradually increasing to 90 %, then it was kept constant for 15 more minutes and finally it was increased back to 10 % for the last 5 minutes. The sample was monitored by UV absorbance at 286 nm. Retention time of methyl prednisolone sulfate was 7.9 min.

### Determination of Trimesate Ligand

The detection of trimesic acid was carried out in a reversed–phase HPLC system Waters Alliance e2695 Separations Module (Waters, Milford, MA) equipped with a UV-Vis detector Waters 2998. The system was controlled by Agilent software. SunFire-C18 reverse-phase column (5 µm, 4.6 × 150 mm<sup>2</sup>, Waters) was employed. For the analysis of BTC, a mobile

phase A consisting of a buffer solution (0.04 M, pH=2.5) and a mobile phase B MeCN (50:50) was used. The injection volume was 50 µL and the detection wavelength was set at 225 nm. The column temperature was fixed at 25 °C. <sup>31</sup> Retention time of BTC was 3.1 min.

Buffer preparation : NaH<sub>2</sub>PO<sub>4</sub> (2.4 g, 0.02 mol) and Na<sub>2</sub>HPO<sub>4</sub> (2.84 g, 0.02 mol) were dissolved in 1 L of Milli-Q water. The pH was then adjusted to 2.5 with H<sub>3</sub>PO<sub>4</sub> (≥85%).

## 2.7. Computational Section

The interactions of Prednisolone, PP and PS with the Fe-oxo-trimer present in MIL-100(Fe) were computationally assessed using cluster-based Density Functional Theory

(DFT) calculations. The geometry optimization of each drug@Fe-oxomer trimer model was performed using B3LYP exchange-correlation functional as implemented in the Gaussian 09 program suite. The TZVP<sup>32</sup> basis set was employed for all atoms. The DFT-D3 method<sup>33</sup> was implemented to include the dispersion contribution. Several starting configurations for the drugs were considered to converge towards the lowest energy minima. The drug/host interaction energy for all these systems was further calculated by the difference between the energy of the optimized drug@Fe-oxomer trimer model and those of the individual constituents.

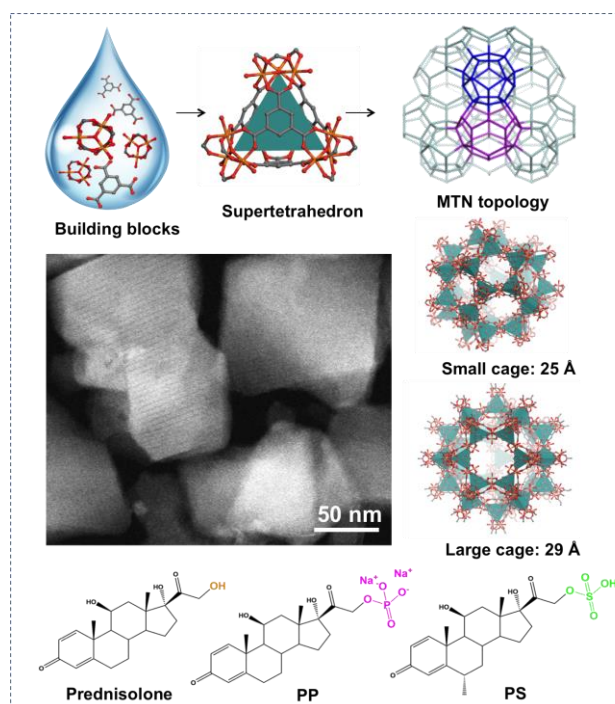
### 3. Results and Discussion

#### 3.1. Synthesis and characterization of empty and loaded nanoMOFs

MIL-100(Fe) is build up from the self-assembly of iron (III) trimers linked with organic trimesate ligands, forming supertetrahedra which further assemble leading to a 3D micro/mesoporous structure of MTN topology.<sup>34</sup> The resulting structure consists of small and large cages with diameters of around 25 Å and 29 Å, respectively. They are accessible through microporous pentagonal (5.6 Å) and hexagonal (8.6 Å) windows, respectively.<sup>35,36</sup> A "green" microwave-assisted hydrothermal method was used here to obtain submicron particles of controlled sizes (nanoMOFs), as it has been previously described.<sup>8,16</sup> The crystallinity of synthesized particles was confirmed from their diffraction patterns (Figure S1), in agreement with previous studies.<sup>37,38</sup> STEM-HAADF electron microscopy investigations revealed that the nanoMOFs possessed faceted structures (Figure 1). The nanoMOF average hydrodynamic diameter was  $230 \pm 20$  nm according to DLS investigations, with a polydispersity index (PdI) of 0.09, indicating their homogeneous distribution.

The three drugs, Prednisolone, PP and PS were successfully loaded within the nanoMOF porosity by overnight incubation from aqueous solutions (Figure 1). The synthesized nanoMOFs acted like molecular sponges soaking the AIs in their internal porosity. The molecular dimensions of Prednisolone ( $14.2 \times 8.5$  and  $7.5$  Å) and its flexible derivatives PP ( $17.8 \times 9.5$  and  $7.3$  Å) and PS ( $17.2 \times 8.4$  and  $8.0$  Å) are compatible only with the hexagonal large windows ( $4.7 \times 5.6$  and  $8.6$  Å) of the rigid nanoMOFs and not with the pentagonal ones. (Table S1).



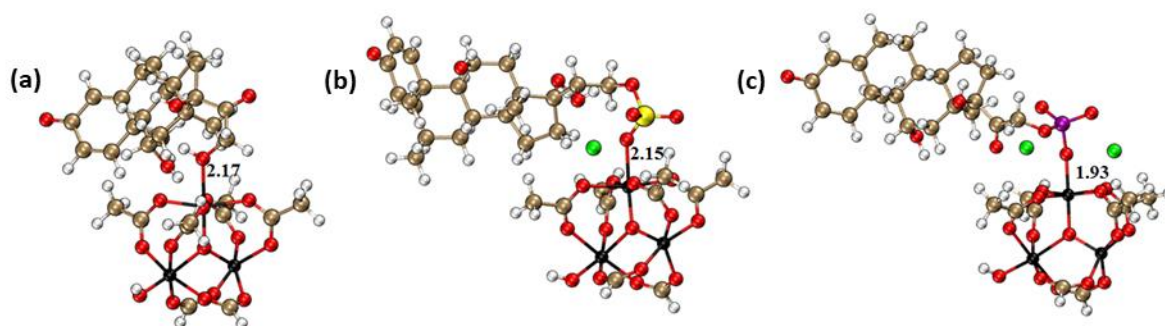


**Figure 1.** Schematic representation of MIL-100(Fe) structure resulting from the assembly of iron (III) trimers and trimesic acid. The three active molecules, Prednisolone, PP and PS were encapsulated into the nanoMOFs large cages by overnight impregnation.

The optimized drug loading and encapsulation efficiencies for Prednisolone, PS and PP were quantified by HPLC. PP, the phosphorylated form of prednisolone presented both the highest drug loadings (30 wt %) and encapsulation efficiencies (~ 95 %) as compared to the other two drugs (19 and 57 wt % for Prednisolone and 15 and 72% for PS). The almost perfect EE for PP is in line with previously reported studies, showing that phosphate drugs such as gemcitabine-phosphate and AZT-phosphate were entrapped with EE close to 100%.<sup>6,20,39</sup>

Prednisolone loading of 19 wt % was achieved after overnight impregnation with the nanoMOFs. Yet, the EE was only 57 %, suggesting that this molecule does not have strong interactions with the nanoMOFs. PS showed a significantly higher EE of more than 70 %, which could be possibly attributed to stronger interactions with the MOF framework. These results are in good agreement with molecular simulations. DFT calculations were performed to reveal the preferential adsorption sites of the three drugs and their affinity for the MIL-100(Fe) MOFs. Figure 2 shows that the three drugs

bind to the coordinatively unsaturated sites (CUS) via the oxygen atoms of their functional groups, i.e.  $-OH$ ,  $-OSO_3$  and  $-OPO_3$  associated with characteristic Fe-O distances of 2.17 Å, 2.15 Å and 1.93 Å respectively (for comparison, the Fe-O distance is 1.79 Å in the case of Fe CUS coordinated by water). The corresponding simulated interaction energies were found to be  $-156 \text{ kJ.mol}^{-1}$ ,  $-228 \text{ kJ.mol}^{-1}$  and  $-289 \text{ kJ.mol}^{-1}$  for Prednisolone, PS and PP, respectively. Therefore, the MIL-100(Fe) affinity to the drugs is predicted to increase according to the following sequence  $P < PS < PP$ , in agreement with the experimental data.



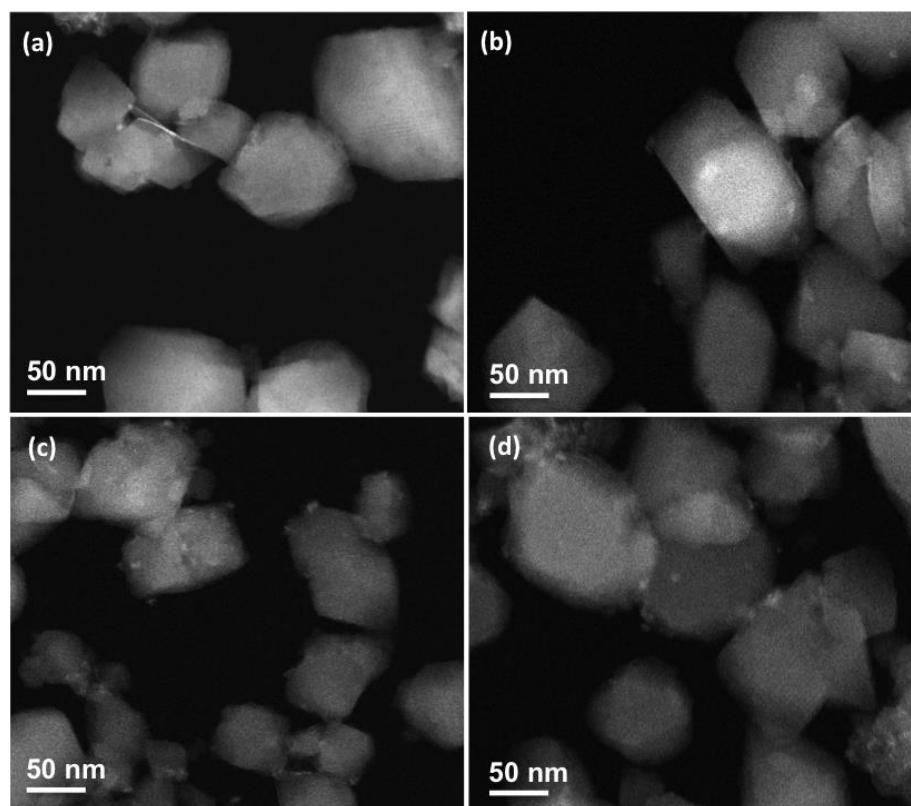
**Figure 2.** DFT-most stable drug@Fe-oxo trimer model for (a) Prednisolone, (b) PP and (c) PS. Color code : C (brown), O (red), H (white), ion (black), S (yellow), P (purple) and Na (green). The distances are in Å.

STEM-HAADF microscopy was performed to observe morphological changes after Prednisolone, PS and PP loading. Whatever the loaded drug, the nanoMOFs maintained their faceted morphology (Figure 3b,c,d) and their average size measured on more than 100 individual particles was similar (Prednisolone;  $155 \pm 57 \text{ nm}$ , PS;  $147 \pm 30 \text{ nm}$ , PP;  $161 \pm 58 \text{ nm}$ ) as compared to the empty nanoMOFs ( $141 \pm 37 \text{ nm}$ ).

PXRD patterns of nanoMOFs before and after loading confirmed the maintenance of their crystalline structure in the presence of Prednisolone, PP and PS (Figure S2). The three incorporated drugs were crystalline (Figure S2) displaying characteristic Bragg peaks. These peaks were undetectable in all drug-loaded nanoMOFs, suggesting the absence of residual free crystalline drug molecules and that the drugs were incorporated in a molecular state inside the cages.

Infrared spectroscopy investigations suggested the presence of interactions between the drugs and the framework after impregnations (Figure S3). More precisely, the bands at  $1700 \text{ cm}^{-1}$ , corresponding to the  $\nu(C=O)$  stretching of P, PP and PS were shifted, once encapsulated into the nanoMOFs.<sup>40,41</sup> These results are in line with previous

studies showing similar shifts in the case of acetylsalicylic acid and caffeine incorporation in MIL-100(Fe) nanoMOFs.<sup>31,42</sup>

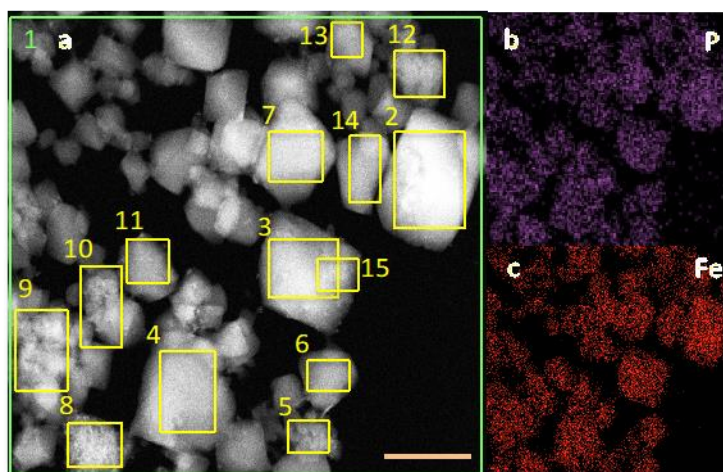


**Figure 3.** STEM-HAADF images of nanoMOFs before (a) and after loading with 19 wt % Prednisolone (b) 30 wt % PP (c) and 15 wt % PS (d).

STEM-HAADF microscopy coupled with X-Ray energy dispersive spectrometry (XEDS) was a powerful tool to shed light on the distribution of the incorporated drugs in the nanoMOFs after loading. Among the three drugs, only PS and PP have distinctive elements (P and S) different from the nanoMOFs containing O, C and Fe atoms. NanoMOFs contain a non-negligible amount of coordinated water molecules, which cannot be removed even under high vacuum. Therefore, information on oxygen distribution arises both from coordinated water, the drug molecules and trimesate ligands. Moreover, sample holders contain carbon, making difficult to separate information arising from carbon atoms in the grids and in the analyzed samples. In conclusion our observations were based on Fe atoms, which were shown to remain associated to the nanoMOFs' without being released in the degradation media.<sup>16</sup>

Figure 4 presents the elemental distribution of Fe (representative of the MOF iron sites) and P (representative of PP) after encapsulation of PP into the nanoMOFs. Globally, PP

appears homogeneously distributed inside the particles (Figure 4b). Additionally, P/Fe ratio was calculated for different regions of interest (indicated by yellow rectangles in Figure 4a, to further confirm samples' homogeneity. The P/Fe ratio corresponds to the P (or drug molecule) bound per each iron site of nanoMOFs. Noteworthy, the P/Fe average values found experimentally by elemental analysis ( $0.5 \pm 0.1$ ) (Table 1) were in good agreement with the theoretical calculations (0.6), representative of the occupancy of the available iron sites from PP, after taking into account the experimental drug loading determined by HPLC (30 wt %). (See Theoretical calculations in SI).



**Figure 4.** a) Typical STEM-HAADF images of nanoMOFs loaded with PP at a DL of 30 wt %. b,c) Elemental distribution of Fe (red) and P (violet) into the nanoMOFs after PP loading. Yellow rectangles represent the selected regions of interest and the green rectangle corresponds to the quantification of the elements in the entire image. Scale bar represents 200 nm.

**Table 1** shows the element distribution (by norm. at.%) and the calculated ratio of P (drug molecule) per each iron trimer. The calculated values correspond to the selected regions of interest as numbered in Figure 3.

Regions	Fe [norm. at.%]	P [norm. at.%]	Ratio trimer=3*(P/Fe)
<b>1</b>	<b>2.0 ± 0.3</b>	<b>0.3 ± 0.1</b>	<b>0.5</b>
2	2.8 ± 0.4	0.4 ± 0.0	0.4
3	2.7 ± 0.4	0.3 ± 0.1	0.3
4	2.8 ± 0.4	0.3 ± 0.1	0.3
5	2.3 ± 0.4	0.2 ± 0.1	0.5
6	2.5 ± 0.5	0.2 ± 0.1	0.2
7	2.5 ± 0.4	0.4 ± 0.1	0.5
8	3.8 ± 0.6	0.6 ± 0.1	0.5
9	2.6 ± 0.4	0.4 ± 0.1	0.5
10	2.7 ± 0.5	0.4 ± 0.1	0.4
11	2.5 ± 0.5	0.4 ± 0.1	0.5
12	2.6 ± 0.5	0.5 ± 0.1	0.6
13	2.5 ± 0.5	0.4 ± 0.1	0.5
14	2.4 ± 0.5	0.3 ± 0.1	0.4
15	2.4 ± 0.9	0.4 ± 0.2	0.5

These results showed the homogeneous distribution of PP in the nanoMOFs and the good agreement between the data obtained by HPLC and by individual STEM-HAADF – EDX investigations. In the case of PS, a similar homogeneous drug distribution was found (Figure S4), as revealed by the constitutive S element distribution. However, more precise quantifications were not possible mainly because contrary to PP, the PS molecules were prone to be released out of the nanoMOFs during sample preparation (washings and drying) for microscopy investigations, due to their weaker interactions with the framework.

### 3.2. Degradation of empty nanoMOFs in media containing phosphates and sulfates

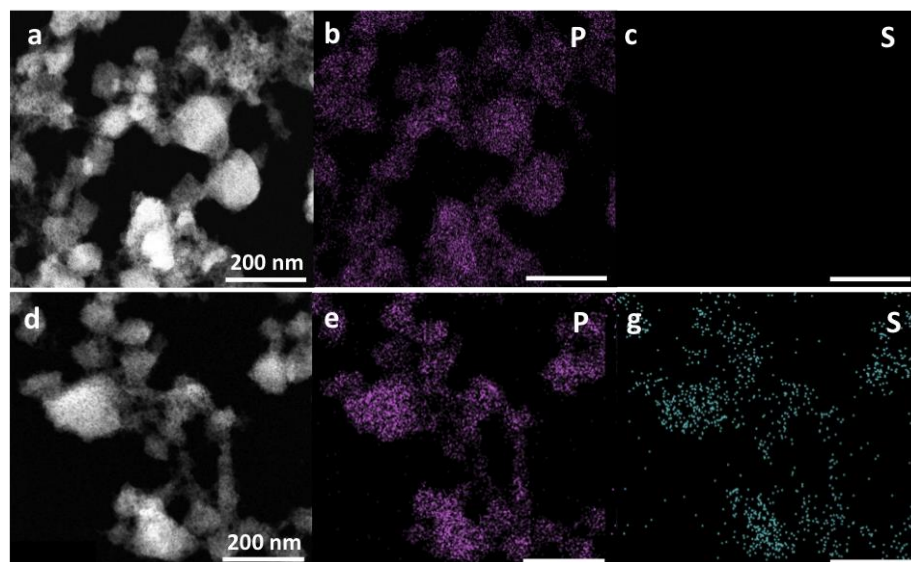
High resolution STEM-HAADF coupled to EDX was further used to investigate the morphological and chemical composition changes of the nanoMOFs upon degradation in the presence of phosphates from PBS. After two days incubation, the structure became amorphous and spongy but the nanoMOFs didn't collapse (Figure 5a). During the same incubation time, the amount of trimesate constitutive ligand was  $98 \pm 2\%$ , suggesting a total degradation. The P/Fe ratio was found  $0.7 \pm 0.1$ , suggesting that one phosphate molecule was bound per each iron trimer.

## Chapter IV

### Drug loading in nanoscale MOFs and release kinetics: new insights from STEM-HAADF microscopy

This amount is higher than the P/Fe ratio obtained in the case of PP loading ( $0.5 \pm 0.1$ ) and could be explained by the fact that PP molecules can only access large cages, whereas the phosphate ones can access both small and large cages. These data support the high affinity of phosphate molecules for the iron sites inside the nanoMOFs.

In a complementary study, nanoMOFs were incubated in a medium containing both sulfate and phosphate ions in an equimolar ratio, in order to investigate their competition for the iron sites. Figure 5c shows that after incubation, the particles presented similar morphologies as those incubated in phosphate media (Figure 6a). They incorporated both P from phosphates and S from sulfates, and these elements were colocalized with Fe, showing that they were located inside the nanoMOF matrix. However, the S amounts were close to the detection limit ( $< 0.1\%$ ) as compared to P amounts, which were  $0.7 \pm 0.1$ , similar to the case of nanoMOF incubation in PBS.



**Figure 5.** a,d) Typical STEM-HAADF images of nanoMOFs ( $0.25 \text{ mg mL}^{-1}$ ) after 48 hours incubation in PBS and in a media containing equimolar amounts of  $\text{Na}_2\text{SO}_4$  and  $\text{Na}_2\text{HPO}_4$ . b,c,e,g) STEM-XEDS elemental analysis of degraded nanoMOFs. P (purple) and S (blue).

These findings highlight the preferential affinity of the nanoMOFs for phosphates as compared to sulfates. It was therefore interesting to study the release of the drugs bearing phosphate and sulfate moieties in media containing phosphates or sulfates.

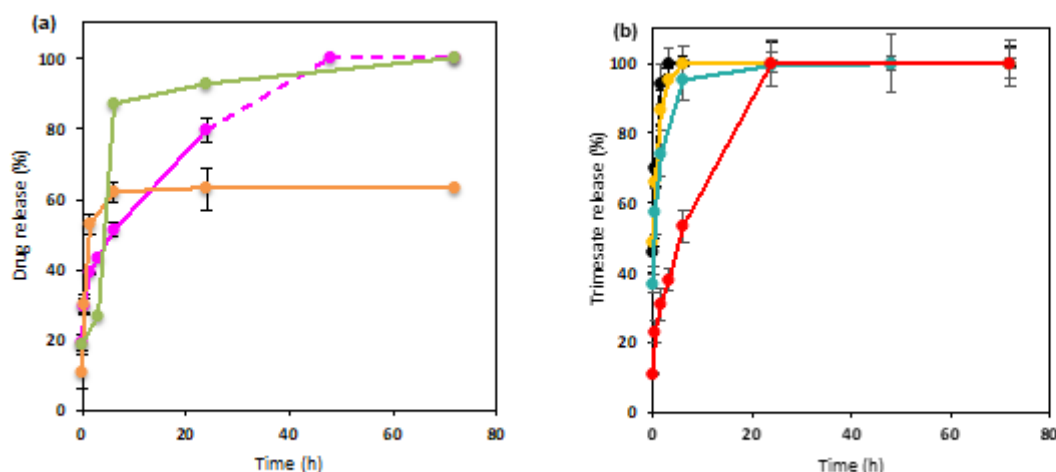
### 3.3. Comparative study of release kinetics of Prednisolone, PS and PP in different media

The release of the three drugs and nanoMOF degradation were first studied in PBS (Figure 6). Even after one month incubation in PBS, Prednisolone release did not exceed 60 %, possibly due to its poor solubility in aqueous media. Indeed, as compared to PP and PS which are freely soluble in aqueous media, prednisolone is a hydrophobic molecule, with a solubility in water of only around  $2 \cdot 10^{-2} \text{ mg L}^{-1}$ .

(Table S2). To release more prednisolone from the nanoMOFs it was necessary to add ethanol, a good solvent for the drug, in the release medium. By this way, prednisolone release reached 75 % within 24 hours, as measured by HPLC.

Prednisolone and PS were released in a “burst manner” with 53 and 87 % in the first and a half hour, and after 6 hours respectively. On the contrary, PP was released in a controlled manner, reaching 40% after 3 h and 100% after 48 hours incubation. This data suggests a lower affinity of Prednisolone and PS for the nanoMOFs as compared to PP and are in agreement with molecular simulations. The sustained release of PP was in agreement with previous studies on the release of phosphate molecules such as AZT-TP from MIL-100(Fe) nanoMOFs.<sup>19</sup>

In parallel, the release of the constitutive ligand (trimesate) was also quantified, to gain insights on the possible influence of the encapsulated molecules on the nanoMOFs stability. Figure 6b summarizes the kinetics of ligand release from the nanoMOFs loaded or not with drugs. Empty nanoMOFs lost 70% of their constitutive ligand within 30 minutes and the totality within 3 hours. These findings clearly indicate the rapid erosion of the nanoMOFs in PBS. The erosion was slightly reduced in the case of nanoMOFs loaded with Prednisolone (60 %) and PS (66 %) at the same time point (30 minutes). Interestingly, ligand release was drastically reduced for PP nanoMOFs loaded with PP (23 % after 30 minutes and 38 % after 3 h), suggesting that the firm binding of PP to the nanoMOFs' iron site stabilizes their structure.

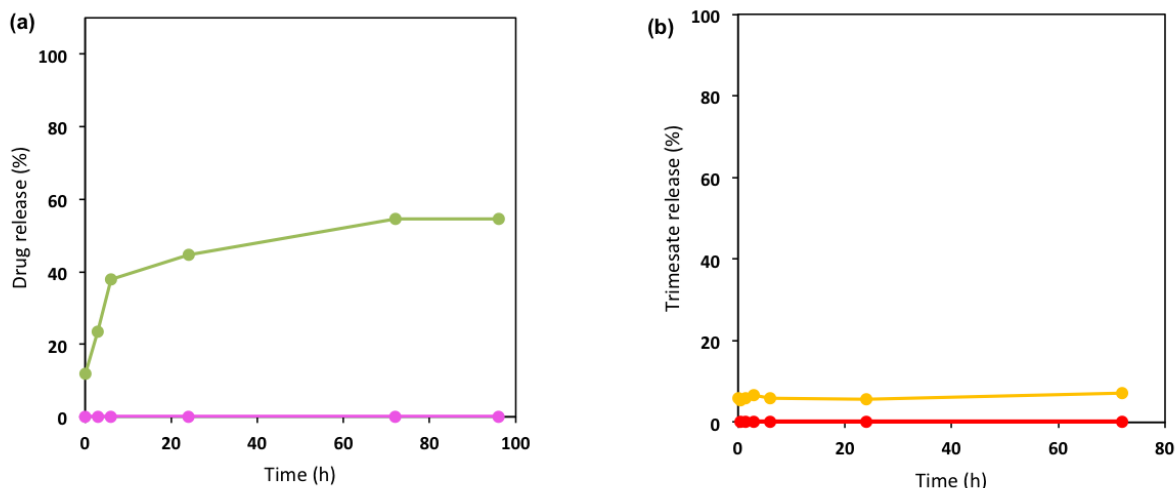


**Figure 6.** a) Comparison of Prednisolone (orange), PP (pink) and PS (green) release in PBS. b) Trimesate loss of loaded nanoMOFs with P (blue), PS (yellow) and PP (red) and empty nanoMOFs (black). Sample concentration was  $0.5 \text{ mg mL}^{-1}$ .

Furthermore, drug and ligand release were evaluated in a medium containing sulfate ions instead of phosphate ones (Fig. 7) in an attempt to gain more insights on the competition between the ions of the degrading solution and the functional groups of the drugs. To note, Prednisolone was not selected for this study, due to its poor solubility in aqueous media, as previously indicated. Interestingly, PP was not released even after 3 days incubation in sulfates, in contrast to PS, that reached around 50 % (Figure 7a). This suggests that sulfate ions from the release media diffuse inside the nanoMOFs and replace the coordinated PS, in a similar manner as phosphate ions from the media replace PP leading to its release.

A low trimesate release ( $< 10\%$ ) was observed for both PP and PS-loaded nanoMOFs. These results clearly show the stability of the nanoMOFs in sulfate media as compared to phosphate ones (Figure 7b). In a nutshell, the release and degradation studies are in agreement with DFT calculations, showing that phosphates (from the media or linked to the drugs) have higher affinity for the MOFs than phosphates.





**Figure 7.** a) Comparison of PP (pink) and PS (green) release in sulfates. b) Trimesate loss of nanoMOFs with PS (DL=15 wt %) (yellow) and PP (DL=30 wt %) (red) in sulfate-containing media, pH 7.4, 37°C. Sample concentration was 0.5 mg mL<sup>-1</sup>.

The studies performed in media containing only a single type of ions (phosphates or sulfates), were a valuable tool to explore the morphological and compositional changes of the particles. Yet, it is important to study the stability of the nanoMOFs in more complex media, close to the living organism to explore the effect of different ions on the degradation mechanism of the MOFs matrices. Therefore, bare nanoMOFs were incubated in serum and blood and their modifications were observed by STEM-HAADF-EDX.

### 3.4. Degradation of empty nanoMOFs in serum and blood

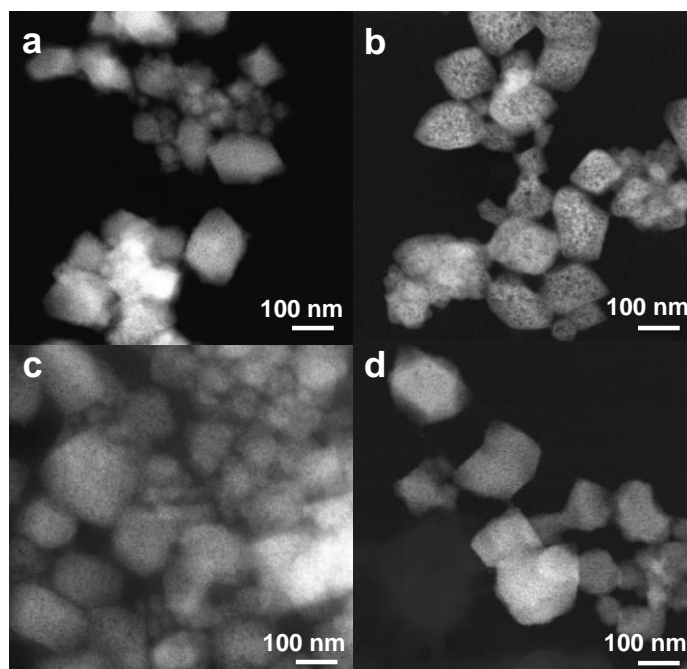
MIL-100(Fe) nanoMOFs were administered by intravenous route and it was found that they released their trimesate ligands<sup>3</sup> but to the best of our knowledge there is no information about the nanoMOF composition once in contact with a complex media such as blood. Blood is composed of various cells suspended in plasma which constitutes around 55 % of blood fluid and is composed mostly of water (92 vol %), more than two thousands proteins, glucose, mineral ions, hormones, carbon dioxide and other molecules. Albumin is the main protein in plasma, whereas mineral ions comprise Na<sup>+</sup>, K<sup>+</sup>, Mg<sup>2+</sup>, Ca<sup>2+</sup>, carbonates, phosphates, sulfates.<sup>43,44</sup>

The results obtained in the competition studies between phosphates and sulfates point out the major role of phosphates in drug entrapment as well as nanoMOFs degradation. More complex competitions are expected to occur when the nanoMOFs interact with blood. It was interesting to further investigate using the methodology based on STEM-

HAADF-EDX microscopy, the nanoMOFs composition after contact with blood, or serum (devoid of cells). To do so, nanoMOFs were incubated in these media at a concentration of  $0.5 \text{ mg mL}^{-1}$  corresponding to the administered dose of nanoMOFs in rats used in previous *in vivo* studies.<sup>13,45</sup> Two different time points were chosen (2 h and 48 h) to account for early and late fate of the nanoMOFs.

Figure 8 presents the aspect of the nanoMOFs recovered from these media and washed with Milli-Q water to remove the proteins and other compounds not firmly bound. Noteworthy, the nanoMOFs maintained a faceted structure with holes clearly visible especially in blood after 2 h (Figure 8b). These holes present a similarity with those observed during nanoMOFs degradation in PBS (Figure 5a). Remarkably, the nanoMOFs average sizes were maintained even after 2 days incubation in both media, as indicated by the slight variation observed after evaluating more than 100 nanoparticles ( $141 \pm 37 \text{ nm}$  to for a)  $145 \pm 30 \text{ nm}$ , b)  $160 \pm 34 \text{ nm}$ , c)  $160 \pm 40 \text{ nm}$  and d)  $144 \pm 25 \text{ nm}$  respectively).

The nanoMOFs degradation could be attributed to the presence of various ions and other molecules from blood and plasma. Indeed, it was found that the nanoMOFs were enriched in various elements, mainly N, P, S, Ca and Mg (Figure S7), which were not initially in the nanoMOFs. Other elements were in trace amounts. We speculate that N could be essentially attributed to proteins, which were demonstrated to readily bind onto the nanoMOFs.<sup>46,47</sup>



**Figure 8.** STEM-HAADF images of nanoMOFs after incubation in (a,b) serum and blood for 2 h and (c,d) serum and blood for 48 h respectively. Sample concentration was  $0.5 \text{ mg mL}^{-1}$ .

As P and N were the main elements in the compositions of the nanoMOFs in contact with blood or serum, the P/Fe and N/Fe ratios were calculated for different regions of interest (single nanoMOF or groups of particles), as described previously. P was evenly distributed in both nanoMOF after contact with serum and blood, a constant ratio of  $0.5 \pm 0.1$  after early (2 h) incubation (Figure S5). This ratio was almost doubled after long (48 h) incubation (Figure S6) reaching  $0.9 \pm 0.1$ . Noteworthy, despite the significantly higher concentration of  $\text{HCO}_3^-$  ( $27 \text{ mmol L}^{-1}$ ),  $\text{Ca}^{+2}$  ( $2.5 \text{ mmol L}^{-1}$ ) and  $\text{Mg}^{+2}$  ( $1.5 \text{ mmol L}^{-1}$ ) concentrations in the blood compared to  $\text{HPO}_4^{2-}$  ( $1.0 \text{ mmol L}^{-1}$ )<sup>44</sup>, P was vastly detected in nanoMOFs structures. As mentioned before, C atoms may refer to the carboxylate ligand, the samples' holders and the  $\text{HCO}_3^-$  from the blood. Thus, EDX analysis hampers the distinction between C elements. Yet, Ca and Mg were found in traces and the calculated ratios could not be precisely defined, in reason of the detection limit.

These findings suggest a higher affinity of P-based compounds for the nanoMOFs as compared to other elements. It could be hypothesized that interaction take place with phosphates from blood or serum. Further investigations will be needed to fully unravel these interactions.

As stated previously, the nanoMOF enrichment with N could be attributed to their interaction with the large variety of proteins present in the two studied media. Indeed, the N/Fe ratio, representative of this binding, was found at  $1.1 \pm 0.5$  (serum 2 h) (Table S3) and at  $1.9 \pm 0.8$  (blood 2 h) (Table S4).

In contrast to the homogeneous distribution of P in the nanoMOFs, N was not evenly presented as shown by the large standard deviations (0.4 and 0.9 for N as compared to 0.1 for P). More specifically, N distribution was strongly dependent on nanoMOFs sizes. Figure S8 is a typical example, showing that the N content was higher on small nanoMOFs as compared to largest ones. Possibly, proteins remain adsorbed onto the nanoMOFs surfaces, which explains why the smallest particles with the highest external surface areas have a larger signal coming from proteins.

#### 4. Conclusions

NanoMOFs acted as efficient host matrices, soaking PP from its aqueous solution with high efficiencies until saturation of the iron available sites. In contrast the pristine hydrophobic drug prednisolone and PS were loaded with lower efficiencies and were released in a burst manner, highlighting their lower affinity for the nanoMOFs, in agreement with molecular modeling studies. In addition, only PP stabilized the nanoMOFs towards degradation. It was revealed that despite massively losing their organic counterpart, the nanoMOFs maintained a faceted structure and similar sizes, before and after degradation. Noticeably, this morphology was practically unaltered after 2 days incubation in biological fluids (blood and serum) despite the appearance of holes. The nanoMOFs composition drastically changed, as a function of the degradation media. STEM-HAADF in conjunction with EDX was a powerful tool to unravel not only drug distribution within the nanoMOF porosity, but also changes in their composition upon degradation. Proteins bulkier than the nanoMOFs' windows adsorbed at the nanoMOFs' surfaces whereas ions diffused through the nanoMOF porosity. These studies suggest that nanoMOFs interact with phosphates and proteins in blood and that these interactions are rapid. Iron trimesate nanoMOFs are peculiar in the sense that they are able to maintain their global morphology despite dramatic changes in their composition, according to the medium they are in contact with. These investigations can be of interest for the design of nanoMOFs as drug carriers and in other fields.

#### Author Contributions:

The author(s) have made the following declarations about their contributions:

Conceived and designed the experiments: Ruxandra Gref, Ioanna Christodoulou

Performed the experiments: Ioanna Christodoulou, Gilles Patriarche, Pengbo Lyu, Guillaume Maurin

Performed data analysis: Ioanna Christodoulou, Pengbo Lyu, Guillaume Maurin, Gilles Patriarche, Christian Serre, Ruxandra Gref

Wrote the paper: Ioanna Christodoulou, Ruxandra Gref

**Funding:** "This research was funded by the Paris Ile-de-France Region – DIM Respire, grant number 'LS 167151'

## Acknowledgments:

We are grateful to Dr A. Machelart (Institut Pasteur de Lille) for the supply of blood and blood plasma from mice. IC thanks the Paris Ile-de-France Region – DIM Respire for a PhD fellowship. This work was supported by a public grant overseen by the French National Research Agency (ANR) as part of the “Investissements d’Avenir” program (Labex NanoSaclay, reference: ANR-10-LABX-0035).

**Conflicts of Interest:** “The authors declare no conflict of interest.”

## References

1. Mitchell, M.J. *et al.* Engineering precision nanoparticles for drug delivery. *Nat. Rev. Drug. Discov.* **20**, 101-124 (2021).
2. Bangham, A. D. *et al.* The surface properties of some neoplastic cells. *Biochem. J.* **84**, 513–517 (1962).
3. Horcajada, P. *et al.* Porous metal-organic-framework nanoscale carriers as a potential platform for drug delivery and imaging. *Nat Mater.* **9**, 172-178 (2009).
4. Li, S. *et al.* Nanoscale Metal-Organic Frameworks: Synthesis, Biocompatibility, Imaging Applications, and Thermal and Dynamic Therapy of Tumors. *Adv Funct Mater.* **30**, 1-26 (2020).
5. Di Nunzio, M.R. *et al.* A “ship in a bottle” strategy to load a hydrophilic anticancer drug in porous metal organic framework nanoparticles: Efficient encapsulation, matrix stabilization, and photodelivery. *J Med Chem.* **57**, 411-420 (2014).
6. Rodriguez-Ruiz, V. *et al.* Efficient “green” encapsulation of a highly hydrophilic anticancer drug in metal-organic framework nanoparticles. *J Drug Target.* **23**, 759-767 (2015).
7. Anand, R. *et al.* Host-guest interactions in Fe(III)-trimesate MOF nanoparticles loaded with doxorubicin. *J Phys Chem B.* **118**, 8532-8539 (2014).
8. Agostoni, V. *et al.* ‘Green’ fluorine-free mesoporous iron(III) trimesate nanoparticles for drug delivery. *Green Mater.* **1**, 209-217 (2013).
9. Grall, R. *et al.* In vitro biocompatibility of mesoporous metal (III; Fe, Al, Cr) trimesate MOF nanocarriers. *J Mater Chem B.* **3**, 8279-8292 (2015).
10. Tamames-Tabar, C. *et al.* Cytotoxicity of nanoscaled metal-organic frameworks. *J Mater Chem B.* **2**, 262-271 (2014).
11. Wuttke, S. *et al.* Validating Metal-Organic Framework Nanoparticles for Their Nanosafety in Diverse Biomedical Applications. *Adv Healthc Mater.* **6**, 1-11(2017).
12. Ruyra, A. *et al.* Synthesis, culture medium stability, and in vitro and in vivo zebrafish embryo toxicity of metal-organic framework nanoparticles. *Chem - A Eur J.* **21**, 2508-2518 (2015).
13. Simon-Yarza, M.T. *et al.* Antineoplastic busulfan encapsulated in a metal organic framework nanocarrier: First in vivo results. *J Mater Chem B.* **4**, 585-588 (2016)
14. Baati, T. *et al.* In depth analysis of the in vivo toxicity of nanoparticles of porous iron(iii) metal-organic frameworks. *Chem Sci.* **4**, 1597-1607 (2013)
15. Simon-Yarza, T. *et al.* A Smart Metal-Organic Framework Nanomaterial for Lung Targeting. *Angew Chemie - Int Ed.* **56** 15565-15569 (2017).
16. Li, X *et al.* New insights into the degradation mechanism of metal-organic frameworks drug carriers. *Sci Rep.* **7**, 1-11(2017).

17. Bellido, E. *et al.* Understanding the colloidal stability of the mesoporous MIL-100(Fe) nanoparticles in physiological media. *Langmuir* **30**, 5911-5920 (2014).
18. Christodoulou, I. *et al.* Metal-Organic Frameworks for Drug Delivery: Degradation Mechanism and in Vivo Fate. *Nanomaterials*, **11**, (2020).
19. Agostoni, V. *et al.* Towards an Improved anti-HIV Activity of NRTI via Metal-Organic Frameworks Nanoparticles. *Adv Healthc Mater.* **2**, 1630-1637 (2013).
20. Agostoni, V. *et al.* Impact of phosphorylation on the encapsulation of nucleoside analogues within porous iron(III) metal-organic framework MIL-100(Fe) nanoparticles. *J Mater Chem B.* **1**, 4231-4242 (2013)
21. Roda, B. *et al.* Flow field-flow fractionation and multi-angle light scattering as a powerful tool for the characterization and stability evaluation of drug-loaded metal-organic framework nanoparticles. *Anal Bioanal Chem.*, **410**, 5245-5253 (2018).
22. Granner, D.K. *et al.* Regulatory actions of glucocorticoid hormones: From organisms to mechanisms. *Adv Exp Med Biol.* **872**, 3-31 (2015).
23. Hua, C. *et al.* Glucocorticoids in rheumatoid arthritis: Current status and future studies. *RMD Open.* **6**, 1-9 (2020).
24. Kearns, N. *et al.* Inhaled Corticosteroids in Acute Asthma: A Systemic Review and Meta-Analysis. *J Allergy Clin Immunol Pract.* **8**, 605-617 (2020).
25. Fizazi, K. *et al.* Abiraterone plus Prednisone in Metastatic, Castration-Sensitive Prostate Cancer. *N Engl J Med.* **377** 352-360 (2017)
26. Lühder, F. *et al.* Novel drug delivery systems tailored for improved administration of glucocorticoids. *Int J Mol Sci.* **18**,1836 (2017).
27. Orange Book: Approved Drug Products with Therapeutic Equivalence Evaluations.
28. DLS technical note from Malvern Instruments Ltd. <http://www.malvern.com/>.
29. Finšgar, M. *et al.* An Improved Reversed-Phase High-Performance Liquid Chromatography Method for the Analysis of Related Substances of Prednisolone in Active Ingredient. *ACS Omega.* **5**, 7987-8000. (2020).
30. Abdullah, N. *et al.* Development and validation of RP-HPLC method for simultaneous quantification of sulfacetamide sodium and prednisolone sodium phosphate. *Acta Pol Pharm - Drug Res.* **76**, 37-47. (2019).
31. Rojas, S. *et al.* Toward Understanding Drug Incorporation and Delivery from Biocompatible Metal-Organic Frameworks in View of Cutaneous Administration. *ACS Omega.* **3**, 2994-3003 (2018).
32. Schäfer, A. *et al.* Fully optimized contracted Gaussian basis sets of triple zeta valence quality for atoms Li to Kr. *J Chem Phys.* **100**, 5829-5835 (1994).
33. Grimme, S. *et al.* A consistent and accurate ab initio parametrization of density functional dispersion correction (DFT-D) for the 94 elements H-Pu. *J Chem Phys.* **132**, (2010).
34. Férey, G. *et al.* A hybrid solid with giant pores prepared by a combination of targeted chemistry, simulation, and powder diffraction. *Angew Chemie - Int Ed.* **43**, 6296-6301 (2004).
35. Horcajada P. *et al.* Synthesis and catalytic properties of MIL-100(Fe), an iron(III) carboxylate with large pores. *Chem Commun.* **100**, 2820-2822 (2007).
36. Horcajada, P. *et al.* Metal-organic frameworks as efficient materials for drug delivery. *Angew Chemie - Int Ed.* **45** 5974-5978 (2006).
37. García, Márquez A. *et al.* Green microwave synthesis of MIL-100(Al, Cr, Fe) nanoparticles for thin-film elaboration. *Eur J Inorg Chem.* **100**, 5165-5174 (2012).
38. Sene, S. *et al.* Maghemite-nanoMIL-100(Fe) Bimodal Nanovector as a Platform for Image-Guided Therapy. *Chem.* **3**, 303-322, (2017).
39. Li, X. *et al.* Highly Porous Hybrid Metal-Organic Nanoparticles Loaded with Gemcitabine Monophosphate: a Multimodal Approach to Improve Chemo- and Radiotherapy. *ChemMedChem.* **15**, 274-283 (2020).
40. Bayard, F.J.C. *et al.* Polyethylene glycol-drug ester conjugates for prolonged retention of small

## Drug loading in nanoscale MOFs and release kinetics: new insights from STEM-HAADF microscopy

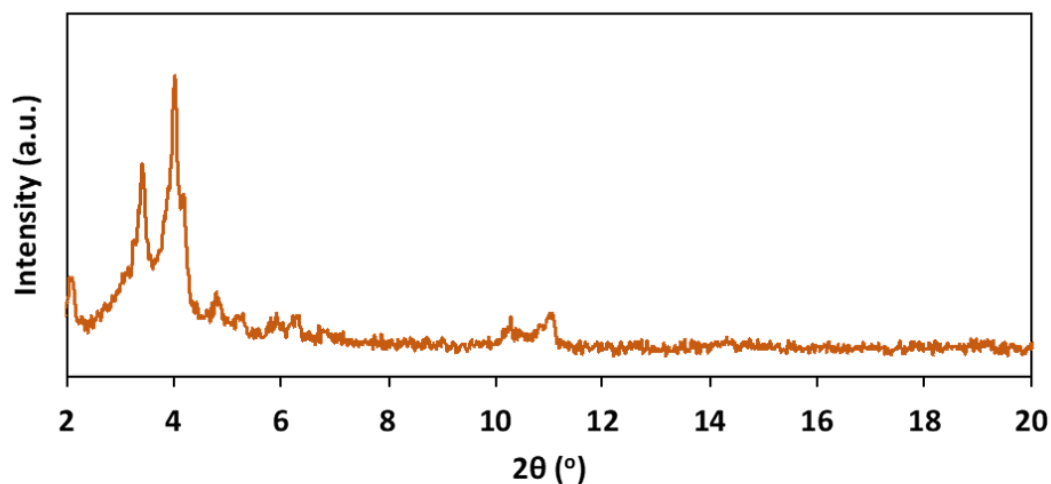
- inhaled drugs in the lung. *J Control Release*. **171**, 234-240, (2013).
41. Huanbutta, K. *et al.* Design and characterization of prednisolone-loaded nanoparticles fabricated by electrohydrodynamic atomization technique. *Chem Eng Res Des*. **109**, 816-823 (2016).
  42. Cunha, D. *et al.* Rationale of drug encapsulation and release from biocompatible porous metal-organic frameworks. *Chem Mater*. **25**, 2767-2776 (2013).
  43. Nezafati, N. *et al.* Surface reactivity and in vitro biological evaluation of sol gel derived silver/calcium silicophosphate bioactive glass. *Biotechnol Bioprocess Eng*. **17**, 746-754 (2012).
  44. Anderson, N.L. *et al.* The human plasma proteome: history, character, and diagnostic prospects. *Mol Cell Proteomics*. **1**, 845-867 (2002).
  45. Simon-Yarza, T. *et al.* In vivo behavior of MIL-100 nanoparticles at early times after intravenous administration. *Int J Pharm*. **511**, 1042-1047 (2016).
  46. Li, X. *et al.* Drug-Loaded Lipid-Coated Hybrid Organic-Inorganic "Stealth" Nanoparticles for Cancer Therapy. *Front Bioeng Biotechnol*. **8**, 1-12 (2020).
  47. Cutrone, G. *et al.* Design of engineered cyclodextrin derivatives for spontaneous coating of highly porous metal-organic framework nanoparticles in aqueous media. *Nanomaterials*. **9**, 1-27 (2019).

## Chapter IV

Drug loading in nanoscale MOFs and release kinetics: new insights from STEM-HAADF microscopy



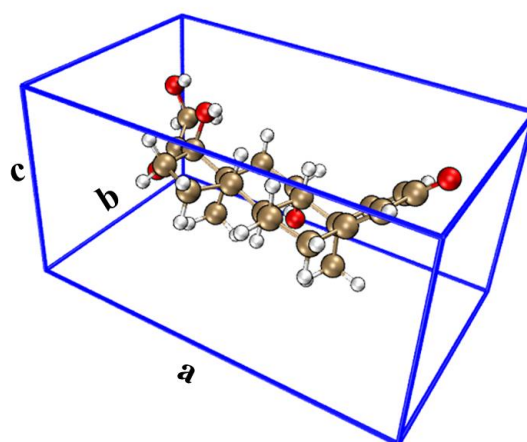
## Supporting information

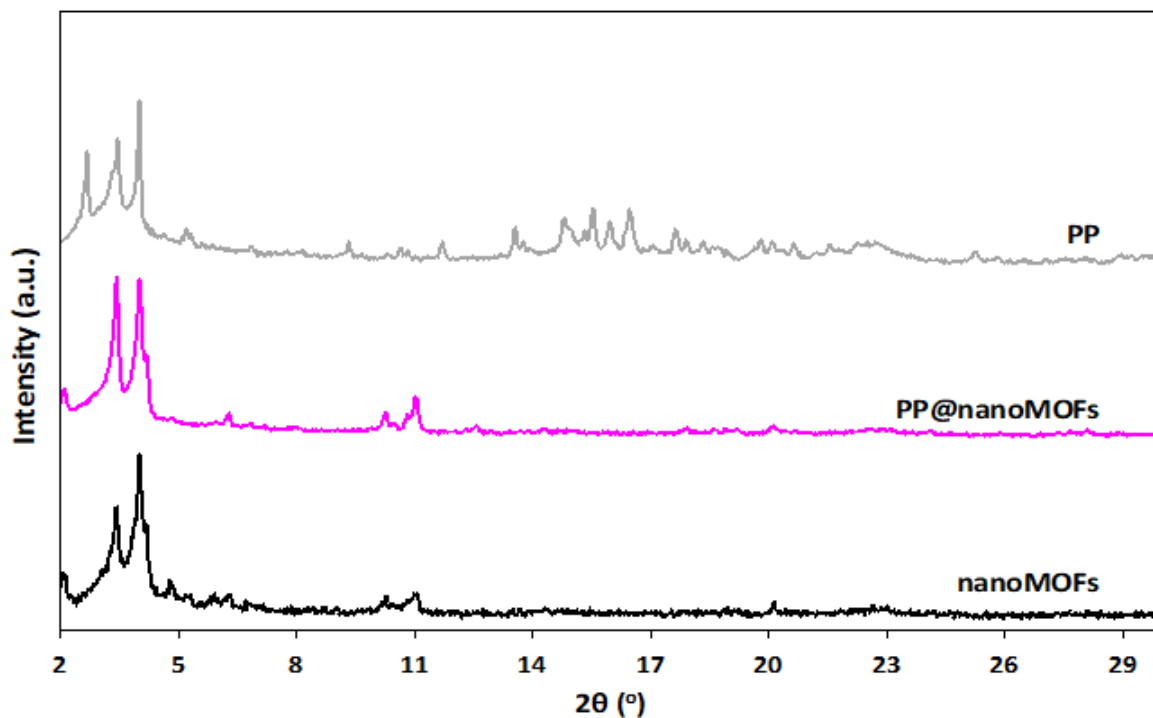
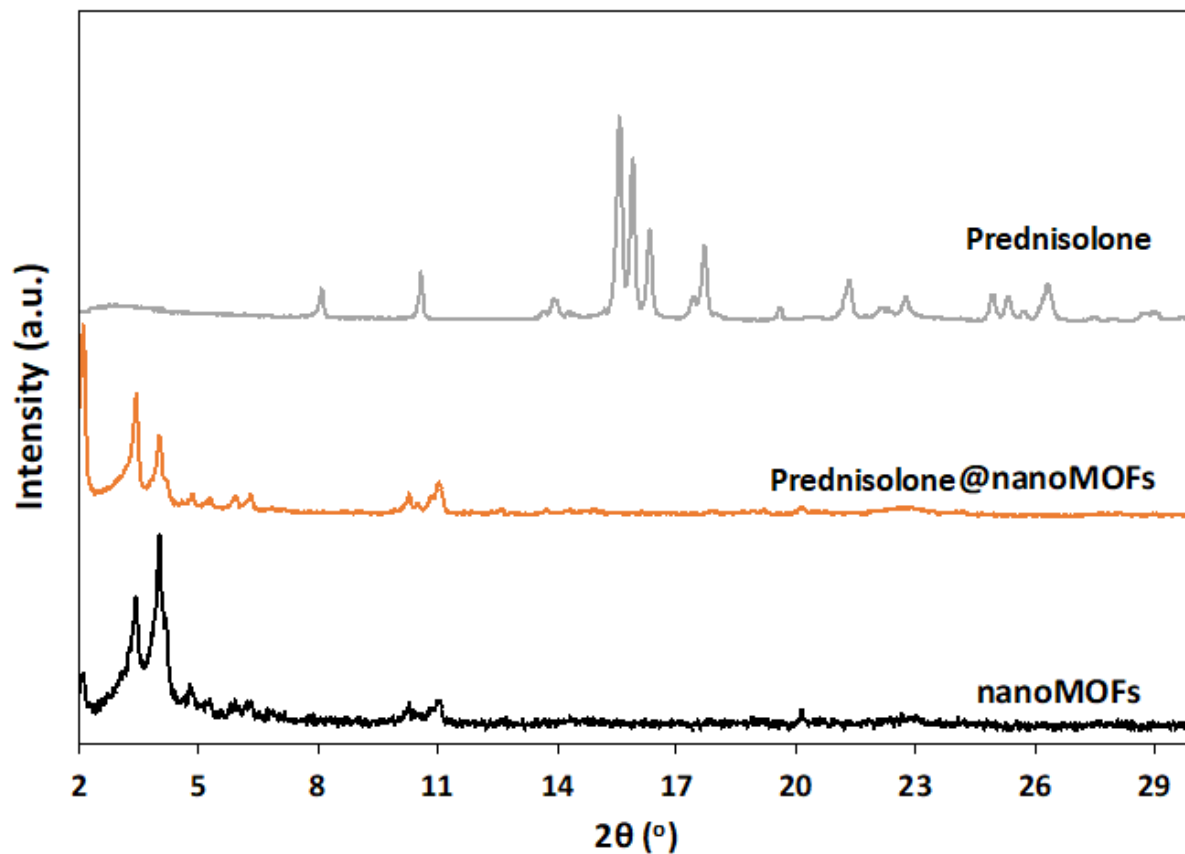


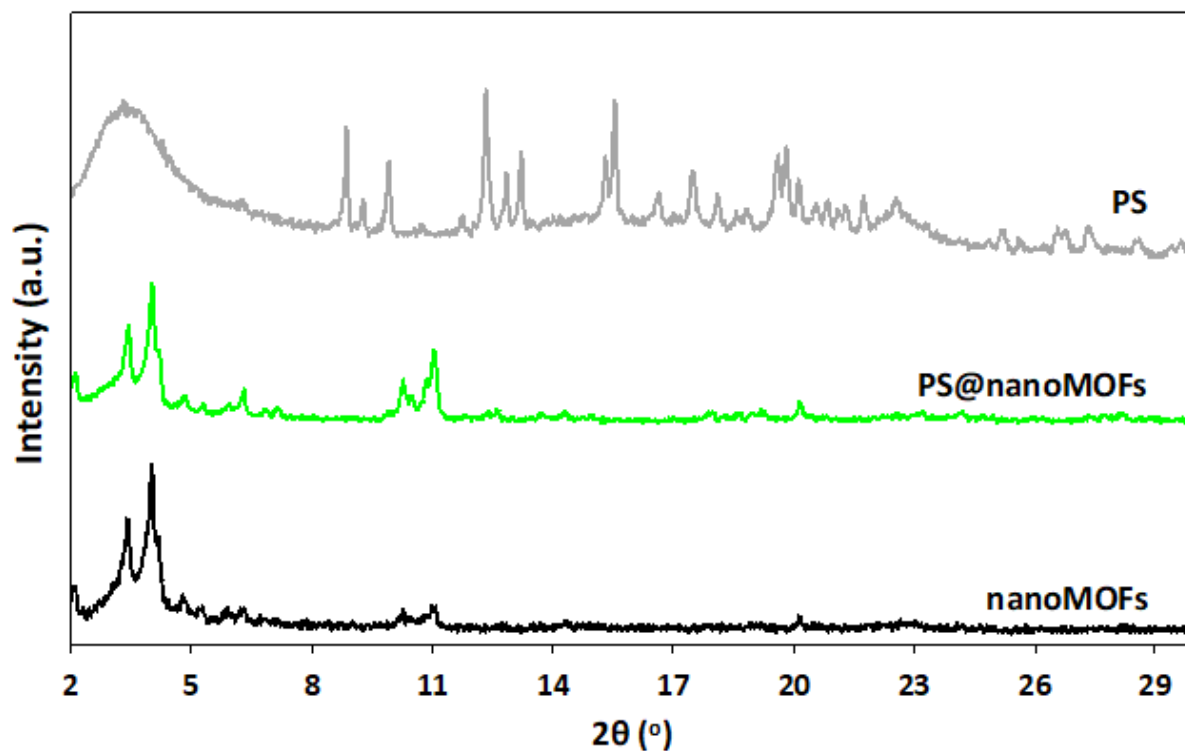
**Figure S1:** Normalized PXRD patterns of nanoMOFs.

**Table S1:** Dimensions and volume occupancies of Prednisolone, PP and PS calculated by DFT modeling. As an example, a, b and c sides of Prednisolone are illustrated.

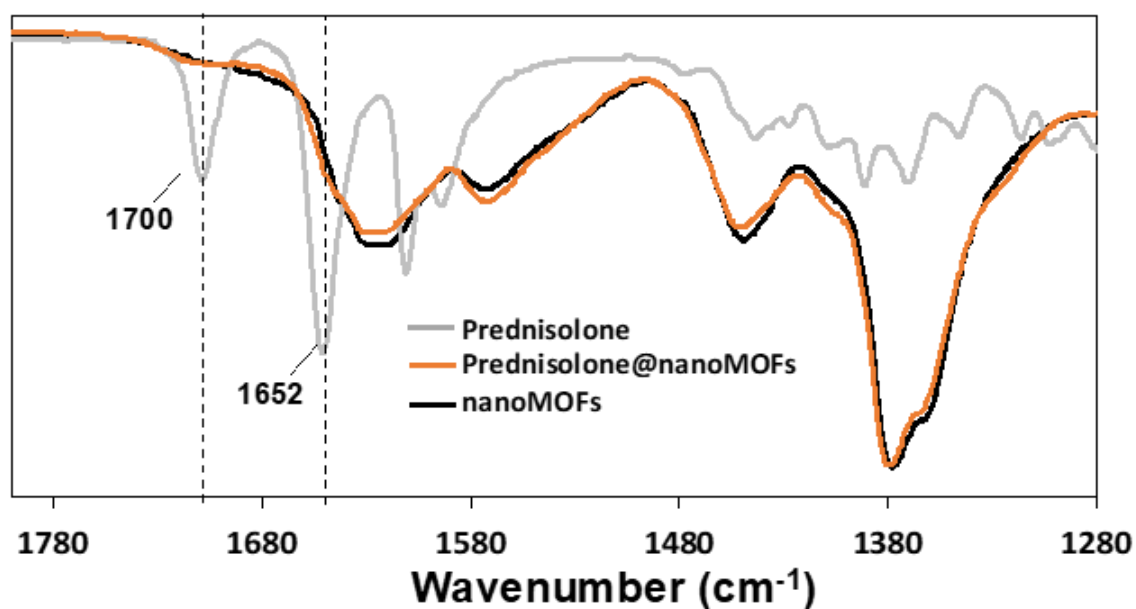
Active Molecule	Volume ( $\text{\AA}^3$ )	Diameter ( $\text{\AA}$ )	Lengths along the 3 sides ( $\text{\AA}$ )		
			a	b	c
Prednisolone	356.6	14.47	14.24	8.51	7.50
PSS	457.6	18.02	17.82	9.53	7.25
PSP	473.8	17.37	17.25	8.38	8.00

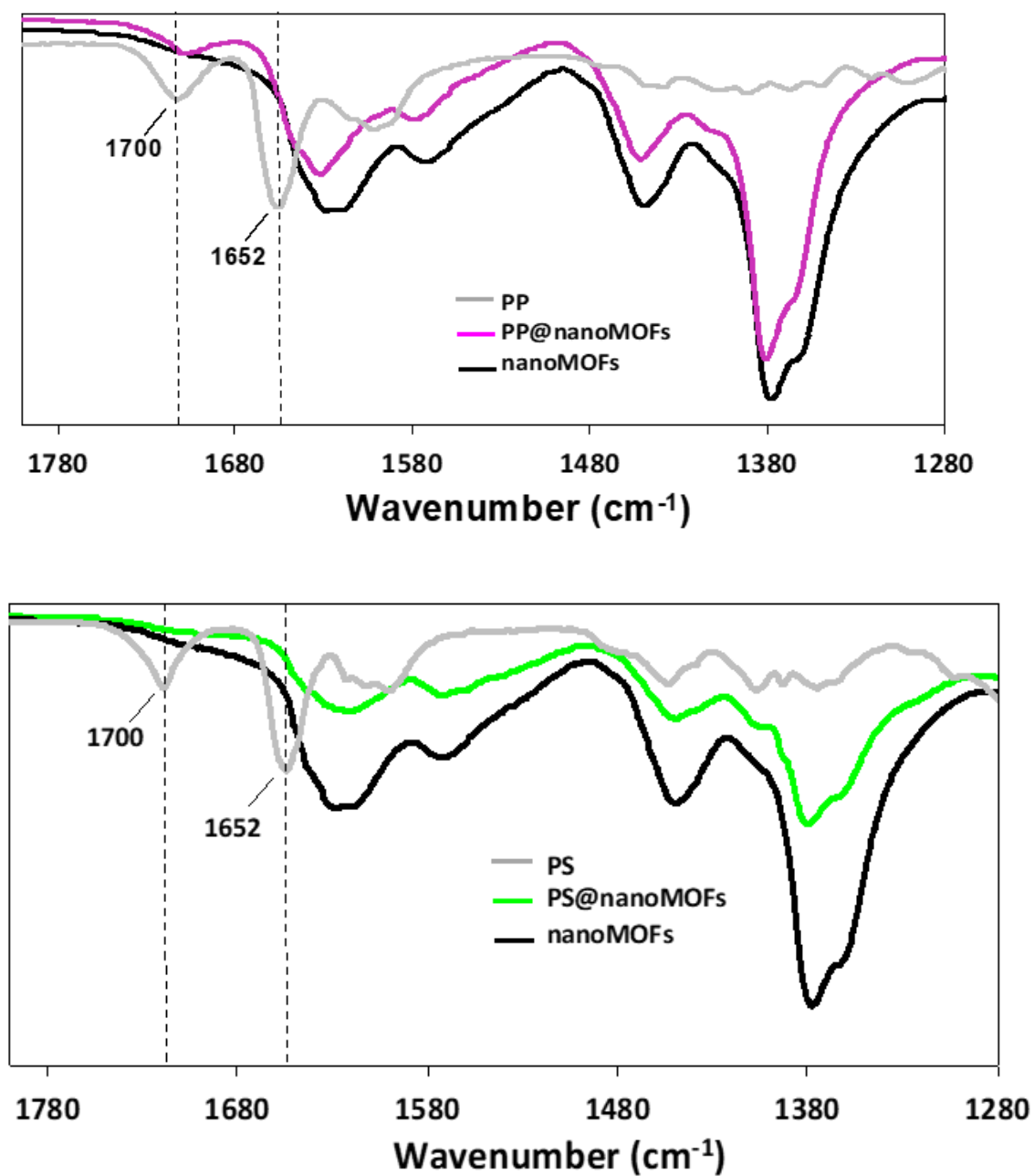






**Figure S2:** Normalized PXRD patterns of MIL-100(Fe) nanoMOFs before (black) and after encapsulation of Prednisolone (orange), PP (pink) and PS (green).

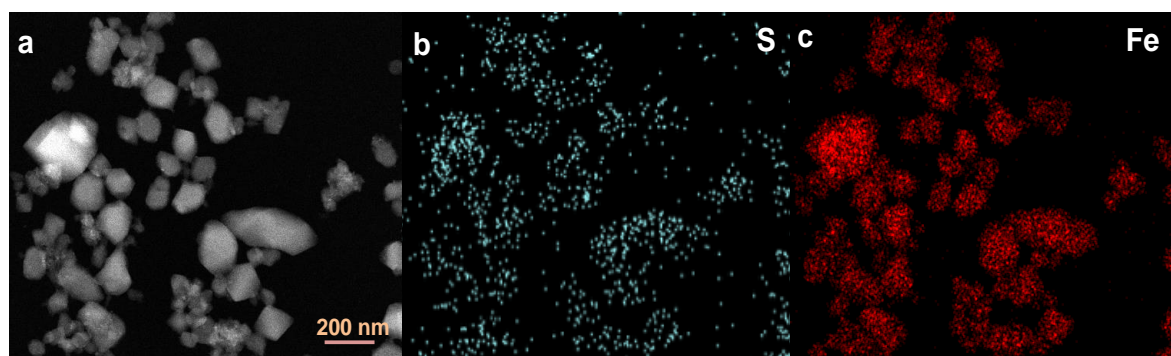
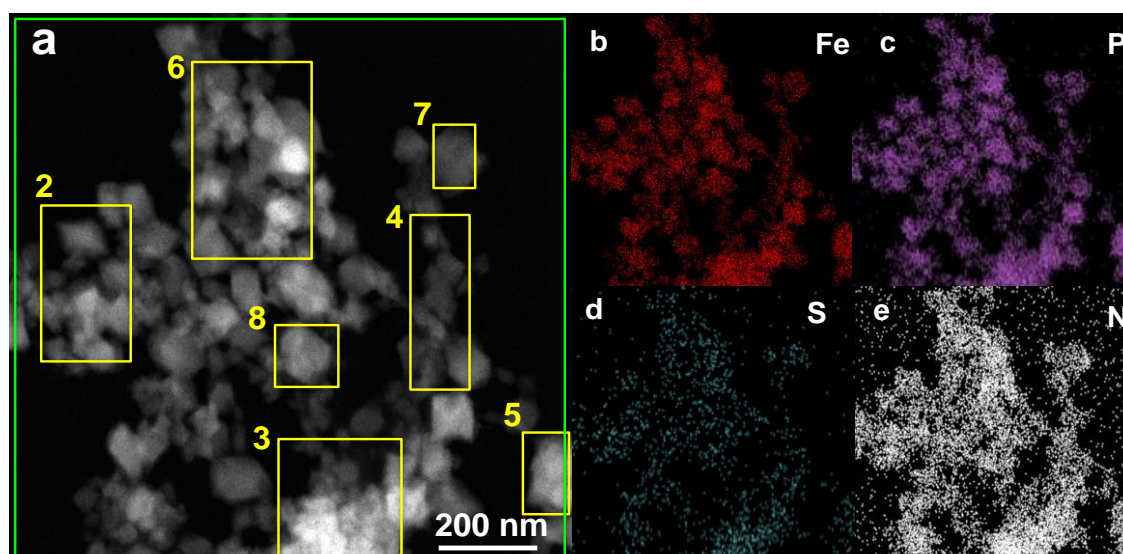


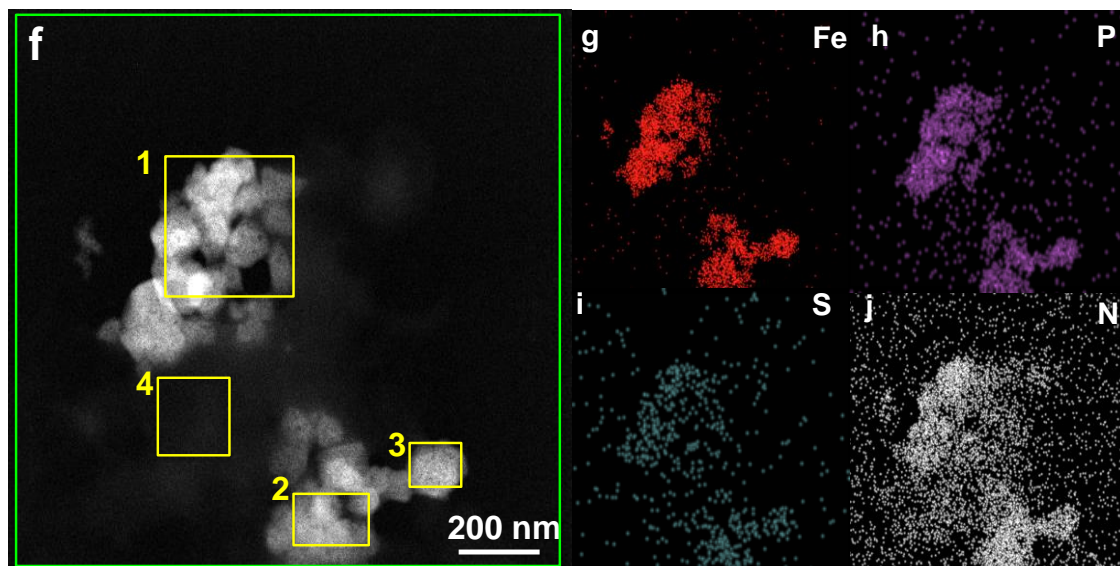


**Figure S3:** FT-IR spectra of MIL-100(Fe) nanoMOFs before (black) and after drug encapsulation of P (orange), PP (pink) and PS (green). Spectra of pure Prednisolone, PP and PS are presented in grey colors.

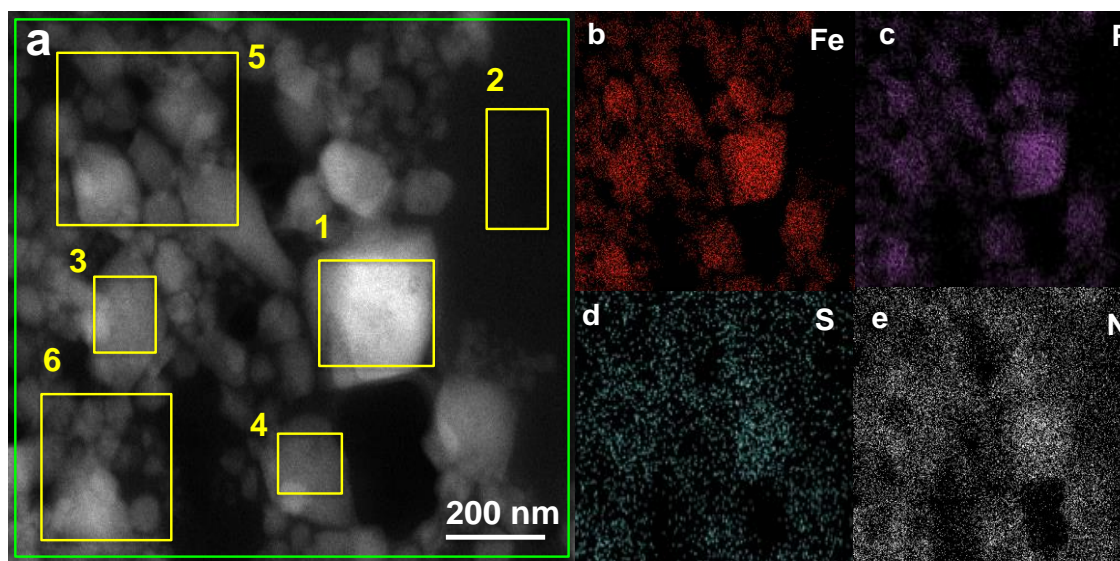
**Table S2:** Solubility of prednisolone in different solvents at 25 °C.

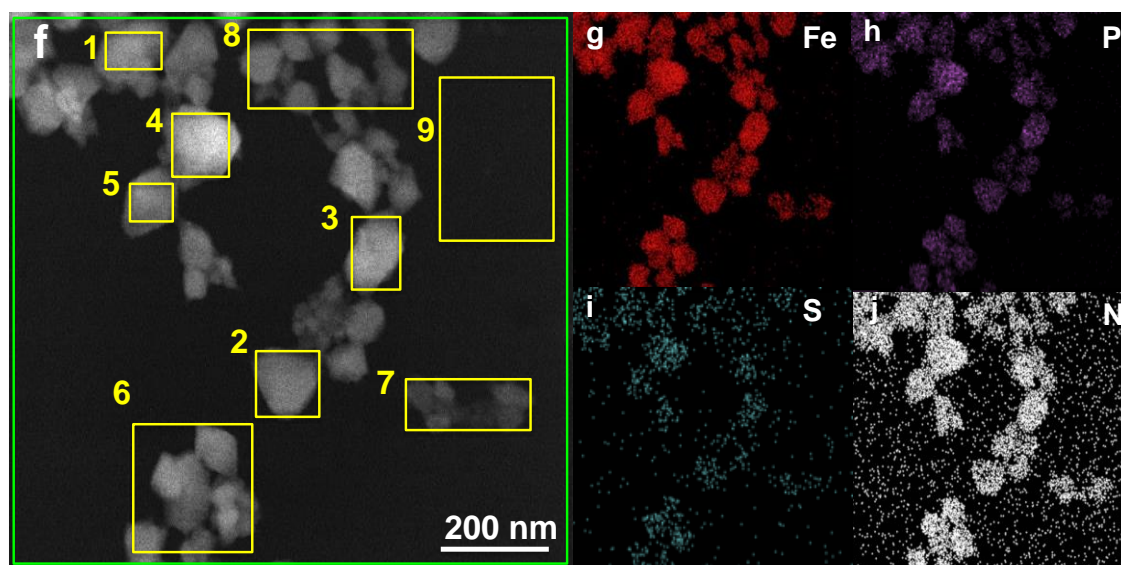
Solvent	Solubility (mg mL <sup>-1</sup> ) at 25 °C
H <sub>2</sub> O	0.22
EtOH	33.33
Chloroform	5.55
Acetone	20
MeOH	soluble
Dioxane	soluble

**Figure S4.** a) Typical STEM-HAADF images of nanoMOFs loaded with PS. b,c) Elemental distribution of Fe (red) and S (blue) into the nanoMOFs after PS loading

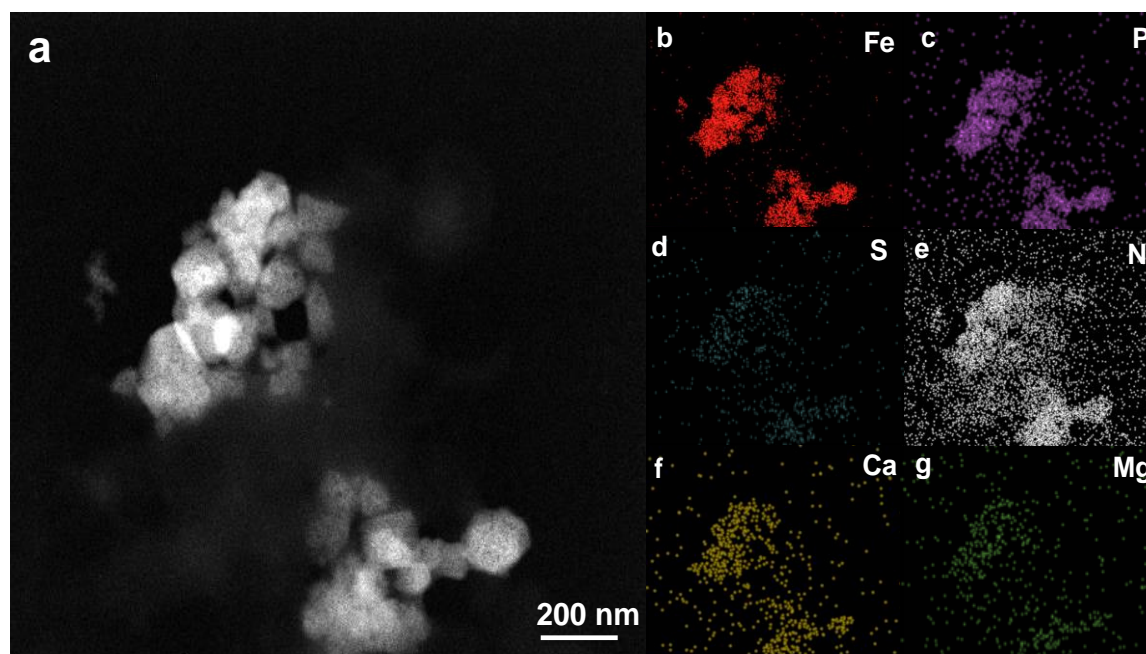


**Figure S5.** a,f) STEM-HAADF images of nanoMOFs upon incubation in serum (2 h) and in blood (2 h). b,c,d,e,g,h,i,j) Elemental distribution of Fe (red), P (violet), S (blue) and N (white). Yellow rectangles represent the selected regions by STEM-XEDS and green rectangle the entire image.





**Figure S6.** a,f) STEM-HAADF images of nanoMOFs upon incubation in serum (48 h) and in blood (48 h). b,c,d,e,g,h,i,j) Elemental distribution of Fe (red), P (violet), S (blue) and N (white). Yellow rectangles represent the selected regions by STEM-XEDS and green rectangle the entire image.

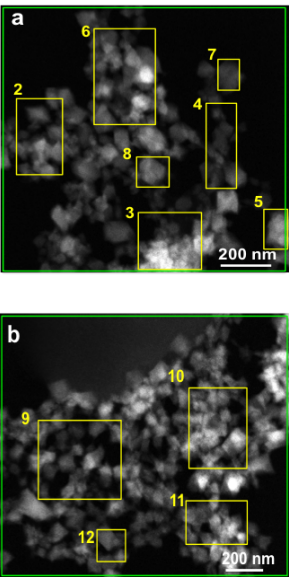


**Figure S7:** a) STEM-HAADF of nanoMOFs after 48 h incubation in blood. b-g) Elemental mapping of blood components into the nanoMOFs. Fe (red), P (violet), S (blue), N (white), Ca (yellow) and Mg (green).

## Chapter IV

### Drug loading in nanoscale MOFs and release kinetics: new insights from STEM-HAADF microscopy

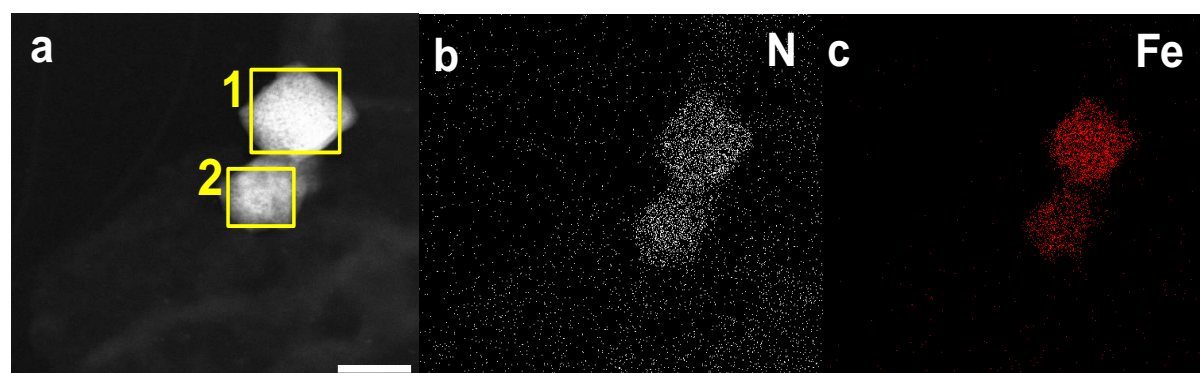
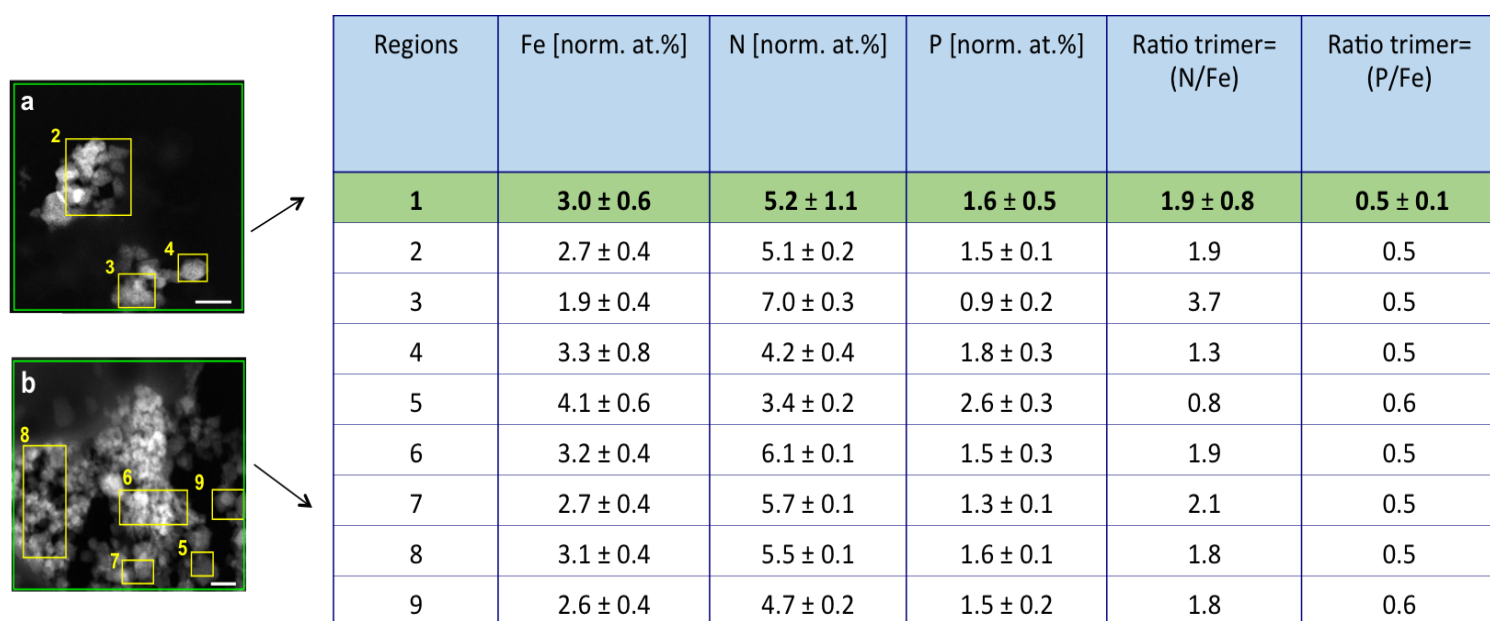
**Table S3:** Element distribution (by norm. at.%) and the calculated ratio of N (protein) per Fe (nanoMOFs) after 2 h incubation in serum ( $0.5 \text{ mg mL}^{-1}$ ). The calculated values correspond to the selected regions of interest as numbered in microscopic images a) and b). Region numbered 1 represents the average values (represented as green rectangles).



Regions	Fe [norm. at.%]	N [norm. at.%]	P [norm. at.%]	Ratio trimer= N/Fe	Ratio trimer= P/Fe
<b>1</b>	<b><math>4.0 \pm 1.1</math></b>	<b><math>4.1 \pm 1.6</math></b>	<b><math>3.4 \pm 0.9</math></b>	<b><math>1.1 \pm 0.5</math></b>	<b><math>0.8 \pm 0.1</math></b>
2	$3.6 \pm 0.5$	$3.8 \pm 0.2$	$3.0 \pm 0.2$	1.1	0.8
3	$4.1 \pm 0.5$	$6.9 \pm 0.1$	$3.3 \pm 0.1$	1.7	0.8
4	$2.6 \pm 0.5$	$3.5 \pm 0.2$	$1.9 \pm 0.2$	1.4	0.7
5	$4.7 \pm 0.7$	$2.7 \pm 0.2$	$4.3 \pm 0.3$	0.6	0.9
6	$2.8 \pm 0.3$	$4.0 \pm 0.1$	$3.0 \pm 0.1$	1.4	0.8
7	$3.8 \pm 0.9$	$2.8 \pm 0.4$	$3.3 \pm 0.5$	0.7	0.9
8	$4.3 \pm 1.0$	$2.0 \pm 0.3$	$3.9 \pm 0.6$	0.5	0.9
9	$3.5 \pm 0.5$	$5.1 \pm 0.1$	$2.5 \pm 0.1$	1.5	0.7
10	$4.3 \pm 0.5$	$4.9 \pm 0.1$	$3.6 \pm 0.1$	1.0	0.8
11	$3.9 \pm 0.5$	$6.3 \pm 0.2$	$3.1 \pm 0.1$	1.6	0.8
12	$6.7 \pm 0.1$	$2.9 \pm 0.3$	$5.3 \pm 0.8$	0.4	0.8

**Table S4:** Element distribution (by norm. at.%) and the calculated ratio of N (protein) per Fe (nanoMOFs) after 2 h incubation in blood ( $0.5 \text{ mg mL}^{-1}$ ). The calculated values correspond to the selected regions of interest as numbered in microscopic images a) and b). Region numbered 1 represents the average values (represented as green rectangles). Scale bar represents 200 nm.





**Figure S8:** a) STEM-HAADF image of nanoMOFs after 2 h incubation in blood. b,c) Elemental distribution of Fe (red) and N (white). The calculated N/Fe was found 1.4 for region 1 and 3.5 for region 2, suggesting that protein is prone to get adsorbed on the external surface of smaller nanoMOFs. Scale represents 200 nm.

## Theoretical calculations

The MTN framework consists of two different cage systems, namely [5<sup>12</sup>] and [5<sup>12</sup>6<sup>4</sup>].<sup>1</sup>

The small [5<sup>12</sup>] cages are interconnected and accessible only through narrow openings of around 4.8-5.8 Å<sup>35</sup> which makes them inaccessible to the drugs Prednisolone, PP and PS studied here. All the large [5<sup>12</sup>6<sup>4</sup>] cages are interconnected through their hexagonal windows (openings around 8.6 Å), so the drugs can penetrate through and locate inside the large cages (Table S1).

According to the MTN secondary building units (SBUs) structure, the number of small cages is twice that of the large cages.<sup>2</sup>

Formula of nanoMOF (Mw) made of iron trimesate: Fe<sub>3</sub>O (H<sub>2</sub>O)<sub>2</sub> OH (BTC)<sub>2</sub> x nH<sub>2</sub>O

where nH<sub>2</sub>O represents the bound water molecules, which are not taken into account in these calculation as drug loading is expressed with regard to the dried MOF material

Mw = 210 x 2 + 56 x 3 + 16 x 4 + 5 = 657 g/mol, so the total available iron site concentration is:

2/ 657 = 3.0 mmol/g (because 2 coordinated water molecules can be replaced by the drug)

Large cages consist of 28 supertetrahedra and 20 small ones.

Given the fact there are twice as more small cages than large ones, the % of iron trimers accessible to large molecules such as PP is:

$$\% = 28 / (2 \times 20 + 28) = 41.17$$

So the available sites in large cages are: 3.0 x 0.4117 = 1.235 mmol/g

A loading of 30% (0.3 g/g) of the PP (Mw=484 g/mol) in nanoMOFs corresponds to:

$$0.3 \text{ (g/g)} / 484 \text{ (g/mol)} = 0.619 \text{ mmol/g of MOF}$$

## References

1. Lin, ZS. *et al.* Investigations of the formation of zeolite ZSM-39 (MTN). *Can J Chem.* **97**, 840-847 (2019).
2. Agostoni, V. *et al.* Towards an Improved anti-HIV Activity of NRTI via Metal-Organic Frameworks Nanoparticles. *Adv Healthc Mater.* **2**, 1630-1637 (2013).

## Chapter IV

Drug loading in nanoscale MOFs and release kinetics: new insights from STEM-HAADF microscopy

# **General Discussion & Perspectives**



The use of nanoparticles as therapeutic agents has attracted the interest of the scientific community worldwide. As already described in the Introduction of this PhD, a plethora of organic and inorganic NPs (micelles, polymeric NPs, dendrimers, etc.) have been studied for the transportation of AIs and their controlled release to the living organism. The last decade, porous metal organic frameworks (MOFs) have been introduced as promising candidates in drug delivery applications, thanks to their high porosities, their versatile hybrid nature and lack of toxicity.

MIL-100(Fe) particles stand out in the field of drug delivery among several other MOFs. Thanks to their extensively high surface areas ( $\sim 2000 \text{ m}^2/\text{g}$ ) and their internal amphiphilic microenvironment, a great variety of active ingredients (hydrophobic, hydrophilic and amphiphilic) can be entrapped, reaching high drug loadings and encapsulation efficiencies.<sup>1-4</sup> Moreover, the numerous possibilities for surface functionalizations with a plethora of biomolecules (polysaccharides, lipids, polymers, etc) improve their colloidal stability, while tuning their pharmacokinetics and biodistribution.<sup>5-7</sup> Additionally, MIL-100(Fe) nanoMOF have been reported as biodegradable from previous *in vitro* and *in vivo* studies.<sup>8-12</sup>

MIL-100(Fe) nanoMOFs were studied in different media. In physiological conditions, it was found that phosphate ions from PBS attacked the framework, leading to a progressive release of the organic trimesate ligands.<sup>13,14</sup> Individual large MOF crystals were studied under the same conditions and it was found that after the trimesate substitution by phosphates, the particles maintained their initial size and shape.<sup>15</sup> In addition to the ionic strength of the medium, its acidity plays a key role for the determination of particles' stability.<sup>11</sup> In some cases, nanoMOFs aggregated *in vivo* in a reversible manner, which was beneficial to target drugs to the lungs. It was hypothesized that disaggregation was due to surface degradation. However several questions remain unaddressed: how rapidly the MOF respond to changes in the composition of the media they are in contact with, what are their surface features in different media, do they degrade faster in neutral media, which is the influence of the loaded drugs and protein coatings? Which are the components of biological media that can diffuse inside the porous structure of the nanoMOFs?

Therefore, this PhD work has focused particularly on solving these questions and determine the main parameters affecting the degradation mechanism of iron (III) based carboxylate porous particles MIL-100(Fe). To achieve this goal, a series of MOF particles were prepared with sizes ranging from around 50 nm to 140 and up to large micron-

sized crystals and were characterized by advanced characterization methods. A special emphasis was given in the use of *in situ* techniques, which allowed the investigation of particles' response in direct contact with the degrading media.

Firstly the degradation of individual particles of largest sizes (microMOFs) was studied (**Chapter 2**). MicroMOFs were observed inside a liquid cell by *in situ* AFM. This technique was selected, as it probes atomic details of sample's surface in real time. For this study, particles of different crystalline quality (synthesized via two different pathways) were compared. In the first case, HF was added to the mixture to obtain particles of high crystallinity [microMOFs (+)], while in the second case synthesis was performed only in the presence of water and crystalline particles with initial defects on their surface were collected [microMOFs (-)]. Both particles were tested in aqueous solution and in the presence of neutral PBS. Upon incubation in water, well-ordered crystal planes were observed for microMOFs (+), while microMOFs (-) surface was a combination of crystalline areas but also of some initial defects. As it was expected, particles were stable upon incubation in water without morphological or dimensional changes during the whole measurement (2 hours). However, in the presence of phosphates, changes on the surface properties were observed, depending on the synthetic procedures. More precisely, microMOFs (+) lost their initial crystallinity and an irregular surface was obtained, while for microMOFs (-), the initial defects enlarged by time, due to the diffusion of phosphates in the internal structure. Noteworthy, height measurements revealed that microMOFs (-) maintained their initial dimensions even after 2 hours incubation in PBS. On the contrary, important changes on the mechanical properties were found for the starting and the degraded materials. The stiffness profile of microMOFs showed an important decrease of their mechanical properties, leading to a softer material, as expected because of constitutive ligand loss.

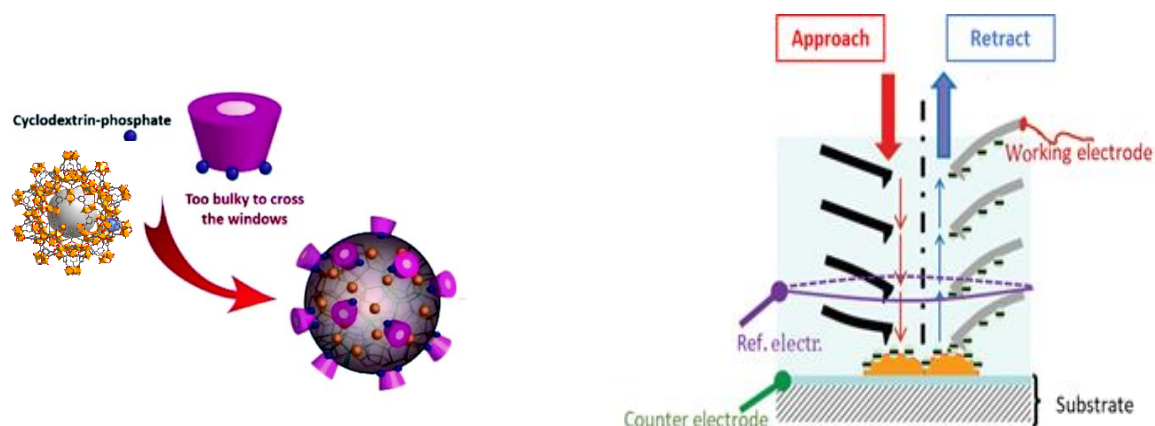
In a further step, we were also interested to investigate the effect of the pH on particles' stability. For this study, microMOFs (+) particles were incubated in acidic PBS (pH=5.4) for 2 hours. Interestingly, the initial surface features with well-defined crystal planes with distances of around 4 nm observed in water were maintained under acidic conditions. Moreover, the AFM experimental set up enabled the *in situ* change of the pH (from acidic to neutral) inside the liquid cell. For this study, microMOFs (+) particles with regular surfaces were chosen, mostly because of our interest to investigate the changes of surface features. It was very fascinating to observe that these planes instantly disappeared, leading to a degraded product of lower rigidity (as indicated by its stiffness profile) but without any dimensional changes.



In a complementary study, smaller particles (nanoMOFs) of around 200 nm were synthesized by a "green" microwave-assisted method and their stability was also tested in water, in acidic and in neutral PBS. Similar to AFM studies, another powerful microscopic technique was chosen to study morphological changes of the nanoMOFs after degradation. STEM-HAADF microscopy allowed the observation of multiple nanoMOFs with an ultrahigh resolution. Noteworthy, same crystalline planes of intact nanoMOFs were revealed, as in the case of microMOFs. After 2 days incubation in PBS at pH=5.4 and 7.4, same particles were tested by STEM-HAADF. Crystal planes were maintained for acidic conditions and they were totally lost for neutral ones, confirming once again the important role of the pH in the degradation process. Finally, size measurements indicated only slight differences after nanoMOFs degradation.

As for the perspectives, *in situ* AFM could also be used to probe the surface charge of the MOFs. Indeed, the AFM that we have used has been upgraded by our collaborator, Dr. C. Marlière, and allowed investigating the surface charge of the bacterial cell membrane in their culture medium.<sup>16</sup> This study provided valuable information about electrical surface distributions at the solid/liquid interface through an indirect measurement, based on the deflections of the cantilever at a spatial resolution better than a few tens of nanometers. In the case of MOFs, the equipment could be used for the investigation of local electrical surface charges of the particles in a wide range of pH and compare their differences in different media or in the presence of other molecules.

Besides, this method could be useful to study the MOF coating processes. As an example, the surface of MIL-100(Fe) nanoMOFs has been successfully coated with beta cyclodextrin-phosphate (CD-P)<sup>17</sup> (**Figure 5-1a**). As the coating process occurred within minutes, AFM *in situ* could be a useful method to track in real time surface modification and probe if the coating is homogeneous onto large crystal surfaces. (**Figure 5-1b**). In the presence of CD-P, the colloidal stability of the nanoparticles was significantly improved, as indicated by Zeta-potential measurements ( $\sim -17 \pm 3$  mV for uncoated against  $-35 \pm 3.5$  mV for CD-P-modified nanoMOFs). Changes on the surface charges of nanoparticles affect the stability of nanovectors and determine their *in vivo* fate. Consequently, it is very important to be able to follow these changes to optimize the features of therapeutic carriers.



**Figure 5-1:** a) Schematic representation of MIL-100(Fe) coated with CD-P. Adapted from<sup>18</sup> b) Experimental set-up for the measurement of surface electrical charges by *in situ* AFM. Surface properties (height and rigidity) were obtained by typical approach/retract movement of the AFM tip (working electrode) to the substrate (counter electrode). Reference electrode is referred to a platinum wire added for electrical potential measurements. Adapted from<sup>17</sup>

Concerning the degraded product, further studies should be performed to determine its chemical composition. AFM findings showed, that degradation preferentially occurs at small crystal defects of the surface. Surprisingly, MOF samples maintain their 3D structure without collapsing nor dimensional changes, possibly because of the formation of a passivation layer. It is therefore of utmost importance to perform analysis of the composition of this layer by different techniques. Mössbauer spectrometry (collaboration with Pr. Grenèche) is a technique of a great interest, to gain information about the oxidation and the spin state of Fe, the type of Fe species and the possible Fe-phases, as derived from the degradation in different media. Moreover, X-Ray Photoelectron Spectroscopy (XPS) would be a valuable tool for the cartography of the outer layers and the chemical environment of the atoms. Raman spectroscopy is another technique, capable of probing the chemical composition of the degraded material to further investigate its possible interactions with the media and determine structural modifications.

Although studying individual microMOFs crystals is interesting for the deeper understanding of the degradation mechanism, the sizes of such particles are adapted for scarce drug delivery applications, such as oral delivery or as implants. For different applications, such as the cancer case, intravenously administered nanoMOFs are

preferable, as they can be targeted to the tumor site and release their cargo in a sustained manner, as discussed in **Chapter 1**. In this context, nanoMOFs were prepared and their stability was investigated by a combination of *ex situ* and *in situ* methods (**Chapter 3**). In this work, nanoMOFs of around 140 nm and 50 nm were synthesized via microwave irradiation and at room temperature, respectively. They displayed a crystalline structure and BET surface areas of around 1600 m<sup>2</sup>/g. Their chemical stability was compared in PBS at different pH using a series of complementary characterization techniques (PXRD, FTIR spectroscopy, N<sub>2</sub> adsorption and electron microscopy). Interestingly, the release kinetics of their constitutive trimesate ligand was unaffected by the nanoMOF size, as determined by HPLC. It was also found that despite the fast diffusion of phosphate ions in their structure, nanoMOFs maintained their crystallinity in acidic environments, while they totally lost it in neutral ones. These results were further confirmed by STEM-HAADF coupled with EDX elemental mapping, revealing the morphological changes of the particles upon degradation. Interestingly, no dimensional changes were recorded after 2 days incubation in PBS. Moreover, nanoMOFs degradation was also studied in PBS enriched with BSA protein. In agreement with protein adsorption onto the external surface of the nanoMOFs, EDX studies showed a significant amount of N in the samples. However, protein adsorption did not affect nanoMOF degradation suggesting that the internal porosity of the nanoMOFs was still permeable by the phosphate ions.

In a further study, thin films coated with nanoMOFs were prepared by dip coating process. The successful elaboration of films of a high optical quality allowed the determination of their thickness and optical constants by spectroscopic ellipsometry. The novelty in this study was the use of thermostatic liquid cell, to evaluate degradation kinetics of the films *in situ* and in extreme diluted conditions. Direct observations of each intermediate step of the analyzed film, detection of its structural changes at short times and preservation of conditions far from saturation, are some of the main benefits of this method. To collect information about films' structural modifications in solution, their optical constant (extinction coefficient *k*) was recorded, based on an ellipsometric model. The results were in good correlation with the *ex situ* studies, showing an important stability in aqueous medium and in acidic PBS, while significant differences were recorded in neutral PBS and in the presence of BSA, denoting the chemical transformation of the nanoMOFs. Overall, we could conclude that microMOFs and nanoMOFs presented a similar behavior, once in contact with degrading media.

In future studies, it could be intriguing to further investigate the degradation

mechanism of nanoMOFs as a function of their coating. Indeed, a variety of materials (functionalized polymers, lipids, cyclodextrins) were used to functionalize the nanoMOFs. It will be of interest to determine if some of these coatings could influence the nanoMOF core (loaded or not with drugs) degradation. It has been shown that certain drugs such as topotecan, stabilize the nanoMOFs towards degradation<sup>1</sup>. Therefore, it will be important to study their degradation mechanism *in situ* by the method that has been set up, to deeper understand the influence of loaded drugs and coatings.

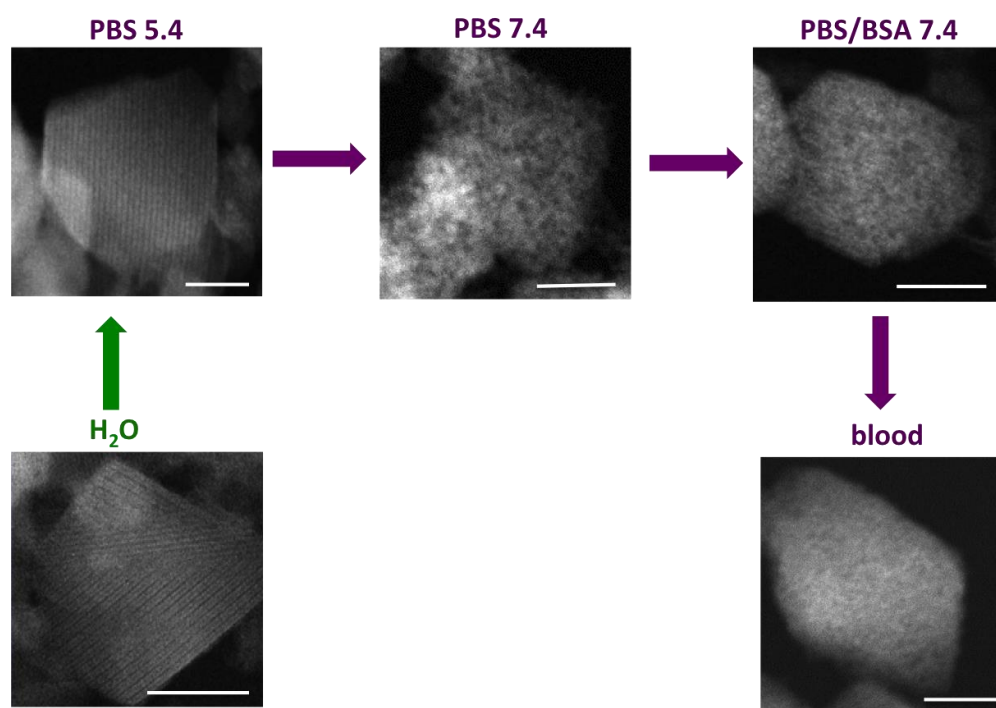
The last part of the thesis (**Chapter 4**) was dedicated to the degradation of empty nanoMOFs in more complex more complex media, containing a plethora of inorganic and organic constituents. Therefore, nanoMOFs were allowed to degrade in serum and blood and their morphology, as well as their composition was observed by STEM-HAADF-EDX at two different time points (2 h and 2 days). It was found that at early time points (within 2 h) nanoMOFs' structure entirely changed, presenting "holes", as previously described in **Chapter 2** and **3**. Of note, the dimensions of the nanoMOFs were maintained even after 2 days incubation in serum or in blood. Also, elemental mapping revealed the incorporation of plenty elements, coming from the composition of the media, such as N,P,S,Mg and Ca. However, P and N had major affinities with the nanoMOFs. N comes from the blood and plasma proteins, whereas P is from phosphates in these media.

Observations of multiple regions of the nanoMOFs, suggested the P was evenly distributed. Concerning N (related to protein amount), despite its vast presence on the nanoMOFs surface (3 to 4 times higher than P), it was not homogeneously distributed. More precisely, it was found that the smallest particles contained more N, as compared to largest ones. It is worth mentioning that larger particles have lower external surfaces on which proteins are prone to adsorb. This suggests that proteins were only adsorbed and couldn't penetrate the MOF's porosity despite the degradation.

In a nutshell, according to the above-presented findings, nanoMOFs once administered in a living media would change rapidly their composition evolving from a hybrid matrix towards an inorganic one. Their surface would be covered with proteins. Proteins such as albumin do not hinder matrix degradation. Despite their dramatic changes in composition, the nanoMOFs size is practically unaffected but they became more fragile. Degradation is more pronounced in neutral media (pH 7.4). While an important progress has been made in the understanding of the degradation mechanism of iron

trimesate MOFs, further studies are needed to fully explore their behavior in biological fluids.

As a general conclusion, all nanoMOFs maintained their microstructure and sizes regardless of the complexity of their surrounding media. **Figure 5-2** clearly demonstrates that apart from acidic conditions, where nanoMOFs kept their initial crystalline regular planes, spongy inorganic structures with more or less intense "holes" were formed, indicating nanoMOFs degradation for all the selected media of this study. Surprisingly, dimensions of the structures did not alter even after 2 days incubation in blood, suggesting that degradation is possibly based on a surface erosion mechanism.



**Figure 5-2:** STEM-HAADF images of nanoMOFs particles upon incubation in water, in acidic conditions (PBS 5.4), in neutral conditions (PBS 7.4), in the presence of BSA protein (37 mg/mL) and in complex biological media (blood). In all cases, incubations were performed at 37 °C for 48 h.

Moreover, the P/Fe and N/Fe ratios for all the studied systems, as calculated by elemental analysis are summarized in the following table (**Table 5-1**). In all cases, nanoMOFs were prepared via a microwave-assisted method, leading to sizes with mean diameters of around 200 nm. The P/Fe ratio of nanoMOFs incubated was found at  $0.3 \pm 0.1$  in acidic PBS, while it became more than double ( $0.7 \pm 0.4$ ) in neutral one, indicating a more pronounced degradation of the structure. Noteworthy, similar values

were calculated for particles in contact to PBS enriched with BSA protein or in more complex media, such as blood and serum. One important remark is that the presence of protein did not impede nanoMOFs degradation, despite its presence ( $0.5 \pm 0.3$ ). More importantly, the remarkable presence of P element in the nanoMOFs structure only after 2 h incubation in biological media ( $0.5 \pm 0.1$  for blood and  $0.8 \pm 0.1$  for serum), denotes the fast degradation of the particles. Yet, even after 48 h of incubation in the same media, similar values were collecting, proposing the total degradation of the frameworks. As for the N element contributed to the presence of protein, important increasing (in the order of 2 to 6) compared to the media containing only BSA ( $0.5 \pm 0.3$ ), was observed, in reason of the existence of several proteins in blood plasma. Finally, it is important to mention, that the standard deviations of the N/Fe compared to the P/Fe ones, differ significantly, mainly due to the non homogeneous adsorption of the protein on MOFs' surface, in contrast to the even distribution of the phosphate ions.

**Table 5-1:** Summarized calculated P/Fe and N/Fe ratios by STEM-HAADF-EDX for empty nanoMOFs.

External media	pH	concentration (mg/mL)	Incubation time (h)	P/Fe	N/Fe
PBS	5.4	0.25	48	0.3 ± 0.1	0
PBS	7.4	0.25	48	0.7 ± 0.4	0
PBS	7.4	0.25	72	0.7 ± 0.4	0
PBS/BSA	7.4	0.25	48	0.7 ± 0.3	0.5 ± 0.3
serum	7.4	0.5	2	0.8 ± 0.1	1.1 ± 0.5
blood	7.4	0.5	2	0.5 ± 0.1	1.9 ± 0.8
serum	7.4	0.5	48	0.9 ± 0.1	3.0 ± 1.0
blood	7.4	0.5	48	0.9 ± 0.1	1.0 ± 0.3

Last but not least, another important part of this thesis (**Chapter 4**) was dedicated to the incorporation of a series of AIs in nanoMOFs and the study of both their release kinetics in different media. A series of glucocorticoids (GCs), prednisolone bearing or not functional groups (sulfate and phosphate) were selected for this study, to explore their effect on the degradation mechanism of the nanoMOFs. It was found that nanoMOFs acted like molecular sponges soaking the AIs and hosting them in their porosity with different yields, based on the affinity of the functional groups of the AIs and the iron sites of the nanoMOFs. Theoretical simulations indicated the strongest complexation with the PP, then the PS and finally the pristine molecule. Indeed, experimental drug loadings confirmed this series, showing that the phosphate form had the highest payload (30 wt %) with excellent encapsulation efficiency (>98 %). Also,

STEM-HAADF compared nanoMOFs morphology before and after drug loading, denoting no changes upon impregnations. Importantly, elemental mapping showed the homogeneous distribution of AIs within nanoMOFs structures after their entrapment. More specifically, P/Fe ratio was calculated and similar values with theoretical calculations for the iron trimer were found. At this point, it is important to mention that contrary to the P/Fe ratios calculated previously in the case of degradation of empty MOFs (**Chapter 2 and 3**), these values found for drug loaded nanoMOFs were multiplied by a factor of 3. This change on the calculated ratios was selected to denote the substitution of water molecules from the phosphorylated active molecule (PP) for each iron (III) trimer, contrary to degradation studies presenting the substitution of water molecules and organic ligands from phosphate ions of the buffer each per iron element. Conversely, the sulfated drug had lower affinity for the nanoMOFs, was incorporated with lower yields and tended to be release readily out of the porous matrices. Therefore, S/Fe values could not be precisely determined.

After successful encapsulations, we were interested to follow the release kinetics of the AI and the trimesate constitutive ligand in different media containing phosphate and/or sulfate ions. In PBS, a sustained release was observed for the PP, while PS was released much faster ("burst" release), suggesting the lower affinity of the latter drug with the nanoMOFs. Considering Prednisolone, a total release could not be achieved, in reason of the low solubility of this drug in aqueous media. The stronger interactions of the PP with the Fe sites of the nanoMOFs were further confirmed by the release kinetics of the organic ligand, which presented a significant difference as compared to empty particles. Interestingly, only in the case of PP-loaded nanoMOFs, ligand release was importantly slowed down, suggesting a stabilization of the framework in the presence of coordinated phosphated drug (PP). In a complementary study, PP and PS release was studied in a sulfated media devoid of phosphates. Noteworthy, any release of PP was detected, in contrast to PS, which was rapidly released. In parallel, trimesate ligand was not released even after 3 days incubation in sulfates. These studies confirm the molecular modelling predictions showing the strongest affinity of the iron trimesate MOFs for phosphate moieties as compared to the sulfate ones.

To conclude, *ex situ* and *in situ* methods were selected to study the parameters affecting nanoMOFs degradation mechanism, revealing the morphological and compositional changes upon their interactions with simple media mimicking biological conditions (PBS or PBS/BSA) up to complex biological ones (blood and serum). In all cases, nanoparticles maintained their sizes, despite the immediate diffusion of labile



phosphate ions in their internal structures, as indicated by *in situ* AFM and ellispometry. Furthermore, it has been shown that incorporation of active molecules containing phosphate groups stabilize nanoMOFs matrices and eventually slowed down the release kinetics of the ligands. Both conclusions are of utmost importance for the future design of nanoMOFs, proposing that a depth research of delicate coatings of nanoMOFs surface should be chosen, in case that nanoMOFs administration into the living organism demands a slower degradation (e.g. intravenously administration). The coated nanoMOFs could in parallel contain active molecules with functionalized groups that from their side delay their degradation.

As a long-term perspective, it should be mentioned that other biodegradable MOFs, belonging to MIL-n series or different families, such as UiO, ZIF or PCN have already gained a special attention in biomedicine. Thus, it would be useful to follow the behavior of these nanoMOFs either bare or/and compare their degradation mechanism in the presence of active molecules entrapped on their porosity.

## References

1. Di Nunzio, M. R. *et al.* A 'ship in a bottle' strategy to load a hydrophilic anticancer drug in porous metal organic framework nanoparticles: Efficient encapsulation, matrix stabilization, and photodelivery. *J. Med. Chem.* **57**, 411–420 (2014).
2. Rodriguez-Ruiz, V. *et al.* Efficient 'green' encapsulation of a highly hydrophilic anticancer drug in metal-organic framework nanoparticles. *J. Drug Target.* **23**, 759–767 (2015).
3. Anand, R. *et al.* Host-guest interactions in Fe(III)-trimesate MOF nanoparticles loaded with doxorubicin. *J. Phys. Chem. B* **118**, 8532–8539 (2014).
4. Li, X. *et al.* Compartmentalized Encapsulation of Two Antibiotics in Porous Nanoparticles: an Efficient Strategy to Treat Intracellular Infections. *Part. Part. Syst. Charact.* **36**, 1–9 (2019).
5. Zimpel, A. *et al.* Imparting Functionality to MOF Nanoparticles by External Surface Selective Covalent Attachment of Polymers. *Chem. Mater.* **28**, 3318–3326 (2016).
6. Giménez-Marqués, M. *et al.* GraftFast Surface Engineering to Improve MOF Nanoparticles Furtiveness. *Small* **14**, 1–11 (2018).
7. Hidalgo, T. *et al.* Chitosan-coated mesoporous MIL-100(Fe) nanoparticles as improved bio-compatible oral nanocarriers. *Sci. Rep.* **7**, 1–14 (2017).
8. Grall, R. *et al.* *In vitro* biocompatibility of mesoporous metal (III; Fe, Al, Cr) trimesate MOF nanocarriers. *J. Mater. Chem. B* **3**, 8279–8292 (2015).
9. Tamames-Tabar, C. *et al.* Cytotoxicity of nanoscaled metal-organic frameworks. *J. Mater. Chem. B* **2**, 262–271 (2014).
10. Baati, T. *et al.* In depth analysis of the *in vivo* toxicity of nanoparticles of porous iron(iii) metal-organic frameworks. *Chem. Sci.* **4**, 1597–1607 (2013).
11. Simon-Yarza, T. *et al.* A Smart Metal-Organic Framework Nanomaterial for Lung Targeting. *Angew. Chemie - Int. Ed.* **56**, 15565–15569 (2017).

## General Discussion & Perspectives

12. Simon-Yarza, T. *et al.* Nanoparticles of Metal-Organic Frameworks: On the Road to *In vivo* Efficacy in Biomedicine. *Adv. Mater.* **30**, 1–15 (2018).
13. Bellido, E. *et al.* Understanding the colloidal stability of the mesoporous MIL-100(Fe) nanoparticles in physiological media. *Langmuir* **30**, 5911–5920 (2014).
14. Agostoni, V. *et al.* Impact of phosphorylation on the encapsulation of nucleoside analogues within porous iron(III) metal-organic framework MIL-100(Fe) nanoparticles. *J. Mater. Chem. B* **1**, 4231–4242 (2013).
15. Li, X. *et al.* New insights into the degradation mechanism of metal-organic frameworks drug carriers. *Sci. Rep.* **7**, 1–11 (2017).
16. Marlière, C. *et al.* An *in vivo* study of electrical charge distribution on the bacterial cell wall by atomic force microscopy in vibrating force mode. *Nanoscale* **7**, 8843–8857 (2015).
17. Agostoni, V. *et al.* A 'green' strategy to construct non-covalent, stable and bioactive coatings on porous MOF nanoparticles. *Sci. Rep.* **5**, 1–7 (2015).
18. Porcino, M., *et al.* New insights on the supramolecular structure of highly porous core-shell drug nanocarriers using solid-state NMR spectroscopy. *RSC Adv.* **9**, 32472–32475 (2019).

## General Conclusion

In this study, degradation mechanism of biodegradable iron trimesate MOFs, MIL-100(Fe) was explored in order to gain new insights of interest in view of possible biomedical applications. The main findings are summarized above:

1. According to their synthesis route, MIL-100(Fe) microMOFs present highly ordered crystalline planes on their surface with more or less defects. *In situ* AFM allowed detecting these features and determined the distance between crystalline planes ( $4.5 \pm 0.3$ ), in good agreement with high resolution STEM-HAADF investigations ( $4.1 \pm 0.3$ ) and theoretical values (4.23 nm). Moreover, *in situ* AFM enabled following changes in morphology, dimensions and mechanical properties of individual crystals in physiological conditions (PBS) and at different pH. It was found that MOFs' surface properties evolve within minutes according to *in situ* changes. Of utmost importance, despite their pronounced degradation in neutral PBS, the MOF particles maintained their dimensions, possibly due to the formation of a passivation layer.
2. To complement these studies, another *in situ* method was employed, ellipsometry. To do so, MIL-100(Fe) nanoMOFs of less than 100 nm were successfully synthesized and used for the elaboration of thin films by a dip coating process. Stability of the films was assessed in acidic and in neutral PBS by *in situ* ellipsometry. Changes in the thickness and the optical properties of the film were more pronounced in neutral environments than in acidic ones, indicating the formation of a degraded product. Moreover, the presence of an albumin coating layer did not influence the degradation of the framework. Noteworthy, it was found that in the extreme dilute conditions used for *in situ* ellipsometry experiments, the MOF properties change within a few minutes according to the composition of the media they are in contact with.
3. MIL-100(Fe) nanoparticles were successfully loaded with a series of AIs. Depending on their functional group, the drugs presented stronger or weaker affinities with the iron (III) metal sites of the structure, leading to slower or faster releases. It was found that phosphorylated drugs had the strongest affinities and that they stabilized the framework towards degradation, thanks to their strong complexation with the iron site of the nanoMOFs, slowing down the release of the constitutive trimesate ligand. Furthermore, degradation of the empty nanoMOFs was followed in the presence of serum and blood. Interestingly, it was concluded that despite the diffusion of various components from blood and serum into the frameworks, these globally maintained their microstructure even after long incubation times. The initial nanoMOF composition composed of Fe, O and C atoms evolved towards a complex one with P, N, S, Mg, Ca elements.

## General Conclusion

These studies open new perspective for the understanding of the fate of nanoMOFs in complex media and show how fast they respond towards changes in the composition of the media they are in contact with. It was shown that numerous parameters (intrinsic and extrinsic) determine the degradation mechanism of the particles. One of the most striking results was the shelf stability (minor dimensional changes) despite major loss of the MOF organic linkers.

In conclusion, it appears essential to carry on thorough stability studies each time a novel drug nanocarrier is developed.

## **Annex**

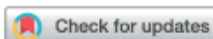
New insights on the supramolecular structure of highly porous core–shell drug nanocarriers using solid-state NMR spectroscopy

## Annex

New insights on the supramolecular structure of highly porous core-shell drug nanocarriers using solid-state NMR spectroscopy

This study is described in the format of a research article, published in RSC Advances ([doi.org/10.1039/C9RA07383C](https://doi.org/10.1039/C9RA07383C)). The main objective of this study, was the investigation of the interactions between phosphated active molecules and coatings with nanoMOFs matrix by solid state NMR spectroscopy (ssNMR). To successfully perform this study, MIL-100(Al) nanoMOFs were chosen, as the paramagnetic Fe centers could not be observed by ssNMR. Adenosine triphosphate (ATP) and CD-P were the molecules of interest for the loading and the coating of nanoparticles, respectively. High loadings and successful coating of the nanoMOFs were achieved, thanks to the strong coordination of the P species with the Al centers of the framework. ssNMR high sensitivity to P and Al nuclei, managed to distinguish P from the ATP molecules entrapped in the internal surface of nanoMOFs from the P centers of CD-P adsorbed on the external surface. The results presented in this study were crucial for the deeper understanding of host-guest interactions of active molecules with nanoMOFs and the effect of surface modifications at the molecular level.

This study was performed in collaboration with Dr. M. Porcino and Dr. C. Martineau-Corcus in CEMHTI, Orléans, France.

Cite this: *RSC Adv.*, 2019, 9, 32472

## New insights on the supramolecular structure of highly porous core-shell drug nanocarriers using solid-state NMR spectroscopy†

Marianna Porcino,<sup>a</sup> Ioanna Christodoulou,<sup>b</sup> Mai Dang Le Vuong,<sup>bc</sup> Ruxandra Gref<sup>id</sup>\*<sup>ab</sup> and Charlotte Martineau-Corcus<sup>id</sup>\*<sup>bc</sup>

Received 13th September 2019  
Accepted 4th October 2019

DOI: 10.1039/c9ra07383c

rsc.li/rsc-advances

Nano-sized metal-organic frameworks (nanoMOFs), with engineered surfaces to enhance the targeting of the drug delivery, have proven efficient as drug nanocarriers. To improve their performances a step further, it is essential to understand at the molecular level the interactions between the nanoMOF interfaces and both the surface covering groups and the drug loaded inside the micropores. Here we show how solid-state NMR spectroscopy allows us to address these issues in an aluminum-based nanoMOF coated and loaded with phosphorus-containing species.

Since their recent discovery, iron-based nanoMOFs have attracted increasing interest due to their potential for medical applications, owing to the versatility of their structural features, *in vivo* biocompatibility and biodegradability, properties as contrast agents and possibility to tailor their surface functionalities.<sup>1-2</sup> Among them, iron trimesate nanoMOF MIL-100(Fe) (MIL stands for Material of Institute Lavoisier) is among the most promising candidates for efficient drug incorporation by a one-step organic solvent-free method and for surface coating with cyclodextrin (CD) molecules which can be further engineered by linking phosphates (CD-P), targeting moieties or polymers.<sup>3,4</sup> The interactions of surface-modified iron trimesate nanoMOFs with cancer cells were increased by means of these versatile “Lego”-type coatings.<sup>3</sup> If the potential applications of the CD-P coated nanoMOFs have been demonstrated,<sup>3,5</sup> little information is known about the interactions at the atomic level between the CD-P coating and the nanoparticle (NP) surface sites. It was hypothesized that, in contrast to drug molecules which cross the windows of the MOFs and adsorb inside the pores, CD-Ps are too bulky and supposed not to bypass windows of around 9 Å in diameter and effectively remain adsorbed onto the external surface (Fig. 1). Having a direct proof of this hypothesis could help guide further CD-P engineering. Understanding the interactions at the molecular level between the

drug and the host solid is also crucial, as these interactions have a strong influence on the delivery processes. This study addresses these important aspects by using up-to-date complementary solid-state spectroscopic methodologies.

In the past decades, magic-angle spinning (MAS) solid-state nuclear magnetic resonance (ssNMR) spectroscopy, sensitive to short-range order, has proven an essential technique to get information about the structure of MOFs,<sup>6</sup> including drug-carrier MOFs.<sup>7</sup> Although it appeared ideally suited to address the questions mentioned above, we faced the presence of strong paramagnetic centers (Fe<sup>3+</sup> cations)

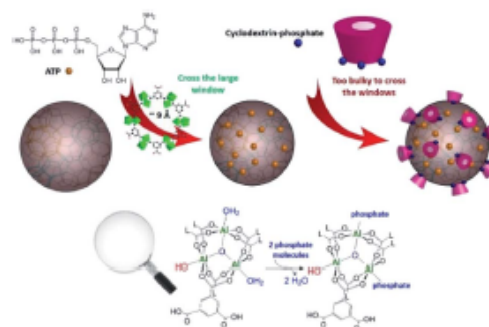


Fig. 1 Upper panel: schematic representation of the highly porous MIL-100(Al) nanoparticles loaded with ATP and then coated with CD-P. Bottom panel: close up of Al trimers coordinated to trimesate ligands (L). Two molecules of bound water can be replaced either by phosphates from the drug or by phosphate grafted on the cyclodextrin molecules. Phosphates bound to CD can only access sites located close to the external MOF surface. CD dimensions: cage 6–6.5 Å, external diameter 15.4 Å, height ~8 Å. ATP molecule has about 7 Å radius.

<sup>a</sup>CNRS, GEMHTI UPR 3079, Université d'Orléans, 1d Avenue de la recherche scientifique, 45071 Orléans, France

<sup>b</sup>ISMO, UMR 8214 CNRS, Université Paris Sud, Université Paris Saclay, 91400 Orsay, France. E-mail: ruxandra.gref@u-psud.fr

<sup>c</sup>MIM, Institut Lavoisier de Versailles (ILV), UMR CNRS 8180, Université de Versailles St-Quentin en Yvelines (UVSQ), 45 Avenue des États-Unis, 78035 Versailles Cedex, France. E-mail: charlotte.martineau@uvsq.fr

† Electronic supplementary information (ESI) available: Experimental section, additional <sup>31</sup>P, <sup>1</sup>H and <sup>27</sup>Al NMR spectra. See DOI: 10.1039/c9ra07383c





Paper

View Article Online  
RSC Advances

that severely reduces the relaxation times hence the amount of available information on the NMR spectra. We therefore have chosen to focus our study on the diamagnetic analogue of nanoMIL-100(Fe), namely nanoMIL-100(Al). The MIL-100(Al) topology<sup>8</sup> is similar to that of MIL-100(Fe),<sup>9</sup> it was shown that large amounts of drugs can be incorporated in this material, and that the NP surface (Fig. 1) can also be efficiently coated by CD-P.<sup>3</sup> Drug of interest here is adenosine triphosphate (ATP), a neurotransmitter with a crucial role in metabolism, which is believed to have a strong affinity with the aluminium species of the nanoMOF framework.

During our investigation, we were confronted to several challenges, including: (i) the complexity of the system, which yields broad overlapping <sup>1</sup>H MAS NMR spectra even at high field (20 T) and fast-MAS (60 kHz, Fig. S1, ESI†), and (ii) the low quantity of the surface species despite the reduced size (150 nm) of the particles. To circumvent the latter difficulty, surface enhanced solid-state NMR spectroscopy such as dynamic nuclear polarization (DNP) methods have been developed. They have proven their efficiency to detect the species present at the external surfaces of silica nanoparticles<sup>10</sup> and the applicability of the method for MOFs was shown.<sup>11</sup> However, DNP-MAS requires the use of a heterogeneous radical, solvent, low temperature (100 K), hence it does not represent the state of NPs as they can potentially be administered *in vivo* in patients. Therefore, we chose to work at room temperature and with simpler MAS NMR methods, namely <sup>27</sup>Al, <sup>31</sup>P and 2D <sup>27</sup>Al-<sup>31</sup>P correlation spectroscopy, that did not involve the use of external molecules such as solvents or radicals.

The <sup>27</sup>Al MAS NMR spectra of pristine and CD-P surface coated nanoMIL-100(Al) (Fig. S2, ESI†) are essentially similar despite the use of high magnetic field (20 T). For quadrupolar nuclei such as <sup>27</sup>Al, greater resolution can often be obtained using the multiple-quantum MAS (MQ-MAS) NMR experiment that separates the aluminium species in the indirect (vertical) dimension. The <sup>27</sup>Al MQMAS NMR spectrum of the nanoMIL-100(Al) recorded at moderate static magnetic field (9.4 T, Fig. S2, ESI†) is similar to that reported earlier for micron-sized MIL-100(Al) recorded at 11.7 T.<sup>12</sup> The <sup>27</sup>Al MQMAS NMR spectrum of nanoMIL-100(Al) recorded at 20 T interestingly has increased resolution which reveals the presence of an additional peak located at around -5 ppm (Fig. 2a). While the bulk Al signals remain similar, the new aluminium sites are in turn slightly modified when the NPs are coated with the CD-P (Fig. 2b), which indicates (i) that this aluminium resonance is due to the Al atoms present at or slightly below the surface of the NPs since CD-P is too bulky (see Fig. 1) to penetrate the open 3D-MOF structure, (ii) the shift of the resonance upon coating results from interactions between some of the surface aluminium species of the NPs and the CD-P coating. In the drug loaded samples (Fig. 3c and d), the bulk Al signals are more affected, indicating the successful incorporation of the drug inside the micropores of the nanoMOF.

To understand further these interactions, through-space <sup>1</sup>H-<sup>27</sup>Al two-dimensional (2D) MAS NMR experiments were performed in an attempt to correlate the protons of the CD-P that are in close proximity to the aluminium species. However

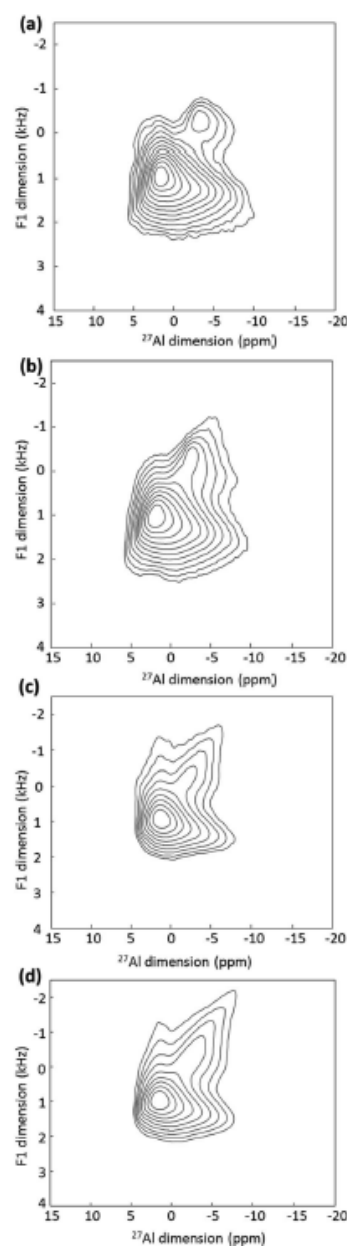


Fig. 2 <sup>27</sup>Al MQMAS NMR spectra of (a) pristine nanoMIL-100(Al) and nanoMIL-100(Al) (b) coated with CD-P, (c) loaded with ATP and (d) loaded with ATP and coated with CD-P.

the <sup>1</sup>H NMR spectrum is dominated by the signal of proton of the linkers, hence only the <sup>1</sup>H-<sup>27</sup>Al correlations from the bulk of the NPs were detected (Fig. S3, ESI†).



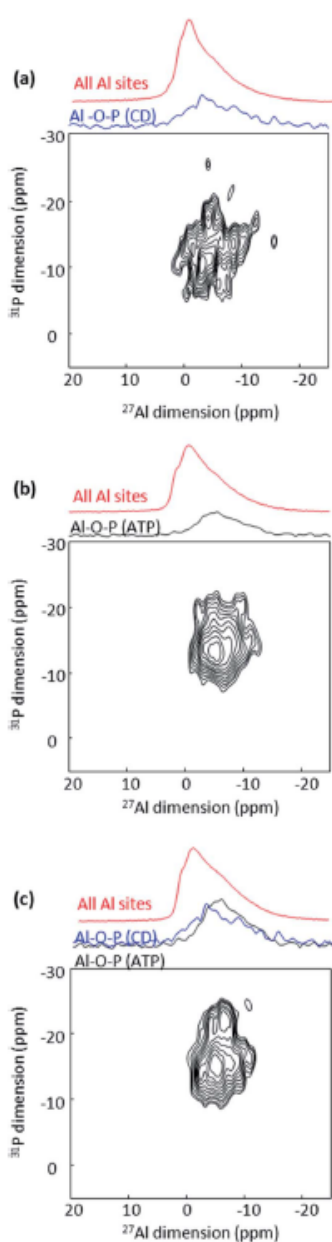


Fig. 3  $^{27}\text{Al}(^{31}\text{P})$  MAS D-HMQC NMR spectra of CD-P coated (a), ATP loaded (b) and CD-P coated ATP loaded nanoMIL100(Al) (c). The top blue spectra are the full projections on the horizontal dimension for the surface sites, the black spectra are the full projection for the interphase sites, while the red spectra are the MAS NMR spectra shown for comparison.

The  $^{31}\text{P}$  MAS NMR signatures of ATP and CD-P are well distinct (Fig. S5, ESI†).  $^{31}\text{P}$ - $^{31}\text{P}$  double-quantum single-quantum (DQ-SQ) NMR experiments were performed, which allow probing the spatial proximity between the phosphate groups. In CD-P, the  $^{31}\text{P}$  DQ-SQ NMR spectrum shows the phosphate groups grafted on the CD cavity. In ATP, such a spectrum allows the distinction of the middle phosphate of the tri-phosphate chain, which is the only  $^{31}\text{P}$  resonance that has two other P neighbours (Fig. S4, ESI†). In both ATP-loaded and ATP-loaded and coated nanoMIL-100(Al), the  $^{31}\text{P}$  DQ-SQ NMR correlations are similar to pure ATP, showing that the triphosphate moieties are preserved after loading (Fig. S6, ESI†). One can notice a shift of the  $^{31}\text{P}$  resonances, which very likely indicates strong interaction with the framework aluminium sites.

To go further in the characterization, we took advantage of the heteronuclei present in the CD-P coated nanoMIL-100(Al):  $^{27}\text{Al}$ , arising solely from the nanoMOF and  $^{31}\text{P}$ , arising solely from the CD-P coating. By recording 2D NMR spectrum between  $^{31}\text{P}$  and  $^{27}\text{Al}$  nuclei, the surface aluminium species of the NPs in close proximity to the CD-P and the bulk aluminium sites located in the vicinity of the loaded drug are expected to be selectively detected. Because of the short  $^{27}\text{Al}$  transverse relaxation time  $T_2$  (Table S1, ESI†), we could not use the through-bond heteronuclear multiple-quantum (J-HMQC) experiment that requires recoupling time in the 8 ms range for optimum efficiency.<sup>13</sup> Instead we employed the through-space dipolar-based version (D-HMQC), for which the optimum dipolar recoupling requires shorter recoupling time.<sup>14</sup> The recoupling time was kept short enough to ensure that only the Al in very close proximity to the  $^{31}\text{P}$  were selected. The resulting 2D  $^{27}\text{Al}$ - $^{31}\text{P}$  MAS NMR spectrum of CD-P-coated nanoMIL-100(Al) is shown Fig. 3a. The  $^{27}\text{Al}$  NMR signal is at  $-5$  ppm (*i.e.*, chemical shift similar to that of the surface peak observed in the MQMAS NMR spectra Fig. 2), which indicates that the observed surface Al species in the vicinity of the CD-P are in six-fold coordination. The  $^{27}\text{Al}$  chemical shift is lower than the  $^{27}\text{Al}$  chemical shifts in pristine MIL-100(Al) which range between 1.1 and 3.4 ppm.<sup>12</sup> It is close to chemical shift observed in aluminophosphate, hence we can hypothesize that the six-fold coordination is preserved by the formation of an Al-O-P bond between the Al surface sites of the nanoMOF and the terminal phosphate groups of the CD-P, which very likely substitute a water molecule (Fig. 1).

A similar six-fold coordinated  $^{27}\text{Al}$  resonance around  $-7$  ppm is observed in the ATP loaded nanoMIL-100(Al) 2D  $^{27}\text{Al}$ - $^{31}\text{P}$  D-HMQC MAS NMR spectrum (Fig. 3b), which suggests a close proximity (formation of a Al-O-P chemical bond) between Al species of the MOF framework and the terminal phosphate of the drug, which  $^{31}\text{P}$  resonance is located at  $-10$  ppm. This  $^{27}\text{Al}$  resonance is the signature of the grafted aluminium sites inside the pores of the MOF. Correlation of lower intensity is also observed between these Al species and the middle P of the triphosphate chain ( $-20$  ppm), in agreement with longer Al-P distance. Here again, the ATP very likely replaces a water molecule from the Al tricluster.

Finally, we performed the same 2D  $^{27}\text{Al}$ - $^{31}\text{P}$  NMR experiment in the target CD-P coated nanoMIL-100(Al) loaded with ATP



(Fig. 3c). The ATP content is much higher than the CD-P loading, hence the spectrum is dominated by the Al-O-ATP interaction. However, the  $^{31}\text{P}$  chemical shift expands to the higher ppm region (–5 to –10 ppm), characteristic of the CD-P coating. The similarity of the spectra in Fig. 3b and c clearly confirms that the CD-P coating on the external surface of the ATP-loaded nanoMOF did not affect the Al–O–ATP bond formed inside the MOF cavities.

In conclusion, by taking advantage of distinct heteroatoms present in an aluminium-based nanoMOF ( $^{27}\text{Al}$ ) which surface was coated by bulky phosphated CD groups ( $^{31}\text{P}$ ), we could circumvent the low resolution of  $^1\text{H}$  MAS NMR spectroscopy and provide for the first time a  $^{27}\text{Al}$  NMR signature at room temperature of aluminium species present at the surface or below the surface of MOF NPs and their interaction (*i.e.*, the formation of Al–O–P covalent bonds) with the CD-P coating. The formation of this strong covalent bonding between the CD and the MOF might be the key to ensure high stability of the core-shell NP *in vivo*. Using the same NMR methodology, we have shown the strong interaction of the triphosphate-drug ATP with the Al atoms of the MOF framework. Finally, we have shown the successful CD-P coating in a ATP-loaded nanoMIL-100(Al), which did not modify the MOF-drug interactions. This set of ssNMR experiment represents an essential characterization tool to guide towards more efficient surface modifications of these NPs, better targeting drugs (mono, di or tri-phosphate) and to help in understanding the effect of drug incorporation on the surface state of the nanoMOF. It could also be very useful in the investigation of nanoMIL-100(Al) NPs degradation in physiological medium (phosphate buffer) in which Al–O–P interactions might occur and be at the origin of the drug release processes. The methodology presented here consisting in covering the surface of porous NPs by bulky groups (unable to penetrate in the porosity of the particles) containing heteroatoms easily accessible by ssNMR (like  $^{31}\text{P}$  or  $^{19}\text{F}$ ) could also become a general strategy to probe surface species of MOF NPs without need of expensive DNP-MAS experiments.

## Conflicts of interest

There are no conflicts to declare.

## Acknowledgements

MP thanks the Région Centre-Val de Loire for a PhD fellowship. CMC is grateful for financial support from the Institut Universitaire de France (IUF). Financial support from the IR-RMN-THC Fr3050 CNRS for conducting the research is gratefully acknowledged. This work was also supported by the Paris Ile-de-France Region – DIM "Respire" and by the Labex NanoSaclay. MP and CMC thank Dr. Franck Fayon (CEMHTI Orléans) for fruitful discussions about the  $^{31}\text{P}$ - $^{31}\text{P}$  DQ-SQ NMR experiments.

## Notes and references

- P. Horcajada, T. Chalati, C. Serre, B. Gillet, C. Sebrie, T. Baati, J. F. Eubank, D. Heurtaux, P. Clayette, C. Kreuz, J. S. Chang, Y. K. Hwang, V. Marsaud, P. N. Bories, L. Cynober, S. Gil, G. Férey, P. Couvreur and R. Gref, *Nat. Mater.*, 2010, **9**, 172.
- T. Baati, L. Njim, F. Neffati, A. Kerkeni, M. Bouttemi, R. Gref, M. F. Najjar, A. Zakhama, P. Couvreur, C. Serre and P. Horcajada, *Chem. Sci.*, 2013, **4**, 1597.
- V. Agostoni, P. Horcajada, M. Noiry, M. Malanga, A. Aykac, L. Jicsinszky, A. Vargas-Berenguel, N. Semiramoth, S. Daoud-Mahammed, V. Nicolas, C. Martineau, F. Taulelle, J. Vigneron, A. Etcheberry, C. Serre and R. Gref, *Sci. Rep.*, 2015, **5**, 7925.
- A. Aykac, M. Noiry, M. Malanga, V. Agostoni, J. M. Casas-Solvas, E. Fenyvesi, R. Gref and A. Vargas-Berenguel, *Biochim. Biophys. Acta*, 2017, **1861**, 1606.
- (a) T. Simon-Yarza, T. Baati, A. Paci, L. L. Lesueur, A. Seck, M. Chipier, R. Gref, C. Serre, P. Couvreur and P. Horcajada, *J. Mater. Chem. B*, 2016, **4**, 585; (b) T. Simon-Yarza, M. Gimenez-Marques, R. Mrimi, A. Mielcarek, R. Gref, P. Horcajada, C. Serre and P. Couvreur, *Angew. Chem., Int. Ed.*, 2017, **56**, 15565.
- C. Martineau-Corcoc, *Curr. Opin. Colloid Interface Sci.*, 2018, **33**, 35.
- S. Devautour-Vinot, C. Martineau, S. Diaby, M. Ben-Yahia, S. Miller, C. Serre, P. Horcajada, D. Cunha, F. Taulelle and G. Maurin, *J. Phys. Chem. C*, 2013, **117**, 11694.
- G. Férey, C. Serre, C. Mellot-Draznieks, F. Millange, S. Surble, J. Dutour and I. Margiolaki, *Angew. Chem., Int. Ed.*, 2004, **43**, 6296.
- C. Volkringer, D. Popov, T. Loiseau, G. Férey, M. Burghammer, C. Riekel, M. Haouas and F. Taulelle, *Chem. Mater.*, 2009, **21**, 5695.
- A. J. Rossini, A. Zagdoun, M. Lelli, A. Lesage, C. Copéret and L. Emsley, *Acc. Chem. Res.*, 2013, **46**, 1942.
- (a) A. J. Rossini, A. Zagdoun, M. Lelli, J. Canivet, S. Aguado, O. Ouari, P. Tordo, M. Rosay, W. E. Maas, C. Copéret, D. Farrusseng, L. Emsley and A. Lesage, *Angew. Chem., Int. Ed.*, 2012, **51**, 123; (b) F. Pourpoint, A. S. L. Thankamony, C. Volkringer, T. Loiseau, J. Trébosc, F. Aussenac, D. Carnevale, G. Bodenhausen, H. Vezin, O. Lafon and J.-P. Amoureux, *Chem. Commun.*, 2014, **50**, 933; (c) Z. Y. Guo, T. Kobayashi, L. L. Wang, T. W. Goh, C. X. Xiao, M. A. Caporini, M. Rosay, D. D. Johnson, M. Pruski and W. Y. Huang, *Chem.–Eur. J.*, 2014, **20**, 16308.
- M. Haouas, C. Volkringer, T. Loiseau, G. Férey and F. Taulelle, *J. Phys. Chem. C*, 2011, **115**, 17934.
- (a) D. Massiot, F. Fayon, B. Alonso, J. Trebosc and J. P. Amoureux, *J. Magn. Reson.*, 2003, **164**, 160; (b) M. Deschamps, F. Fayon, J. Hiet, G. Ferru, M. Derieppe, N. Pellerin and D. Massiot, *Phys. Chem. Chem. Phys.*, 2008, **10**, 1298.
- J. Trebosc, B. Hu, J. P. Amoureux and Z. Gan, *J. Magn. Reson.*, 2007, **186**, 220.



Electronic Supplementary Material (ESI) for RSC Advances.  
This journal is © The Royal Society of Chemistry 2019

**New insights on the supramolecular structure of highly porous core-shell drug nanocarriers using solid-state NMR spectroscopy.**

Marianna Porcino, Ioanna Christodoulou, Mai Vuong Dang Le, Ruxandra Gref and Charlotte Martineau-Corcos

**Electronic Supplementary Information**

Experimental Section

Fig. S1. TEM images of nanoMIL-100(Al).

Fig. S2. TEM images of CD-P-coated nanoMIL-100(Al).

Fig. S3. TEM images of nanoMIL-100(Al) degraded 48 hours in PBS solution.

Fig. S4.  $^1\text{H}$  1D and  $^1\text{H}$ - $^1\text{H}$  2D MAS NMR spectra

Fig. S5.  $^{27}\text{Al}$  MAS and MQMAS NMR spectra

Table S1.  $^{27}\text{Al}$   $T_2$  values

Fig. S6.  $^{27}\text{Al}\{^1\text{H}\}$  MAS *D*-HMQC NMR spectra

Fig. S7.  $^{31}\text{P}$ - $^{31}\text{P}$  MAS DQ-SQ NMR spectrum of pure ATP

Fig. S8.  $^{31}\text{P}$  CPMAS NMR spectra

Fig. S9.  $^{31}\text{P}$ - $^{31}\text{P}$  MAS DQ-SQ NMR spectra of pure loaded or coated nanoMIL-100(Al)

## New insights on the supramolecular structure of highly porous core-shell drug nanocarriers using solid-state NMR spectroscopy

### Experimental Section

#### *Synthesis*

Al MIL(100) NPs were prepared and characterized as previously described.<sup>1</sup> The crystalline particles had a mean hydrodynamic diameter of  $160 \pm 15$  nm, BET surface area of  $1670 \pm 20$  m<sup>2</sup>/g. ATP was loaded according to previous organic solvent-free method reported in the case of other phosphorylated drugs.<sup>2-4</sup> Loadings reached 20 wt%.

#### *Elemental analysis*

Elemental analysis was performed to quantify the C and H elemental weight contents in the MOF particles loaded or not with ATP after sample combustion at 1050°C using an Elemental Analyzer (Perkin-Elmer 2400 CHNS/O Series II System).

#### *Transmission Electron Microscopy (TEM)*

Morphology and size of the solids were observed by Transmission Electron Microscopy (TEM), under a JEOL JEM-1400 microscope with acceleration voltage of 120 kV. Nanoparticle suspensions were deposited on copper grids, left to dry and observed without further staining.

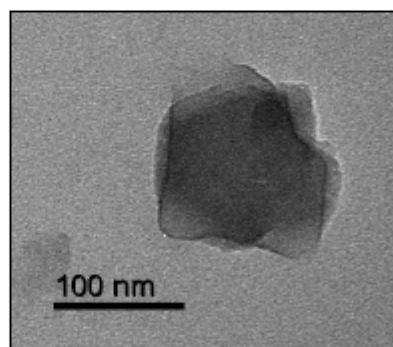
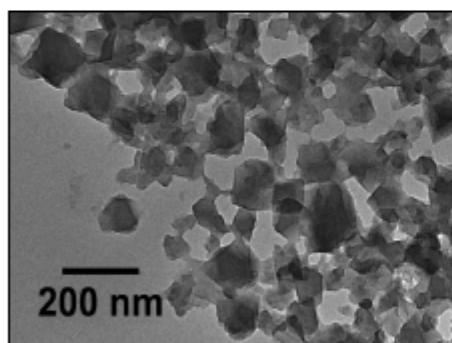
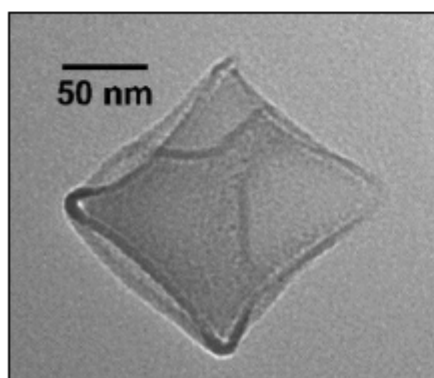


Figure S1. TEM images of nanoMIL-100(Al).



## Annex

New insights on the supramolecular structure of highly porous core-shell drug nanocarriers using solid-state NMR spectroscopy

Figure S2. TEM images of CD-P coated nanoMIL-100(Al).

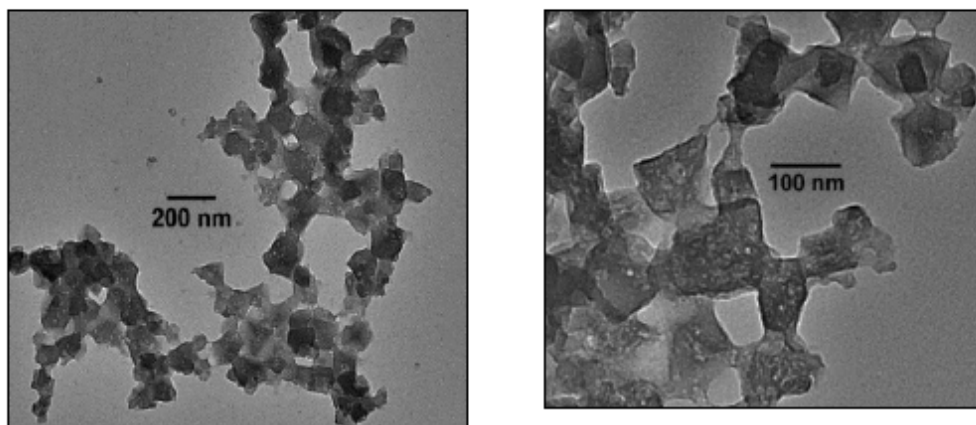


Figure S3. TEM images of nanoMIL-100(Al) degraded 48 hours in PBS solution.

All TEM images show no dissolution of the nanoparticles. Degradation in PBS occurs through the formation of holes in the NPs.

### *Solid-state NMR Spectroscopy*

The  $^{27}\text{Al}$  MAS and MQMAS NMR spectra were recorded at 20 T using a H/X/Y 3.2 mm double-resonance probehead, spinning at 20 kHz MAS frequency. The z-filter MQMAS pulse sequence was used, with radiofrequency (RF) field for the excitation and reconversion of the triple-quantum coherence. The  $^{27}\text{Al}\{^{31}\text{P}\}$  D-HMQC NMR spectrum was recorded at 17.6 T using a 4 mm  $^1\text{H}$ - $^{31}\text{P}$ - $^{27}\text{Al}$  triple resonance probe spinning at 14 kHz MAS frequency. The symmetry-based R412 scheme<sup>5</sup> was used to recouple the Al-P dipolar interaction. The rotor-synchronized recoupling time was set to 1.7 ms.  $^{27}\text{Al}$  double-frequency sweep (DFS) was applied to boost the  $^{27}\text{Al}$

magnetization. Recycling delay was set to 0.25 s. 20  $t_1$  slices were recorded with 32432 (for the coated material) and 28800 (for the ATP-loaded ones) transients each, leading to a total of experimental time of about 45 hours. All spectra are treated with 200 Hz LB apodization in the F2 dimension. The  $^{27}\text{Al}$  and  $^{31}\text{P}$  chemical shifts are referenced to  $\text{Al}(\text{NO}_3)_3$  and  $\text{H}_3\text{PO}_4$  solution at 0 ppm, respectively. All spectra were analysed using the Dmfit software.<sup>6</sup>

The  $^1\text{H}$  MAS NMR spectra were recorded at a magnetic field of 20 T, using a Bruker 850 MHz WB NMR spectrometer and a HXY 1.3 mm probe in double mode. The spectra were acquired using a Hahn echo pulse sequence, with a  $90^\circ$  pulse duration of 3.5  $\mu\text{s}$ , an inter-pulse delay synchronized with one rotor period and a spinning rate of 60 kHz. The recycle delay was set to 5 s and 16 transients were recorded for each sample. The  $^1\text{H}$  chemical shifts were referenced to TMS at 0 ppm.

The  $^{27}\text{Al}$  MAS NMR spectra were recorded at the same magnetic field of the  $^1\text{H}$  spectra, using a HXY 3.2 mm probe in double mode, with a spinning rate of 20 kHz. The recycle delay was set to 0.3 s, the  $90^\circ$  pulse to 2.2  $\mu\text{s}$  with a RF field of 38 kHz. The  $^{27}\text{Al}$  chemical shifts are referenced to  $\text{Al}(\text{NO}_3)_3$  solution at 0 ppm.

The  $^{27}\text{Al}\{^1\text{H}\}$  D-HMQC (dipolar-Heteronuclear multiquantum correlation) 2D experiment is performed under a MAS frequency of 60 kHz in a 1.3 mm probe using the same spectrometer mentioned before.  $\text{R}4_2^1$  was used as the recoupling sequence in order to reintroduce  $^1\text{H}$ - $^{27}\text{Al}$  heteronuclear dipolar interactions, with 1.4 ms of recoupling time. 80  $t_1$  slices with 1024 transients were co-added. The States-TPPI procedure provides a phase sensitive 2D NMR spectrum.

The  $^{27}\text{Al}$  MQMAS (Multi-Quantum Magic-Angle Spinning) was carried out at 9.4 T (Larmor Frequency of 104 MHz), using a HXY 2.5 mm probe in double mode with a spinning rate of 25 kHz, using a triple-quantum z-filtered pulse sequence and is shown after a shearing transformation.

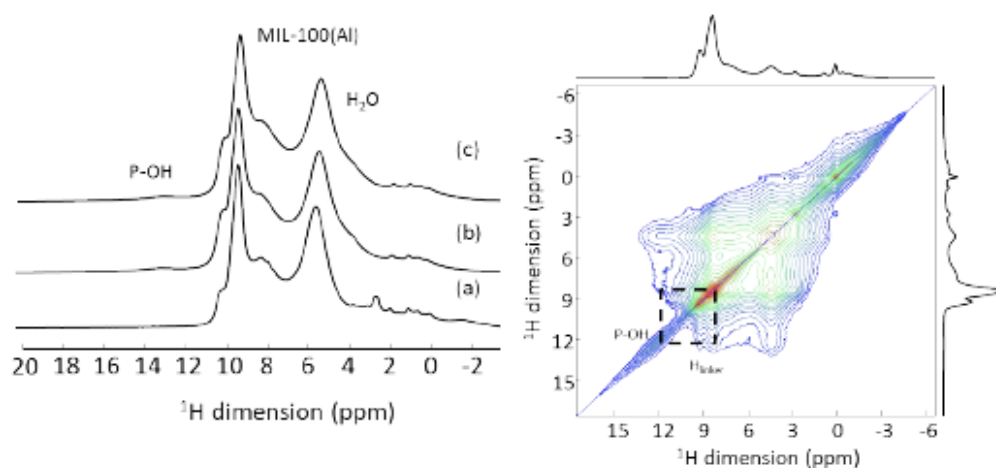
The  $^{31}\text{P}$  cross-polarization experiments were recorded on a 9.4 T magnet ( $^1\text{H}$  and  $^{31}\text{P}$  Larmor frequency of 400 and 160 MHz, respectively) with a Bruker spectrometer, using a 4 mm double resonance probe and spinning at 14 kHz MAS frequency. The  $^{31}\text{P}$  chemical shifts are referenced to  $\text{H}_3\text{PO}_4$  solution at 0 ppm. Recycling delay was set to 5 s, the initial  $90^\circ$  pulse on  $^1\text{H}$  to 4  $\mu\text{s}$  with a RF field of 62 kHz and the contact time was set to 5 ms.  $^1\text{H}$  SPINAL-64 decoupling was applied during the  $^{31}\text{P}$  acquisition.

The  $^{31}\text{P}$ - $^{31}\text{P}$  DQ-SQ MAS spectra were recorded on the same 9.4 T spectrometer, using the same probe and the same spinning speed as mentioned before. The INADEQUATE pulse sequence was used with a recoupling delay of 7 ms, for a total experimental time of 4 hours.  $^1\text{H}$  SPINAL-64 decoupling was applied

## Annex

### New insights on the supramolecular structure of highly porous core-shell drug nanocarriers using solid-state NMR spectroscopy

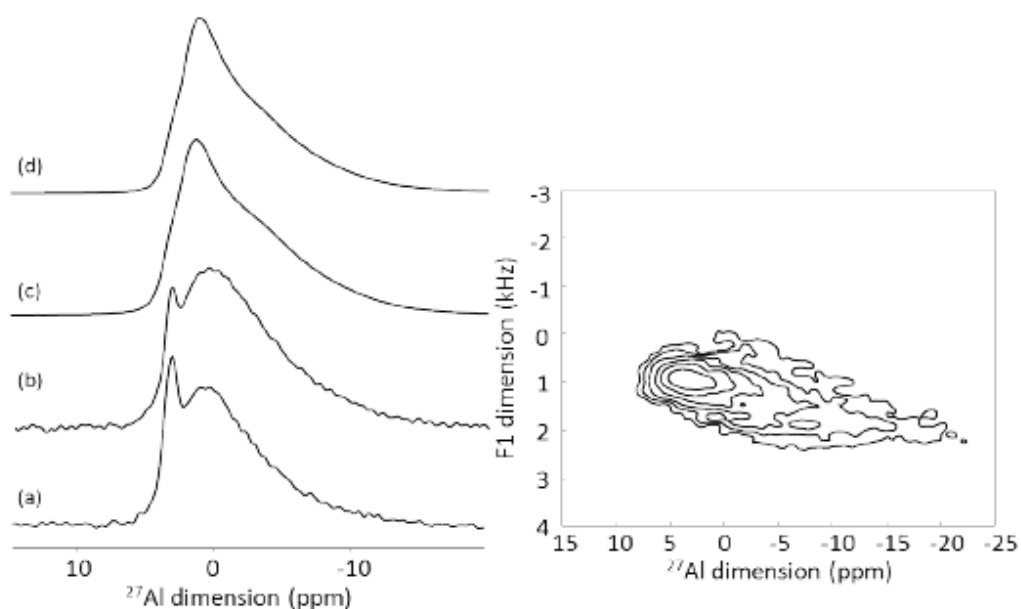
during recoupling time and acquisition with RF fields of 70 kHz and 79 kHz respectively. The  $S_3$  pulse sequence was used with a recoupling delay of 2.8 ms.  $^1\text{H}$  CW (RF field of 52 kHz) and SPINAL-64 (RF field of 70 kHz) decoupling were applied during recoupling time and acquisition respectively. Using a recycling delay of 4 s, 60  $t_1$  slices with 192-960 transients were co-added, leading to a total of experimental times of 16-64 hours. For both INADEQUATE and  $S_3$ , the sensitivity was boosted by an initial  $^1\text{H} \rightarrow ^{31}\text{P}$  CP block.



**Figure S4.** Left:  $^1\text{H}$  MAS NMR spectra of (a) nanoMIL-100(Al), (b) ATP-loaded nanoMIL-100(Al) and (c) CD-P coated ATP-loaded nanoMIL-100(Al). Right: 2D  $^1\text{H}$ - $^1\text{H}$  spin diffusion NMR spectrum of CD-P coated ATP-loaded nanoMIL-100(Al). The dash lines indicate the spatial proximity between a phosphate proton and a proton from the linker of the MOF.



New insights on the supramolecular structure of highly porous core-shell drug nanocarriers using solid-state NMR spectroscopy



**Figure S5.** Left:  $^{27}\text{Al}$  MAS NMR spectra of (a) nanoMIL-100(Al), (b) CD-P coated nanoMIL-100(Al), (c) ATP-loaded nanoMIL-100(Al) and (d) CD-P coated ATP-loaded nanoMIL-100(Al) recorded at 20.0 T. Right:  $^{27}\text{Al}$  MQMAS NMR spectrum of nanoMIL-100(Al) recorded at 9.4 T.

The  $^{27}\text{Al}$  MQMAS NMR spectrum of nanosized MIL-100(Al) is similar to the one previously reported in the literature for micro sized MIL-100(Al)<sup>7</sup> and display resonances in the chemical shift range of the six-coordinated aluminum atom (0 to -10 ppm).

## Annex

New insights on the supramolecular structure of highly porous core-shell drug nanocarriers using solid-state NMR spectroscopy

Sample	$^{27}\text{Al}$ $T_2$ (ms, $\pm 0.1$ )
MIL100(Al)	3.8
MIL100(Al)@ATP	3.4
CD-P coated MIL100(Al)	3.8
CD-P coated MIL100(Al)@ATP	3.5

Table S1.  $^{27}\text{Al}$   $T_2$  measured from a spin echo experiment of the samples studied.

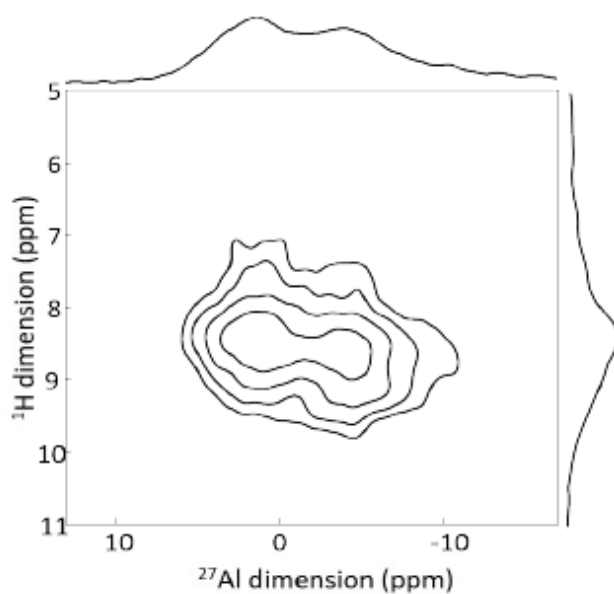
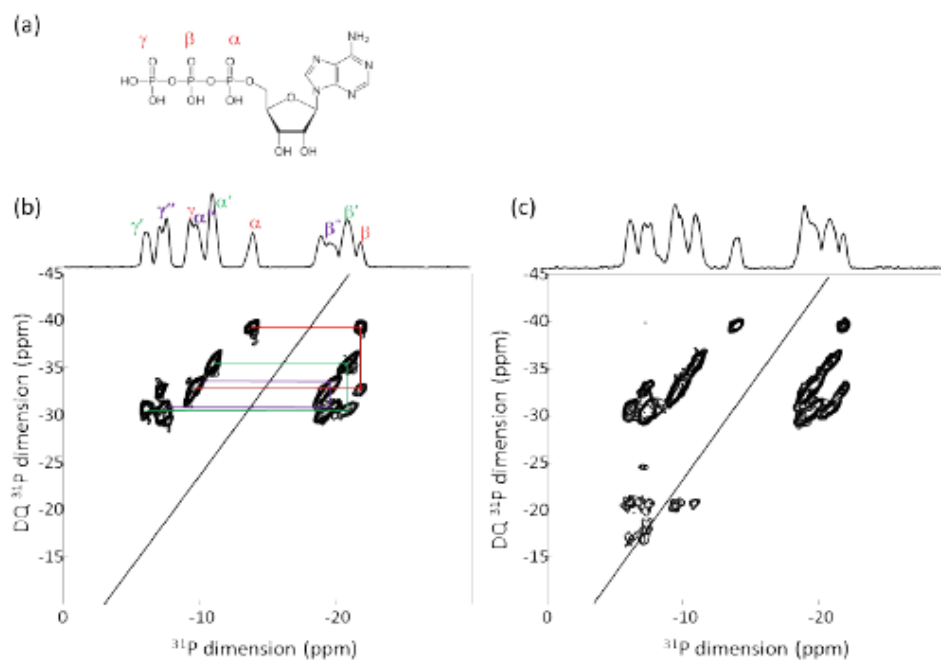


Figure S6.  $^{27}\text{Al}\{^1\text{H}\}$  MAS D-HMQC NMR spectrum of CD-P coated MIL-100(Al). Only a correlation between the  $^{27}\text{Al}$  signal and the protons of the linkers is observed.

New insights on the supramolecular structure of highly porous core-shell drug nanocarriers using solid-state NMR spectroscopy

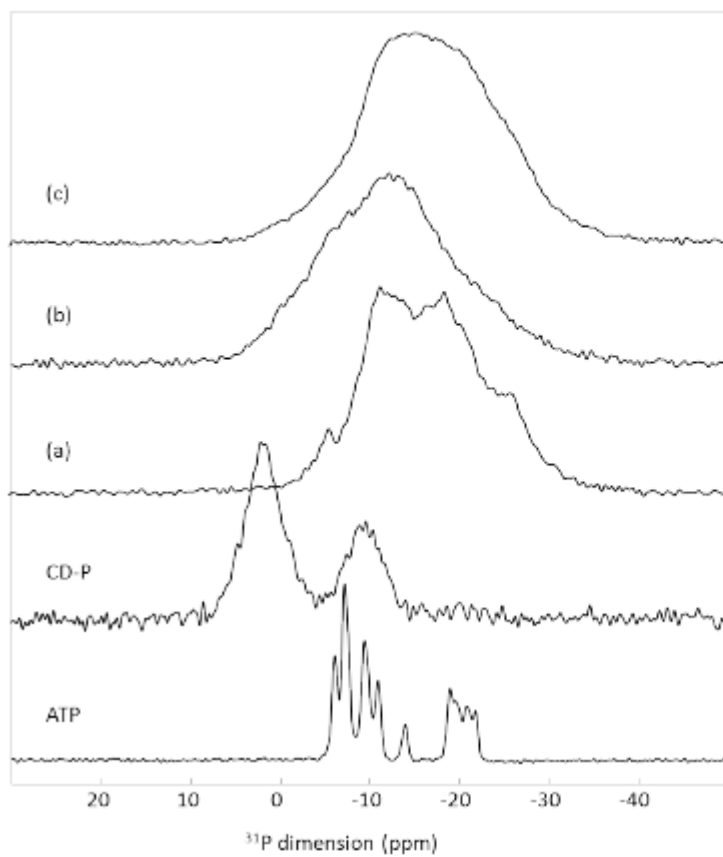


**Figure S7.**  $^{31}\text{P}$ - $^{31}\text{P}$  MAS DQ-SQ NMR spectrum of ATP recorded at 9.7 T with CP-INADEQUATE (left) and  $S_3$  (right) pulse sequence. The lines represent the different hydrated forms of ATP present in the commercial product. Additional peaks are seen on the  $S_3$  NMR spectrum (dipolar-based), which are due to longer range interactions.

In the 2D  $^{31}\text{P}$ - $^{31}\text{P}$  homonuclear correlation experiments ( $J$ -type and through space-proximity), the  $\beta$ -phosphorus atom (the middle of the tri-phosphate) is identified as it is the only one having correlation with two other P atoms. The commercial ATP is a mixture of several phases that differ by their hydration states. Additionally, the through-space correlation experiment (right part of Figure S4) gives the opportunity to observe the inter-molecular interactions.

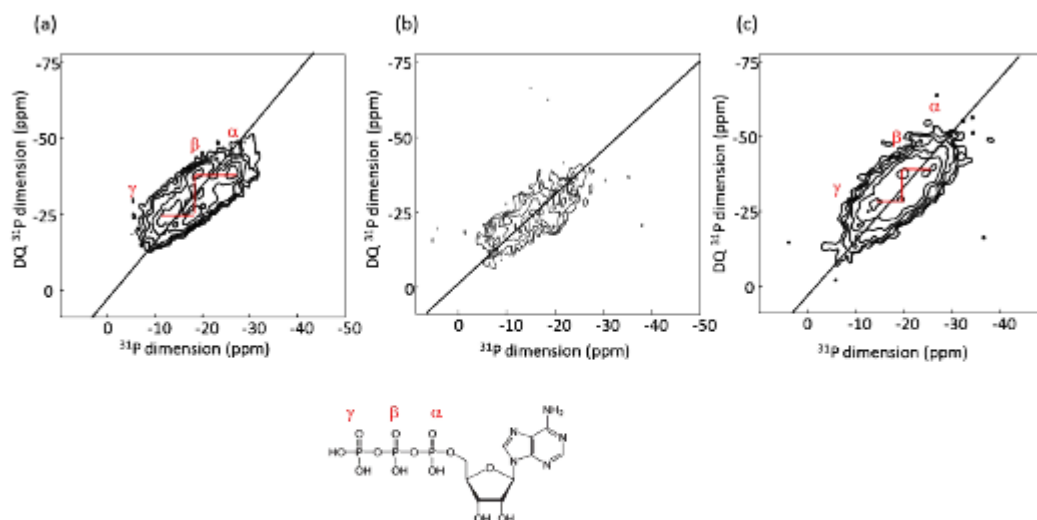
## Annex

New insights on the supramolecular structure of highly porous core-shell drug nanocarriers using solid-state NMR spectroscopy



**Figure S8.**  $^{31}\text{P}$  CPMAS NMR spectra of pure ATP, CD-P, (a) ATP loaded nanoMIL-100(Al), (b) CD-P coated nanoMIL-100 and (c) CD-P coated ATP loaded nanoMIL-100.

## New insights on the supramolecular structure of highly porous core-shell drug nanocarriers using solid-state NMR spectroscopy



**Figure S9.**  $^{31}\text{P}$ - $^{31}\text{P}$  DQ-SQ MAS NMR spectra of (a) ATP loaded nanoMIL-100(Al), (b) CD-P coated nanoMIL-100 and (c) CD-P coated ATP loaded nanoMIL-100. Below is shown the ATP molecule with the triphosphate groups labeled.

Similar to the experiment performed on the pure ATP, the middle  $\beta$ -phosphate is identified as it is linked to two other phosphorus atoms. The triphosphate structure is preserved once the ATP is loaded in the pores of the nanoMOF. The  $^{31}\text{P}$  resonance at *ca* - 15 ppm shows correlation with the aluminum atoms in the  $^{27}\text{Al}$ - $^{31}\text{P}$  D-HMQC NMR spectrum (see main text). It therefore corresponds to the terminal phosphate group.

### References

1. V. Agostoni, P. Horcajada, M. Noiray, M. Malanga, A. Aykac, L. Jicsinszky, A. Vargas-Berenguel, N. Semiramo, S. Daoud-Mahammed, V. Nicolas, C. Martineau, F. Taulelle, J. Vigneron, A. Etcheberry, C. Serre, R. Gref, *Sci. Reports* 2015, **5**, 7925.
2. V. Rodriguez-Ruiz, A. Maksimenko, R. Anand, S. Monti, V. Agostoni, P. Couvreur, M. Lampropoulou, K. Yannakopoulou, R. Gref, *J. Drug Target.*, 2015, **23**, 759.
3. V. Agostoni, R. Anand, S. Monti, S. Hall, G. Maurin, P. Horcajada, C. Serre, K. Bouchemal, R. Gref, *J. Mater. Chem. B*, 2013, **1**, 4231.

## Annex

New insights on the supramolecular structure of highly porous core-shell drug nanocarriers using solid-state NMR spectroscopy

4. V. Agostoni, T. Chalati, P. Horcajada, H. Willaime, R. Anand, N. Semiramothe, T. Baati, S. Hall, G. Maurin, H. Chacun, K. Bouchemal, C. Martineau, F. Taulelle, P. Couvreur, C. Rogez-Kreuz, P. Clayette, S. Monti, C. Serre, R. Gref, *Adv. Healthcare Mater.*, 2013, **2**, 1630.
5. A. Brinkmann, A.P.M. Kentgens *J. Am. Chem. Soc.*, 2006, **128**, 14758.
6. D. Massiot, F. Fayon, M. Capron, I. King, S. Le Calvé, B. Alonso, J. O. Durand, B. Bujoli, Z. Gan, G. Hoatson, *Magn. Reson. Chem.*, 2002, **40**, 70.
7. M. Haouas, C. Volkringer, T. Loiseau, G. Ferey, F. Taulelle, *J. Phys. Chem. C*, 2011, **115**, 17934.

**Titre :** Mécanisme de dégradation de particules poreuses hybrides organiques-inorganiques pour des applications biomédicales

**Mots clés :** MOFs, délivrance des médicaments, mécanisme de dégradation, techniques *in situ*

**Résumé :** Les particules hybrides poreuses nommées Metal Organic Frameworks (MOFs) sont des candidats prometteurs pour l'administration de molécules actives dans le domaine biomédical. Parmi une grande variété de MOFs, le trimesate de fer (III) micro/mésoporeux MIL-100(Fe) (MIL signifie Matériaux de l'Institut Lavoisier) sont les particules de choix, grâce à leur capacité d'incorporer de médicaments à la fois hydrophiles et hydrophobes, (ii) leur libération ciblée et contrôlée et (iii) leur nature biocompatible et biodégradable. Une fois les MOF administrées dans l'organisme vivant, elles devraient présenter une bonne stabilité pendant la circulation, jusqu'à ce qu'elles atteignent la cible concernée. Une fois la cible atteinte, ils doivent se dégrader et libérer la molécule active, sans induire de cytotoxicité dans l'organisme. Si les particules de MIL-100(Fe) sont stables dans les solutions aqueuses et éthanoliques, elles se dégradent rapidement dans des conditions physiologiques simulées, libérant une quantité importante de leur ligand trimesate constitutif. Plus précisément, en présence d'une solution saline tampon de phosphate (PBS), les ions phosphates se coordonnent fortement aux sites de Lewis acides du fer (III) du MOF, ce qui initie la dégradation. Il a été montré par ailleurs que les particules MIL-100(Fe) de taille micrométrique se dégradent avec formation d'une couronne inorganique fragile autour d'un cœur intact, sans cependant aucune modification de leur taille initiale. Par ailleurs, les mêmes MOFs s'agrègent d'une manière pH-et dégradation dépendante. Il a été conclu que le mécanisme de dégradation des MOF à base de MIL-100(Fe) dépend fortement de la composition du milieu externe, mais les paramètres impliqués n'ont pas été explorés de manière systématique. L'objectif principal de cette thèse est l'étude des paramètres principaux (pH du milieu, taille et qualité de cristaux MOF, présence de molécules actives incorporées dans les pores et/ou d'un recouvrement) afin d'avoir une vision plus approfondie des mécanismes de dégradation des particules MIL-100(Fe). Pour cela, en première étape, des particules de grande taille (microMOFs d'environ 50  $\mu\text{m}$ ) ont été synthétisées et étudiées avec succès par une technique *in situ* innovante, L'AFM en liquide. Cette méthode de choix a permis de suivre en temps réel et avec une résolution nanométrique les changements morphologiques, dimensionnels et mécaniques de la surface des microMOFs en contact avec divers milieux liquides et suite à un changement *in situ* du pH. L'AFM en liquide a permis de mettre en évidence des principaux paramètres attribués à la dégradation des MOF (pH du milieu, taille et qualité des cristaux MOF) et a ouvert la voie à d'autres études sur des particules plus petites (nanoMOFs), d'intérêt en nanomédecine. L'ellipsométrie *in situ* a permis d'étudier le mécanisme de dégradation des nanoMOF déposés en couches minces sur un support. Cette technique a fourni des données cruciales sur les interactions des nanoMOF avec le milieu externe (PBS avec ou sans protéine) dans des conditions de sous-saturation afin de mimer les conditions *in vivo* dans l'organisme. Après avoir exploré les paramètres importants qui contrôlent la dégradation des micro et nanoMOF vides, une famille principes actifs (prednisolone, prednisolone sulfatée et prednisolone phosphorylée) a été choisie pour l'encapsulation, afin d'étudier leurs interactions de type hôte-invité avec les nanoMOF. L'affinité des groupements fonctionnels avec les sites de fer du MOF a été étudiée par modélisation moléculaire (DFT) ce qui a permis de mieux comprendre les interactions mis en jeu lors de la dégradation. Dans l'ensemble, les techniques complémentaires utilisées dans cette thèse ont fourni des renseignements nouveaux sur le mécanisme de dégradation des particules poreuses de carboxylate de fer en vue de leur utilisation comme vecteurs thérapeutiques.

**Title:** A comprehensive study of the erosion mechanism of porous hybrid particles for biomedical applications

**Keywords:** MOFs, drug delivery, degradation mechanism, *in situ* techniques

**Abstract:** Hybrid porous particles named Metal Organic Frameworks nanoparticles (MOFs) are promising candidates for the delivery of active molecules in the biomedical field. Among a large variety of MOFs, the micro/mesoporous iron (III) trimesate MIL-100(Fe) (MIL stands for Materials of Lavoisier Institute) are the particles of choice, thanks to: i) their high drug payloads (up to 30 wt %) of both hydrophilic and hydrophobic drugs; ii) their controlled release properties; iii) convenient surface modifications and (iv) biocompatible and biodegradable nature. Once administered in the living organism, MOFs should present a good stability during circulation, until they reach their target. Once targeting is achieved, they should degrade and release their cargo, without inducing any cytotoxicity in the body. This thesis focuses on the study of the fine balance between stability and degradation, through in-depth investigations of the degradation mechanisms. While MIL-100(Fe) particles are stable in aqueous and ethanolic solutions, they are rapidly degraded under simulated physiological conditions, releasing a significant amount of their constitutive trimesate ligand. More precisely, when MOFs are incubated in phosphate buffer saline (PBS), phosphate ions strongly coordinate to the iron (III) acid Lewis sites of the framework, initiating degradation. Previous studies showed that MOFs degrade without size modifications and that they have a pH and degradation-dependent aggregation. It is therefore of main interest to study the influences of the main parameters involved in MOFs degradation (the pH of the media, the size and the presence of defects in the crystalline structures, the presence of loaded drugs in the pores and/or the presence of coating layers). The primary objective of this thesis was the rigorous study of these parameters to gain a deeper vision of the MIL-100(Fe) MOF degradation mechanisms. To do so, first, MOFs crystals of around 50  $\mu\text{m}$  (microMOFs) of different crystallinity degrees were successfully synthesized and studied by an innovative *in situ* technique. AFM in liquid was the method of choice to follow in real time and at nanoscale resolution, morphological, dimensional and mechanical changes of microMOFs surface in media of different compositions and upon *in situ* modification of the pH. This method proved to be a powerful tool by highlighting some of the main parameters attributed to MOFs degradation (pH of the media, size and crystallinity degree of the particles). It paved the way for further studies of smaller particles (nanoMOFs), mainly used in drug delivery applications. *In situ* ellipsometry was selected to study the degradation mechanism of thin films of nanoMOFs, fabricated by a dip coating process. The developed *in situ* technique was used to analyze the interactions of MIL-100(Fe) nanoMOFs with the external medium (PBS with or without protein) at undersaturated conditions to mimic the *in vivo* conditions of the organism. After having explored the important parameters that regulate the degradation of empty micro- and nanoMOFs, a series of drugs containing different functional groups was chosen as molecules of interest for the study of host-guest interactions with the nanoMOFs. The affinity of the groups with the iron sites of the framework were assessed by Density Functional Theory (DFT) modelling, which helped to gain a better understanding over the intermolecular interactions, crucial parameters for the stability of the particles. Overall, the sum of techniques used for this thesis brought new insights into the degradation mechanism of iron-based carboxylate porous particles for their use as therapeutic vectors.